Experimental Deformation of Olivine Aggregates

A DISSERTATION

SUBMITTED TO THE FACULTY OF THE

UNIVERSITY OF MINNESOTA

BY

Cameron David Meyers

IN PARTIONAL FULFILLMENT OF THE REQUIREMENTS

FOR THE DEGREE OF

DOCTOR OF PHILOSOPHY

David L. Kohlstedt, PhD

December 2023

Copyright Page

Acknowledgements

The author wishes to acknowledge the help of his Ph.D. advisor, David Kohlstedt, who was critical to the completion of this thesis. David was a constant source of encouragement, critical feedback, creative scientific ideas, and, most of all, patience. The author would also like to acknowledge the help of all his collaborators throughout the Ph.D. process, especially those in the Kohlstedt research group. The technical and scientific advice of Mark Zimmerman was crucial in the work included in this thesis and also played a large influence in the author's later endeavors as a laboratory technician and staff researcher at Brown University. The specific assistance of Amanda Dillman, Jacob Tielke, Matej Pec, and Miki Tasaka in teaching experimental methods is also particularly acknowledged. Additional scientific discussions with Harison Weisberg, Leila Hashim, Lars Hansen and many others were also greatly appreciated. The author would also like to acknowledge Nick Seaton, Seth Kruckenberg, Zachary Michels and Andrew Cross for their assistance in collecting EBSD measurements. Additionally, this work was supported by the DOE NNSA SSGF fellowship.

The author would also like to thank his friends and family for their unwavering support throughout the tough process of earning his Ph.D. Specifically, the author would like to thank his mother, Rebecca, for her steadfast encouragement and his father, Roger, who passed away during the writing of this work. Roger was a constant supporter throughout this process, and it is a shame that he did not get to see it come to completion. This thesis is dedicated to his memory.

Abstract

Mechanical modeling of deformation in the Earth's upper mantle relies on flow laws derived from deformation experiments on olivine aggregates. Olivine is the primary phase in Earth's upper mantle and is thought to control its bulk mechanical behavior. In particular, it is critical to understand the dependence of strain rate on grain size, temperature, and stress. Additionally, as olivine rocks are deformed their microstructures evolve by dynamic recrystallization and formation of crystallographic preferred orientation (CPO), which influence their mechanical properties. In this thesis, we add to the large body of work attempting to understand the physics of high-temperature deformation of olivine aggregates by presenting new experimental data, using both hot-pressed olivine aggregates and naturally sourced dunite rocks as starting material. In Chapter 1, the thesis is broadly summarized in an introductory chapter. This is followed by the description and characterization of a new method for synthesizing fine-grained, nearly pore-free olivine aggregates by evacuated hot pressing of naturally sourced olivine powders in Chapter 2. In this chapter, the material is thoroughly characterized, densification kinetics are examined, and differences in grain growth kinetics between this new method and conventional methods are demonstrated. In Chapter 3, we examine data from experiments on evacuated hot-pressed aggregates that were deformed in torsion in a gas-medium deformation apparatus. These data are used to understand the microstructural evolution of olivine aggregates deformed to high strain. Microstructures were characterized by electron backscatter diffraction (EBSD) to investigate grain size and CPO evolution. This is followed, in Chapter 4, by the presentation of an experimental, wherein evacuated hot-pressed olivine aggregates were deformed in a deadweight creep apparatus at 1 atm confining pressure at conditions where diffusion creep was active. The data are examined to evaluate the diffusion creep flow law for olivine. Finally, in Chapter 5, we present an experimental study aimed at measuring the anisotropy in viscosity of naturally sourced dunite rocks with a preexisting CPO. These studies, together, represent a significant contribution to our understanding of the physics of olivine deformation, and in turn, mantle dynamics.

Keywords: olivine, experimental rock deformation, plate tectonics, mantle dynamics, crystallographic preferred orientation, deformation mechanisms

Table of Contents

List of Tables

List of Figures

Chapter 1 Introduction

1.1 Introduction

The expression of plate tectonics on Earth, wherein rigid lithospheric plates translate at the surface accommodated by viscous flow in the mantle asthenosphere below, is distinct among the rocky planets of the solar system. This unique behavior leads to the recycling of geological materials and plate motions at Earth's surface. Plate tectonics is the process that underlies the expression of Earth's topography and the generation of earthquakes. To understand plate tectonics, it is critical to investigate the physical processes of flow in Earth's upper mantle.

Olivine is the dominant phase in Earth's upper mantle and is generally considered to control its bulk mechanical properties. Therefore, experiments on olivine aggregates have been the focus of the community's understanding of mantle strength. This perspective is outlined in the seminal work of Hirth and Kohlstedt, (2003), wherein experimental data from several studies were compiled to establish an easily applied flow law for olivine across a range of stress, grain size, temperature, and water contents. A flow law is a constitutive equation that is used to compute the strain rate of the material when subjected to stress, which may depend on a number of both intrinsic and extrinsic variables. A flow law typically aims to parameterize the outcome of specific deformation mechanism or the physical process that leads to strain, such as diffusion creep, dislocation creep, or dislocation-accommodated grain boundary sliding.

The extensive use of these flow laws in the earth sciences literature demonstrates the interest of geodynamicists and geophysicists in such data. However, deformation experiments at high temperature and confining pressures are technically challenging to execute, and, therefore, the number of data points is relatively small to constrain a very complex problem. Further, data produced by laboratory experiments are limited to the timescales and lengthscales of the laboratory and, therefore, the results require extrapolation in order to be applied to Earth problems. This situation compounds the need to understand the underlying physics of mantle deformation, rather than simply relying on empirical results.

This document is designed to add to the body of work addressing this topic through the presentation of four experimental projects that explore the properties of olivine aggregates. First, a new method for synthesizing experimental starting materials is introduced. When conducting laboratory experiments aimed at characterizing material properties, it is critical that

the material tested is representative of the material that one aims to study. Toward that goal, a new method for synthesizing olivine aggregates formed from naturally sourced material is outlined, wherein the porosity of the samples was reduced to extremely low values. Next, we explore the microstructural evolution of these materials when deformed to high strains in a torsional geometry. These experiments are aimed at understanding the evolution of the microstructures of mantle rocks during deformation, including changes in grain size, shape, and crystallographic preferred orientation (CPO), all of which in turn influence the mechanical properties. Next, we present an experimental study wherein these same materials were deformed at relatively low stresses, conditions at which the diffusion creep mechanism was dominant. This study applies several perspectives in order to understand the flow law for diffusion creep of olivine aggregates, including detailed comparisons to the results from published datasets. Finally, another experimental study is presented, wherein natural dunite rocks with a preexisting CPO were deformed in varying orientations relative to the CPO. This study again addresses our understanding of the influence of the microstructure of a rock on its mechanical properties. In combination, the following document contributes new data and perspectives toward our understanding of high-temperature experimental deformation of olivine aggregates and, therefore, toward our understanding of flow in Earth's upper mantle.

1.2 References

Hirth, G., & Kohlstedt, D. (2003). Rheology of the upper mantle and the mantle wedge: A view from the experimentalists. Geophysical monograph-American Geophysical Union, 138, 83-106.

Chapter 2 Synthesis of Evacuated Hot-Pressed Olivine Aggregates

2.1 Abstract

Data from deformation and grain growth experiments on synthetic olivine ceramics have been broadly applied to model processes occurring in the Earth's upper mantle; however, synthesis of olivine samples with a controlled microstructure and chemical composition is a technical challenge. In the present study, naturally derived, fine-grained olivine ceramics were synthesized by an evacuated hot-pressing method that yielded samples with porosities of <0.1%, a marked reduction compared to samples synthesized by conventional hot-pressing, which typically retain ~1% porosity. Evacuated hot-pressing results in olivine samples that are transparent at the mm-scale and bright green, resembling the appearance of the single crystals from which they are synthesized, while conventionally hot-pressed aggregates are opaque and milky-green. The contrast in macro-scale transparency reflects the difference in micro-scale porosity. Fourier transform infrared (FTIR) and Raman spectroscopy revealed a prominent CO_2 signature in conventionally hot-pressed aggregates, which was nearly eliminated by the evacuated hot-pressing method. Annealing experiments, some at 1 atm and others at 300 MPa confining pressure, on samples synthesized by both methods, demonstrate contrasting grain and pore growth in samples synthesized by the two different methods. At high temperatures, grains in the evacuated hot-pressed samples coarsen rapidly by abnormal grain growth, while conventionally hot-pressed aggregates retain a fine-grained microstructure for long annealing times. When annealed at 1 atm, conventionally hot-pressed samples eventually disaggregate due to extensive pore growth. In contrast, pore growth is limited in samples synthesized by evacuated hot-pressing and abnormal (exaggerated) grain growth proceeds. The rate of coarsening is substantially faster for samples annealed at a confining pressure of 300 MPa relative to those annealed at 1 atm at the same temperature. After hot-pressing, any trapped porosity has a pore pressure of ~300 MPa. As such, these pores grow slowly if a sample is annealed at a confining pressure of 300 MPa, however, they grow rapidly, driven by the pressure gradient, during annealing at 1 atm.

2.2 Introduction

As the primary phase in Earth's upper mantle, olivine is generally recognized as controlling this regions bulk mechanical behavior during high-temperature convective flow. However, many mantle processes occur on spatial and temporal scales that prohibit direct observation or replication in the laboratory. Therefore, carefully designed experiments on mantle materials are used to constrain the underlying physics that is needed to model mantle processes critical to understanding plate tectonics. Materials for experiments must be selected carefully, as most natural dunites have fractured or chemically altered microstructures, inclusion of secondary phases, and/or large grain sizes that limit their use in laboratory experiments. This situation has motivated a body of laboratory experiments on synthetic, olivine-rich aggregates. Flow laws, used to extrapolate data from experimental deformation studies on laboratory-fabricated, olivine-rich rocks to natural conditions, form much of the basis for estimating the viscosity of the mantle, critical when modelling Earth dynamics (e.g., Karato, 1986; Hirth and Kohlstedt, 1995a,b; Hansen et al., 2011; Yabe and Hiraga, 2020). Other studies that focus on microstructural characterization have also helped identify deformation mechanisms and associated grain size and fabric evolution in polycrystalline olivine aggregates, in order to identify physical processes that may influence deformation in the upper mantle (e.g., Bystricky et al., 2000; Hansen et al., 2012; Hansen et al., 2014). In addition to studies of deformation, high-temperature static annealing experiments have yielded insights into the kinetics of physical processes such as diffusion, dislocation recovery, and grain growth (e.g., Karato 1989; Nichols and Mackwell, 1991; Farver et al., 1994; Farla et al., 2011). Bulk electrical conductivity results obtained on laboratory-synthesized olivine aggregates have also been applied to interpretations of geophysical conductivity data (e.g., Pommier et al., 2015). Similarly, the nature of seismic attenuation, an important geophysical probe, has also been informed by attenuation experiments on synthetic polycrystalline olivine aggregates (e.g., Gribb and Cooper, 1998; Jackson et al., 2002; Jackson and Faul 2010). Such examples illustrate a portion of the growing body of laboratory measurements on synthetic olivine aggregates, which underlay attempts at understanding and quantifying physical processes that occur in Earth's upper mantle. However, synthesis of olivine samples with controlled microstructure and chemical composition is a technical challenge. Grain-size distribution, impurities, and porosity often influence physical properties of interest, including grain-growth kinetics, viscosity, seismic attenuation, and chemical diffusion.

The experimental work described above relies on the synthesis of high-density (low-porosity), fine-grained (1 to 10s of μm) olivine ceramics with controlled chemical composition and microstructure. A number of methods for synthesizing polycrystalline olivine aggregates have been developed for experimental studies that differ in both feedstock material and synthesis/densification conditions. In many cases, sample feedstocks were prepared by pulverization of naturally sourced olivine from either hand-selected, gem-quality single crystals (e.g., Schwenn and Goetze, 1978; Karato 1986; Hirth and Kohlstedt, 1995a,b; Hansen et al., 2011) or from dunite rocks (e.g., Gribb and Cooper, 1998). In other cases, olivine feedstock powders were synthesized by reacting reagent-grade oxide powders (e.g., Koizumi et al.,2010; Yabe et al., 2020) or solution-gelation (sol-gel) preparations containing tetraethyl orthosilicate (TEOS) as their silica source (e.g., Burlitch et. al.,1991; Jackson et al., 2002; Faul and Jackson, 2007; Faul et al., 2011). A few studies have also employed a mix of natural olivine reacted with oxides to change the Fe/Mg ratio of the final sample (Zhao et al., 2009; Hansen et al., 2012; Tasaka et al., 2016). In the present study, we followed the lead of many other experimentalists, synthesizing samples from naturally sourced olivine feedstock, generated by pulverization of hand-picked, gem-quality San Carlos olivine single crystals. San Carlos olivine has become a commonly used feedstock material due to the abundance and quality of this xenolith-derived olivine, which has forsterite content (major element composition) that is thought to be typical of Earth's upper mantle (~Fo_{90}) and similarly contains trace elements such as Ni, Ti, Ca, and Al in natural abundances. Major and trace element chemistry likely play a role in critical properties, such as hydroxyl-defect solubility, melting temperature, and viscosity (Zhao et al., 2004; Zhao et al., 2009; Faul et al, 2016; Yabe et al., 2020) and, therefore, data from experiments on naturally derived aggregates are more directly applicable to earth processes. However, studies using oxide and sol-gel derived feedstocks have specifically provided critical insights into the role of trace element impurities on high temperature deformation (Faul and Jackson 2007; Faul et al., 2011; Faul et al, 2016; Yabe and Hiraga 2020, Yabe et al., 2020).

Fine-grained, low-porosity olivine ceramics used in experimental studies are typically densified from olivine feedstock powders at high temperatures. Several methods of densification have been used, including vacuum sintering (Koizumi et al., 2010; Hiraga et al., 2010; Yabe et al., 2020), spark plasma sintering (Guignard et al., 2011, Koizumi et al. 2020), uniaxial hot pressing (in some cases vacuum assisted) (Shwenn and Goetze, 1978; Cooper and Kohlstedt, 1984; Gribb and Cooper, 1998), and hot isostatic pressing (HIP), referred to within as conventional hot pressing (Karato, 1986; Hirth and Kohlstedt, 1995a,b; Faul and Jackson, 2007;

Hansen et al., 2011; Faul et al., 2011). A large body of experimental work has been produced using samples synthesized by the conventional hot-pressing technique, specifically using San Carlos olivine starting powders. In this method, cold-pressed starting powders are sealed in a metal capsule (typically made of Ni to act as a buffer against oxidation or reduction) and subjected to elevated confining pressures and temperatures. When synthesized in a gas-medium apparatus (as in this study), pressures of about 200-300 MPa and temperatures between 1150-1300°C are typically applied to promote densification. Conventionally hot-pressed olivine aggregates retain roughly 1% porosity after quenching from high pressure. These residual pores are trapped at high pressures, and therefore, must be at nearly the pressure of hot pressing when removed from the rig and brought to ambient conditions.

In this study, we present an improved, evacuated hot-pressing method for producing samples of a similar composition and grain-scale microstructure but with porosity reduced by over an order of magnitude. Samples generated by this method retain less gas during densification and thus are nearly pore free at the microscale. Consequently, they are transparent at the mm-scale. In addition to being motivated by an interest in understanding earth processes, these experiments offer a contribution to the growing field of transparent ceramics (Wang et al., 2013; Goldstein and Krell, 2016; Xiao et al., 2020). A major motivation for this synthesis method is the potential for sample material that can be used in deformation experiments at one atmosphere, which are relatively simple to perform, while achieving excellent resolution of mechanical data (See Chapter 4). The results from static annealing experiments on both conventional and evacuated hot-pressed samples demonstrate dramatic differences in the rate and style of grain growth, suggesting that porosity pins grain boundaries, slowing the rate of grain boundary migration.

2.3 Methods

2.3.1 Synthesis

For this study, both conventional and evacuated hot-pressed dunites were synthesized from powders of pulverized, naturally sourced olivine crystals densified in a gas-medium apparatus. Gem-quality single crystals of San Carlos olivine were hand-picked to avoid secondary phase inclusions and surface alteration. These crystals were mechanically ground to grain sizes of <1 mm using a disc mill. The resulting material was then milled to fine grain sizes

using a fluid-energy mill. Powders with different average grain sizes were retained from separate millings.

Powder-size distributions were measured using laser diffraction in a Microtrac Bluewave. Powders were suspended in recirculating deionized water for particle size analyses. To understand the grain-size sensitivity of the densification process, we synthesized evacuated hot-pressed aggregates from powders with measured mean sizes of 2.2, 2.7, 6.2, 8.2, and 23.4 μm, with grain-size distributions presented in Fig. 1. The powders were dried in a mixed-gas furnace at ~1100°C for ~10 h under a flowing mixture of CO/CO_2 in an alumina boat lined with nickel foil. The gas mixture was chosen to maintain fO_2 conditions near that corresponding to the Ni/NiO solid-state buffer at this temperature. Powders were then stored in a vacuum drying oven maintained at ~100°C.

Powder compacts were prepared by uniaxially cold-pressing San Carlos olivine powders into a nickel capsule. Powder was added in ~0.5 gm increments to the nickel can; each layer of powder was uniaxially pressed with a steel punch at approximately 100 MPa. This method of cold-pressing results in a powder compact with 60-70% theoretical density (TD), the density depending on the grain size distribution of the feedstock powder. The remaining pore space is filled with atmospheric gas. Cold-pressed powder compacts prepared for conventional hot-pressing were sealed with press-fit nickel caps on either end of the nickel can. This step ensured that the powder and pore gasses were sealed into the can creating a closed system wherein pore gasses could not escape during subsequent hot pressing. In contrast, cold-pressed compacts prepared for evacuated hot pressing had a porous alumina cap on one end. The porous cap was vented to vacuum during subsequent hot-pressing to minimize the amount of gas trapped during the process of densification and the resulting isolation of porosity. In this design, powder compacts were hot pressed in an open system, such that it was critical to control fO_2 during hot-pressing to maintain the chemical environment within the olivine stability field. In general, the retainment of oxygen (from air) in pore gases during conventional hot pressing has the fortunate consequence of establishing a solid-state fO_2 buffer by reaction of the oxygen with the metal capsule. In the case of evacuated hot pressing, pore gas is not effectively trapped, such that the chemical environment within the capsule is controlled by the solid materials present near the sample. For thoroughly dried powders, the addition of NiO powders to the sealed end of the capsule was necessary to buffer the fO_2 at Ni/NiO to avoid

reduction of olivine. The active buffering of the sample was confirmed by the reduction of much of the NiO powder to Ni metal during the hot press.

Powder compacts were hot pressed using a gas-medium, Paterson-type apparatus at 1250°C under a confining pressure of 300 MPa. The pressure compensated piston design of this apparatus ensured that the material was densified under nearly isostatic conditions. Each nickel-encapsulated powder compact was loaded into the apparatus between dense alumina pistons with a narrow bore containing an alumina sheathed thermocouple to monitor the temperature close to the sample. The temperature is estimated to vary by <2°C across the length of the sample based on furnace calibrations with the sample replaced by an alumina rod with a small-diameter axial hole for a sliding thermocouple. In the case of evacuated hot-pressed samples, the opposing side was evacuated through a bore in a dense alumina piston, which was in contact with the porous alumina cap, allowing active evacuation of pore gasses during heating and early stages of densification, during which the porosity is interconnected. The alumina column was terminated by bored zirconia pistons on either end. The entire column was jacketed in a steel tube and placed between bored steel pistons that mate with the ends of the pressure vessel in the apparatus. Column designs for conventional and evacuated hot-presses are shown in Fig. 2.

In the case of evacuated hot-pressing experiments, the sample compact was evacuated for ~12 h before heating and pressurization with a vacuum pressure of <0.3 mbar. This vacuum pressure was maintained throughout the experiment, often improving to <0.1 mbar during the process. Temperature was ramped at a rate of ~0.25°C/s, which was reduced to ~0.05°C/s between ~400 and ~600°C, allowing additional time for adsorbed gasses and moisture to escape. The experimental apparatus used for synthesis is equipped with a pressure compensated axial position, with internal load and displacement sensors. Thus, changes in column length during densification were monitored by applying a small stress (<2 MPa) for a few seconds periodically during densification. During periods when the temperature or pressure were changing, displacement measurements were also influenced by thermal expansion and compliance of the apparatus. Data were corrected for these effects using a linear function of pressure and temperature derived from monitoring the axial position at intermediate temperatures, where negligible diffusional densification took place. Once run conditions were reached, the temperature and pressure were held constant, during which time most of the densification of samples occurred. Therefore, this correction has little influence on the

interpretation of the data. If compaction is isotropic, density is related to linear shortening through the following relationship:

$$\rho = \frac{\rho_0}{(1 + \Delta L/L_0)^3} \ , \qquad (1)$$

where ρ_0 is the reference density at a reference position at which the change in length, ΔL, is equal to 0. L_0 is the length of the sample at the reference density (Rahaman, 2008). We used estimates of the final density from polished micrographs and sample length as the reference in our calculations of relative density. For simplicity, all densities were normalized to the density of olivine in our analyses, such that ρ = 1 in a pore-free sample (therefore, ρ is relative to the theoretical density, TD, in our analyses – this quantity is referred to as the relative density). Measurements of the final sample length can be obscured by the sample jacket, such that the reported initial relative densities are considered to be accurate to within ±5%. Further, compaction of the NiO buffer powder layer, which densified simultaneously with the olivine powder, had some variation in thickness between experiments, further influences the data. However, estimates of density and densification rate during the intermediate stages of compaction (ρ = 0.85-0.95), which are less sensitive to estimates of L_0 are useful for interpreting densification kinetics. The volumetric densification strain rate is equal to

$$\dot{\varepsilon_v} = \frac{1}{\rho}\frac{d\rho}{dt} \ . \qquad (2)$$

In general, high-temperature conditions were sustained until the volumetric strain rate slowed to at least 10^{-6} s^{-1}. However, in many cases the final volumetric strain rate was less than 10^{-8} s^{-1}, a value below the practical resolution of the apparatus (i.e., given typical experimental time constraints, approximately 0.1 micron of linear displacement over about 1500 s).

2.3.2 Annealing Experiments

Several static annealing experiments were performed on sub-samples of conventional and evacuated hot-pressed samples, some at 1 atm (0.1 MPa) and others at 300 MPa, to observe microstructural evolution of both grains and pores. All of the annealing experiments presented within were performed on hot-pressed samples prepared from powders with an average starting size of 6.2 μm.

In the case of 1-atm experiments, sub-samples of an evacuated and a conventional hot-pressed sample were placed on a bed of loose olivine powder in an Al_2O_2 boat lined with Ni foil.

A thermocouple was placed directly above the sample to monitor the annealing temperature. The samples were heated to annealing temperatures of between 1250° and 1350°C at a rate of roughly 200°C/h and cooled at the same rate. Samples were annealed in a CO/CO_2 gas mixture, using a ratio calculated to maintain fO_2 near the Ni/NiO buffer in the hot zone.

In the case of confined static annealing at 300 MPa in a gas-medium apparatus, sub-samples of evacuated hot-presses were surrounded by San Carlos olivine powder and uniaxially pressed into a sealed Ni capsule. The surrounding powder was the same as that used to synthesize the evacuated hot-pressed sample. Sub-samples were annealed for up to 21 h at either 1250° or 1300°C, while at confining pressure. In this configuration, the surrounding matrix is, itself, a conventional hot-press. Therefore, we were able to directly observe differences in grain growth between the evacuated hot-pressed sample and the surrounding conventionally hot-pressed material annealed under the same conditions. However, it is noted that the conventionally hot-pressed sample is initially low density and densifies in the early portion of the experiment, while the evacuated hot-pressed sub-sample is fully dense throughout the annealing experiment. This difference becomes negligible for experimental annealing times that are long compared to the timescale of densification.

2.3.3 Microstructural Characterization

The microstructures of hot-pressed and annealed sub-samples were characterized by a combination of optical microscopy and SEM techniques, including backscatter electron (BSE) images and electron backscatter diffraction (EBSD) analyses. All microstructural characterization presented below was performed on samples prepared from 6.2 µm starting powder, chosen for their superior transparency relative to other samples. Sample surfaces were prepared for imaging by progressive polishing with diamond lapping films to a final grit of 0.5 µm, followed by roughly 30 minutes of manual polishing and etching with colloidal silica (Syton). For SEM imaging, the sample surface was coated with a 0.5 nm thick carbon layer. EBSD mapping was performed on some samples with a JEOL 6500 field emission gun SEM using Oxford HKL Channel 5 software. We also oxidized some evacuated hot-pressed samples to decorate dislocations and grain boundaries (Kohlstedt et al., 1976). Polished surfaces were oxidized in air at 900°C for 45 minutes in a box furnace, then repolished to remove the iron-magnesium oxide surface coating (Wu and Kohlstedt, 1988), revealing a decorated microstructure. BSE images of decorated sample surfaces were used to image porosity, dislocations, and grain boundaries.

2.3.4 Chemical Composition

One evacuated hot-pressed sample and two annealed sub-samples were characterized with an electron microprobe to investigate the elemental composition and quantify the degree of compositional variability. EDS analyses were made using a Cameca SX100 microprobe operated at 15kV and 20 nA. Microprobe measurements were also used to find and identify secondary phases. Several linear profiles and random point measurements were taken, yielding 105 quantitative chemical analyses.

2.3.5 FTIR and Raman Spectroscopy

FTIR and confocal Raman spectroscopy were used to further characterize differences between evacuated and conventionally hot-pressed olivine aggregates. FTIR spectra were acquired in transmission mode on specimens of approximately 100 µm thickness through a 50 µm aperture using a Bruker Hyperion system. We measured IR absorption from 1300 to 5000 cm^{-1} wavenumber, a range that spans the spectral features typically important in studies on olivine, ranging from the cluster of SiO_2 peaks at wavenumbers below 2200 cm^{-1} to the region in which OH-related defects cause absorption in the 3750 to 3100 cm^{-1} range (Bell et al., 2003). We collected thickness-normalized FTIR absorbance spectra from several samples including conventionally hot-pressed material (6.2 µm starting powder) prepared for this study, conventionally hot-pressed material prepared by Hirth and Kohlstedt (1995), evacuated hot-pressed material (6.2 µm starting powder) prepared for this study, and San Carlos olivine single crystals cut along perpendicular sections.

To further assess the spatial distribution of trapped pore phases, we collected 2-D spectral maps of Raman shifts using a Witec Alpha300R confocal Raman microscope. Maps were collected at submicron resolution at a depth chosen to maximize the Raman shift signal of olivine associated peaks (~5 µm beneath the sample surface). We produced false color maps of integrated peak intensities taken from peaks of interest to highlight differences between conventional and evacuated hot-pressed samples.

2.4 Results

2.4.1 Densification Measurements

The densification rate during evacuated hot-pressing, calculated from the measured axial shortening, was strongly particle-size dependent, with fine-grained powder compacts densifying more quickly than coarse-grained compacts. The relative density is plotted as a function of time in Fig. 3a for samples prepared from powders with particle sizes of 2.2, 2.7, 2.9, 6.2, 8.2, and 23.4 μm. This information was used to extract the densification strain rate, which is plotted as both a function of relative density and time in Figs. 3b and c, respectively. We note that some densification occurred during ramping of pressure and temperature to run conditions, especially in the case of the smallest powder size for which densification is rapid. Also, not all samples reached full density, especially those prepared from the largest powder size for which long times were necessary to reach full density.

2.4.2 Chemical Composition

Compositional measurements revealed a uniform chemical composition in both the evacuated hot-pressed sample and the annealed sub-samples that were analyzed with the microprobe. The average chemical composition and its variability are reported in Table 1. Linear profiles, measured from annealed sub-samples that underwent extensive abnormal grain growth, revealed no systematic compositional variation between large abnormal grains and the fine-grained matrix. These analyses also confirmed the existence of <0.1 vol% of Cr-spinel. Additionally, individual enstatite grains were identified, indicating that the silica activity was buffered by the powder composition despite densification in contact with NiO powder. The starting powder likely contains a small amount of contamination from Si-enriched melt inclusions or enstatite inclusions that buffer the silica activity. Enstatite is present in our samples at the <0.1 vol% level.

2.4.3 Microstructural Characterization of Hot-Pressed Samples

Qualitative observation of the macroscopic color and transparency was an excellent indicator of the relative amount of grain-scale porosity in the microstructure, consistent with observations across the field of transparent ceramics (Wang et al., 2013). Conventionally hot-pressed aggregates typically are milky green and opaque at the mm-scale, retaining 1-2% porosity. The evacuated hot-pressed aggregates that we produced, using the same powders, were darker green and transparent at the mm-scale, such that one could easily read text

through a 1-mm-thick, polished slice. This point is demonstrated in the photographs presented in Fig. 4.

The side-by-side reflected light micrographs in Fig. 5 of conventional and evacuated hot-pressed aggregates, synthesized from powder with a particle size of roughly 6 μm, illustrate the dramatic reduction in porosity at the grain scale of the latter. We note that it is challenging to determine porosity from optical images because focus and exposure can be easily manipulated to hide porosity. These samples were carefully prepared and cleaned such that we are confident that dark features in reflected light represent porosity and not polishing defects, which can be difficult to distinguish. A simple way to investigate the pore structure is to focus through the sample surface looking for bright reflections below the polished surface, a method we used frequently to evaluate sample porosity.

Porosity and grain-scale microstructure were further examined by BSE imaging of oxidation-decorated evacuated hot-pressed samples. Images from oxidation-decorated samples allow for easy identification of grain boundaries, pores, and some dislocation structures, as demonstrated in Fig. 6. Pores in these images appear as dark spots. For the sample imaged in Fig. 6, a small number of submicron pores were identified typically at triple junctions, with others trapped in grain interiors as well. From these images, the density of these samples is estimated to be >99.9% TD. Dislocation densities estimated from these images are on the order of 10^{10}-10^{11} m^{-2} corresponding to stresses between 10-30 MPa, using the relation presented by Kohlstedt and Goetze (1974). San Carlos olivine single crystals have been measured to contain roughly 10^{11} m^{-2} (Toriumi ,1979); however, substantial variation in the feedstock powder is expected due to the combination of many crystals (that are likely to have different initial dislocation densities) and the nucleation of dislocations during pulverization of the starting powder.

The EBSD map in Fig. 7 of the evacuated hot-pressed material reveals a uniform fine-grained microstructure with an average grain size of ~5 μm, with a few isolated large grains (10-20 μm) with straight boundary segments (see arrows in Fig. 7). The material has a nearly random distribution of grain orientations with an M-index of 0.02. However, a subtle maximum of the [010] axis occurs parallel to the sample axis. Subgrain boundaries (misorientation <10°) are highlighted in red, demonstrating that many grains contain subgrain boundaries after hot pressing. Note that subgrain boundaries do not appear to be present in the larger grains with straight boundary segments.

2.4.4 FTIR and Raman Spectroscopy of Hot-Pressed Samples

FTIR spectra from conventionally hot-pressed aggregates prepared for multiple studies have an absorption peak at 2345 cm^{-1} wavenumber, typically associated with CO_2; this peak was absent in spectra from evacuated hot-pressed aggregates. The FTIR spectra for a variety of samples, including samples used as starting material for the experimental studies of Hirth and Kohlstedt (1995a), are plotted in Fig. 8. This peak appears significantly above atmospheric background and as a singlet, rather than a doublet, as is expected from atmospheric CO_2. This peak was not detected in spectra collected from evacuated hot-pressed material or single crystals of San Carlos olivine. This absorption peak may result from trapping and concentrating of atmospheric gas in pores, adsorption of atmospheric gasses on powder surfaces, and/or deposition of carbon during drying of powder in a mixed gas furnace that is later oxidized during oxygen-buffered hot-pressing.

Two-dimensional maps of Raman shifts provided further evidence of a CO_2 phase trapped in the pores of conventionally hot-pressed San Carlos olivine prepared for this study. Two distinct spectra were identified, as presented in Figs. 9a,b. The primary spectra measured from our samples is associated with olivine, matching known reference peaks. In some regions, olivine-associated peaks were depressed relative to neighboring regions, indicating interaction of the laser beam with a trapped pore. In many cases, depressed olivine-associated peaks occurred simultaneously with other peaks, notably Raman shifts of 1277 and 1382 cm^{-1}, which are associated with CO_2 (including sub-maxima typical of CO_2) (Windisch et al., 2012). The spatial distribution of these distinct spectra is illustrated by the maps presented in Figs. 9c,d, which are colored by the integrated area beneath the 850 cm^{-1} olivine-associated peak (green intensity) and integrated area beneath the 1382 cm^{-1} CO_2-associated peak (red intensity). Maps of spectral features measured from conventionally hot-pressed material reveal substantial regions with depressed olivine peaks, areas in which the laser beam presumably interacted with a nearby trapped pore. In many cases, CO_2 peaks are associated with these regions. Because Raman measurements were focused at a depth of 5-10 μm below the sample surface, we infer that these features are related to trapped porosity (as opposed to being related to features at the polished surface). Maps of evacuated hot-pressed material have relatively few regions in which olivine peaks are depressed, and the CO_2-related peaks are nearly eliminated. The spectral signature of CO_2 in conventionally hot-pressed samples is an indication of trapped gas, which expands to increase the porosity in a sample when it is annealed at low pressure, as

described in the following section. The elimination of CO_2 related peaks in evacuated hot-pressed samples is likely related to reduced pore growth relative to conventionally hot-pressed samples during annealing at low pressure. This observation indicates that much of the gas was removed during the evacuation, resulting in less stored gas to drive pore growth.

2.4.5 Static Annealing Experiments

Static annealing experiments, both at 1 atm (0.1 MPa) in a mixed-gas furnace and at 300 MPa in a gas-medium apparatus, demonstrated dramatic enhancement of grain growth in evacuated hot-pressed San Carlos olivine relative to conventionally hot-pressed material. Extensive pore growth and limited grain growth occurred in conventionally hot-pressed samples annealed at 1 atm. However, pore growth was greatly reduced in parallel experiments on evacuated hot-pressed material, and abnormal grain growth was pervasive. This contrast in microstructural evolution is demonstrated by the micrographs presented in Fig. 10 and Fig. 11. In both cases, the micrographs of annealed samples are presented at the same scale along with micrographs of the original, hot-pressed sample. After long anneal times at high temperatures, the microstructure of evacuated hot-pressed material is saturated by abnormal grain growth with many grains on the scale of 100 μm or larger. In the micrograph presented in Fig. 11b, etched grain boundaries appear as large-scale topographic features. These micrographs also reveal pervasive intracrystalline cracking of large abnormal grains. We infer that these cracks resulted from stresses related to quenching due to crystallographic anisotropy of thermal expansion, which is amplified by the large grain size (Evans, 1978; Cooper, 1990). In conventionally hot-pressed material, which remained fine grained, intracrystalline cracks were not observed. Based on the micrograph presented in Fig. 10b, porosity increased to over 10% in a conventionally hot-pressed sample annealed at 1350°C at 1 atm. Such pore growth results from expansion of high-pressure pores. Annealed and quenched conventionally hot-pressed material become whiter in color, more opaque, and more fragile. Evacuated hot-pressed material was opaque after annealing at 1 atm but retained a green color, appearing macroscopically similar in color to a conventional hot press containing roughly one percent porosity. While pore growth in annealed, evacuated hot-pressed material is difficult to quantify due to cracking and grain growth, the macroscopic appearance indicates that the samples remain fairly dense after annealing at 1350°C for the longest times tested, increasing the amount of porosity by only a few percent.

After static annealing at 300 MPa, the contrast in grain growth kinetics is even more apparent. Abnormal grain growth occurred even more rapidly in evacuated hot-pressed material

annealed at 300 MPa than during the parallel experiment at 1 atm. Micrographs, presented in Fig. 12a,b, of evacuated hot-pressed samples, which were embedded in a conventionally hot-pressed material for high-pressure annealing, provide a clear demonstration of the difference in grain growth behavior resulting from each technique. Although the evacuated hot-pressed sample was already densified at the start of this experiment, the long side-by-side annealing demonstrates that the conventionally hot-pressed material could not have similar grain growth rates. Further examination by EBSD revealed that the grain-size of the annealed evacuated hot-pressed material is highly bimodal, evidence that abnormal or discontinuous grain growth was the primary mechanism of microstructural evolution. This rapid microstructural evolution is demonstrated in the EBSD band-contrast maps presented in Fig. 13. After annealing at high pressure, a few isolated abnormal grains were also observed in the conventionally hot-pressed material. The micrographs presented in Fig. 14 demonstrate that abnormal grain growth in evacuated hot-pressed samples proceeds much more rapidly during annealing at 300 MPa relative to samples annealed at 1 atm. Both annealing experiments presented in these micrographs used the same evacuated hot-pressed starting material, annealed at 1250°C for 12 h; however, the contrast in the microstructures is striking. In the sample annealed at 1 atm, only a few grains appear to have grown abnormally, while the sample annealed at 300 MPa is dominated by coarse grains. Pore growth occurred in the sample annealed at 1 atm, such that the resulting sample has about 2% porosity. In contrast, grain-scale cracking is observed in the sample annealed at 300 MPa, which likely occurred during decompression/cooling due to anisotropy in elasticity or thermal expansion of individual olivine grains.

2.5 Discussion

2.5.1 Role of Porosity in Transparency

The primary challenge in synthesizing transparent ceramics is eliminating the residual porosity that scatters incident light (Goldstein and Krell, 2016). Therefore, this macroscopic optical effect of transparency is representative an attribute of the microstructure that may be important to consider in experimental work done on olivine aggregates. Given the evidence that porosity influences grain-boundary mobility, the role of porosity should be considered when studying processes that involve grain-boundary motion. In many cases, the ideal specimen is pore-free and, therefore, transparent.

Transparency of ceramic materials is an excellent indicator of very low porosity due to the role of pores in optical scattering resulting from local variation in the refractive index. For ceramics containing a single transparent crystal phase, a porosity of <0.1% is typically necessary to achieve bulk transparency (Wang et al., 2013). Transparency in our samples is a first-order indicator of low porosity in our samples; however, other factors also influence optical transparency. Secondary phase inclusions of Cr-spinel (<0.1%) likely diminish transparency. Additionally, the distribution of crystallographic orientation of grains that are individually optically anisotropic leads to additional scattering of light due to local variation in the refractive index.

Interest in transparent ceramics has largely been driven by their unique optical and mechanical properties. A well-known early example is translucent alumina, originally branded “Lucalox”, which is credited as the first, fully crystalline, translucent ceramic, which was achieved in 1959. The key to synthesizing this first translucent alumina was the addition of a small amount of MgO, which limited abnormal grain growth and the associated occlusion of pores during early stages of sintering (Goldstien and Krell, 2016). Since then, applications for transparent ceramics have boomed, and transparent ceramic materials have now been synthesized with a broad variety of chemical compositions and crystal structures. The evacuated hot-pressing method described in this study is reminiscent of the procedures used for synthesizing many transparent ceramics. In many cases, the green body (powder compact), is first vacuum sintered, during which incomplete densification isolates evacuated porosity. This step is followed by a stage of hot isostatic pressure sintering (HIPing) (equivalent to hot-pressing in Earth Sciences literature), wherein the applied pressure eliminates the residual evacuated porosity (Wang et al., 2013; Xiao et al., 2020). The methods developed for synthesizing transparent ceramics may benefit rock physicists who aim to synthesize pore-free samples and should be further explored.

2.5.2 Densification Kinetics

Densification during hot pressing occurs by mass transport of solid material into available pore spaces. Mass transport may occur by surface diffusion, lattice diffusion, vapor transport, grain boundary diffusion, or plastic flow by dislocation motion (Rahaman, 2008). Only the processes that move material from grain boundaries or grain interiors to available pore space lead to densification. Therefore, surface diffusion around and vapor transport across pores do not contribute to densification. In general, the driving force for densification results from applied pressure and surface energy. In the case of isostatic hot-pressing, the driving force

for densification due to the applied pressure is typically much greater than that due to surface curvature, which can therefore be neglected. By modification of equations for creep to account for porosity, Coble (1970) derived the following hot-pressing relationship to model densification:

$$\frac{1}{\rho}\frac{d\rho}{dt} = \frac{HD\psi^n P^n}{d^m \mathrm{R}T}, \quad (3)$$

where *H* is a numerical constant, *D* is the diffusion coefficient of the rate-controlling species, ψ is the stress intensification factor (depends primarily on density, ρ), *d* is the grain size, R is the gas constant, *T* is the absolute temperature, *P* is the pressure, and *m* and *n* are mechanism dependent exponents that reflect the rate-limiting process for densification (Rahaman, 2008). At a given density, pressure, and temperature, the model predicts that densification rate has an inverse dependence on grain size. The sensitivity of the grain-size dependence of densification rate is related to the rate-limiting mechanism, expressed as the grain size exponent, *m*. The exponents and appropriate diffusion coefficients based on this model for possible rate-limiting process are presented in Table 3.

Variation of the starting powder size in our hot-pressing experiments allows for a fit for a grain-size exponent, *m*, from our determinations of density. The grain size sensitivity of densification was investigated by extracting the densification rate for each sample during the intermediate stages of sintering (ρ = 0.87-0.95) by linearly interpolating our results in increments of Δρ = 0.005. This analysis, presented in the plots contained in Fig. 15, demonstrates the grain-size sensitivity of densification. In these plots, the mean powder size determined by laser diffraction is considered the “grain size.” The value of *m* systematically increased from ~1.6 to ~2.3 through this interval in density. Based on the models presented in Table 3, this behavior could be interpreted to reflect a transition from densification rate-limited by grain boundary sliding to densification rate limited by grain boundary/lattice diffusion toward the final stages of densification. However, these models do not account for grain growth during sintering or changes in pore topology or distribution that might influence the grain-size sensitivity of densification, such that identifying a transition in densification mechanism from a subtle change in grain-size sensitivity is likely an over interpretation of the data. That said, considering the evidence that pores pin grain boundaries (discussed below), it is likely that that the grain size remains nearly constant during the densification process when there is significant porosity. It is difficult to incorporate grain growth into these models due to the observed sensitivity of grain growth to porosity and the challenge of characterizing abnormal grain growth.

Regardless of interpretation, the densification data presented in this study demonstrate that densification occurs by one or more grain-size sensitive mechanisms and are particularly useful for practical considerations when estimating the time to reach full density for a given powder size distribution. We found that using a powder with a mean particle size of ~6 μm densified by evacuated hot-pressing for 3-4 h at 1250°C, resulted in highly dense aggregates with a satisfactory uniform, fine grain-size similar to that of the starting particle size, which were considered excellent samples for subsequent annealing and deformation experiments (presented in following chapters).

Densification rates were not systematically monitored during conventional hot-pressing experiments; however, we speculate that the intermediate stages of densification will not be strongly influenced by the differences in method. Anecdotally, a similar amount of time (3-4 h) is needed for both conventional and evacuated hot-pressed compacts to reach the point where densification slows to a rate that is below the practical resolution of the apparatus (considered the final density) when using an intermediate powder size of 5-10 μm (despite the differences in final porosity). During conventional hot pressing, in a sealed capsule, pore gasses are pressurized during densification, which counters the driving force for densification. This issue leads to a breakdown of the model presented in Equation 3, which does not consider pressurization of the pores, such that conventionally hot-pressed samples indefinitely retain ~1% porosity. It is possible that for very long times, pores could coalesce, increasing the density of local regions of the microstructure, however, this behavior has not been observed to occur at laboratory timescales.

2.5.3 Abnormal Grain Growth and Pore-Boundary Interactions

Abnormal grain growth proceeded rapidly in evacuated hot-pressed aggregates, in strong contrast to conventionally hot-pressed counterparts. The difference is interpreted to reflect the influence of pore drag that leads to grain boundary pinning. This difference is highlighted by experiments in which evacuated hot-pressed sub-samples were annealed at high pressure by enclosing them within a conventionally hot-pressed sample. The difference in grain growth rate between the sub-sample and its surroundings is striking (Fig. 12). Further support for the strong influence of porosity on grain growth kinetics arises from the observation that abnormal grain growth was enhanced in evacuated hot-pressed aggregates annealed at elevated confining pressure relative to those annealed at 1 atm. Small amounts of pore growth occurred in samples annealed at atmospheric pressure, indicating that the increase in pore drag

is responsible for slowing abnormal grain growth. In conventionally hot-pressed samples, high-pressure porosity pins grain boundaries, such that grain growth becomes limited by pore coalescence and is effectively halted at laboratory timescales. When annealed at 1 atm, conventionally hot-pressed samples nearly disaggregate, evidence of the extent of the high-pressure gas stored in closed porosity.

Abnormal grain growth has been reported in several other cases in olivine aggregates, particularly in the case of high-pressure annealing under water-added conditions (Karato, 1986) or if a melt phase was intentionally added (Cooper and Kohlstedt, 1984). In these cases, grain boundaries migrated rapidly, entrapping porosity. However, isolated abnormal grain growth has been reported in conventionally hot-pressed aggregates annealed for long times at elevated confining pressure (Hansen et al., 2011). We also observed isolated abnormal grain growth in conventionally hot-pressed aggregates that were annealed for long times; however, we did not observe entrapped pores inside abnormal grains, indicating that pore-boundary separation was limited, again highlighting the role of pore pinning under dry, nominally melt-free conditions. The strong influence of pore drag on grain growth in olivine aggregates has been noted in several other studies as well (Karato, 1989; Nichols and Mackwell, 1991; Evans et. al., 2001). The evacuated hot-pressing method reduces porosity and therefore the role of pore drag in olivine grain growth, offering an experimental advantage for many scientific problems.

The pinning of grain boundaries by pores can be examined in the framework of Zener pinning, a phenomenon known to limit grain growth in polycrystalline aggregates as discussed in detail in the material science and earth sciences literature (e.g. Manohar et al., 1998; Bercovici and Ricard, 2012). The original theoretical treatment of Zener pinning by Smith (1948) assumes that the grain-scale structure is composed of randomly dispersed second-phase particles that are smaller than the grains of the primary matrix phase. As a moving grain boundary meets a pinning particle, it is influenced by a drag force, that is, a force that opposes boundary motion. For a rigid spherical particle, the maximum pinning force is $\gamma\pi d/2$, where *d* is the particle diameter (Evans et al., 2001). The net force on the boundary, F_n, using the approximation of a rigid spherical particle is, therefore,

$$F_n = F - \frac{N\gamma\pi d}{2} \quad , \tag{4}$$

where N is the number of pores along the boundary. However, deformable pores can flatten along boundaries to occlude a larger area as swept through by a moving grain boundary,

increasing its drag force. Grain boundary velocity is proportional to the net force on the boundary, such that drag by pores slows grain growth. Without coalescence or grain boundary detachment of pinning phases, Zener pinning leads to a saturation of grain growth with a maximum grain-size, G_{max}, that depends on both the diameter of the pinning particle or of the pore and the fraction of pores, f, following the relation

$$G_{max} = A\frac{d}{f^p} \quad , \tag{5}$$

where *A* and *p* are constants, close to unity, determined by the grain topology. The ratio of d/f roughly describes the average distance between pinning particles. As a simple example using the above analysis, for pores 1 µm in diameter, 2% porosity would lead to a maximum grain size of 50 µm, while 0.1% porosity would lead to a maximum grain size of 1000 µm. This model describes an endmember case; however, in reality, pores can coalesce, deform, or become included within grains. If pores coalesce or become included, the distance between pinning pores increases, such that the maximum grain-size will increase, therefore, there is no maximum grain-size when considering a dynamic system.

2.5.4 Speculation on the Role of Carbon

The results of our FTIR and Raman spectroscopy measurements indicate that the pores of conventionally hot-pressed material typically contain a CO_2-rich phase. However, it is unknown whether this CO_2 is a result of compression of atmospheric gasses, adsorption of CO_2 on powder surfaces during storage, or deposition of elemental C occurring during the cooling of powders conditioned in mixed CO/CO_2 that is later oxidized during hot pressing. Some experimental evidence suggests that carbon bearing phases (<100 nm in size) form on some olivine fracture surfaces very quickly after exposure to air and that this contamination is difficult to remove by cleaning or polishing because it reappears quickly in air (Olsson, 2012).

When fully sealed in a Ni capsule, conventionally hot-pressed material does not need to be buffered with NiO added to remain in the olivine stability field, while Fe-Ni precipitates formed in some of our attempts at synthesizing evacuated hot-pressed samples without added NiO. It is not clear why the evacuated capsule is so reducing; however, O_2 trapped in pores of conventionally sealed capsules helps maintain fO_2 within the olivine stability field by reacting with the Ni capsule to form NiO, which has been noted after sample recovery. It is likely that the outer Fe jacket is responsible for more reducing conditions when the capsule is evacuated, by acting as an oxygen “getter.”

Karato et al. (1986) is one of the few studies using samples prepared by conventionally hot-pressing San Carlos olivine that presented FTIR spectra covering the wavenumber range of interest in which no anomalous peak associated with CO_2 appeared near 2345 cm^{-1}. However, their samples were enclosed in Fe rather than Ni capsules, bringing the fO_2 of the capsule interior at or below the Fe/FeO buffer, which is out of the stability field for San Carlos olivine, such that Fe-Ni precipitates formed within the aggregates. Using the calibration of fO_2 of French and Eugster (1965) for the graphite-gas system at high-pressure, one would expect graphite to form in equilibrium with Fe/FeO at the experimental conditions tested. Therefore, while these samples retain a few % porosity, CO_2 is unlikely to exist at such reducing conditions. In one of our samples that was evacuated hot pressed with the NiO layer replaced by an Ni can that was pre-oxidized in air, broad D and G peaks were present in Raman maps. These peaks are associated with nanocrystalline graphite (Bertrand et al., 2013). The relevant spectra are presented in Fig. 16. This sample is also darker in color than other evacuated hot-pressed samples, although still transparent. The presence of reduced carbon indicates that this sample experienced more reducing conditions than those with added NiO powder. Thus, an fO_2 below the C/CO buffer may explain the lack of CO_2 associated peaks in Fe-jacketed samples that are present in Ni-encapsulated conventionally hot-pressed San Carlos olivine aggregates prepared for this and other studies. Additionally, Karato et al. (1986) also attempted to avoid carbon deposition during cooling from 1 atm conditioning in mixed CO/CO_2 by flushing the furnace with argon gas, a step that has been skipped by many other researchers but may be critical to avoiding trapped CO_2 in the final hot-pressed material. However, flushing with argon could result in oxidation due to oxygen levels typically present in commercial argon. Therefore, the appropriate temperature and timing of argon flushing during sample cooling is critical.

2.6 Conclusions

While conventional hot-pressing of naturally derived powders leads to a well-densified, fine-grained ceramic suitable for many types of experiments, the resulting olivine samples typically retain ~1% porosity. The present study describes results from an improved method of sample fabrication, wherein the pore space of the powder compact is actively evacuated during densification at high confining pressure, greatly reducing the trapped porosity, achieving <0.1% porosity. This reduction in porosity results in significantly increased transparency of the aggregates. Our results demonstrate that the processes of pore drag and grain boundary

pinning by pores have a strong influence on the grain growth behavior of hot-pressed olivine aggregates. Experimentalists attempting to study olivine aggregates may prefer to adopt this method for sample synthesis in cases where the process being investigated is impacted by the presence of porosity. For our intended annealing and deformation experiments (presented in the following chapters), we found that the optimal samples were synthesized using a powder with a mean particle size of ~6 μm densified by evacuated hot-pressing for 3-4 h at 1250°C, which resulted in highly dense aggregates with a satisfactory uniform, fine grain-size similar to that of the starting particle size.

2.7 References

Bell, D. R., Rossman, G. R., Maldener, J., Endisch, D., & Rauch, F. (2003). Hydroxide in olivine: A quantitative determination of the absolute amount and calibration of the IR spectrum. Journal of Geophysical Research: Solid Earth, 108(B2), 2105.

Bercovici, D., & Ricard, Y. (2012). Mechanisms for the generation of plate tectonics by two-phase grain-damage and pinning. Physics of the Earth and Planetary Interiors, 202, 27-55.

Bertrand, A., Carreaud, J., Delaizir, G., Duclère, J. R., Colas, M., Cornette, J., et al. (2013). A comprehensive study of the carbon contamination in tellurite glasses and glass-ceramics sintered by spark plasma sintering (SPS). Journal of the American Ceramic Society, 97(1), 163–172.

Burlitch, J. M., Beeman, M. L., Riley, B., & Kohlstedt, D. L. (1991). Low-Temperature Syntheses of Olivine and Forsterite Facilitated by Hydrogen Peroxide. Chemistry of Materials, 3(4), 692–698.

Bystricky, M., Kunze, K., Burlini, L., & Burg, J.-P. (2000). High shear strain of olivine aggregates: Rheological and seismic consequences. Science, 290(5496), 1564–1567.

Coble, R.L. (1970) Diffusion models for hot pressing with surface energy and pressure effects as driving forces, J. Appl. Phys., 41, 4798.

Cooper, R. F., & Kohlstedt, D. L. (1984). Sintering of olivine and olivine-basalt aggregates. Physics and Chemistry of Minerals, 11, 5-16.

Cooper, R. F. (1990). Differential stress ‐ induced melt migration: An experimental approach. Journal of Geophysical Research: Solid Earth, 95(B5), 6979-6992.

Evans, A. G. (1978). Microfracture from thermal expansion anisotropy—I. Single phase

systems. Acta Metallurgica, 26(12), 1845-1853.

Evans, B., Renner, J., & Hirth, G. (2001). A few remarks on the kinetics of static grain growth in rocks. International Journal of Earth Sciences, 90(1), 88–103.

Farla, R. J. M., Kokkonen, H., Fitz Gerald, J. D., Barnhoorn, A., Faul, U. H., & Jackson, I. (2011). Dislocation recovery in fine-grained polycrystalline olivine. Phys Chem Minerals, 38, 363–377.

Farver, J. R., Yund, R. A., & Rubie, D. C. (1994). Magnesium grain boundary diffusion in forsterite aggregates The reproducibility. Journal of Geophysical Research: Solid Earth, 99(94), 19,809-19,819.

Faul, U. H., Cline II, C. J., David, E. C., Berry, A. J., & Jackson, I. (2016). Titanium-hydroxyl defect-controlled rheology of the Earth's upper mantle. Earth and Planetary Science Letters, 452, 227-237.

Faul, U. H., Fitz Gerald, J. D., Farla, R. J. M., Ahlefeldt, R., & Jackson, I. (2011). Dislocation creep of fine-grained olivine. Journal of Geophysical Research: Solid Earth, 116(1), 1–12.

Faul, U. H., & Jackson, I. (2007). Diffusion creep of dry, melt-free olivine. Journal of Geophysical Research: Solid Earth, 112(4), 1–14.

French, B. M., & Eugster, H. P. (1965). Experimental control of oxygen fugacities by graphite-gas equilibriums. J. Geophys. Res., 70(6), 1529–1539.

Gribb, T. T., & Cooper, R. F. (1998). Low-frequency shear attenuation in polycrystalline olivine: Grain boundary diffusion and the physical significance of the Andrade model for viscoelastic rheology. Journal of Geophysical Research: Solid Earth, 103(B11), 27,267-27,279.

Goldstein, A., & Krell, A. (2016). Transparent ceramics at 50: Progress made and further prospects. Journal of the American Ceramic Society, 99(10), 3173-3197.

Guignard, J., Bystricky, M., & Béjina, F. (2011). Dense fine-grained aggregates prepared by spark plasma sintering (SPS), an original technique in experimental petrology. Eur. J. Mineral., 23, 323–331.

Hansen, L. N., Zimmerman, M. E., & Kohlstedt, D. L. (2011). Grain boundary sliding in San Carlos olivine: Flow law parameters and crystallographic-preferred orientation. Journal of Geophysical Research: Solid Earth, 116(8), 1–16.

Hansen, L. N., Zimmerman, M. E., & Kohlstedt, D. L. (2012). The influence of microstructure on deformation of olivine in the grain-boundary sliding regime. Journal of Geophysical Research: Solid Earth, 117(9), 1–17.

Hansen, L. N., Zhao, Y. H., Zimmerman, M. E., & Kohlstedt, D. L. (2014). Protracted fabric evolution in olivine: Implications for the relationship among strain, crystallographic fabric, and seismic anisotropy. Earth and Planetary Science Letters, 387, 157–168.

Hiraga, T., Tachibana, C., Ohashi, N., & Sano, S. (2010). Grain growth systematics for forsterite ± enstatite aggregates: Effect of lithology on grain size in the upper mantle. Earth and Planetary Science Letters, 291(1–4), 10–20.

Hirth, G., & Kohlstedt, D. L. (1995a). Experimental constraints on the dynamics of the partially molten upper mantle: Deformation in the diffusion creep regime. Journal of Geophysical Research, 100(B2), 1981–2001.

Hirth, G., & Kohlstedt, D. L. (1995b). Experimental constraints on the dynamics of the partially molten upper mantle: 2. Deformation in the dislocation creep regime. Journal of Geophysical Research: Solid Earth, 100(B8), 15441-15449.

Jackson, I., Fitz Gerald, J. D., Faul, U. H., & Tan, B. H. (2002). Grain-size-sensitive seismic wave attenuation in polycrystalline olivine. Journal of Geophysical Research: Solid Earth, 107(B12), ECV 5-1-ECV 5-16.

Jackson, I., & Faul, U. H. (2010). Grainsize-sensitive viscoelastic relaxation in olivine: Towards a robust laboratory-based model for seismological application. Physics of the Earth and Planetary Interiors, 183(1–2), 151–163.

Karato, S. (1989). Grain growth kinetics in olivine aggregates. Tectonophysics, 168(4), 255–273.

Karato, S.-I., Paterson, M., & Fitzgerald, J. D. (1986). Rheology of Synthetic Olivine Aggregates: Influence of Grain Size and Water. Journal of Geophysical Research, 91(B8), 8151–8176.

Kohlstedt, D. L., & Goetze, C. (1974). Low-stress high-temperature creep in olivine single crystals. Journal of Geophysical Research, 79(14), 2045-2051.

Kohlstedt, D. L., Goetze, C., Durham, W. B., & Vander Sande, J. (1976). New Technique for Decorating Dislocations in Olivine. Science, 191(4231), 1045–1046.

Koizumi, S., Hiraga, T., Tachibana, C., Tasaka, M., Miyazaki, T., Kobayashi, T., Takamasa, A., Ohashi N. & Sano, S. (2010). Synthesis of highly dense and fine-grained aggregates of mantle composites by vacuum sintering of nano-sized mineral powders. Physics and Chemistry of Minerals, 37(8), 505–518.

Manohar, P.A., Ferry, M., & Chandra, T. (1998). Five decades of the Zener equation. ISIJ international, 38(9), 913-924.

Nichols, S. J., & Mackwell, S. J. (1991). Grain growth in porous olivine aggregates. Physics and Chemistry of Minerals, 18(4), 269–278.

Olsson, J., Bovet, N., Makovicky, E., Bechgaard, K., Balogh, Z., & Stipp, S. L. S. (2012). Olivine reactivity with CO2 and H2O on a microscale : Implications for carbon sequestration. Geochemica et Cosmochimica Acta, 77, 86–97.

Pommier, A., Leinenweber, K., Kohlstedt, D. L., Qi, C., Garnero, E. J., MacKwell, S. J., & Tyburczy, J. A. (2015). Experimental constraints on the electrical anisotropy of the lithosphere-asthenosphere system. Nature, 522(7555), 202–206.

Rahaman, M. N. (2008). Sintering of Cermaics.

Schwenn, M. B., & Goetze, C. (1978). Creep of olivine during hot-pressing. Tectonophysics, 48(1-2), 41-60.

Smith, C. S. (1948). Zener pinning. Trans. Met. Soc. AIME, (175), 15–51.

Tasaka, M., Zimmerman, M. E., & Kohlstedt, D. L. (2016). Evolution of the rheological and microstructural properties of olivine aggregates during dislocation creep under hydrous conditions. Journal of Geophysical Research: Solid Earth, 121(1), 92-113.

Toriumi, M. (1979). Relation between dislocation density and subgrain size of naturally deformed olivine in peridotites. Contributions to Mineralogy and Petrology, 68, 181-186.

Wang, S. F., Zhang, J., Luo, D. W., Gu, F., Tang, D. Y., Dong, Z. L., et al. (2013). Progress in Solid State Chemistry Transparent ceramics: Processing, materials and applications. Progress in Solid State Chemistry, 41, 20–54.

Windisch Jr., C. F., Glezakou, V.-A., Martin, P. F., McGrail, B. P., & Schaef, H. T. (2012). Raman spectrum of supercritical C18O2 and re-evaluation of the Fermi resonance. Physical Chemistry Chemical Physics, 14(8), 2560–2566.

Wu, T., Kohlstedt, D.L. (1988) A rutherford backscattering spectroscopy study of kinetics of oxidation of (Mg,Fe)2SiO4, J. Am. Ceram. Soc. 71:540-545.

Xiao, Z., Yu, S., Li, Y., Ruan, S., Kong, L. B., Huang, Q., ... & Tang, D. (2020). Materials development and potential applications of transparent ceramics: A review. Materials Science and Engineering: R: Reports, 139, 100518.

Yabe, K., Sueyoshi, K., & Hiraga, T. (2020). Grain-boundary diffusion creep of olivine: 1. Experiments at 1 atm. Journal of Geophysical Research: Solid Earth, 125(8), e2020JB019415.

Yabe, K., & Hiraga, T. (2020). Grain-Boundary Diffusion Creep of Olivine: 2. Solidus Effects and Consequences for the Viscosity of the Oceanic Upper Mantle. Journal of Geophysical Research: Solid Earth, 125(8), 1-22.

Zhao, Y. H., Ginsberg, S. B., & Kohlstedt, D. L. (2004). Solubility of hydrogen in olivine: dependence on temperature and iron content. Contributions to Mineralogy and Petrology, 147, 155-161.

Zhao, Y. H., Zimmerman, M. E., & Kohlstedt, D. L. (2009). Effect of iron content on the creep behavior of olivine: 1. Anhydrous conditions. Earth and Planetary Science Letters, 287(1-2), 229-240.

2.8 Tables

Table 2-1: Microprobe measurements

Table 1. Microprobe measurements

(wt %)	mean	min	max	std
NaO	b.d.	-	-	-
SiO_2	40.81	40.56	41.07	0.11
MgO	49.32	48.96	49.48	0.10
Al_2O_3	0.01	b.d.	0.06	0.01
K2O	b.d.	-	-	-
CaO	0.09	0.06	0.13	0.01
Cr_2O_3	0.03	b.d.	0.06	0.01
MnO	0.14	0.11	0.18	0.01
FeO	9.21	8.95	9.57	0.13
NiO	0.38	0.30	0.51	0.04
TiO	0.01	b.d.	0.03	0.01
Fo #	90.52	90.12	90.78	0.13

b.d. – below detection limit

Table 2-2: Summary of annealing experiments

Table 2. Summary of annealing experiments

Experiment ID	T (°C)	P (MPa)	t (10^4 s)	method
PT1254	1250	300	1.4	evacHP
PT1254_A1	1250	0.1	21.6	MG
PT1254_A2	1250	0.1	4.3	MG
PT1254_A3	1250	0.1	1.4	MG
PT1254_A4	1250	0.1	0.4	MG
PT1254_A5	1300	0.1	1.4	MG
PT1254_A6	1300	0.1	0.4	MG
PT1254_A7	1300	0.1	4.3	MG
PT1254_PT1269	1250	300	1.4	HP
PT1254_PT1270	1250	300	4.3	HP
PT1193	1250	300	1.2	evacHP
PT1193_A1	1350	0.1	7.2	MG
PT1285	1250	300	1.4	evacHP
PT1285_PT1298	1250	300	2.5	HP
PT1285_PI1988	1300	300	2.5	HP
PT1285_PI1989	1300	300	7.2	HP
PT1285_PI1990	1300	300	0.7	HP
PT1285_PI1991	1250	300	7.2	HP
PT1285_PI1992	1300	300	7.2	HP

evacHP – 300 MPa evacuated hot press
MG – 1 atm. mixed gas annealing
HP – 300 MPa high pressure annealing (sample embedded in a conventional hot press)

Table 2-3: Densification model parameters

Table 3. Densification model parameters

Mechanism	Grain Size Exponent, m	Stress Exponent, n	Diffusion Coefficient
Lattice diffusion	2	1	lattice
Grain boundary diffusion	3	1	grain boundary
Dislocation motion	0	≥3	lattice
Grain boundary sliding/ Particle rearrangement	1	1 or 2	lattice or grain boundary

(reproduced from Rahaman, 2008)

2.9 Figures

Figure 2-1: Powder size distributions

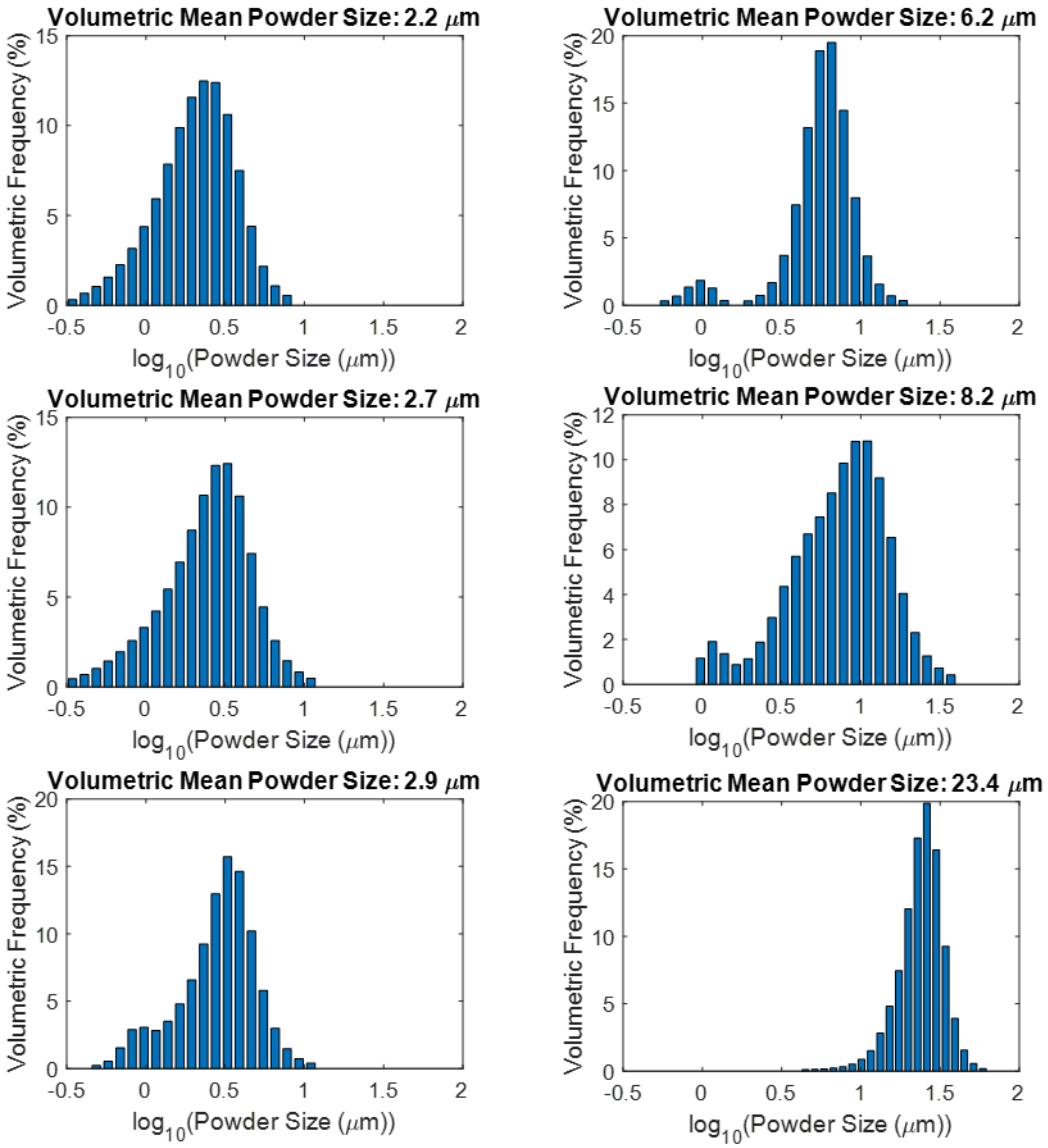

Figure 1: Size distributions of powders used in evacuated hot-pressing experiments, measured by laser diffraction.

Figure 2-2: Diagrams of experimental assemblies

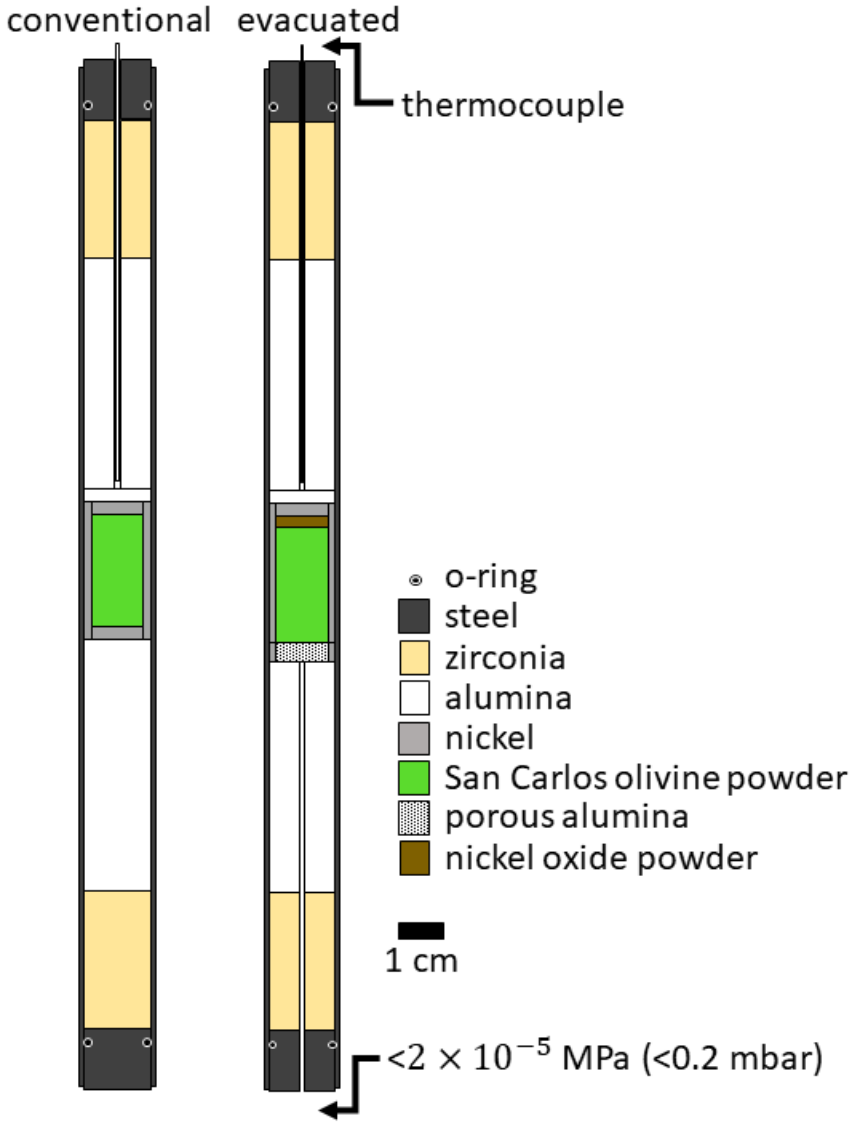

Figure 2: Diagrams of hot-pressing assemblies for densification by conventional and evacuated hot pressing in an internally heated, high-pressure gas-medium apparatus.

Figure 2-3: Densification data

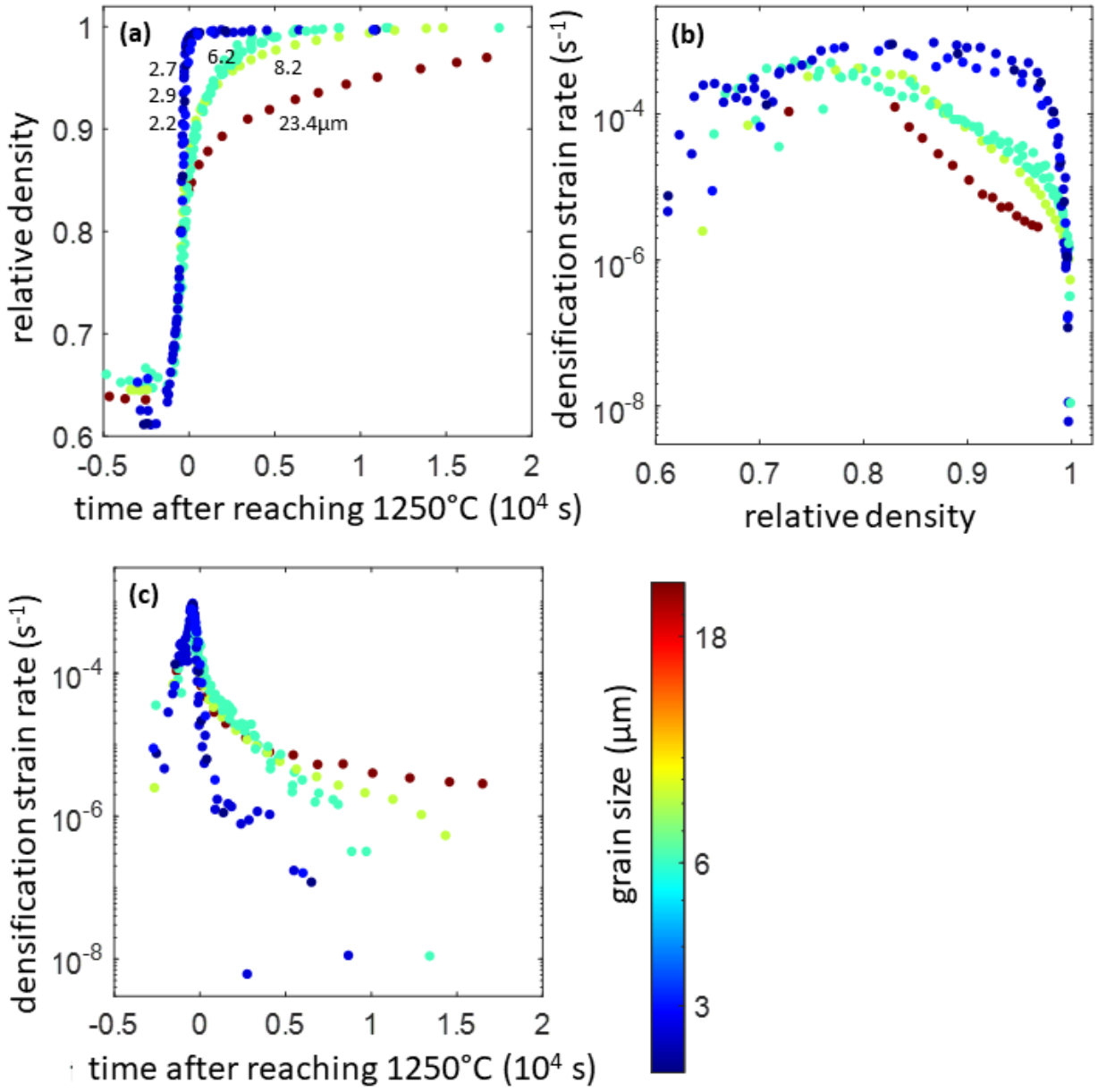

Figure 3: (a) Relative density of evacuated hot-pressed aggregates plotted against time after reaching the peak experimental temperature, (b) densification strain rate plotted against relative density, and (c) densification strain rate plotted against time.

Figure 2-4: Photographs of hot-presses specimens

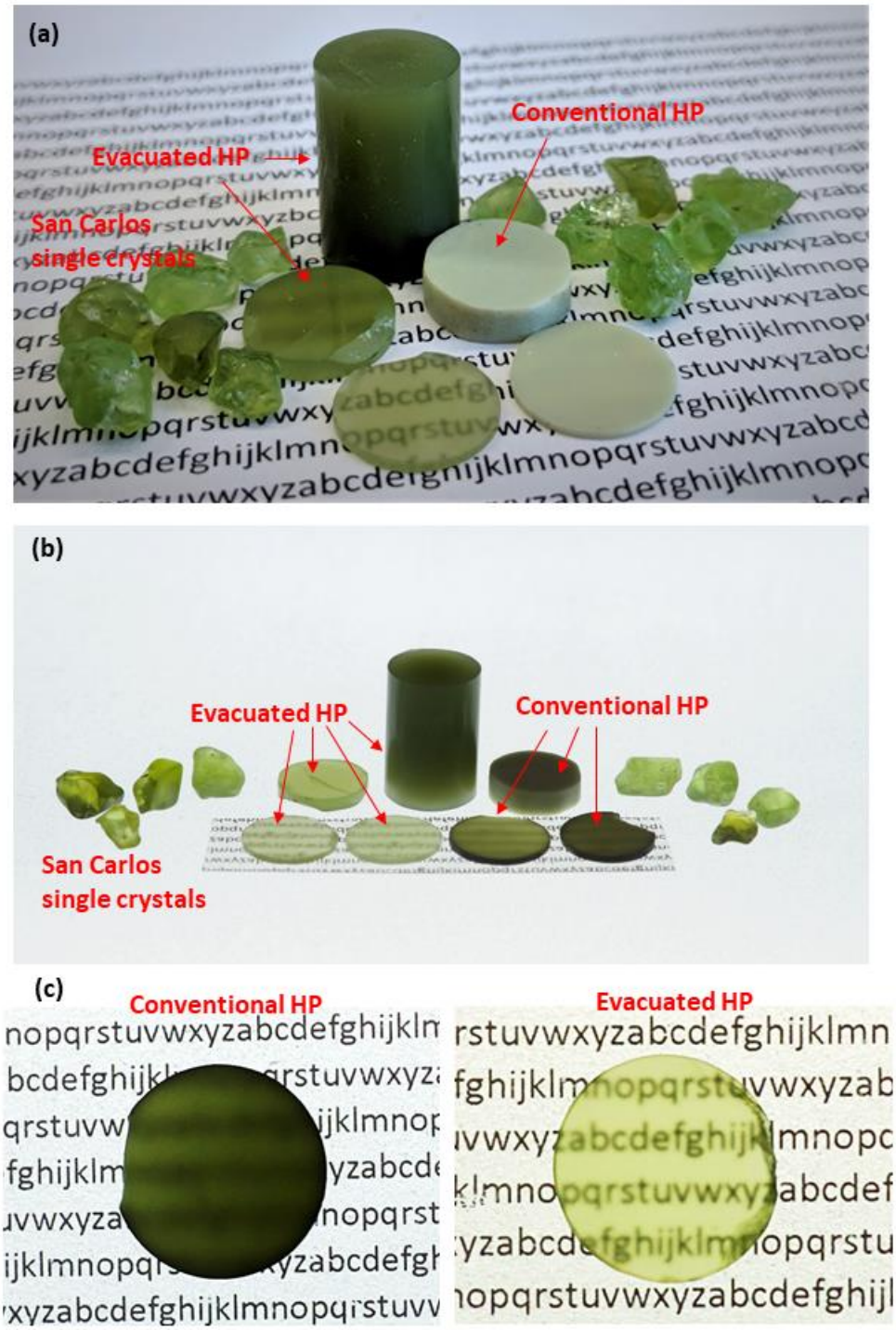

Figure 4: Photographs of conventional and evacuated hot-pressed specimens in ambient light, (b) the same specimens photographed on a light table, and (c) photographs of selected specimens on top of text on a light table (both samples are ~1 mm thick).

Figure 2-5: Reflected-light micrographs of hot-pressed specimens

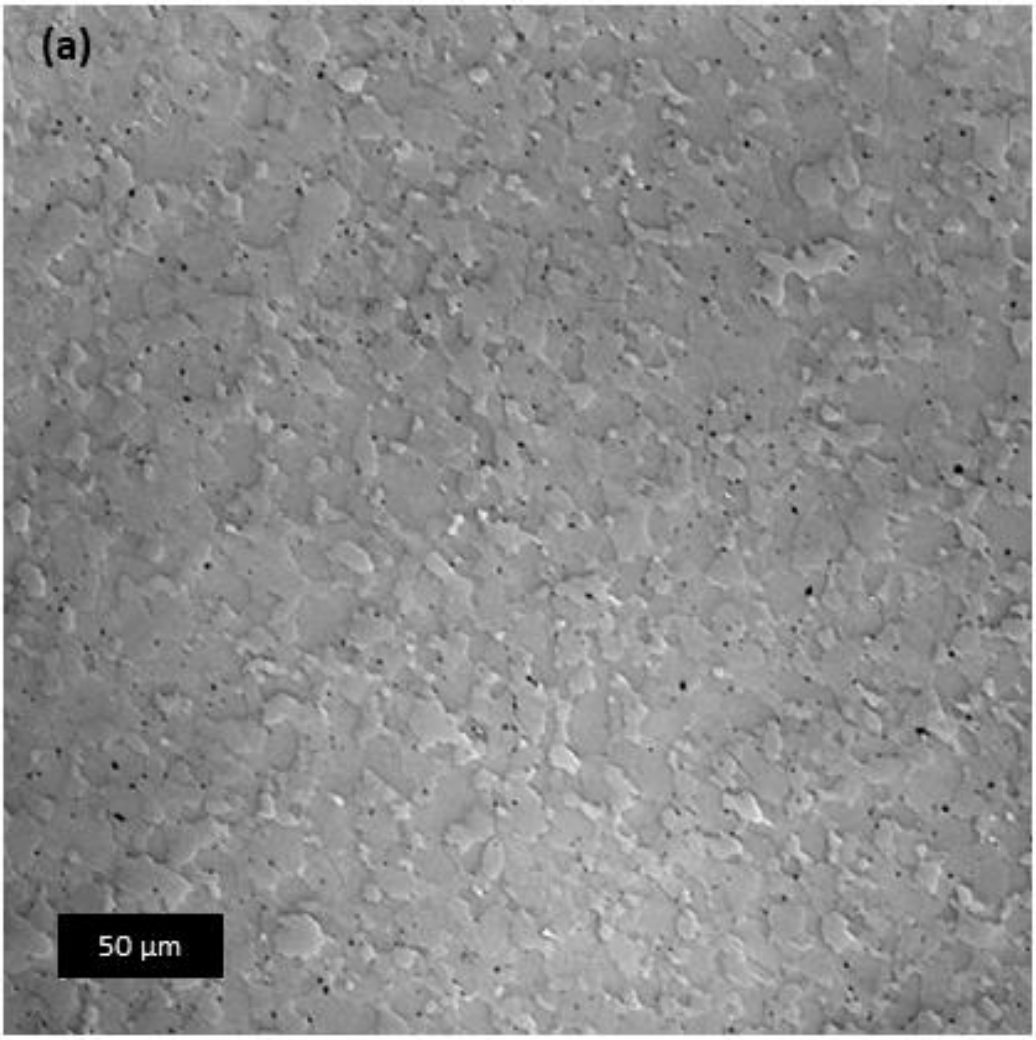

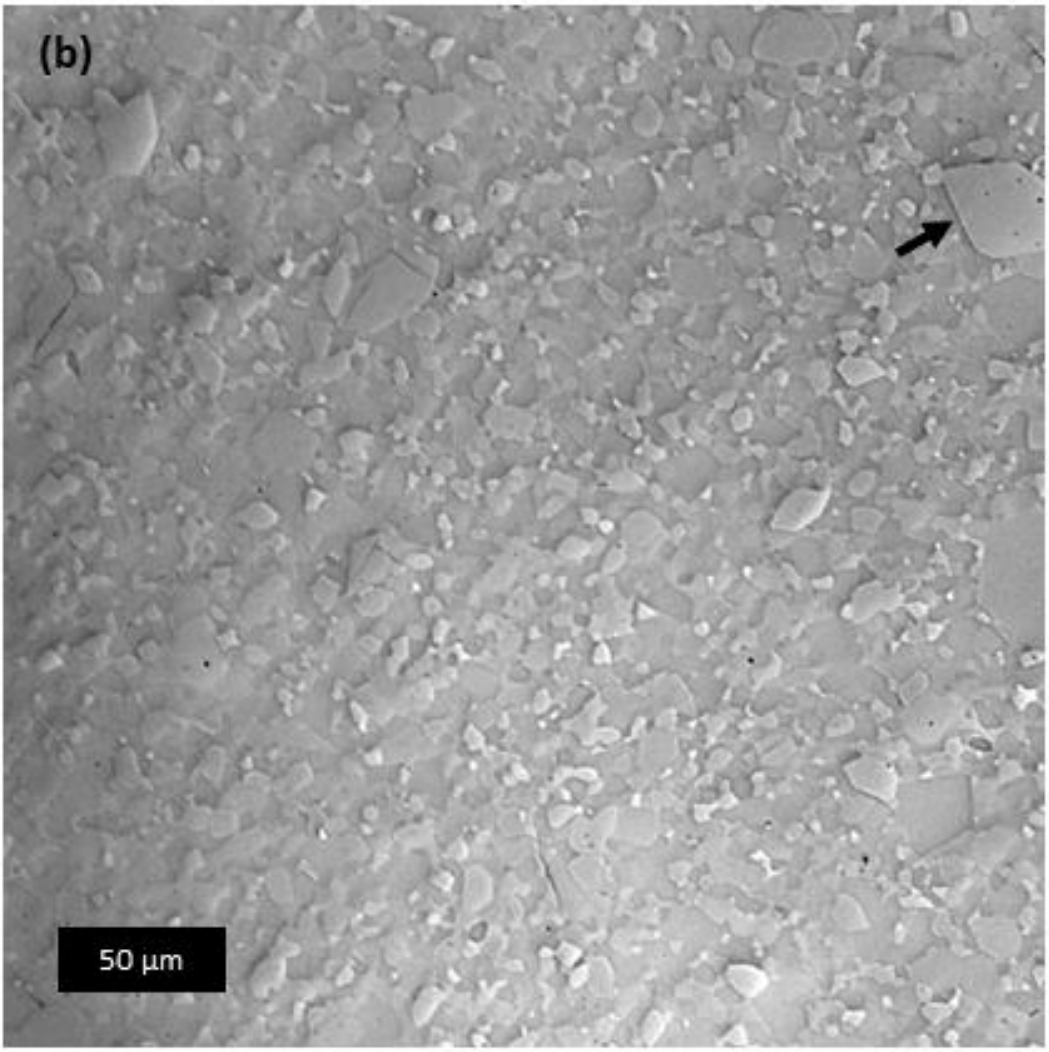

Figure 5: Reflected-light micrograph of a (a) conventional hot-pressed specimen and (b) an evacuated hot-pressed specimen. Both were prepared by polishing with diamond lapping films followed by colloidal silica (Syton) polishing, which results in grain scale relief. Broadly, both specimens have a similar scale of grain size, however, there is roughly 1 % porosity in the conventionally hot-pressed specimen (seen as black spots in the image) that are not observed in the evacuated hot-pressed specimen. Additionally, a few particularly large grains with long straight segments (black arrow) are observed in the evacuated hot-pressed specimen, indicative of the early stages of abnormal grain growth.

Figure 2-6: Backscatter electron micrographs of an oxidation decorated specimen

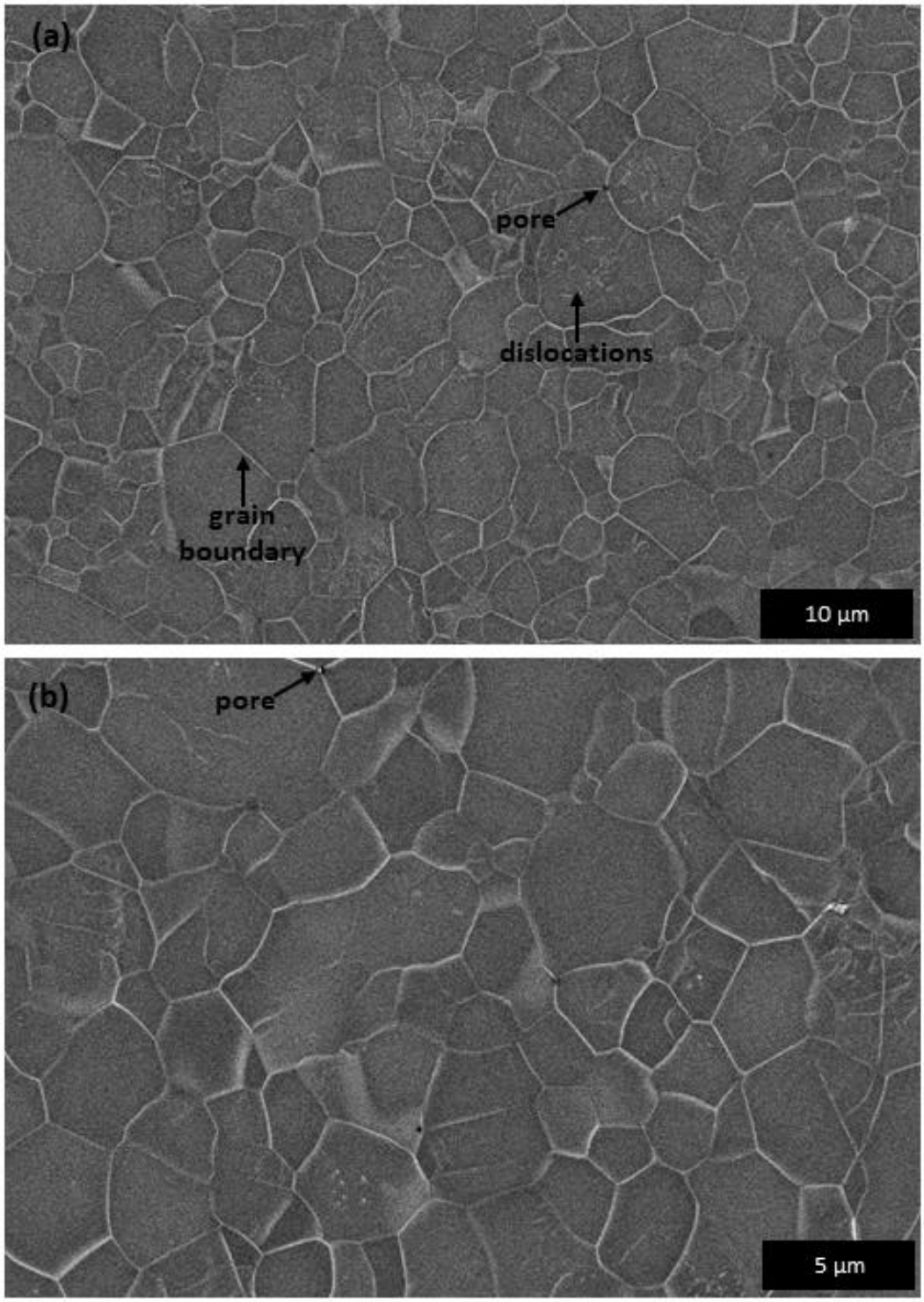

Figure 6: Backscatter electron micrographs of an oxidation-decorated evacuated hot-pressed specimen at two magnifications. Examples of pores, dislocations, and a grain boundary are labeled.

Figure 2-7: EBSD map of evacuated hot-pressed specimen

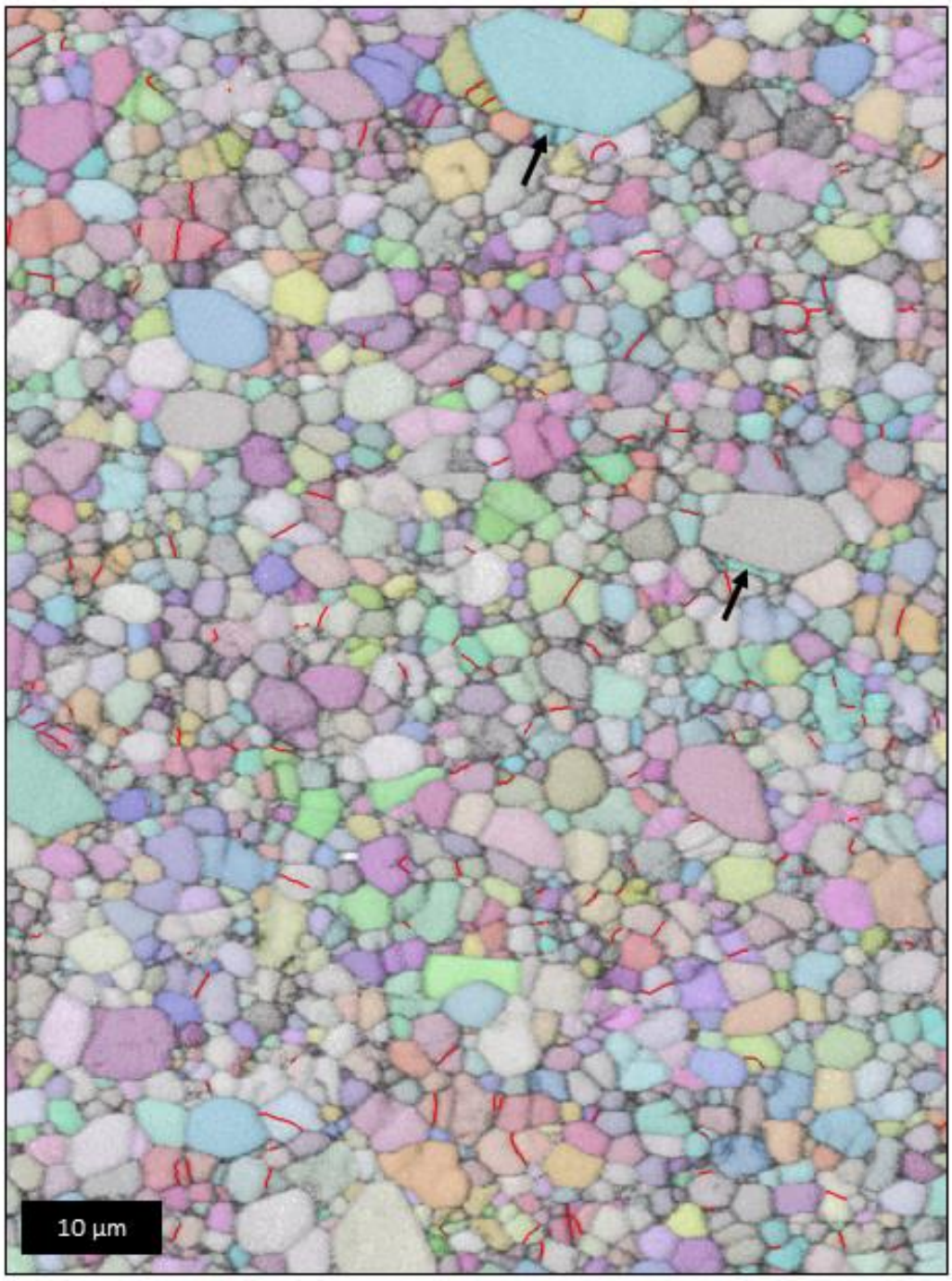

Figure 7: EBSD map of evacuated hot-pressed specimen. Inverse pole figure false color is overlain on band contrast. Subgrain boundaries (misorientation <10°) are highlighted in red. Black arrows point to examples of straight grain boundary segments of particularly large grains.

Figure 2-8: FTIR spectra of olivine specimens

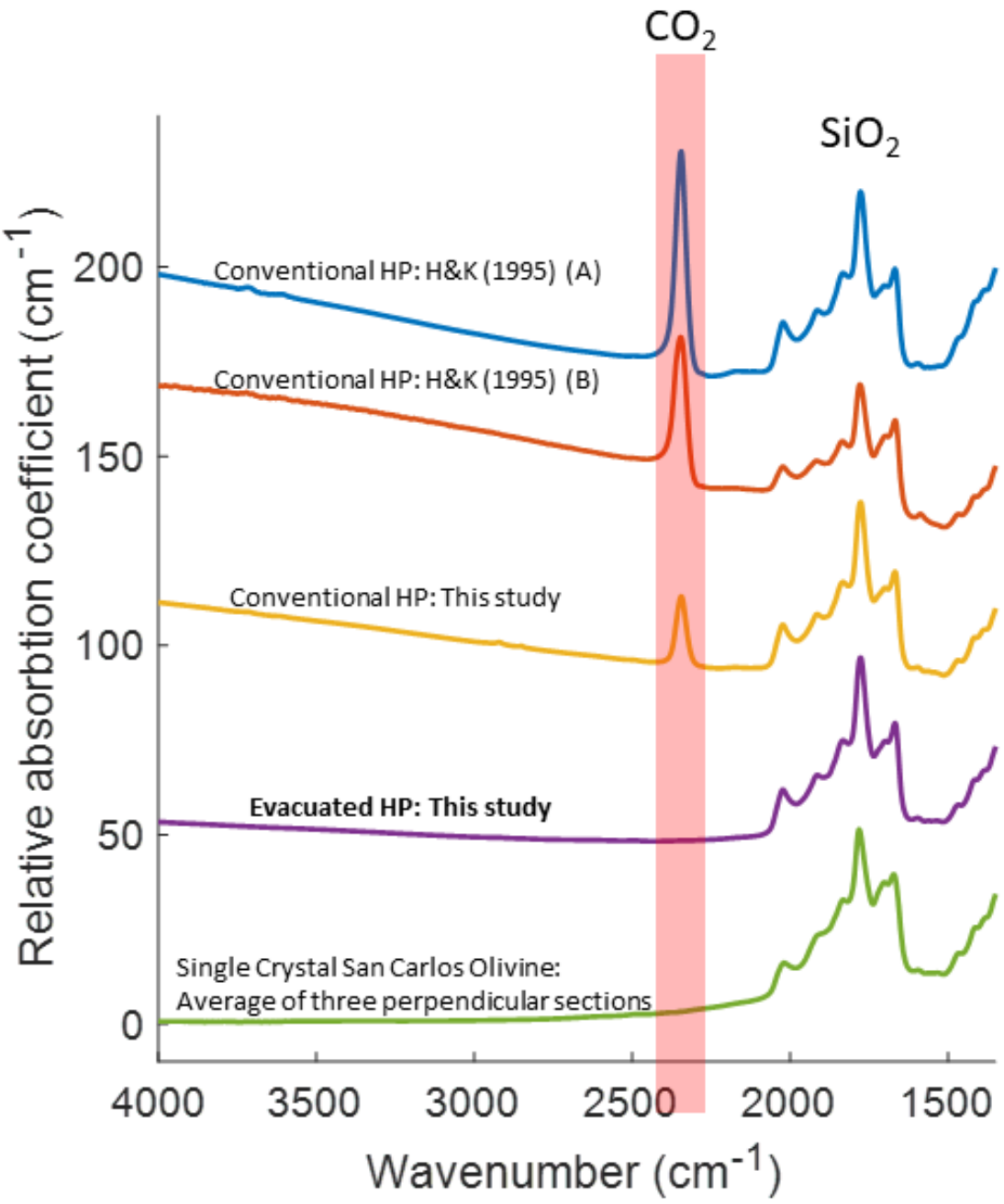

Figure 8: FTIR spectra collected from a variety of olivine specimens fabricated for this study and others. The peak associated with CO_2 is prominent in conventionally hot-pressed specimens and absent in the evacuated hot-pressed specimen. Spectra are offset for clarity. Spectra labeled H&K were taken from specimens prepared for Hirth and Kohlstedt (1995) using both powder preparations (A and B) from their study.

Figure 2-9: Raman spectra and maps

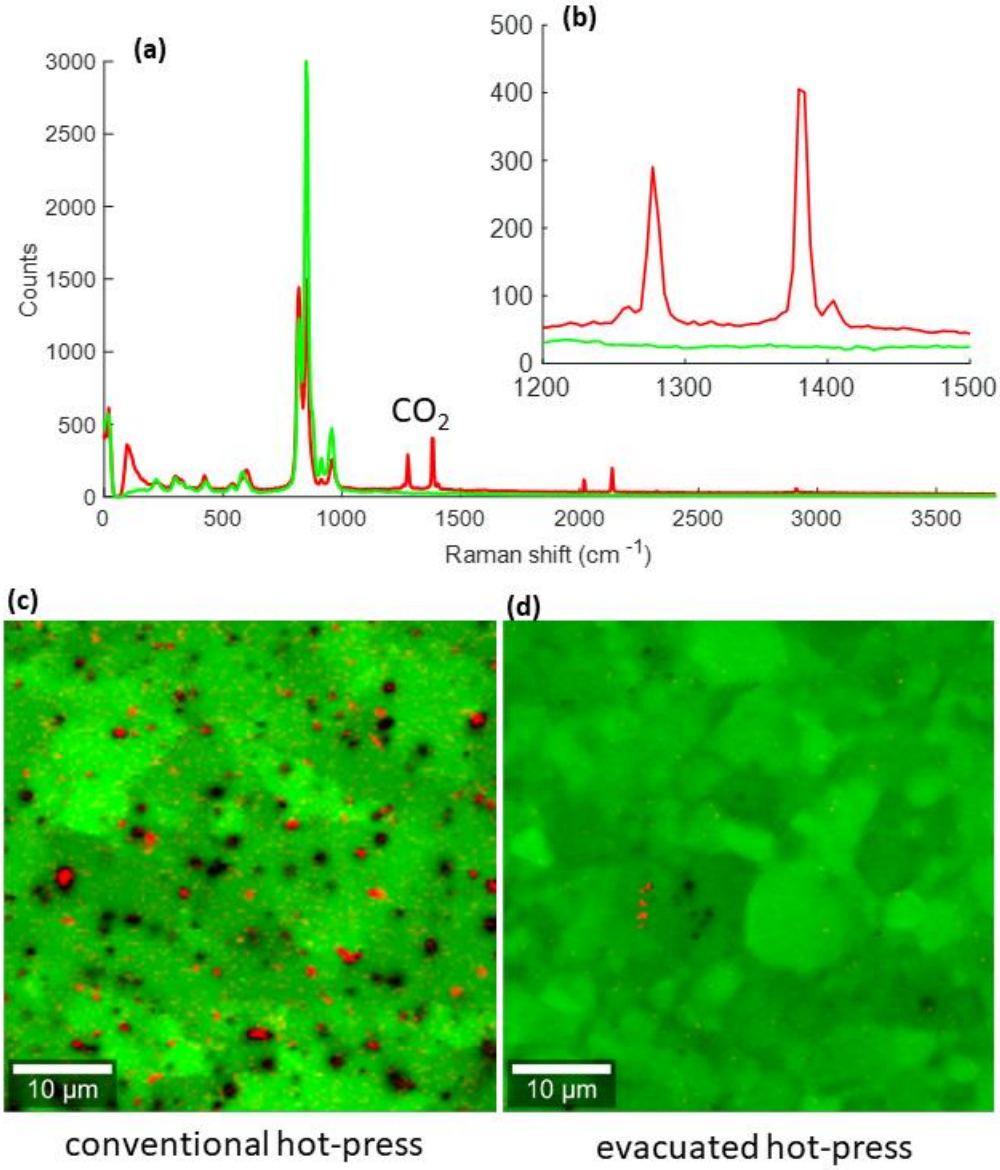

Figure 9: Example Raman spectra taken from two regions in (a) a conventionally hot-pressed specimen, demonstrating a olivine-dominated spectra (green) and a CO_2-contaminated spectra (red). (b) Inset of Raman spectra highlighting the characteristic CO_2 related peaks. (c and d) False color maps made using Raman data, with green representing the intensity of a characteristic olivine peak and red represents the intensity of a characteristic CO_2-related peak for both (c) conventional and (d) evacuated hot-pressed specimens.

Figure 2-10: Reflected-light micrographs of annealed conventionally hot-pressed specimen

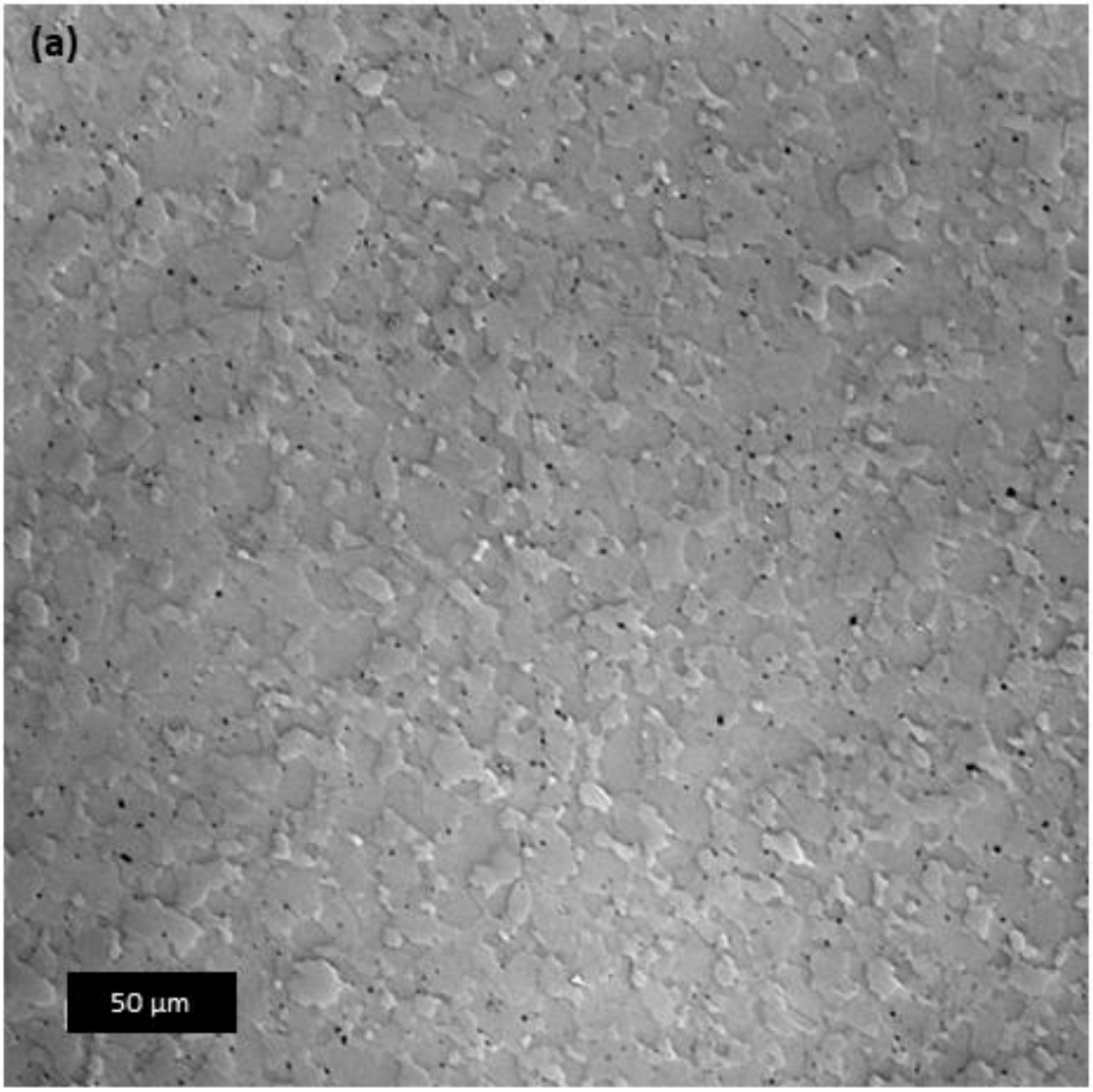

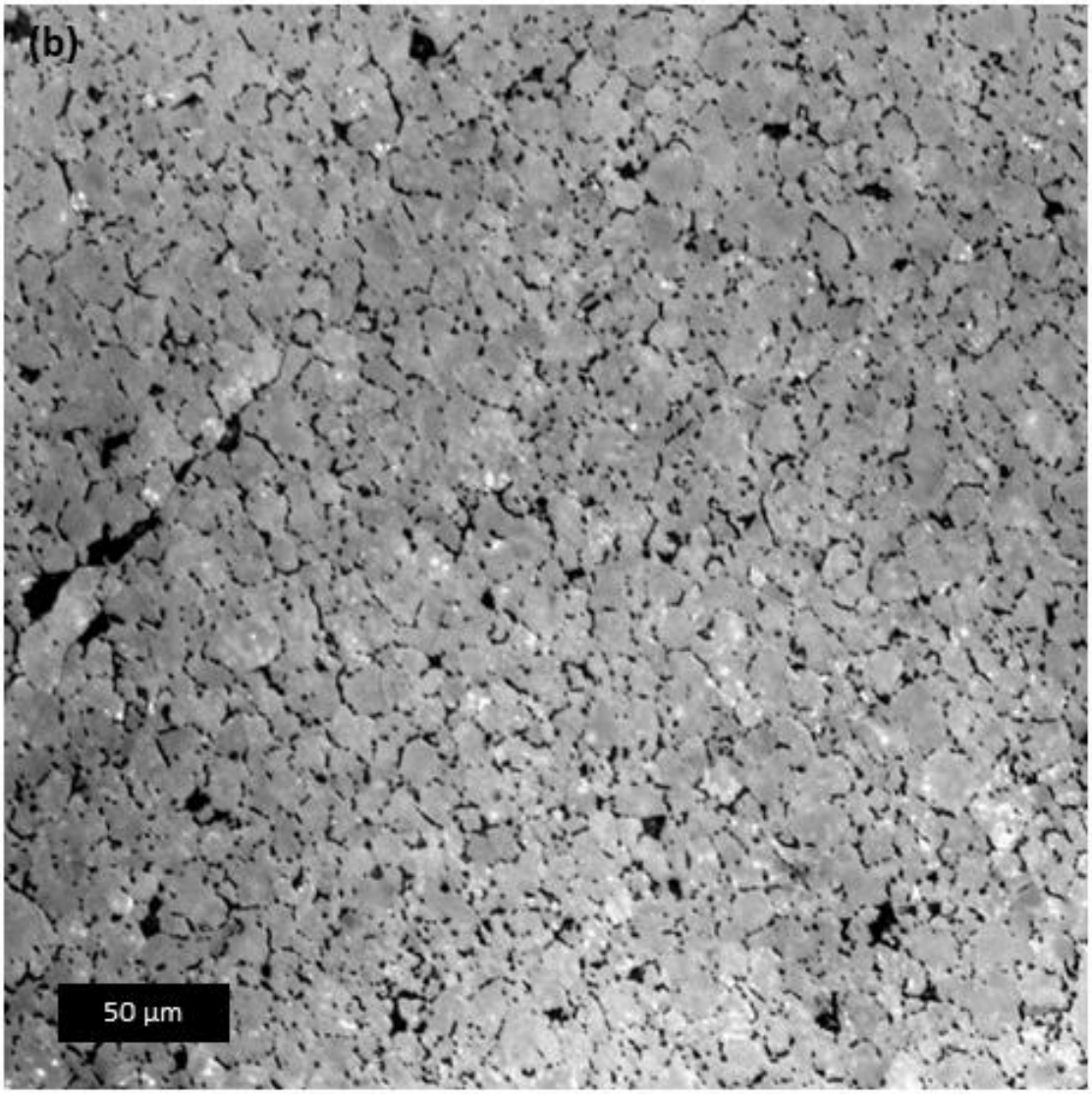

Figure 10: Reflected-light micrographs of a conventionally hot-pressed specimen after (a) hot-pressing and (b) after annealing at 1350°C for 20 h at 1 atm. The sample initially contains about 1% porosity, which grows to >10%, leading to near disaggregation of the specimen.

Figure 2-11: Reflected-light micrographs of annealed evacuated hot-pressed specimen

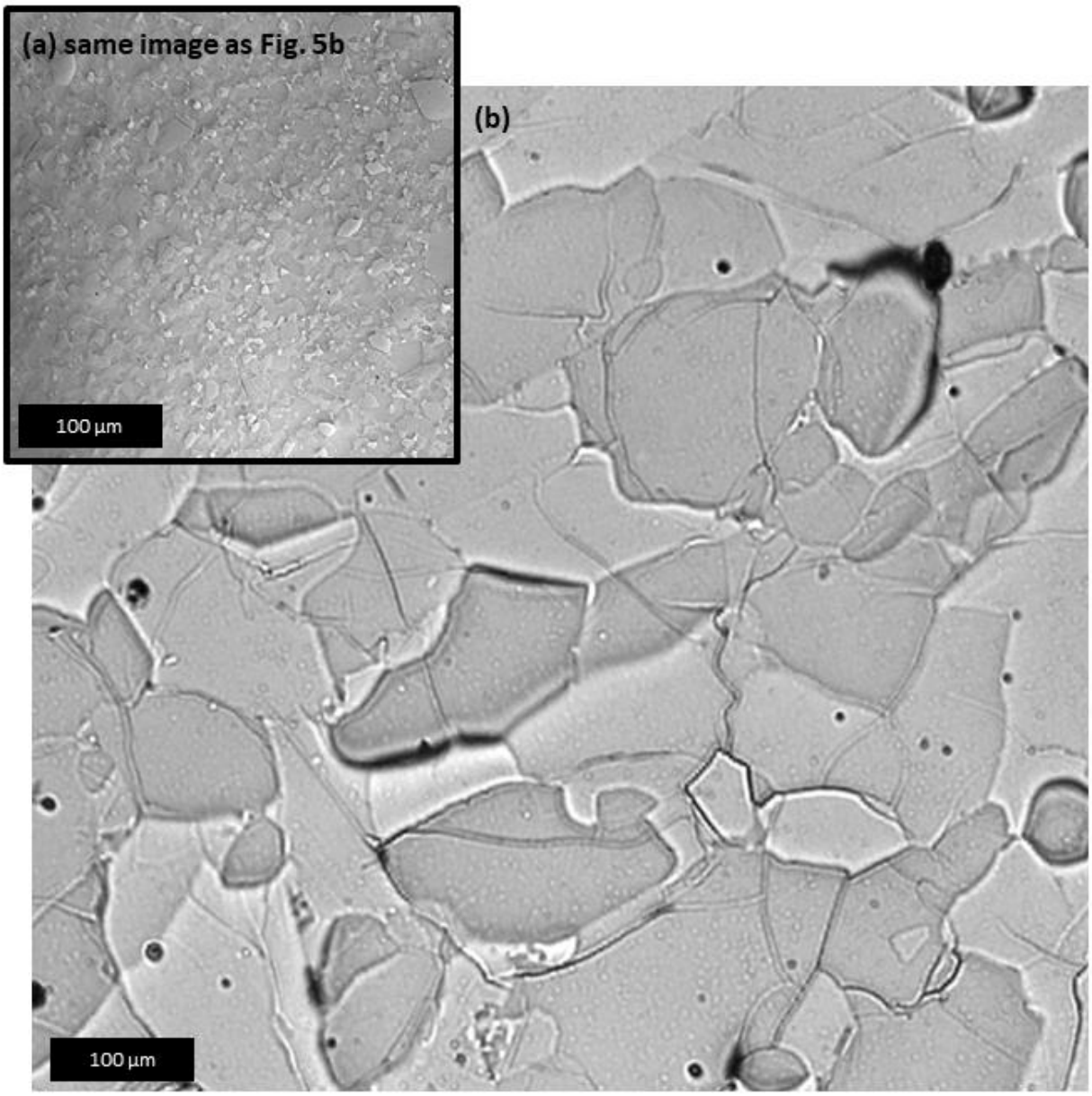

Figure 11: Reflected-light micrographs of an evacuated hot-pressed specimen (a) after hot-pressing and (b) after annealing at 1350 °C for 20 h at 1 atm. The latter specimen underwent dramatic abnormal grain growth resulting in a coarse aggregate with grain-scale cracks. The figures are presented this way so that they are at the same spatial scale, demonstrating the dramatic coarsening of the microstructure.

Figure 2-12: Reflected-light micrographs of specimen annealed at high pressure

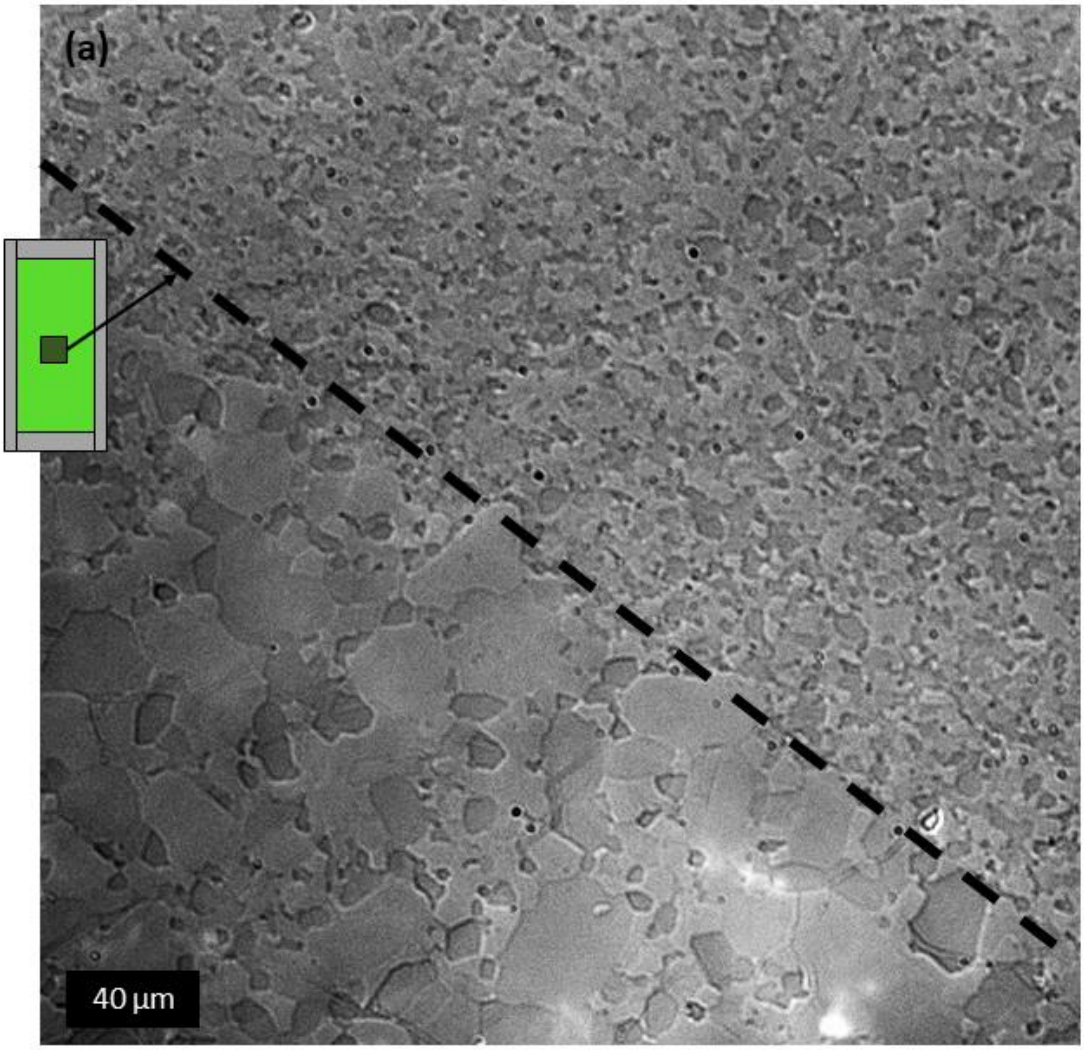

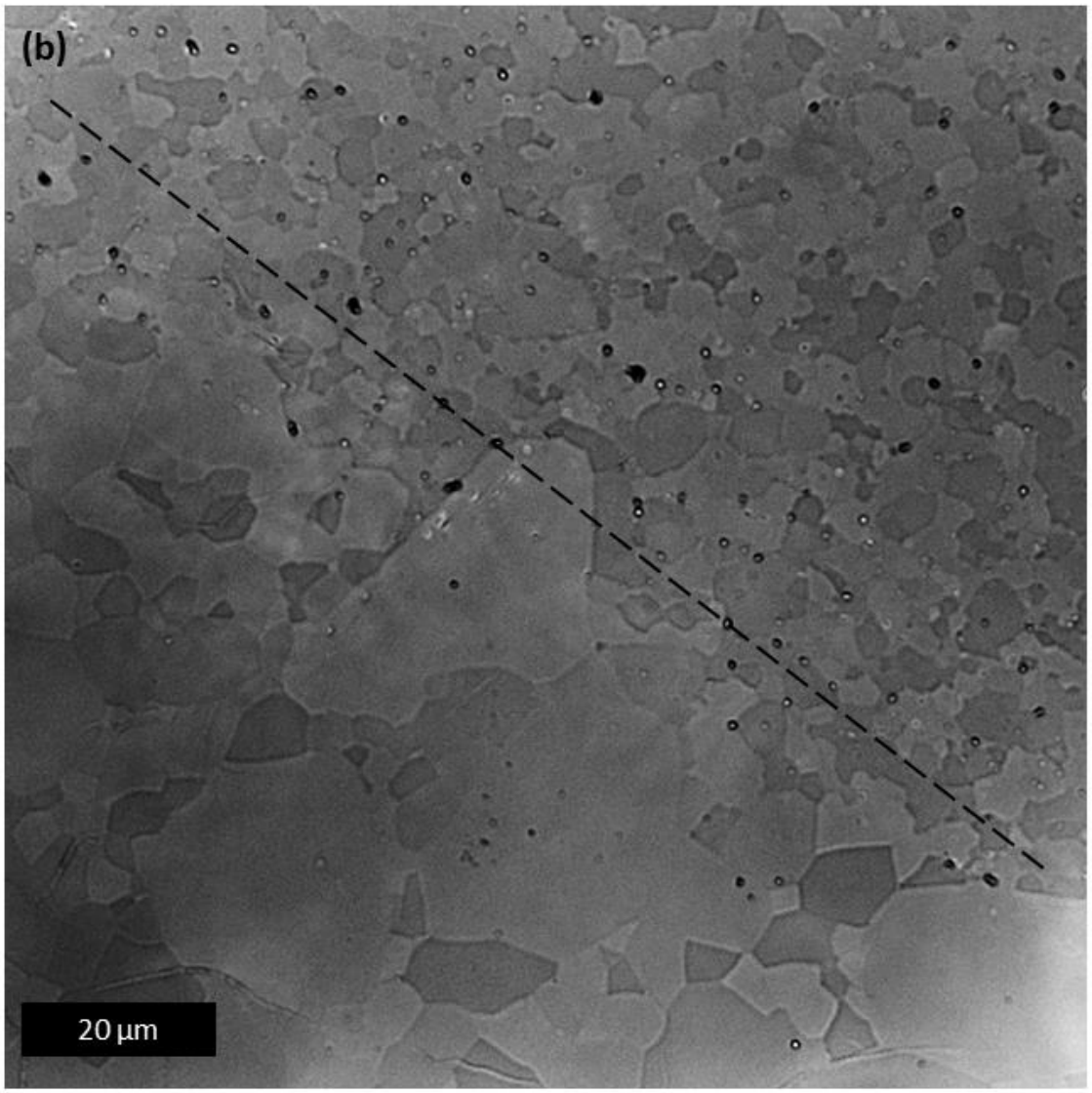

Figure 12: Reflected light micrographs taken at different magnifications of an evacuated hot-pressed specimen that was later embedded into a powder compact that was conventionally hot pressed at 1250°C for 12 h (PT1254_PT1270). The images are taken at the boundary (marked by a dashed line) between the evacuated hot-pressed specimen and the surrounding conventionally hot-pressed material into which it was embedded. The boundary is distinct, with a contrast in both grain size and porosity.

Figure 2-13: Band contrast maps of annealed specimen

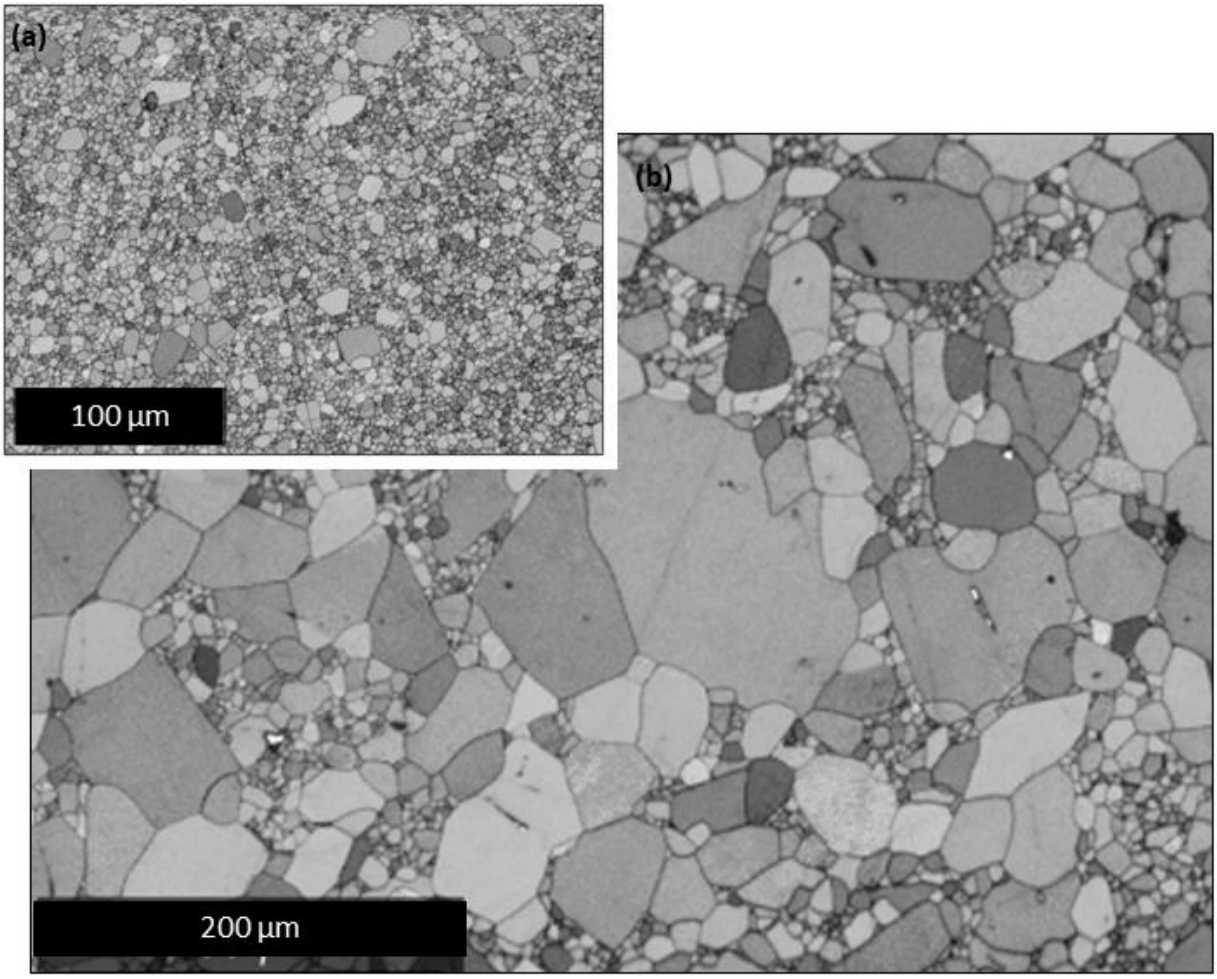

Figure 13: Band contrast maps of an evacuated hot-pressed specimen that was later embedded into a powder compact that was conventionally hot pressed at 1250°C for 12 h. (a) Map of the original specimen before annealing. (b) Map of the annealed specimen. The two maps are presented at the same scale, demonstrating the dramatic coarsening that occurred.

Figure 2-14: Reflected light micrographs comparing specimens annealed at 1 atm and 300 MPa

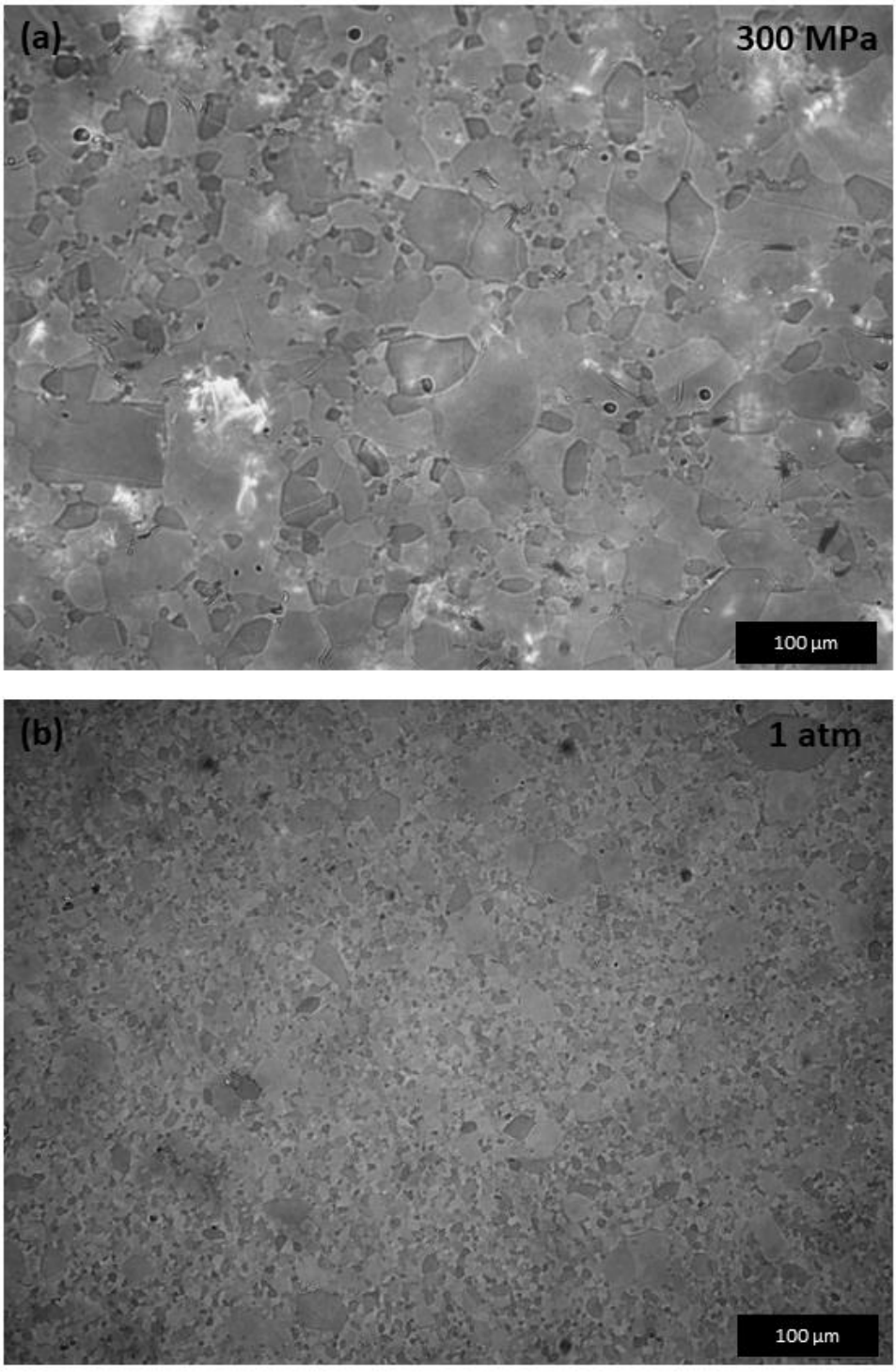

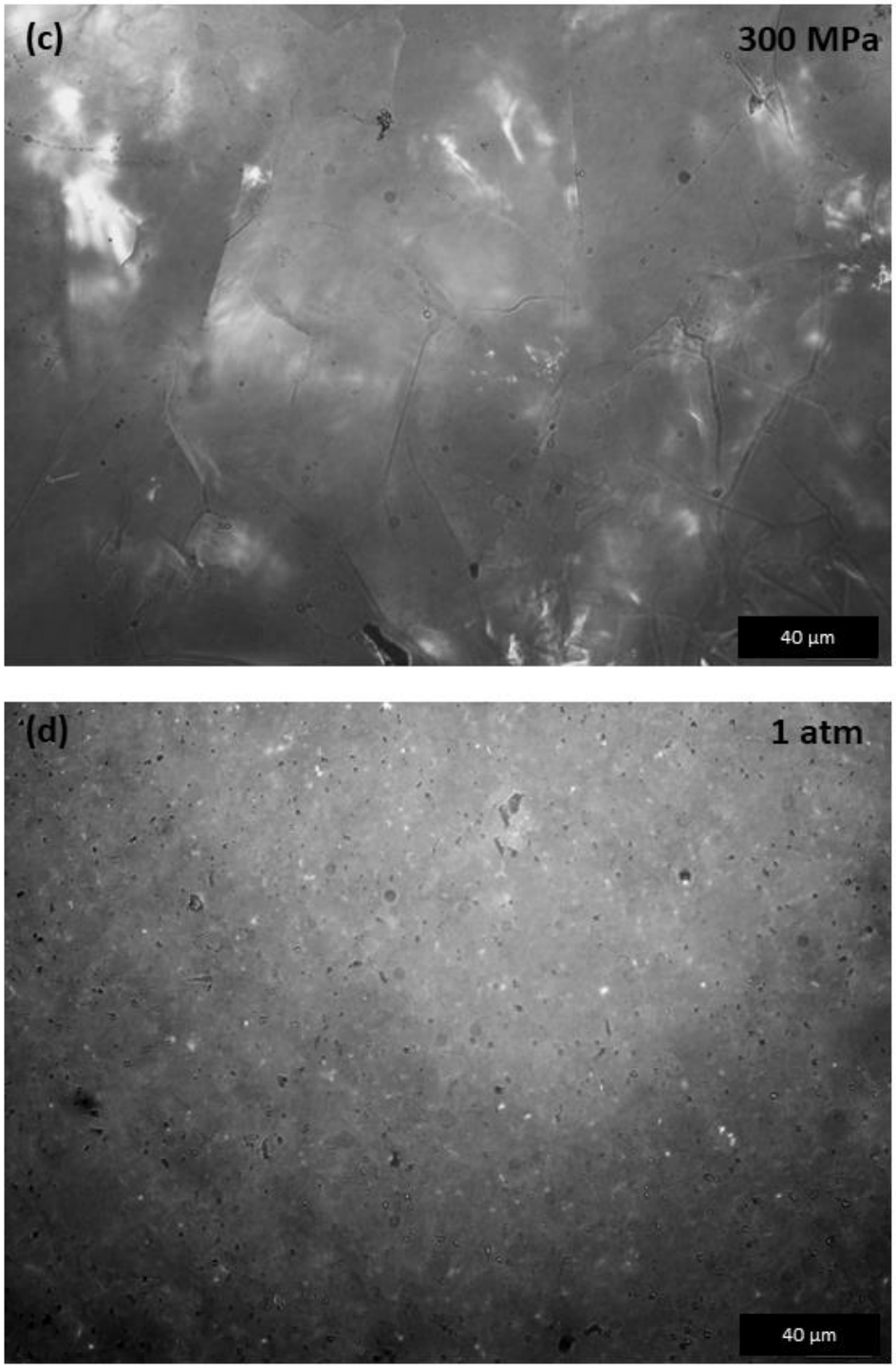

Figure 14: Reflected light micrographs of an evacuate-hot pressed specimen that was (a,c) annealed at 300 MPa) and (b,d) annealed at 1 atm at 1250°C for 12 h. Figures (a) and (b) demonstrate the difference in coarsening rate related to confining pressure. The micrographs in (c) and (d) were taken with the optics focused to highlight grain-scale cracking in the sample annealed at 300 MPa and pore growth in the sample annealed at 1 atm.

Figure 2-15: Densification analysis

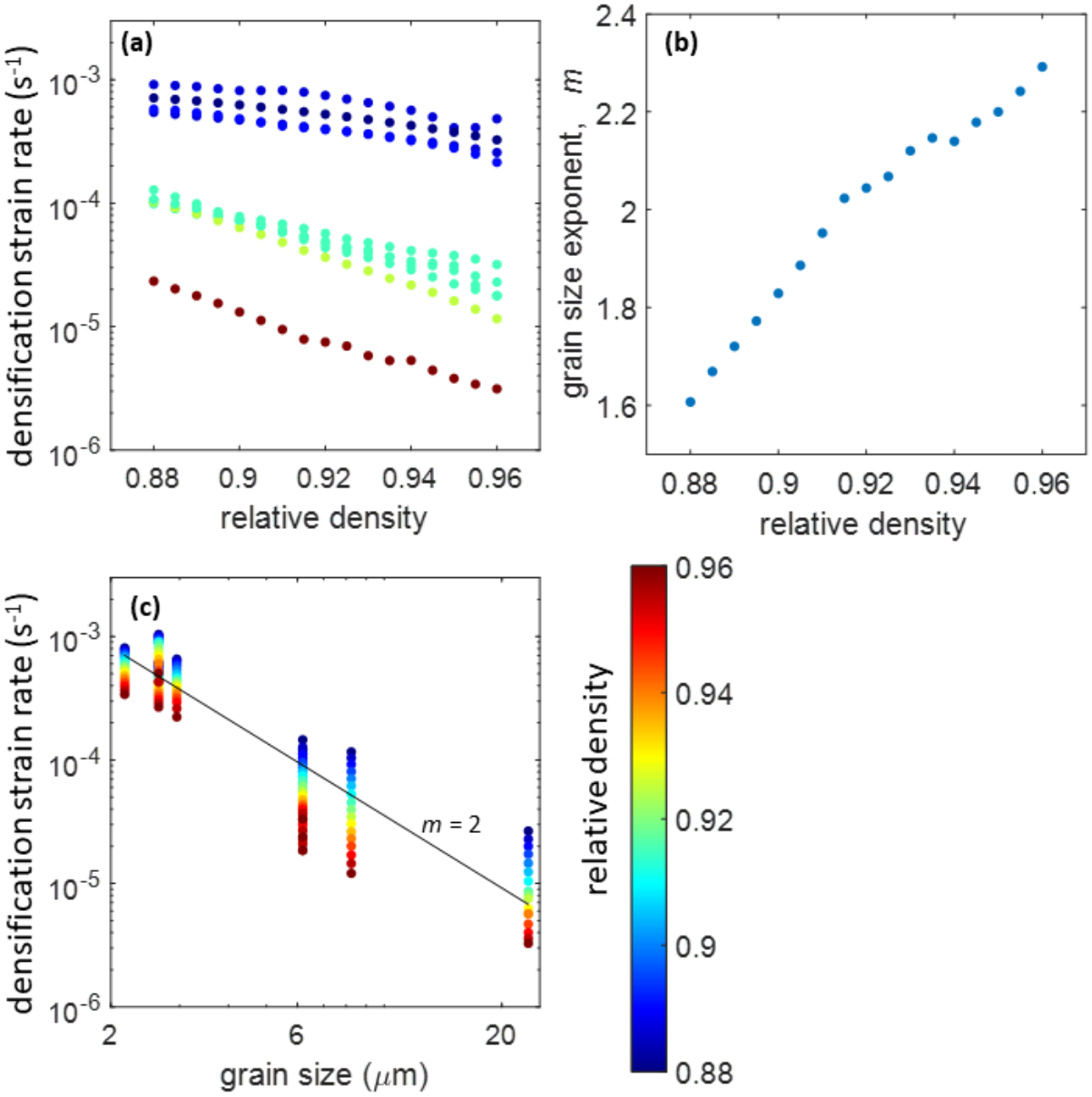

Figure 15: Analysis of densification data. (a) Densification strain rate plotted against relative density, interpolated to a uniform interval. (b) Grain size exponent plotted against relative density, calculated using the data presented in (a). (c) Plot of densification strain rate against grain size with data colored to represent the relative density at each data point. The black line illustrates a grain size exponent of 2.

Figure 2-16: Raman spectra – detection of elemental carbon

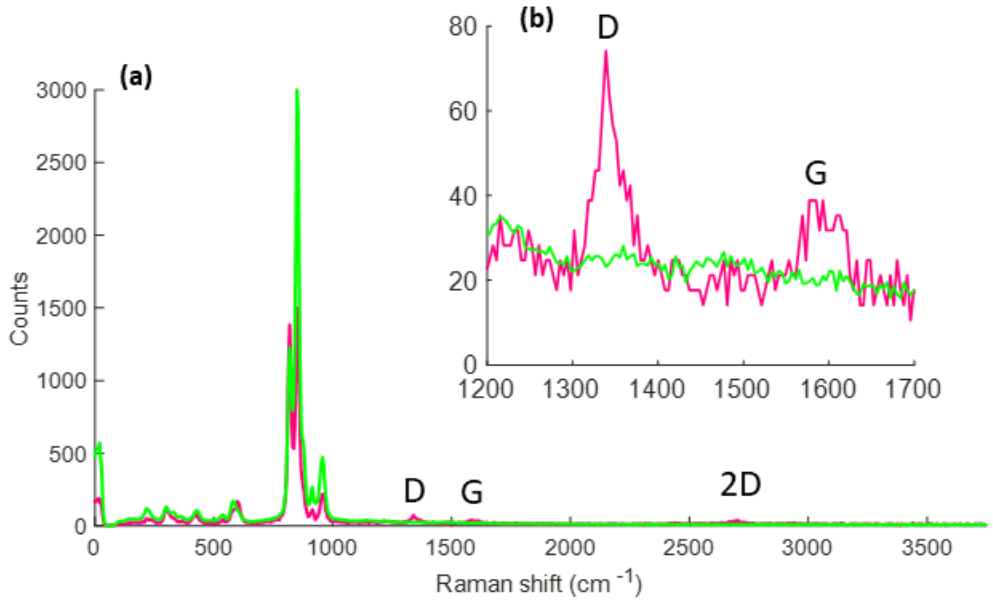

Figure 16: Example Raman spectra indicating the detection of elemental carbon in one evacuated hot-pressed specimen. Inset (b) highlights the characteristic region containing the D and G bands.

Chapter 3 Microstructural Evolution of San Carlos Olivine Aggregates Deformed to High Strain in Torsion

3.1 Abstract

Detailed microstructural analyses of olivine aggregates experimentally deformed to large strains at high temperatures provide a new, high-resolution view of deformation-induced microstructural evolution, across a range of stress and strain conditions. Data were collected from a series of torsional deformation experiments on nearly pore-free, evacuated hot-pressed San Carlos olivine aggregates at 1250°C and 300 MPa confining pressure in a gas-medium, Paterson-type deformation apparatus. EBSD mapping of deformed samples was used to analyze the evolution of grain-size, shape preferred orientation (SPO), and crystallographic preferred orientation (CPO).

A grain-size piezometer was determined from the data, taking advantage of the radial stress gradient that results from torsional deformation. The deformed samples have a grain size gradient, with the finest grains toward the highest stress region at the outer radius, reflecting the piezometric relationship between grain size and stress resulting from dynamic recrystallization. Grain sizes measured by EBSD analyzes of our samples deformed to high strains are significantly smaller than predicted by previously published recrystallized grain-size piezometers but rather correspond well with previously published subgrain-size piezometers.

The evolution of CPO with increasing strain along the radius is quantified using standard measures of fabric strength and eigenvalue analysis. Fabric evolution is protracted with a major transition in fabric geometry at an equivalent strain of ~2, after which the fabric becomes distinctly A-type and strengthens with increasing strain. This protracted CPO evolution likely reflects the competition between different dislocation slip systems in olivine and, therefore, these data could be a useful benchmark for micromechanical models attempting to model the physics of CPO evolution.

3.2 Introduction

Deformation of mantle rocks leads to microstructural evolution that influences their mechanical properties. The strength of the upper mantle is typically considered to be controlled

by the strength of olivine, the dominant phase. Therefore, experiments on laboratory synthesized olivine aggregates have been the focus of many studies aimed at understanding the processes by which microstructural evolution influences the strength of the upper mantle. During deformation that is dislocation-mediated, such as dislocation accommodated grain boundary sliding (disGBS) and dislocation creep, the processes of dynamic recrystallization and CPO formation are typically thought to lead mechanical feedbacks that results in strain weakening. Alternatively, during deformation by diffusion creep, static grain growth may lead to time dependent strengthening. In the case of polyphase rocks, there may be interphase reactions or grain-size pinning that can have varying effects on strength, which may also evolve with strain due to phase mixing/unmixing or changes in grain size.

In the present study, San Carlos olivine aggregates were deformed in torsion to high strains leading to detailed observations of changes in grain-size, SPO and CPO under variable stress and strain conditions. Characterization of microstructural evolution in experimentally deformed rocks provides diagnostic tools for understanding the deformation conditions of naturally exhumed mantle rocks and interpretations of geophysical observations such as seismic anisotropy and attenuation.

Several experimental studies have examined microstructural evolution of nominally melt-free olivine-rich rocks deformed to high strain in torsion (Bystricky et al. 2000, Hansen et al., 2012a; Hansen et al., 2012b; Hansen et al., 2012c; Hansen et al., 2014; Hansen et a. 2016a; Hansen et al., 2016b; Tasaka et al., 2016; Tielke et al., 2016; Tasaka et al., 2017a; Tasaka et al., 2017b; Weissman et al., 2018). However, in most cases, only tangential sections from the outer radius (highest stress and strain region) of experimentally deformed samples were analyzed, producing a single snapshot of the deformation induced microstructural evolution within the sample. In this study, the stress and strain gradient inherent to the torsional geometry is utilized to extract additional information using EBSD analyses of radial sections of deformed samples. Our work is easily compared to the results of Hansen et al. (2014), who attempted to compile experimental results across published studies to understand olivine CPO evolution with strain. However, there is substantial scatter in the reported data, which likely reflects the varied methods and starting materials used in the compiled studies. Many of the experiments included in their analysis were either deformed in a general shear geometry or with Fo_{50} starting material. In this work, results from the experiments are easily compared to each other, due to a consistent simple shear geometry and San Carlos olivine chemistry. By utilizing the stress and

strain gradient, many data points are collected from each deformed sample. The detailed features of CPO evolution can be used as targets to benchmark micromechanical models of CPO evolution in Earth's upper mantle.

Results from previous high strain torsion experiments on fine-grained San Carlos olivine aggregates demonstrated grain-size refinement by dynamic recrystallization and formation of strong CPOs (Bystricky et al., 2000). A stress exponent of $n = 3.3$ was measured by applying strain rate-steps during deformation. The relatively high strengths measured from these experiments and laboratory time constraints motivated several subsequent studies using Fo_{50} aggregates, which are much weaker due to their high iron content, allowing exploration of a larger range of deformation conditions; (however, extrapolation of the effect of iron content is required in order to apply the results to Earth's mantle). Grain-size sensitivity of the strength was found to be important to deformation at experimental conditions (Hansen et al., 2012a). Deformation was attributed to disGBS, a potentially important deformation mechanism in Earth's upper mantle considering the results of axial compression experiments on San Carlos olivine aggregates (Hansen et al. 2011). Similarly, the microstructures of the deformed samples contained evidence of dynamic recrystallization with a recrystallized grain-size that depended on the stress of deformation and increasing CPO strength with increasing strain (Hansen et al., 2012a).

In this study, high strain torsion of San Carlos olivine aggregates (with a chemistry relevant for Earth's mantle) are examined to further understand these processes of microstructural evolution. Additionally, by taking advantage of the stress and strain gradients inherent to torsional deformation, we were able to investigate microstructural evolution over a large range of deformation conditions on the same sample. These experiments permitted precise characterization of CPO, SPO and grain-size evolution across a range of stress and strain histories.

3.3 Background

3.3.1 Mechanics of Torsion

The innovation of apparatuses for torsional rock deformation in the laboratory has opened the possibility for studying microstructural evolution at high-strains, critical for many geological problems. Inherent to the torsional geometry is a radial strain and strain-rate

gradient. Rate-dependent deformation, therefore, also results in a radial stress gradient. During deformation, mechanical properties are monitored by measuring the total torque on the sample. Thus, a mechanical model, such as power-law creep, is required to generate estimates of stress in the sample. The use of thin-walled hollow cylinders minimizes this complication (Paterson and Olgaard, 2000). Several studies have used samples with soft Ni-cores to deform thin-walled olivine-rich rocks, allowing for potentially higher resolution of mechanical properties (Hansen et al., 2012a; Hansen et al., 2012b; Hansen et al., 2012c; Tasaka et al., 2017a; Tasaka et al., 2017b; Weisman et al., 2018). However, in this study, we take advantage of the torsional stress and strain gradients to generate a detailed view of microstructural evolution. By analyzing radial sections of samples deformed in torsion, only a few experiments are needed to study a broad set of deformation conditions. We supplement this analysis with data from experiments using soft Ni-cores to support the consistency of results between these two experimental designs.

The mechanics of torsional deformation by power-law creep were analyzed by Paterson and Olgaard (2000), forming the basis for our analysis. In torsion, shear strain increases linearly from 0 at the center to a maximum value at the outer radius, given by

$$\gamma = r\theta/l, \tag{1}$$

where γ is the shear strain, r is the radius, θ is the twist angle, and l is the height of the sample. It follows that

$$\dot{\gamma} = r\dot{\theta} \,/\, l, \tag{2}$$

such that strain rate, $\dot{\gamma}$ also increases linearly with radius. For power-law creep, the radial stress profile can be directly calculated from the total torque. The relationship between torque, W, and shear stress integrated over annular rings, dr, each experiencing a radially dependent shear stress of, τ_r, is described by

$$W = 2\pi \int_0^r \tau_r r^2 \, dr. \tag{3}$$

Substituting in a power-law relation gives the relationship between torque and stress at the outer radius, τ_0, of

$$W = 2\pi r^3 \tau_o / (3 + n^{-1}) \tag{4}$$

for a solid cylinder deformed in torsion. With the appropriate choice of stress exponent, n, the

radial stress and strain profiles are calculated using the relations

$$\frac{\tau}{\tau_o} = \left(\frac{r}{r_o}\right)^{\frac{1}{n}} \quad (5)$$

and

$$\frac{\gamma}{\gamma_o} = \frac{r}{r_o}. \quad (6)$$

Examples of normalized radial stress-strain profiles, presented in Fig.1, illustrate that the maximum curvature of the stress profile increases with stress exponent, such that the variation in stress is smaller over the outer portion of the sample for a higher stress exponent. The typical thickness of a sample with a Ni-core is shown, illustrating that when $n > 1$ the variation in stress is small through the radial thickness of a thin-walled sample. Therefore, samples with a soft Ni-core are considered more reliable for determining the absolute value of stress.

The mechanical results from torsion experiments can be directly compared with those obtained from other deformation geometries using equivalent or von Mises values, by transformation of the stress and strain tensors. Since torsional geometry maintains nearly simple shear throughout deformation this transformation is relatively simple. For simple shear, the equivalent stress, σ, is

$$\sigma = \sqrt{3}\tau \quad (7)$$

and the equivalent strain, ε, is

$$\varepsilon = \gamma/\sqrt{3}. \quad (8)$$

Equivalent stress and strain are the values that would be measured in axial compression. The results of our analyses are typically expressed in terms of equivalent values.

3.3.2 Recrystallized Grain-Size Piezometry

During deformation by dislocation-mediated mechanisms, such as disGBS or dislocation creep, dynamic recrystallization is expected to result in a recrystallized grain size that depends on the stress of deformation. If this relationship is known, it can be used as a piezometer to interpret deformation conditions of naturally exposed rocks or make estimates of the grain size in the upper mantle. Therefore, understanding this relationship can inform field studies of exhumed mantle rocks, interpretations of geophysical data, and the parameters used in geodynamic models of mantle flow. A combination of theory and empirical experimental results form the basis for the application of recrystallized grain-size piezometry to natural systems.

Most theories of dynamic recrystallization lead to the basic expectation that recrystallized grain-size has a power-law dependence on stress, such that

$$d = K\sigma^{-p}, \quad (9)$$

where K is a material-dependent parameter and p is the grain-size exponent. This relationship can be scaled for a variety of materials across crystalline systems by normalizing by the elastic shear modulus, μ, and Burgers vector, b:

$$\frac{d}{b} = K'\left(\frac{\sigma}{\mu}\right)^{-p} \quad (10)$$

(Twiss, 1977; Derby, 1991; Austin and Evans, 2007; Shimizu, 2008; Holtzman et al., 2018). A similar relationship is expected to hold for subgrain size. However, the subgrain-size piezometer typically has an exponent of p_{sub} near unity, while the grain-size piezometer exponent is typically slightly greater than 1. (Twiss, 1977).

During deformation, dynamic recrystallization occurs by a variety of physical processes. Broadly, mechanisms of dynamic recrystallization can be divided into two categories, boundary migration and subgrain rotation (Shimizu, 2008). Migration is initiated by differences in dislocation density and associated strain energy across a grain boundary, causing bulging that nucleates a new grain. Rotation is achieved by the climb of dislocations into subgrain walls, which progressively rotate as dislocations are accumulated. As the dislocations in the boundary become closely spaced, the rotation becomes large enough that a new high-angle grain boundary is formed. Rotation recrystallization is a continuous process, whereas, nucleation by grain boundary bulging is discontinuous. The dynamic recrystallization regime that dominates may depend on the deformation conditions, as observed experimentally in quartz (Hirth and Tullis, 1992) and halite (Guillope and Poirier, 1979)

Several studies have attempted to establish a theoretical basis for the observed power-law piezometric relationship, justifying extrapolation of laboratory results to natural settings. Theoretical models of dynamic recrystallization are essentially either energy balance models (e.g. Twiss, 1977; Austin and Evans, 2007) or nucleation and growth models (e.g. Derby and Ashby 1987; Shimizu, 1998). In general, these models provide a way to calculate the steady state grain size that results from high strain deformation at constant stress. Taking a more simplified approach, De Bresser et al. (2001) hypothesized that grain size reduction during dislocation creep and grain growth during diffusion creep would lead to a steady-state grain size

at the field boundary, such that the recrystallized grain-size is related to the competition between different deformation mechanisms. Holtzman et al. (2018) present a model that is especially relevant to the observations in this study. Their model predicts that the recrystallized grain size and subgrain-size piezometers merge at high stresses, resulting in a change in recrystallized grain-size exponent. Merging of recrystallized grain size and subgrain size has been observed in some metals that were deformed in torsion to high strains (e.g., Solberg et al., 1989). In this case, progressive thinning of grains, along with continuous recrystallization, is proposed to result in the observed, uniform, fine-grained microstructure with a recrystallized grain size equal to the predicted subgrain size.

3.3.3 Experimentally Determined Recrystallized Grain-Size Piezometers for Olivine

The most commonly used, experimentally determined, recrystallized grain-size piezometers for olivine were generated from microstructural analyses of olivine single crystals (Karato, 1980) and naturally sourced, coarse-grained dunite deformed to low strains in axial compression experiments (Ross et al., 1980; Van der Wal, 1993). In the first case, combined data from oriented single crystals of San Carlos olivine deformed to strains of 40 to 60% led to a grain-size piezometer with $p = 1.18$, reported from mean linear-intercept measurements of recrystallized grains (Karato, 1980). Measurements of subgrain size on the same samples yielded $p_{sub} = 0.67$. However, we note that the relatively high strains of these axial-compression experiments leads to large uncertainties in the measured stress.

Low-strain, axial-compression experiments on naturally sourced dunite cores revealed similar relationships. Van der Wal (1993) determined a recrystallized grain-size piezometer from experiments on coarse-grained naturally sourced dunites in a gas-medium, Paterson-type apparatus, with $p = 1.33$. In this case, recrystallized grains were identified as grains that appeared much smaller than the initial grain size as measured by maximum diameter. Other experiments conducted in a solid-medium apparatus obtained $p = 1.27$ and $p_{sub} = 0.62$ (Ross et al., 1980). However, again there is substantial uncertainty in their measurements of stress due to the influence of the high strength of the confining medium, which likely led to significantly overestimated values of stress.

Recently Goddard et al. (2020), presented a subgrain-size piezometer based on applying the linear intercept method to EBSD data (in contrast to previously mentioned studies that made measurements from optical micrographs), with a threshold of 1° identifying boundary intercepts, such that both low and high angle boundaries are included in the measurement. This

value is related to the subgrain scaling and is therefore a function of stress. In their work, they parameterize a piezometer where $p = 1.0$ or $p = 1.2$ depending on the interpretation of the data.

3.3.4 Implications of Dynamic Recrystallization on Mechanical Properties

Experiments on synthetic San Carlos olivine aggregates have identified a grain-size dependent, power-law regime attributed to a deformation mechanism called dislocation-accommodated grain boundary sliding (disGBS), which may be important for deformation in the upper mantle and is likely to dominate at the conditions of our experiments (Hansen et al., 2011). High-temperature creep is typically modeled by a power-law relationship of the form

$$\dot{\varepsilon} = A\sigma^{n} d^{-m} \exp\left(-\frac{Q}{\mathrm{R}T}\right), \quad (11)$$

where A is a mechanism-dependent parameter, n is a mechanism-dependent stress exponent, m is a mechanism-dependent grain-size exponent, and Q is the mechanism-dependent activation energy. A stress exponent of 2.9 and grain size exponent of 0.7 were determined for deformation of San Carlos olivine aggregates that deformed by disGBS. Deformation of olivine by disGBS results in grain-size refinement by dynamic recrystallization (Hansen et al., 2012a). The feedback between mechanical grain-size sensitivity and dynamic recrystallization, with grain size reflecting stress, leads to an increase in the apparent stress exponent from transient to steady-state deformation conditions, with the flow-law

$$\dot{\varepsilon} = A'\sigma^{n+(mp)} \exp\left(-\frac{Q}{\mathrm{R}T}\right) \quad (12)$$

(Hansen et al. 2012a). This result applies at large strains, after the microstructure is fully recrystallized and long-term steady-state deformation is achieved.

3.4 Methods

3.4.1 Sample Preparation

Fine-grained, nearly pore-free aggregates of San Carlos olivine were synthesized using the evacuated hot-pressing method. Detailed description of the sample preparation methods and their properties during static annealing are described in Chapter 2. To summarize, aggregates were densified from fine-powders with a narrow particle-size distribution made from pulverized, hand-picked San Carlos olivine single crystals. We used powder with a volumetric mean powder-size of 6.2 ± 2.6 μm, dried in a Ni-lined alumina boat at roughly 1100°C for 10 hours in a 1-atm mixture of CO/CO_2. Powders were uniaxially cold pressed at approximately

100 MPa into a Ni capsule. The Ni capsule was sealed at one end and capped with porous alumina at the other to allow for active evacuation of the powder compact during densification. A layer of NiO powder was added to the sealed end of the capsule to buffer the fO_2 at Ni/NiO throughout densification, ensuring that the chemical environment was maintained within the olivine stability field. The pore space of the sample compact was connected to a vacuum of <0.2 mbar through the porous alumina cap and bore holes in the dense alumina pistons. The samples were densified at 1250°C under a confining pressure of 300 MPa in a gas-medium Paterson-type apparatus for roughly 3 hours. This procedure resulted in fine-grained aggregates with less than 0.1 % porosity as observed with a SEM. Evacuated hot-pressed samples were dark green, translucent at the centimeter scale and transparent at the millimeter scale, an indication of their low porosity.

A few variations were made in sample preparation among the six experiments presented in this study. In two cases, powders were densified around a soft Ni-metal core (PT1223 and PT1226), allowing more accurate stress measurement as described above. In one case, the sample was densified *in situ* (i.e., without being removed before initiating deformation) between porous alumina spacers and without using a Ni metal core (PT948). In the other three cases, standard full cylindrical evacuated hot-pressed samples were used in deformation experiments (PT1292, PT1296, and PT1297).

3.4.2 Deformation Experiments

Evacuated hot-pressed aggregates were deformed in torsion in a gas-medium Paterson apparatus (Paterson, 1990). A schematic of the deformation column is presented in Fig. 2 along with the three variations of sample preparation. The *in situ* hot-pressed sample and the two samples with a Ni-core were deformed between porous alumina pistons. The solid-cylinder samples were deformed between coarse-grained, naturally sourced dunite spacers that had been dehydrated at 1100°C in a 1-atm furnace in mixed CO/CO_2. Ultimately coarse grained dunite spacers were used because it appeared that samples maintained their dark green color and centimeter-scale translucency, with fewer cracks from depressurization and quenching, when deformed between dunite spacers. When the dunite spacers were excluded, the color of the samples became lighter and became gray with more cracks, when removed from the deformation apparatus.

All experiments were performed by applying a constant twist rate at 1250°C and a confining pressure of 300 MPa. The temperature, which was monitored by a thermocouple

placed near the sample, varied by <2°C across the length of the hot zone based on calibration experiments. The imposed twist rates resulted in equivalent strain rates, $\dot{\varepsilon}$, at the outer-radius of 1.8×10^{-5} s^{-1} to 1.4×10^{-4} s^{-1} (shear strains rates, $\dot{\gamma}$, of 3.1×10^{-5} s^{-1} to 2.5×10^{-4} s^{-1}), leading to equivalent strains, ε, of up to 5.9 (shear strains, γ, of up to 10.2). In one case (PT1297), several twist-rate steps were applied within this range. In all other cases, a single twist-rate was applied. In general, with increasing strain, torque initially increased rapidly to a peak value, followed by an extended decrease of torque over the remainder of the experiment. A 2π-sinusoidal fluctuation was observed in the measured torque for one sample (PT1296) deformed to the highest strain ($\gamma \approx 6$), which is a consistent feature in studies using this type of apparatus and is considered to be due to slight misalignments in the assembly (i.e., Hansen et al., 2012a; Tasaka et al., 2017a). However, in contrast to these studies, we do not attempt to correct the data to remove the sinusoidal oscillation in torque. After deformation, all samples had a right cylindrical shape with no apparent localization or off-axis deformation. The data were corrected to account for the compliance of the apparatus by twisting a dummy solid-alumina sample and measuring the elastic stress-strain response across the relevant torque range. The data were also corrected to account for the strength of the Ni capsule and Fe jacket using the flow laws of Frost and Ashby (1982).

In all cases, mechanical data were analyzed using a stress exponent of 3.5 (justified by fits of our mechanical data using equations 11 and 12). The calculated peak equivalent stresses, σ_{peak}, at the outer radius reached between 181 and 299 MPa (peak shear stresses, τ_{peak}, of 105 to 172 MPa). The samples then weakened to final equivalent stresses, σ_{final}, at the outer radius of 141 to 260 MPa (final shear stresses, τ_{final}, of 81 to 150 MPa). The deformation conditions are summarized in Table 1. Mechanical data collected across experiments at similar points were used to compare our data to the previously published flow law of Hansen et al. (2011) and to validate our choice of stress exponent necessary for microstructural interpretations of radial sections.

3.4.3 Microstructural Analysis

The microstructures of deformed samples were analyzed by EBSD to obtain information on grain size, SPO, CPO, and subgrain-boundary character. Samples were prepared for EBSD analysis by polishing the section of interest on a series of diamond lapping films of progressively finer grit size to a minimum of 0.5 µm, followed by approximately 30 minutes of polishing with colloidal silica. Polished sections were coated with carbon to prevent charging during analysis.

A transverse section of PT1254 (an undeformed, evacuated hot-pressed sample) and tangential sections of samples PT948, PT1223, and PT1226 were mapped at 0.5 μm step-size on a JEOL 6500 field emission SEM using Oxford HKL Channel 5 software with an indexing rate of ~70% in all cases. These maps were relatively small, containing 273 to 4771 grains. Tangential and radial sections of samples PT1292, PT1296, and PT1297 were mapped using a Tescan Mira 3 field emission SEM equipped with an Oxford Symmetry detector and Aztec acquisition software, achieving indexing rates >90% in all cases. Tangential sections from these samples were mapped at 0.5-μm step size; mapped regions contained 13,891 to 24,403 grains. Radial sections were mapped at 1-μm step size; mapped regions contained 98,385 to 201,634 grains. The high-quality, detailed mapping of these three samples, form the basis of the bulk of our analysis and interpretation; however, information from the other samples is used to support the consistency of our results.

All EBSD data were analyzed using the MTEX toolbox for MATLAB (Bachmann et al., 2010). A grain boundary threshold of 10° misorientation was used for grain-based analyses, while a threshold of 1°, 2°, and 5° misorientation were used to analyze subgrain boundaries. Radial profiles were analyzed by grouping grains in 100-μm radial bins, resulting in roughly 50 bins across the stress and strain gradients for each sample. The stress, strain, and strain rate were calculated for the center point of each radial bin in our analyses.

3.4.4 Grain-Size Measurement

Grain sizes were estimated by calculating the circular diameter of an equivalent area composed of clusters of points with angular misorientation of <10° from their neighbors. Equivalent areas were multiplied by 4/π to correct for the stereographic sectioning effect (Underwood, 1972). While grains analyzed in this study generally have anisotropic grain shapes, which influences the true stereographic correction, this standard practice was employed to make our data easily translatable across studies. Grain sizes were fit with a log-normal curve, which did a reasonably good job of fitting the data across tangential sections and spatially binned radial sections. The grain size is reported as the arithmetic mean of the measured grain-size distribution, $\mathrm{d}_{\mathrm{EA\,grain}}$. We also applied the mean linear intercept method as an alternative measure of grain size. A stereographic correction of 1.5 was applied to the reported grain size when using the linear-intercept method. Both methods were repeated using a 1° threshold to identify subgrain boundaries and make comparisons to the analysis of Goddard et al. (2020). Goddard et al. (2020) did not include a stereographic correction factor in their analysis. When

analyzing our data, we account for stereographic correction factors, which we therefore apply to the piezometers of Goddard et al. (2020) when making comparisons to our data. Mean grain-size measurements were plotted against calculated equivalent stress to calibrate a recrystallized grain-size piezometer.

3.4.5 Other Measures of Grain Dimension and SPO – Grain Boundary Angle Distribution, Mean Linear-Intercept, and Caliper Dimensions

To characterize grain shape and SPO, specimen reference frame grain-boundary angle distributions, angle varied mean linear intercept lengths, and caliper dimensions were measured from EBSD maps of deformed specimens. The specimen reference frame grain-boundary angle distribution provides a measure of average grain dimensions, yielding detailed information on grain shape and SPO. This distribution represents the density of grain boundaries that are oriented at each angle relative to the analyzed section of each specimen. To make this measurement, grain boundaries represented in the EBSD grain reconstructions were smoothed in several iterations using a smoothing algorithm to reduce artifacts from gridded data acquisition.

By applying the approximation that grain boundaries are evenly distributed among grains, the grain boundary angle distribution was used to generate a synthetic mean grain shape representing the average grain dimensions and shape-orientation. The circular diameter of the equivalent area of this polygon, $d_{\mathrm{EA\ boundary}}$, provides yet another way to measure grain size. The ratio of the longest dimension, $d_{\mathrm{long\ boundary}}$, to the shortest dimension, $d_{\mathrm{short\ boundary}}$, of the generated polygon provides an estimate of the strength of the SPO in the tangential section. The angle of the longest dimension of the generated polygon, $\theta_{\mathrm{boundary}}$, provides a measure of the orientation of the SPO. This method of characterizing the SPO provides an easily translatable procedure that does not rely on fitting of ellipses to irregular grain shapes (as is frequently used). This method also provides an easy way to visualize the SPO by plotting the resulting synthetic mean grain shape.

Further characterization of grain shapes was made by calculating the mean maximum caliper dimension, $d_{\mathrm{long\ caliper}}$, and the mean dimension perpendicular to the long caliper dimension, $d_{\mathrm{short\ caliper}}$, which are also reported. The ratio of these values provides an additional measure of the average aspect ratio of grains, but it is not a truly a measure of the strength of the SPO because it does not directly measure the alignment of grains. However, the mean angle of the long caliper dimension, $\theta_{\mathrm{caliper}}$, which is an indicator of the geometry of the

SPO is also reported.

Finally, we apply an additional method for characterizing the SPO of deformed samples using an angle varied mean linear-intercept method. Mean linear intercepts taken from transects spaced 10 μm apart at 3° intervals are reported (with no stereographic correction applied in this analysis). The angle-dependent maximum and minimum values of the mean linear-intercept length, $d_{\text{long intercept}}$ and $d_{\text{short intercept}}$, provide an additional measure of average grain dimension and SPO. The ratio of these values yields a measure of the strength of the SPO, similar in magnitude to that obtained from the grain-boundary angle distribution. A third measure of the SPO geometry is the angle with the longest mean intercept, $\theta_{\text{intercept}}$. The mean value of the linear intercept, multiplied by a factor of 1.5 to correct for the stereographic sectioning effect, $d_{\text{intercept}}$, provides yet another measure of grain size.

In this study we include a broad variety of approaches, described above, to characterize the grain size, grain shape, and SPO because the community has not yet agreed on standard methods. By providing a number of characterization procedures we not only allow for our data to be easily compared to other studies, we may also find that some measures are more robust than others in describing sample to sample variation.

3.4.6 CPO Analysis

Crystallographic preferred orientations (CPOs) were used to calculate orientation distribution functions (ODFs) for an undeformed sample and tangential and radial sections of deformed samples. The CPO is visually illustrated using standard pole figures typical of olivine CPO analyses, wherein, the three principal crystallographic directions are plotted in the specimen reference frame.

Fabric evolution in deformed samples was further analyzed using standard measures of fabric strength and geometry. The overall fabric intensity was determined by calculating the M-index (Skemer et al., 2005) and J-index from both radial profiles and tangential sections. The M- and J-index are given, respectively, by

$$M = \frac{1}{2}\int |R(\theta) - R_0(\theta)|\, d\theta\,, \tag{13}$$

where $R(\theta)$ is the observed misorientation angle distribution and $R_0(\theta)$ is the theoretical random misorientation angle distribution, and

$$J = \int f(g)\, dg\,, \tag{14}$$

where $f(\mathrm{g})$ is the orientation distribution function. The M-index ranges from 0 to 1 for a random distribution to a single orientation, while the J-index ranges from 0 to infinity.

To quantify fabric geometry, the eigenvalue analysis originally described by Woodcock (1977) and modified by Vollmer (1990) was applied. Eigenvalue analysis of grain orientations allows for evaluation of clustering of specific crystallographic directions, quantifying the geometrical patterns observed in standard pole figures. This approach provides measures of the tendency of point clustering, girdling, and overall randomness for a given crystallographic direction. In this analysis, a normalized orientation tensor is defined as

$$O = \frac{1}{N}\begin{bmatrix} \sum l_i^2 & \sum l_i m_i & \sum l_i n_i \\ \sum m_i l_i & \sum m_i^2 & \sum m_i n_i \\ \sum n_i l_i & \sum n_i m_i & \sum n_i^2 \end{bmatrix}, \tag{15}$$

where l_i, m_i, and n_i are components of the unit vector in specimen coordinates along the chosen crystallographic direction. N is the number of orientations evaluated. We analyzed our data on a one point per grain basis. Normalized eigenvalues S_i, are calculated from the orientation tensor such that they sum to 1 with indexes in descending order such that $S_1 \geq S_2 \geq S_3$.

Woodcock (1977) proposed that the tendency for point clustering could be quantified by

$$P_w = ln\,(S_1/S_2), \tag{16}$$

and the tendency of girdling by

$$G_w = ln\,(S_2/S_3). \tag{17}$$

The ratio of these values gives a measure of the tendency of point clustering relative to girdling, termed the shape factor, defined as

$$K_w = P_w/G_w, \tag{18}$$

with large values of K_w representing more prolate distributions and low values of K_w indicating more oblate distributions.

Vollmer et al. (1990) introduced alternative metrics to describe the same properties, where the tendency for point clustering is given by

$$P_v = S_1 - S_2 \quad , \tag{19}$$

and the tendency of girdling by

$$G_v = 2(S_2 - S_3) \quad , \tag{20}$$

with the shape factor defined as

$$K_v = P_v / G_v \quad . \tag{21}$$

An additional quantity, *R*, also results from the eigenvalue analysis and is a measure of the overall randomness of clustering for a specific crystallographic direction:

$$R_v = 3(S_3) \quad , \tag{22}$$

where a value of 1 represents a random distribution and a value of 0 corresponds to a single orientation. For completeness, values using both the Woodcock and Vollmer method are presented. However, the measures of fabric geometry presented by Vollmer et al. (1990) can be nicely visualized on a ternary diagram, tracking their evolution with strain, since they vary from 0 to 1. The eigenvalue analysis was applied using the MTEX toolbox (Mainprice et al., 2015).

Additionally, we applied an orientation clustering algorithm to several EBSD maps taken from tangential sections where large numbers of grains were mapped (N>10000). The algorithm was instructed to sort the grain orientations into up to 4 clusters. These clusters can be compared to prototypical fabric types to quantify the competition between different slip systems during CPO formation. This analysis provides information that is easily hidden by the typical presentation of pole figures for olivine. The clustering algorithm is included in the MTEX toolbox (Mainprice et al., 2015).

3.4.7 Subgrain-Boundary Analysis

Subgrain-boundaries were also analyzed using EBSD maps taken from tangential sections to further investigate variation in microstructures resulting from separate experiments. The spatial geometry and density of subgrain boundaries was quantified by calculating the specimen frame subgrain-boundary angle distribution in the specimen coordinates. The crystallographic character of subgrain boundaries was also analyzed by plotting inverse pole figures of subgrain-boundary misorientation axis distribution and subgrain-boundary crystallographic normal (as observed in the tangential section). This approach yields a characterization of the crystallographic character of subgrain boundaries, assuming that boundaries are on average roughly normal to the section surface. Combining subgrain-

boundary axis distribution and normal distribution permits inferences of the types of dislocation structures that formed these boundaries.

3.5 Results

3.5.1 Mechanical Data

The stress during deformation, calculated for the outer radius of samples deformed at a constant twist rate, as presented in the stress-strain curves in Fig. 3, exhibits an initial strengthening to a peak stress at equivalent strains below 0.5, followed by extended weakening throughout the remainder of each experiment. In the case of the highest strain experiment, sinusoidal variation with an amplitude of ~10 MPa in equivalent stress (~6 MPa in shear stress), likely due to slight misalignments of components in the sample column overprints the gradual weakening trending toward steady state. This variation is accepted as uncertainty in the data.

Mechanical data are compared in Fig. 4 to the flow laws for diffusion creep and disGBS determined by Hansen et al. (2011) on conventionally hot-pressed San Carlos olivine aggregates. Values of stress and strain rate are plotted for the peak stress, for an equivalent strain of 1, and for the final strain. Our data are initially compared to the flow law calculated for a grain size of 9 μm – a reasonable estimate of grain size for our experiments. In general, the flow law determined from axial compression agrees well with our data – falling between the strength recorded at peak stress and that at an equivalent strain of 1. However, as demonstrated in Fig. 5, fits to the data yield stress exponents higher than the value of 2.9 expected from the flow law.

Under the assumption that stress determines grain size, a grain-size corrected flow law was calculated by incorporating the grain-size piezometer determined from our data into the flow law as described in Eq. 12. This flow law roughly fits the experimental data obtained at an equivalent strain of 1. Fitting our data, while considering the radial variation in grain size (incorporating a grain-size piezometer) led to a stress exponent for disGBS of 3.4. While, the choice of stress exponent used to process mechanical data also influences our calculation of the radial stress gradient, varying the stress exponent from 2.5 to 4.5 when fitting the grain-size piezometer leads to a variation of less than ±0.1 in the calculated stress exponent for the disGBS flow law, the deformation mechanism assumed most active during deformation of our samples (meaning the choice of stress exponents when fitting the piezometer does not have a large impact on the result). Therefore, 3.5 is a reasonable value for our calculations, as it is

broadly consistent with our data and with the results of other published studies (Bystricky et al., 2000; Hirth and Kohlstedt, 2015; Wiesman et al., 2018). At higher strains, samples continue to weaken beyond the grain-size corrected flow law, likely due to the influence of continued CPO evolution. The conditions and results from the mechanical data from our experiments are summarized in Table 1.

3.5.2 Characterization of the Undeformed Starting Material

An EBSD map was made from a transverse section of sample PT1254, an example of undeformed starting material, parts of which were later used in torsion experiments. This map is presented in Fig. 6 with band contrast overlain by semi-transparent inverse pole figure (IPF) coloring, where the color corresponds to the crystallographic direction corresponding to the shear direction in the specimen frame. This same representation is used in all maps where IPF coloring represented throughout this chapter. The variation in color demonstrates the nearly random distribution of the starting material, presented quantitatively in the following sections. The starting microstructure is fine grained, however, several larger than average grains appear that represent the initial stages of abnormal grain growth observed during annealing under isostatic stress conditions (see Chapter 2). The grain size distribution for the starting material is presented along with a log-normal fit to the data in Fig 7, demonstrating that the initial grain size distribution is roughly log-normal.

3.5.3 EBSD Maps of Deformed Specimens

EBSD maps made from the tangential sections of deformed samples reveal the development of a strong CPO and SPO. Additionally, the grain size distribution appears to be more uniform, with no indication of the microstructures associated with abnormal grain growth observed under static conditions (see Chapter 2). The strong CPO is apparent by the overall blue/purple color of maps, presented in Figs. 8-13, wherein grain orientations are represented by IPF coloring. Again, this point is explored quantitatively in the following sections. The SPO is apparent in the alignment of grain boundaries at an angle approximately 30° to the shear plane, synthetic with the sense of shear deformation (all maps are presented with top-to-right sense of shear). The SPO is also described quantitatively in the following sections.

EBSD maps made from radial sections of deformed samples reveal two distinct features. First, the fabric intensity increases toward the outer edge of the deformed samples. This observation is apparent by the gradient in color in the EBSD maps presented in Fig. 14, wherein grain orientations are represented by IPF coloring. Additionally, there is a radial grain size

gradient in the sample, with finer grain sizes toward the outer edge of the deformed samples. This observation is apparent in the gradient in color in the EBSD maps presented in Fig 15, which is colored by grain size.

3.5.4 Grain-Size Analysis

Grain-size distributions from tangential sections are roughly log-normal, as demonstrated by the histograms of grain size calculated from equivalent area circular diameter presented in Fig. 16. As the number of grains per map increases, the distributions become smoother, as is apparent in the maps that include a large number of grains, N>10000 (Fig 16 d-f). In detail, this analysis reveals that grain size distributions may be slightly skewed toward fine grain sizes relative to a log-normal distribution. Grain size was additionally characterized by linear intercept method. The mean grain sizes measured from EBSD maps of tangential sections are included in Table 2. Radially binned EBSD maps taken from radial sections of deformed samples (Fig. 15) were also used to characterize the grain size using the equivalent area circular diameter method. Grain sizes determined near the edge of radial sections are roughly equal to those determined from tangential sections.

The grain sizes determined from EBSD maps were plotted against the calculated stress of deformation to examine the piezometric grain-size relationship described in the background section of this chapter. These data are presented along with published recrystallized grain size and subgrain size piezometers in Fig. 17. The piezometer calculated from our data matches closely the published subgrain-size piezometer of Karato (1980) and lies well below the published recrystallized grain-size piezometers of Karato (1980) and Van der Wal et al. (1994). The grain size data calculated using a 10° threshold fall slightly coarser than the recent subgrain size piezometer of Goddard et al. (2020), which may be expected. However, applying a 1° threshold to calculate subgrain size, consistent with their method, results in near correspondence with their analysis. A least-squares fit to grain sizes calculated from tangential and radially binned sections, using a 10° threshold, and the corresponding values of stress yields the grain-size piezometer

$$d_{\mathrm{EA}} = (315\ \ \mu\mathrm{m\ MPa}^{0.71})\sigma^{-0.71} \quad . \tag{23}$$

A fit to the grain size determined using the mean linear intercept method, using a 10° threshold resulted in the grain size piezometer of

$$d_{\mathrm{LI}} = (992\ \ \mu\mathrm{m\ MPa}^{0.92})\sigma^{-0.92} \quad . \tag{24}$$

If a 1° threshold is used in the analysis, fits to the data result in the piezometers

$$d_{\mathrm{subEA}} = (318\ \mu\mathrm{m\ MPa}^{0.77})\sigma^{-0.77} \quad (25)$$

and

$$d_{\mathrm{subLI}} = (1373\ \mu\mathrm{m\ MPa}^{1.0})\sigma^{-1.0} \quad , \quad (26)$$

using both the mean equivalent area circular diameter and mean linear intercept methods, respectively. The relationship between the grain-size calculated using a 10° threshold and the grain size calculated using a 1°, which represents the subgrain size (Goddard et al., 2020), is examined in Fig. 18. The ratio of grain size and number of grains determined using both measures reveals that the subgrain size was consistently a factor of between 0.7 and 0.9 of the grain size (Fig. 18a) and that there were roughly 1.5 to 2 subgrains per grain (Fig 18b), with no apparent correlation of this relationship with stress. Therefore, a given grain in our deformed samples typically has either one or zero subgrain boundaries and the subgrain size is essentially the same as the grain size.

3.5.5 Mean Grain Shape and SPO

The SPO of deformed samples, characterized from tangential sections, was consistently oriented with long axes of grains ~30° to the shear plane, synthetic with the shear sense. This observation was characterized through a variety of methods, from which the overall results are presented in Tables 2 and 3. Grain shape evaluated simply by caliper dimensions exhibits a narrow range of mean aspect ratios of 1.59 to 1.65 among all deformed samples without an obvious relationship to deformation conditions or total strain. The average angle of the long axis to the shear direction ranges only between 30° and 33°. However, this measure of average aspect ratio does characterize SPO strength since the grains do not necessarily need to be strongly aligned to measure large average aspect ratios and a consistent average long axis angle in the specimen reference frame.

The distribution of grain-boundary angles, measured in 2-D sections relative to specimen coordinates, provides a better measure of SPO strength, with consistent results across all deformed samples, as demonstrated in Fig. 19. Angle-binned grain-boundary densities reveal a consistent sub-sinusoidal curve indicating alignment of grains (Fig. 19a). When normalized to the mean, the consistency of SPO between samples becomes more apparent (Fig. 19c). Large maps containing over 10000 grains have the smoothest distributions. These data are used to generate a synthetic mean grain shape, presented in Figs. 19 b,d (the polygons in Fig. 19d are

normalized to the mean radius of the synthetic mean grain shape), which provides a useful way to visualize the SPO in the sample. In Fig. 19b, the synthetic mean grain shapes from different samples have variable size, reflecting differences in grain size between samples; however, each curve has a similar aspect ratio and orientation. This point is highlighted in the normalized synthetic mean grain shapes presented in Fig. 19d. The ratio of the longest to shortest dimension of the synthetic mean grain shape ranges from 1.33 to 1.41. While this range is narrow, this measurement of SPO strength appears to correlate with stress, as demonstrated in Fig. 20. In applying this method, the angle of the long axis is more variable than the average orientation of the long caliper dimension. Large maps, where N>10000, range in long axis angle from 25° to 28°; however, smaller maps show angles up to 37°, when measured using the specimen frame grain boundary angle distribution. The equivalent circular area of the idealized average grain-shape produced by this method provides another measure of grain-size, which is reported in Table 2 for completeness and is consistently about a factor of 1.2 larger than the grain-size measured by equivalent area circular diameter.

Angle varied mean linear-intercept length provides yet another way of measuring SPO strength, which produces results that are broadly consistent with those obtained from the grain-boundary angle distribution, as presented in Fig. 21. Mean intercept lengths taken from transects of variable angle form a roughly sinusoidal curve with the smoothest data obtained from the large maps (Fig 21 c,d). Maxima consistently lie ~30° to the shear plane. When normalized to the mean intercept length, all curves reveal a similar shape (Fig. 21 b,d). The ratio of maximum to minimum intercept length ranges from 1.39 to 1.51 and the angle of maximum intercept length ranges from 15 to 45°. These relatively large ranges point to the sensitivity of this method to angle binning and distance between transects.

3.5.6 CPO Evolution: Pole Figures and Eigenvalue Analysis

During deformation, the olivine CPO evolves by both strengthening of the fabric and through changes in fabric geometry. The qualitative features of CPO evolution can be examined in the pole figures presented in Figs 22 to 25, with pole figure colored both by the minimum and maximum value for each individual pole figure and for a uniform scaling (MUD = 0 to MUD = 15). The pole figure of an undeformed sample (PT1254) is presented in the first line of Fig 22. While there is a slight maxima of b-axes along the central axis of the sample, overall the CPO is weak with an M-index of M = 0.006. Deformed samples demonstrate a complicated CPO evolution when examining the pole figures in Figs 22 to 25.

Initially the fabric evolves from a nearly random to a complex pattern with several maxima. Primarily, allignment of the [100] axis parallel to the shear direction and a second sub-maximum roughly 60° to the shear plane is evident even at low strains ($\varepsilon < 0.5$). Additionally, [010] axes form a girdle that is strongest perpendicular to the shear plane; and [001] axes form a complex pattern with a girdle perpendicular to the shear direction that is strongest along the vorticity axis and a sub-maxima aligned sub-parallel to the shear direction. This mixed fabric likely reflects deformation partitioned between the primary slip systems for olivine, taking advantage of whichever is best aligned given the initial orientation of each grain in the sample. Further characterization of this mixed fabric is explored in the orientation clustering analysis presented below. However, even at equivalent strains as low as 0.24 (Fig. 23), the dominant alignment of [100] in the shear direction and [010] perpendicular to the shear plane is apparent, interpreted to reflect deformation on the (010)[100] slip system. Additionally, strong initial girdling of the [010] and [001] axes indicate that (001)[100] is also contributing to deformation. Further, the [001] sub-maximum near the shear direction, points to activity of slip systems with [001] Burgers vectors. As deformation proceeds, the sub-maxima in the [100] and [001] axes weaken, nearly disappearing at an equivalent strain of ~2 (Fig. 24).

At even higher strains, the initial girdling of the [010] and [001] axes begins to favor a strong point maxima, leading to a transition from fabrics with a D-type character (point maxima of [010] roughly perpendicular to shear direction and girdle of [100] and [001] with a rotation axis near the shear direction) character to fabrics with strong A-type character (point maxima of [010] roughly perpendicular to the shear direction and point maxima of [100] near the shear direction) (Fig. 24). However, even at equivalent strains of nearly 6 (shear strain >10) some D-type character is maintained. At high strains, the girdling tendency of the [001] axes appears at an angle synthetic with the shear sense, while the [100] axes are roughly perpendicular to the shear direction. The observed protracted fabric development is similar to that previously described by Hansen et al. (2014), who compiled data from several published studies. This qualitative description of CPO evolution was further quantified by applying standard measures of fabric strength indexes eigenvalue analysis.

Comparing fabric strengths and results from eigenvalue analysis of EBSD data from deformed specimens reveals that CPO intensity and geometry appear to be primarily controlled by strain, with a roughly consistent strain evolution between experiments and radial position in the sample. Measures of fabric intensity, the M-index and J-index, exhibit a consistent increase

with increasing strain through radial sections, with a distinct change in slope at an equivalent strain of roughly 2, as demonstrated by Figs. 26 a,b. This change is slope is coincident with elimination of the [100] sub-maximum that initially appears at an angle oblique to the shear direction. A secondary observation made from these figures is the sudden drop in fabric intensity measured in the outermost radial bin (Fig. 26a,b - colored stars), interpreted to be the effect of partitioning of strain into the Ni jacket. Fabric intensities measured from tangential sections are slightly lower than those measured from outer regions of radial sections but between values measured from the two outermost radial bins (Fig. 26a,b – black stars), pointing to this potential edge effect. Eigenvalue analysis produces other overall measures of CPO randomness for individual crystallographic axes, R_v, presented in Figs. 26 d-f. In each case, this measure drops rapidly for each principal crystallographic direction as strain increases to an equivalent strain of $\varepsilon = 2$, after which the slope in the data becomes shallow while continuing to decrease with increasing strain. These measures are complemented by another relatively simple characterization of fabric geometry, the angle of clustering of the [100] determined by eigenvalue analysis to the shear plane (Fig. 26 c). At low strains, this value is oriented 27° synthetic to the shear plane, evolving to slightly negative values by an equivalent strain of $\varepsilon = 2$ and trending toward 0° at the highest strains of our experiments.

The results of the eigenvalue analysis of the CPO determined for each principal crystallographic direction is presented using the values of both Woodcock (1977) and Vollmer (1990) in Figs. 27-28. These measurements provide a characterization of clustering versus girdling tendency of each crystallographic direction. Broadly speaking, the features described qualitatively from the pole figures presented in Figs. 22-25 are reflected quantitatively in the plots presented in Figs. 27-28.

Additionally, ternary plots of R_v, G_v, and P_v assembled from data for all three radial sections provide another useful way to visualize the fabric evolution, as illustrated in Fig. 29. As strain increases, the [100] axes trend rapidly toward point clustering, with low values of R_v (<0.2 by an equivalent strain of 2) and high values of P_v (>0.8). Values of G_v remain very low throughout deformation. The [010] axes initially trend toward strong girdling, with $G_v > 0.7$ by an equivalent strain of roughly 2. This evolution is followed by a sharp change in the trend of [010] axes toward strong point clustering with $G_v < 0.4$ and $P_v > 0.6$ by an equivalent strain of 6. The overall trend of the [001] axes is similar to the [010] axes but is less strongly girdled and clustered. Initially, [001] axes trend toward slight point clustering, which is quickly overtaken by

girdling with maximum G_v values of roughly 0.6 at an equivalent strain of roughly 3 followed by point clustering with maximum P_v of roughly 0.5 at an equivalent strain of 6. Again, this quantification of CPO geometry matches the qualitative observations made from pole figures. In general, tangential sections show similar trends; however, edge effects lead to scatter in the data, a complication that the use of radial sections avoids. This edge effect may explain some of the scatter in data compiled by Hansen et al. (2014).

3.5.7 Orientation Clustering Analysis

The analyses presented above use pole figures to isolate individual crystallographic axes. As such, the full orientation of each grain is not considered. We applied an orientation clustering analysis to investigate the full orientations of different orientation clusters, which appear as sub-maxima in pole figures. These clusters can easily be obscured by typical presentations of pole figures. The results of the clustering analysis, presented in Figs. 30 to 32, reveal clusters that are suggestive of prototypical olivine fabric types. Only samples for which N > 10000 in tangential section were analyzed. In samples deformed to equivalent strains of roughly $\varepsilon = 2$, as in samples PT1292 and PT1296, four distinct clusters of data were identified. The clusters were suggestive of A, E, C, and B type fabrics, with population sizes decreasing in this order (Figs 30a,31a,32a). In sample PT1296, deformed to higher strain, only two distinct clusters could be identified, suggestive of A and E type fabrics (Fig. 31a). In this case, even the second cluster appeared to be trending away from the prototypical E-type orientation, toward a more A-type orientation. These data are represented as EBSD maps wherein grains are colored by their cluster ID (Figs. 30b,c;31b,c;32b,c). These images illustrate that for lower strain samples (PT1292, Fig.30; PT1297, Fig.31) there are significant populations of grains from each cluster and often grains of the same cluster ID are neighbors. At higher strains ($\varepsilon \approx 6$), as in sample PT1297 (Fig. 32) nearly all of the grains are identified in the primary cluster. Low-angle boundaries (misorientation 2-10°) are also represented on these images, illustrating their spatial orientation and distribution. These boundaries are frequently oriented perpendicular to the shear direction, as expanded on in the next section.

3.5.8 Subgrain Boundary Analysis

The alignment and specimen frame orientation of subgrain boundaries was characterized by the specimen frame subgrain boundary angle distribution. This analysis revealed that low-angle boundaries are dominantly aligned perpendicular to the shear direction, as demonstrated in Fig. 33, consistent with the typical model of subgrain wall formation. This

relationship is emphasized by isolating subgrain boundaries with angular misorientation of 2-5° (Fig. 33a). However, when isolating subgrain boundaries with angular misorientations of 5-10° the data appear to reflect a contribution from the underlying SPO (Fig. 33b, compared to Fig. 19). This situation is most prominent in the highest strain sample with the strongest fabric. This behavior is likely due to the strong CPO, wherein the grain-to-grain mean angular misorientation is relatively low due to the alignment of grains, regardless of neighbor grain relationships.

Additionally, in the crystallographic reference frame, subgrain (low-angle) boundaries have misorientation axes dominantly along the [010] and [001] axes and subgrain boundary normal (in 2D section) near the [100] direction, as is evident in Fig. 34. This observation is consistent with subgrain walls formed by edge dislocations with [100] Burgers vectors slipping on either (001) or (010) planes. The dominant rotation axes of [010], especially at lower fabric strength, indicate that slip primarily on (001) results in stable subgrain boundaries. As the fabric strengthens toward A-type, tilt boundaries formed by slip on (010) appear to become more important (see results of 2-5° misorientation axes in PT1296, deformed to higher strain than other samples, Fig. 34). Again, when including boundaries with misorientation of 5-10°, the data appear to be influenced by the strong CPO.

3.6 Discussion

The analyses presented in this study provide new perspectives on mechanical and microstructural evolution of olivine aggregates deformed to high strain. By combining mechanical data and detailed microstructural analyses, the above results describe the influence of stress and strain in modifying grain size, grain shape, SPO, and CPO of olivine aggregates deformed in a simple shear geometry. Other studies that have explored the microstructural evolution of olivine aggregates have either used a general shear (shear between angled pistons subjected to axial compression) (Zhang and Karato, 1995; Zhang et al., 2000) or Fo_{50} starting material (Hansen et al., 2012a; Hansen et al., 2014). Bystricky et al. (2000) present data on San Carlos olivine (~Fo_{90}) aggregates deformed in torsion, however, they do not present a detailed analysis of the microstructural development. Hansen et al., (2014) combine data from a variety of studies to generated a description of the strain dependence of CPO development. However, the combination of data from experiments with different composition and deformation geometry leads to uncertainty. The central impact of this detailed and descriptive dataset, with a material

chemistry relevant to Earth's mantle and a simple shear deformation geometry, is that it provides an excellent benchmark for geodynamicists attempting to develop and apply micromechanical models that incorporate CPO formation, dynamic recrystallization, and grain growth. These types of models are needed to apply experimental results, such as those produced in this study, to mantle-scale deformation processes (e.g., Tommasi et al, 2000; Ribe et al., 2019).

Broadly, the strength of samples measured in our experiments follow the flow law for disGBS presented by Hansen et al. (2011), generated from axial compression experiments at similar conditions and using similar starting materials. Further, the similarity of the microstructures produced in this study to those presented in Hansen et al. (2012a), who conducted similar high strain torsion experiments using Fo_{50} starting material, further suggests the activity of the disGBS mechanism in our experiments. According to deformation mechanism maps extrapolated to natural conditions presented by Hansen et al. (2011), disGBS is likely to be an important deformation mechanism in Earth's mantle. Hence, the microstructural evolution resulting from the deformation generated in our experiments is also likely relevant to mantle deformation processes. Therefore, it may be appropriate to use data from these experiments to benchmark models that couple microstructural evolution and mechanical properties, which can then be applied to understand deformation in the Earth.

Microstructural characterization of our deformed samples demonstrated four central features of microstructural evolution. First, torsional deformation produced a radial grain size gradient that was inversely correlated with stress when compared across experiments (Figs. 15 and 17). The measured grain size did not correspond well with published recrystallized grain size piezometers, rather, the grain size appeared to correspond more closely with published subgrain size piezometers. Second, the grain shape and SPO (analyzed from tangential sections) evolved to a consistent geometry in all samples (Figs. 19 and 21). Finally, the CPO measured from radial sections and tangential sections demonstrated a complex evolution, wherein initially several populations of preferred grain orientation arise (Figs 30 and 32). Compared across experiments, the CPO evolution was strain-dependent with consistent features and geometry (Figs. 26-29) and, after an equivalent strain of about $\varepsilon = 2$, trended toward a strong, unimodal A-type fabric. Analyses of low-angle boundaries support the inference that multiple dislocation slip systems lead to the formation of subgrain walls in samples with complex fabrics (Figs. 33 and 34).

3.6.1 Stress Dependence of Grain Size

As demonstrated in the plots of grain size versus stress in Fig. 17, deformed samples had a consistently stress dependent grain size based on analyses from both tangential and radial sections. The resulting measured grain sizes were both smaller in magnitude and had less stress dependence (low value in fit for piezometric exponent, p) than published recrystallized grain size piezometers. The piezometers of both Karato et al. (1980) and Van Der Wal et al. (1993) were calibrated from samples deformed in axial compression, wherein the small grains found in a single crystal or an originally coarse grained dunite that had been deformed in axial compression were identified as recrystallized grains. Further, measurements were made from optical micrographs, which can obscure grain size measurements. In contrast, the samples deformed in this study are initially fine grained and stabilize to a grain size that corresponds well with published subgrain size piezometers (Karato et al., 1980; Goddard et al. 2020). If held at experimental temperatures for similar times to those used in our deformation experiments at isostatic stress conditions, the grain size of these samples would grow to produce a sample dominated by grains larger than 80 μm, a value nearly an order of magnitude larger than observed in deformed samples. Rather, we interpret our results to represent the stabilization of the grain size at a value very close to the subgrain size due to continuous dynamic recrystallization by subgrain rotation. Our analysis reveals that the grain size and subgrain size are closely related (Fig. 18) and that most grains contain either no subgrain boundaries or one subgrain boundary with an orientation consistent with a model of subgrain walls composed of dislocations associated with the [100](010), [100](001)/[001](001), and/or [001](010) slip systems (Figs 33 and 34). It is possible that high strain deformation in the disGBS regime leads to the merging of the recrystallized grain size and subgrain size piezometers (as has been also observed in some metals deformed in high strain torsion, e.g., Solberg et al., 1989). This interpretation leads to the inference that the grain size is ultimately controlled by the energetic considerations (elastic distortions of the lattice due to the presence of dislocations) that determine the subgrain size.

3.6.2 Grain Shape and SPO

Analyses of tangential sections of deformed samples demonstrated a consistent grain shape and SPO orientation, with the long axis oriented roughly 30° to the shear direction, synthetic with the shear sense. Both the specimen angle grain boundary distribution (Fig. 19) and angle varied mean linear intercept lengths (Fig. 21) demonstrated that the overall SPO

orientation and strength was similar for all experiments. However, as demonstrated in the plot of aspect ratio versus stress presented in Fig. 20, the overall strength of the SPO may be subtly stress dependent. This result is expected for the microstructure of specimens deformed to steady state, as we expect the grain shape represents the competition between flattening that results from shear deformation and circularization driven by the minimization of energy that results from reducing grain boundary curvature. The rate of shearing depends on stress through the flow law, while the driving force for circularization increases with increasing aspect ratio. Therefore, we expect that a steady state SPO is established when the rates of these processes balance each other, which ultimately will depend on stress.

3.6.3 Protracted CPO Evolution

The pole figures presented in Figs. 22-25 illustrate strain dependent fabric evolution, with initially complex features that are later overprinted by a strong A-type fabric. However, pole figures are challenging to interpret because they contain features that are complicated to describe and only a single axis is considered in each plot, obscuring full orientation information.

The fabric intensity indexes and eigenvalue analyses presented in Figs. 26-29 quantify features of the CPO and individual pole figure shapes. These analyses demonstrate that fabric evolution is consistently strain dependent in our experiments and has a distinct change in geometry at an equivalent strain of $\varepsilon = 2$, wherein an initial girdling of [010] and [001] trends strongly toward point clustering (as similarly described by Hansen et al., 2014). Fabric intensity and eigenvalue quantities are helpful in describing the CPO evolution and could be used as quantitative benchmarks in micromechanical models. However, these measures are also limited in that they only consider overall intensity and the tendency toward girdling or point-clustering. These analyses do not account for the possibility of multiple submaxima occur for a single crystallographic direction or that a single maxima observed in a pole figure may be composed of multiple distinct clusters when considering the full orientation.

The orientation clustering analysis, presented in Figs. 30-33 attempts to address the limitations of the pole figure and eigenvalue analyses described above. Orientation clustering analysis of samples deformed to an equivalent strain of roughly $\varepsilon = 2$, produced four distinct clusters suggestive of the prototypical olivine fabrics, A-type, E-type, C-type, and B-type, in descending order of population size. This result is obscured in the pole figures and is not described by the eigenvalue analysis. Previously, the protracted fabric development has been described as evolving from D-type (girdle of [010] and [001] perpendicular to the shear direction

and [100] parallel to the shear direction) toward an-A type fabric at high strain. However, our analysis presents a more complex picture, wherein multiple populations of orientation submaxima initially form, which are each consistent with prototypical olivine fabrics. The generation of these distinct submaxima likely reflects the competition between different dislocation slip systems. As strain accumulates, the populations suggestive of B-type, C-type, and E-type fabric clusters diminish as the A-type cluster dominates. For a sample deformed to an equivalent strain of roughly $\varepsilon = 6$, the data were almost entirely categorized in an A-type cluster (Fig. 31), however, a weak cluster suggestive of the E-type fabric persisted (such that the resulting pole figure has the imprint of D-type shape, as described by Hansen et al. 2014).

3.7 Conclusions

The experiments and analyses described in this Chapter provide a detailed view of microstructural evolution in olivine aggregates deformed to high strains in a simple shear geometry. Grain size, grain shape, SPO, and CPO are thoroughly characterized, taking advantage of the strain and stress gradient inherent to a torsional deformation geometry.

The resulting dynamically recrystallized grain size was stress dependent and corresponded well with published subgrain size piezometers, rather than published recrystallized grain-size piezometers. Further, the grain size was similar to the subgrain size, with a typical grain containing either no subgrain boundaries or a single subgrain boundary oriented in a geometry consistent with subgrain wall formation. We propose that during high strain deformation, continuous dynamic recrystallization by subgrain rotation leads to a steady-state grain size that is closely related to the subgrain size, which ultimately depends on stress.

The grain shape in all of our samples evolved to an orientation with the long axis of grains oriented roughly 30° to the shear direction, synthetic with the sense of shear. The orientation and strength of the SPO measured from tangential sections did not appear to be strain dependent (note that the minimum equivalent strain experienced by a tangential section in our study was $\varepsilon = 1.4$). However, a plot of aspect ratio versus stress indicates that SPO strength may be stress dependent (Fig. 20).

Finally, deformed samples underwent a complex protracted CPO evolution, which was quantified in detail in this study. Our analyses lead to a more complex conceptualization of CPO than previously appreciated development in deformed olivine aggregates, wherein initially

multiple submaxima form, representing different prototypical olivine fabric types. As deformation proceeds these submaxima populations diminish in size in favor of a strong A-type fabric.

The primary impact of this dataset is to provide benchmarks for micromechanical models attempting to describe microstructural evolution of deformed olivine aggregates and the influence of dynamic recrystallization and CPO formation on mechanical properties.

3.8 Acknowledgements

This work is supported in part by the DOE NNSA SSGF. Parts of this work were carried out in the Characterization Facility, University of Minnesota, which receives partial support from NSF through the MRSEC program. The authors would also like to acknowledge Seth Kruckenberg for help with EBSD measurements.

3.9 References

Austin, N. J., & Evans, B. (2007). Paleowattmeters: A scaling relation for dynamically recrystallized grain size. Geology, 35(4), 343–346.

Bachmann, F., Hielscher, R., & Schaeben, H. (2010). Texture Analysis with MTEX – Free and Open Source Software Toolbox. Solid State Phenomena, 160, 63–68.

Bystricky, M., Kunze, K., Burlini, L., & Burg, J.-P. (2000). High shear strain of olivine aggregates: Rheological and seismic consequences. Science, 290(5496), 1564–1567.

De Bresser, J. H. P., Ter Heege, J. H., & Spiers, C. J. (2001). Grain size reduction by dynamic recrystallization: Can it result in major rheological weakening? International Journal of Earth Sciences, 90(1), 28–45.

Derby, B. (1991). The dependence of grain size on stress during dynamic recrystallisation. Acta Metallurgica Et Materialia, 39(5), 955–962.

Derby, B., & Ashby, M. F. (1987). On dynamic recrystallisation. Scripta Metallurgica, 21(6), 879–884.

Frost, H. J., & Ashby, M. F. (1982). Deformation-mechanism maps: the plasticity and creep of metals and ceramics.

Guillope, M., & Poirier, J. P. (1979). Dynamic recrystallization during creep of single-crystalline

halite: An experimental study. Journal of Geophysical Research: Solid Earth, 84(B10), 5557-5567.

Hansen, L. N., Zimmerman, M. E., & Kohlstedt, D. L. (2011). Grain boundary sliding in San Carlos olivine: Flow law parameters and crystallographic-preferred orientation. Journal of Geophysical Research: Solid Earth, 116(8), 1–16.

Hansen, L. N., Zimmerman, M. E., & Kohlstedt, D. L. (2012a). The influence of microstructure on deformation of olivine in the grain-boundary sliding regime. Journal of Geophysical Research: Solid Earth, 117(9), 1–17.

Hansen, L. N., Zimmerman, M. E., Dillman, A. M., & Kohlstedt, D. L. (2012b). Strain localization in olivine aggregates at high temperature: A laboratory comparison of constant-strain-rate and constant-stress boundary conditions. Earth and Planetary Science Letters, 333–334, 134–145.

Hansen, L. N., Zimmerman, M. E., & Kohlstedt, D. L. (2012c). Laboratory measurements of the viscous anisotropy of olivine aggregates. Nature, 492(7429), 415–418.

Hansen, L. N., Conrad, C. P., Boneh, Y., Skemer, P., Warren, J. M., & Kohlstedt, D. L. (2016a). Viscous anisotropy of textured olivine aggregates: 2. Micromechanical model. Journal of Geophysical Research: Solid Earth, 121(10), 7137–7160.

Hansen, L. N., Warren, J. M., Zimmerman, M. E., & Kohlstedt, D. L. (2016b). Viscous anisotropy of textured olivine aggregates, Part 1: Measurement of the magnitude and evolution of anisotropy. Earth and Planetary Science Letters, 445, 92–103.

Hansen, L. N., Zhao, Y. H., Zimmerman, M. E., & Kohlstedt, D. L. (2014). Protracted fabric evolution in olivine: Implications for the relationship among strain, crystallographic fabric, and seismic anisotropy. Earth and Planetary Science Letters, 387, 157–168.

Hirth, G., & Kohlstedt, D. L. (2015). The stress dependence of olivine creep rate: Implications for extrapolation of lab data and interpretation of recrystallized grain size. Earth and Planetary Science Letters, 418, 20–26.

Hirth, G., & Tullis, J. (1992). Dislocation creep regimes in quartz aggregates. Journal of Structural Geology, 14(2), 145–159.

Holtzman, B. K., Chrysochoos, A., & Daridon, L. (2018). A Thermomechanical Framework for Analysis of Microstructural Evolution: Application to Olivine Rocks at High Temperature. Journal of Geophysical Research: Solid Earth, 123(10).

Humphreys, J., Rohrer, G. S., & Rollett, A. (2017). Continuous Recrystallization During and After Large Strain Deformation. Recrystallization and Related Annealing Phenomena, 509–526.

Karato, S., Mitsuhiro, T., & Fujii, T. (1980). Dynamic recrystallization of olivine single crystals during high-temperature creep, 7(9), 649–652.

Mainprice, D., Bachmann, F., Hielscher, R., & Schaeben, H. (2014). Descriptive tools for the analysis of texture projects with large datasets using MTEX : strength, symmetry and components. Geological Society, London, Special Publications, 409(1), 251–271.

Paterson, M. S., & Olgaard, D. L. (2000). Rock deformation tests to large shear strains in torsion. Journal of Structural Geology, 22, 1341–1358.

Ribe, N. M., Hielscher, R., & Castelnau, O. (2019). An analytical finite-strain parametrization for texture evolution in deforming olivine polycrystals. Geophysical Journal International, 216(1), 486-514.

Ross, J. V., Ave Lallemant, H. G., & Carter, N. L. (1980). Stress dependence of recrystallized-grain and subgrain size in olivine. Tectonophysics, 70(1–2), 39–61.

Shimizu, I. (2008). Theories and applicability of grain size piezometers: The role of dynamic recrystallization mechanisms. Journal of Structural Geology, 30(7), 899–917.

Skemer, P., Katayama, I., Jiang, Z., & Karato, S.-I. (2005). The misorientation index: Development of a new method for calculating the strength of lattice-preferred orientation. Tectonophysics, 411(1–4), 157–167.

Solberg, J. K., McQueen, H. J., Ryum, N., & Nes, E. (1989). Influence of ultra-high strains at elevated temperatures on the microstructure of aluminium. Part I. Philosophical Magazine, 60(4), 447–471.

Tasaka, M., Zimmerman, M. E., & Kohlstedt, D. L. (2016). Evolution of the rheological and microstructural properties of olivine aggregates during dislocation creep under hydrous conditions. Journal of Geophysical Research : Solid Earth, 121, 92–113.

Tasaka, M., Zimmerman, M. E., & Kohlstedt, D. L. (2017a). Rheological Weakening of Olivine + Orthopyroxene Aggregates Due to Phase Mixing: 1. Mechanical Behavior. Journal of Geophysical Research: Solid Earth, 122(10), 7584–7596.

Tasaka, M., Zimmerman, M. E., Kohlstedt, D. L., Stünitz, H., & Hielbronner, R. (2017b). Rheological Weakening of Olivine + Orthopyroxene Aggregates Due To Phase Mixing: Part 2. Microstructural Development. Journal of Geophysical Research: Solid Earth, 122(10), 7597–7612.

Tielke, J. A., Hansen, L. N., Tasaka, M., Meyers, C., Zimmerman, M. E., & Kohlstedt, D. L. (2016). Observations of grain size sensitive power law creep of olivine aggregates over a large range of lattice-preferred orientation strength. Journal of Geophysical Research: Solid Earth, 121(2), 506–516.

Tommasi, A., Mainprice, D., Canova, G., & Chastel, Y. (2000). Viscoplastic self-consistent and equilibrium-based modeling of olivine lattice preferred orientations: Implications for the upper mantle seismic anisotropy. Journal of Geophysical Research: Solid Earth, 105(B4), 7893-7908.

Twiss, R. J. (1977). Theory and applicability of a recrystallized grain size paleopiezometer. Pure and Applied Geophysics PAGEOPH, 115(1–2), 227–244.

Underwood, E. E. (1972). The Mathematical Foundations of Quantitative Stereology. In Stereology and Quantitative Metallography (pp. 3–38).

Van der Wal, D., Chopra, P., Drury, M., & Gerald, J. F. (1993). Relationships between dynamically recrystallized grain size and deformation conditions in experimentally deformed olivine rocks. Geophysical Research Letters, 20(14), 1479–1482.

Vollmer, F. W. (1990). An application of eigenvalue methods to structural domain analysis. Bulletin of the Geological Society of America, 102(6), 786–791.

Wiesman, H. S., Zimmerman, M. E., & Kohlstedt, D. L. (2018). Laboratory investigation of mechanisms for phase mixing in olivine+ferropericlase aggregates. Philosophical Transactions of the Royal Society A: Mathematical, Physical and Engineering Sciences, 376(2132).

Woocock, N. H. (1977). Specification of fabric shapes using an eigenvalue method. Geological Society of America Bulletin, 88, 1231–1235.

Zhang, Shuqing, and Shun-ichiro Karato. "Lattice preferred orientation of olivine aggregates deformed in simple shear." Nature 375.6534 (1995): 774-777.

Zhang, S., Karato, S. I., Gerald, J. F., Faul, U. H., & Zhou, Y. (2000). Simple shear deformation of olivine aggregates. Tectonophysics, 316(1-2), 133-152.

3.10 Tables

Table 3-1: Summary of torsion experiments

exp. #	assembly type	$\dot{\gamma}$ $(10^{-5}s^{-1})$	$\dot{\varepsilon}$ $(10^{-5}s^{-1})$	τ_{peak} (MPa)	σ_{peak} (MPa)	τ_{final} (MPa)	σ_{final} (MPa)	γ	ε
PT948	in-situ HP	10	5.8	137	237	123	214	3.1	1.8
PT1223	evacHP, Ni-core	3.1	1.8	105	181	81	141	3	1.7
PT1226	evacHP, Ni-core	12	7	140	242	118	205	2.3	1.4
PT1292	evacHP, dunite spacers	6.1	3.5	119	206	94	162	3.1	1.8
PT1296	evacHP, dunite spacers	12	7	137	237	92	159	10.2	5.9
PT1297	evacHP, dunite spacers	11-25	6.4 -14.4	172	299	150	260	3.9	2.2

Note: Values are given are calculated for outer diameter of the sample

Table 3-2: Summary of microstructural analysis of tangential sections

exp. #	$d_{EA\ grain}$ (μm)	$d_{intercept}$ (μm)	$d_{EA\ boundary}$ (μm)	$d_{long\ boundary}$ (μm)	$d_{short\ boundary}$ (μm)	$\frac{d_{long\ boundary}}{d_{short\ boundary}}$	θ (°)	N_{grains}	M
PT1254 (undeformed)	5.0	5.1	5.6	4.5	4.2	1.07	-	4771	0.006
PT948	7.2	7.5	8.7	8.1	5.8	1.38	32	273	0.29
PT1223	10.5	11.2	12.7	11.5	8.7	1.33	37	963	0.16
PT1226	6.9	7.4	8.2	7.7	5.5	1.40	34	2200	0.10
PT1292	7.3	8.6	8.7	7.9	5.9	1.33	25	13891	0.23
PT1296	7.8	8.7	9.6	8.7	6.5	1.34	28	12510	0.56
PT1297	6.0	6.0	7.1	6.6	4.7	1.41	28	24403	0.23

Table 3-3: Microstructrual analysis of grain shapes from tangential sections

exp. #	$d_{long\ axis}$ (μm)	$d_{long\ intercept}$ (μm)	$d_{long\ caliper}$ (μm)	$d_{long\ axis}$ (μm)	$d_{short\ intercept}$ (μm)	$d_{short\ caliper}$ (μm)	$\frac{d_{long\ boundary}}{d_{short\ boundary}}$	$\frac{d_{long\ intercept}}{d_{short\ intercept}}$	$\frac{d_{long\ caliper}}{d_{short\ caliper}}$	$\theta_{boundary}$ (°)	$\theta_{intercept}$ (°)	$\theta_{caliper}$ (°)
PT1254 (undeformed)	4.5	3.6	5.2	4.2	3.2	3.8	1.07	1.10	1.42	-	-	-
PT948	8.1	6.2	8.5	5.8	4.1	5.2	1.38	1.51	1.61	32	45	31
PT1223	11.5	8.9	12.3	8.7	6.4	7.5	1.33	1.39	1.63	37	39	30
PT1226	7.7	6.0	8.2	5.5	4.1	4.9	1.40	1.46	1.65	34	33	33
PT1292	7.9	6.8	8.6	5.9	4.9	5.1	1.33	1.40	1.61	25	18	31
PT1296	8.7	6.8	9.1	6.5	4.9	5.5	1.34	1.39	1.59	28	30	33
PT1297	6.6	4.7	7.1	4.7	3.4	4.2	1.41	1.39	1.61	28	15	32

3.11 Figures

Figure 3-1: Radial stress profiles of sample deformed in torsion by power-law creep

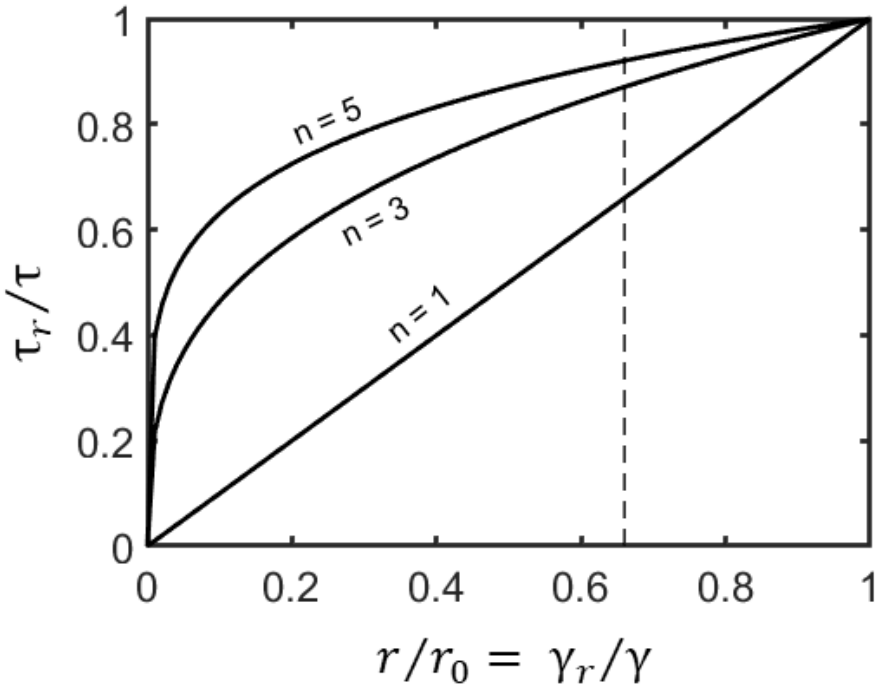

Figure 1: Normalized radial stress profiles for a sample deformed in torsion by power-law creep. The dotted line marks the inner boundary of a typical sample prepared with a soft Ni metal core.

Figure 3-2: Schematic of experimental assemblies

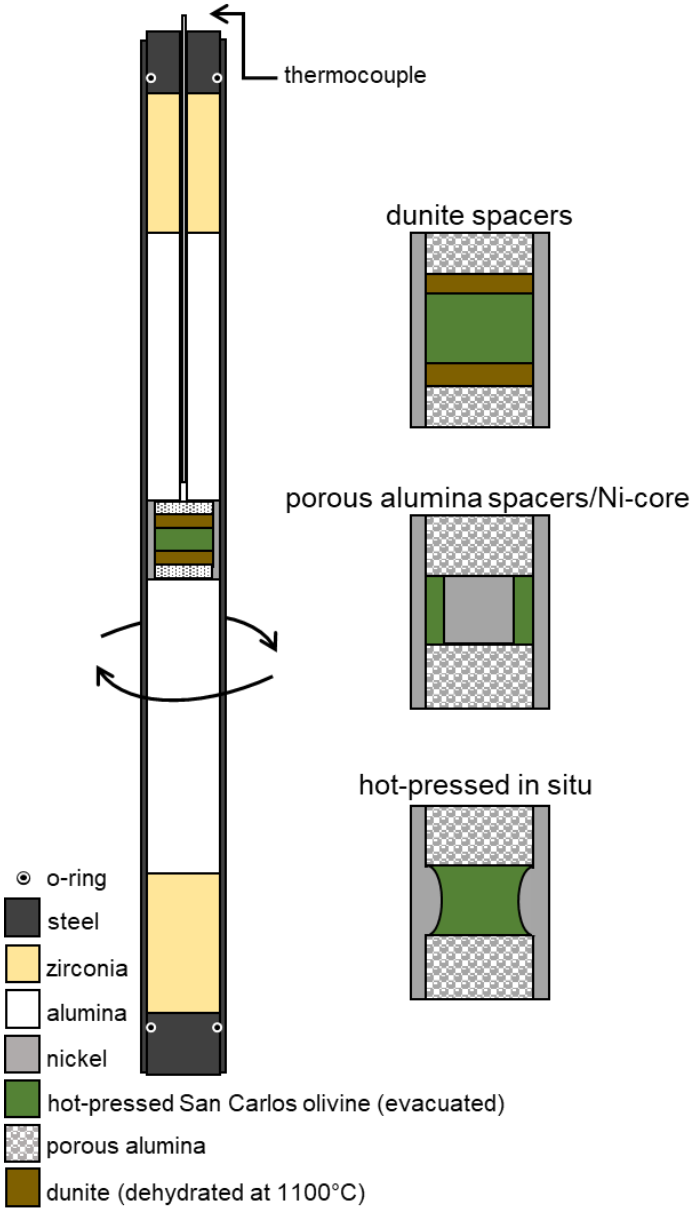

Figure 2: Schematic of the experimental deformation column and sample assemblies used in this study

Figure 3-3: Stress versus strain data from torsion experiments

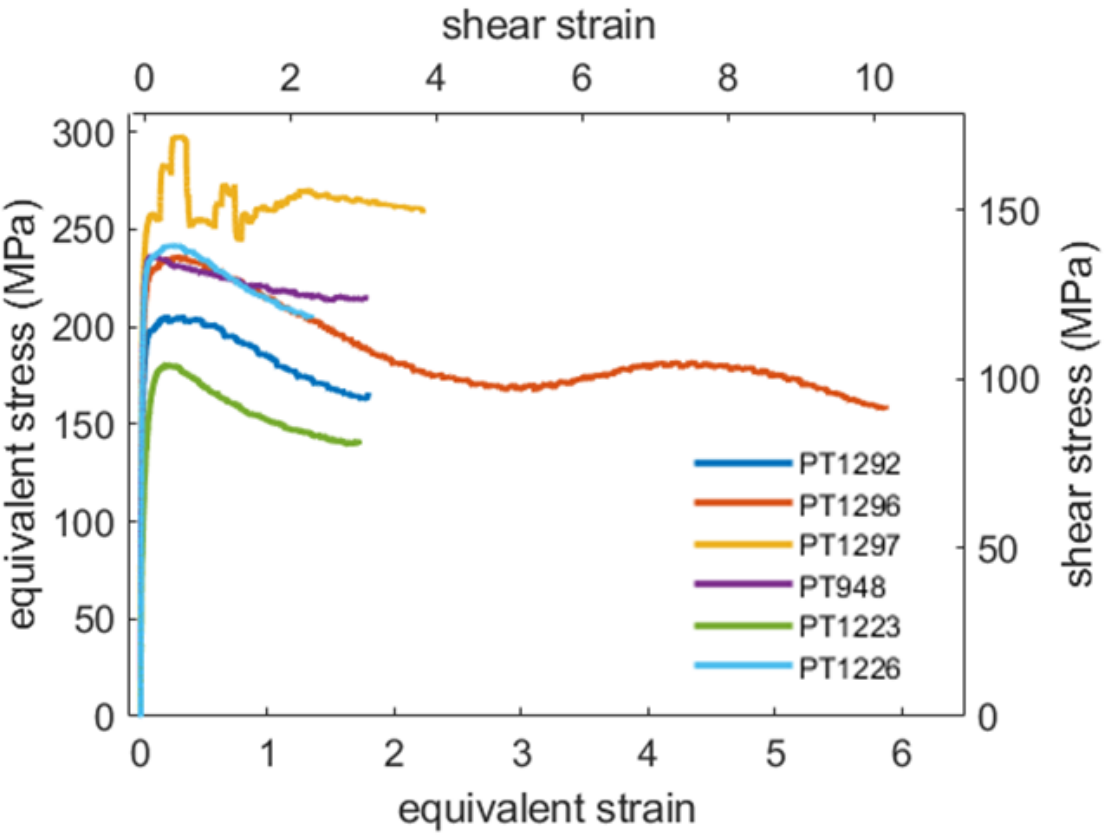

Figure 3: Stress versus strain data calculated for the outer radius of samples deformed in torsion using both shear and equivalent values.

Figure 3-4: Strain rate versus stress data with comparison to flow laws

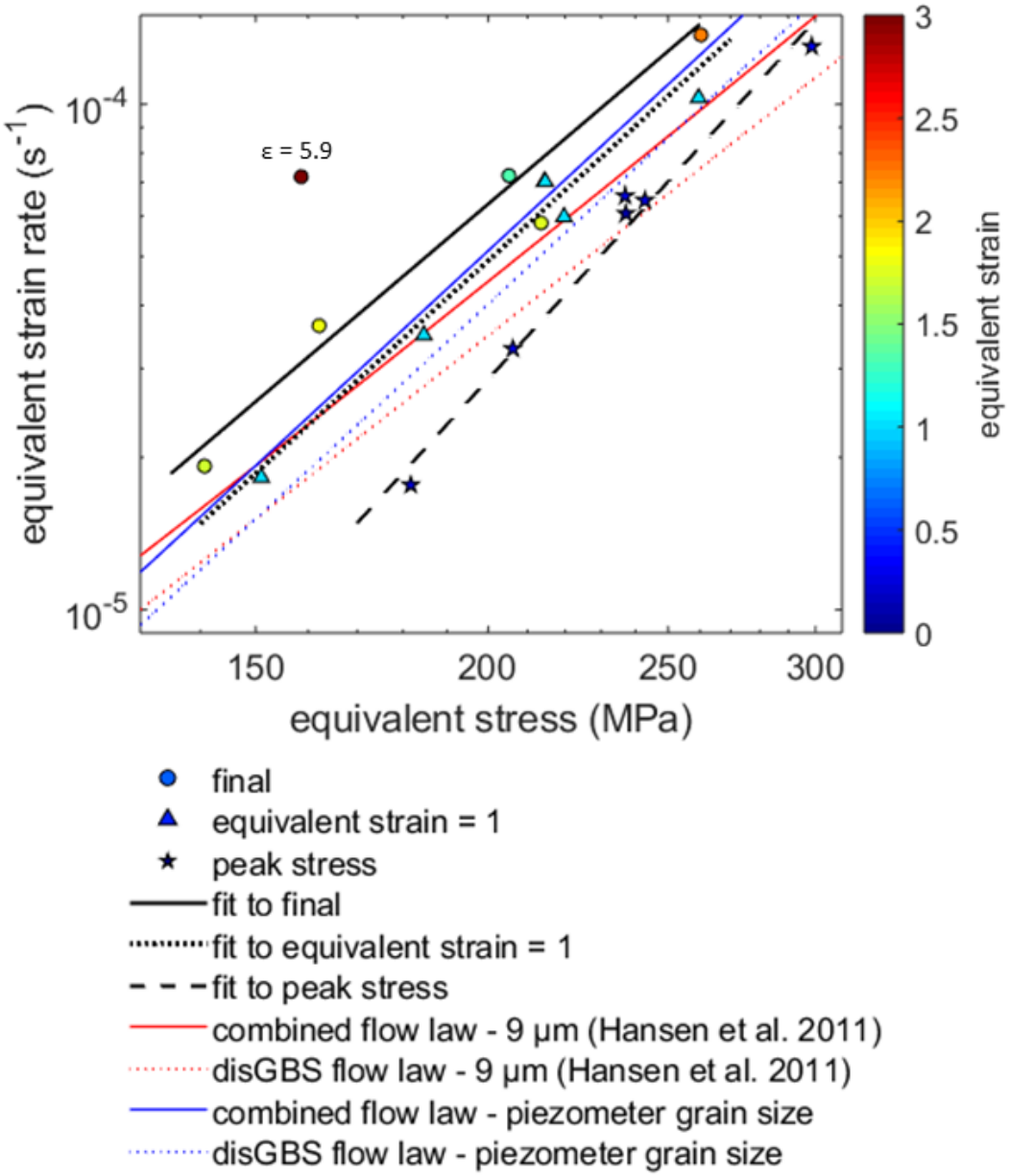

Figure 4: Strain rate versus stress data plotted with power law fits (black lines) and comparisons to the flow laws presented by Hansen et al. (2011) (colored lines). Data are plotted from different stages of the deformation and colored by equivalent strain. When comparing to the combined (diffusion creep + disGBS) and disGBS flow laws from Hansen et al. (2011), we either applied a constant grain size of 9 µm (representing an intermediate value when analyzing the microstructures of radial sections; red lines) or accounted for grain size using the grain-size piezometer generated in this study (blue lines).

Figure 3-5: Stress exponents calculated from fits to mechanical data

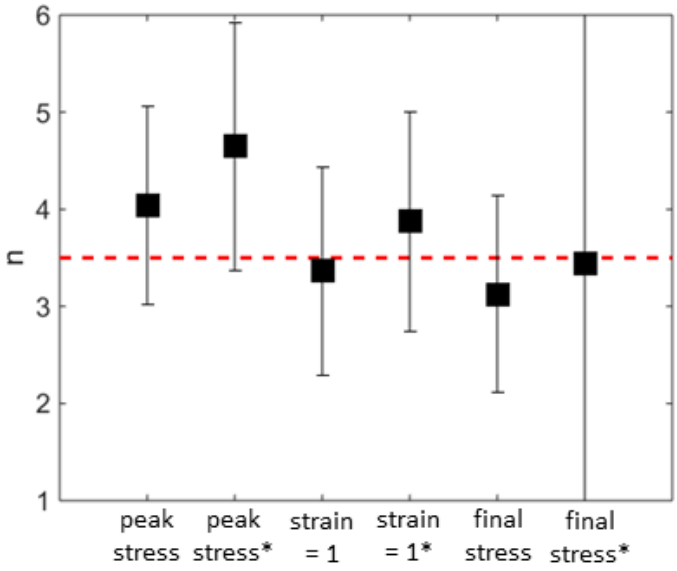

Figure 5: Stress exponents calculated from power-law fits to the mechanical data. The resulting stress exponents ranged between 3 and 5, with the 95% confidence bounds of all fits overlapping the value of n = 3.5, which is used in our analysis to calculate the radial stress profile (rate stepping experiment excluded in fit).*

Figure 3-6: EBSD map of undeformed starting material, PT1254

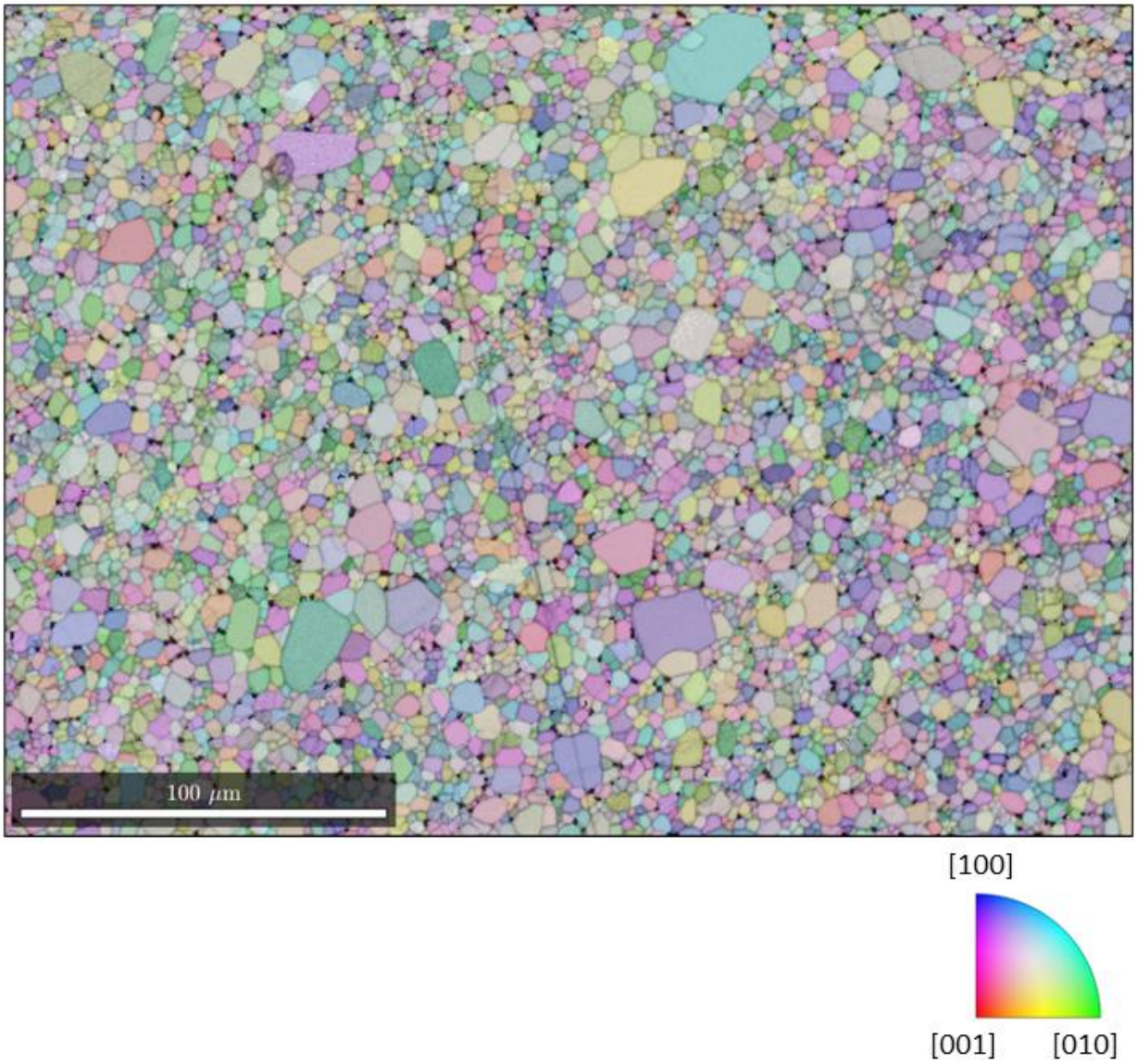

Figure 6: EBSD map of a transverse section of undeformed starting material, PT1254, represented with the band contrast overlain by semi-transparent inverse pole figure (IPF) coloring. The legend for the IPF coloring is presented below, where the color is referenced to the shear direction (consistent for all IPF colored figures). This same color scheme is used throughout the following figures where IPF color is used. Black regions are unindexed points that are not used in the analysis.

Figure 3-7: CPO and grain-size distribution of undeformed starting material, PT1254

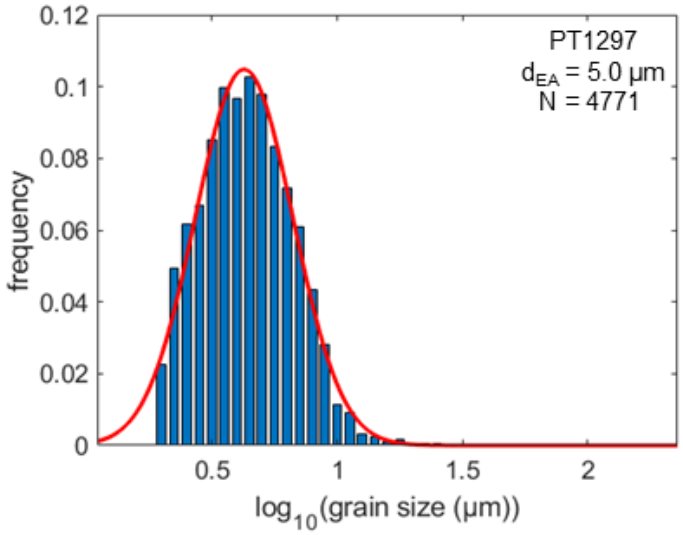

Figure 7: The grain size distribution of the undeformed starting material. Histogram represents binned data calculated using the equivalent circular area method. The red curve is a log-normal fit to the data.

Figure 3-8: EBSD map of deformed sample, PT948

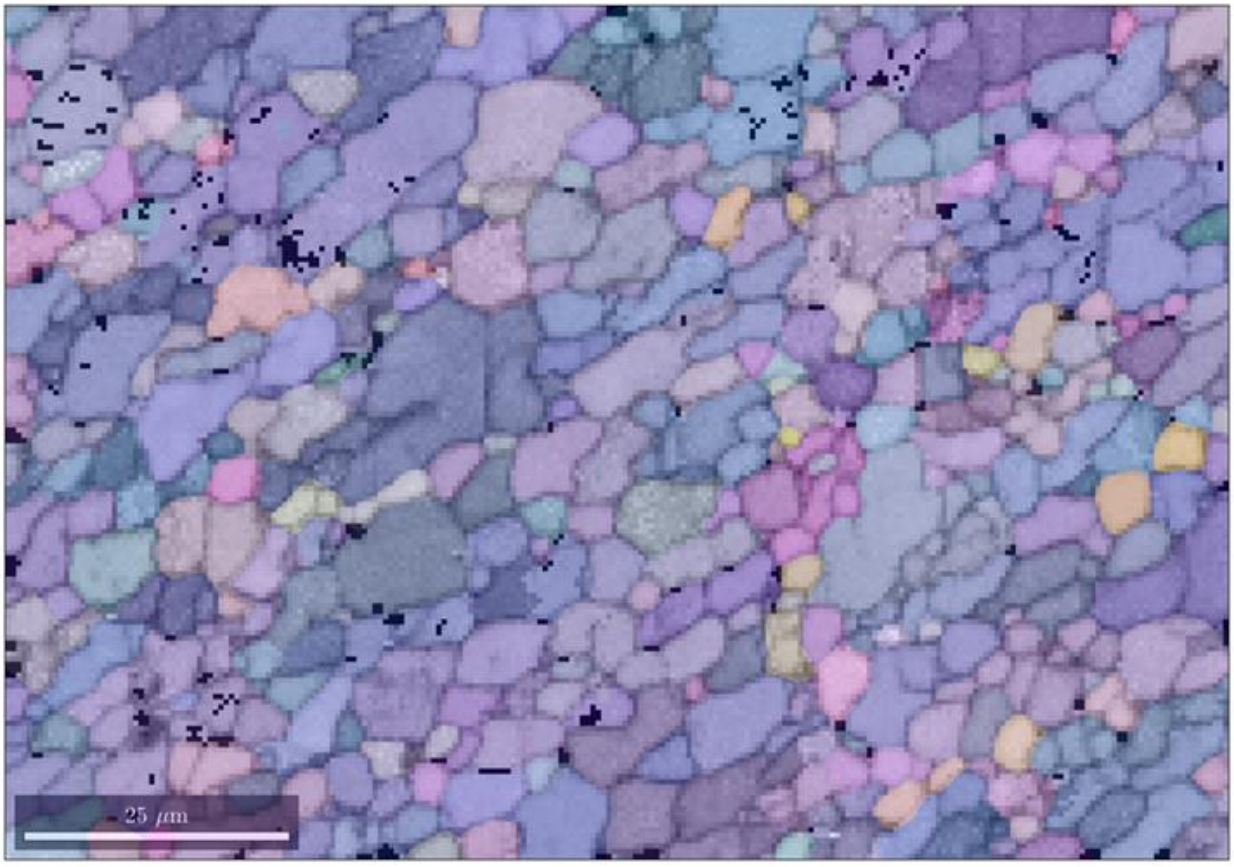

Figure 8: EBSD map of a tangential section of deformed sample, PT948, represented with the band contrast overlain by semi-transparent inverse pole figure (IPF) coloring.

Figure 3-9: EBSD map of deformed sample, PT1223

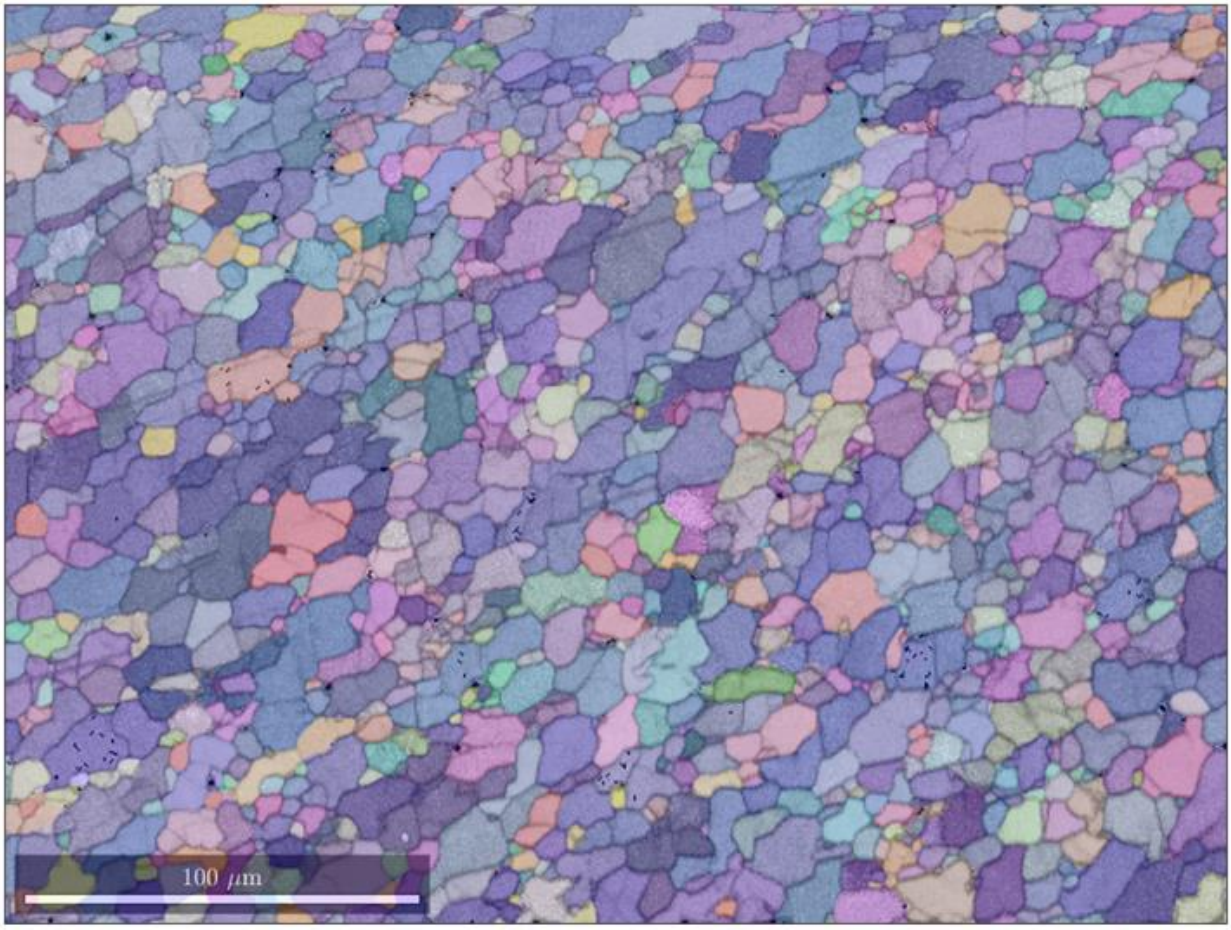

Figure 9: EBSD map of a tangential section of deformed sample, PT1223, represented with the band contrast overlain by semi-transparent inverse pole figure (IPF) coloring.

Figure 3-10: EBSD map of deformed sample, PT1226

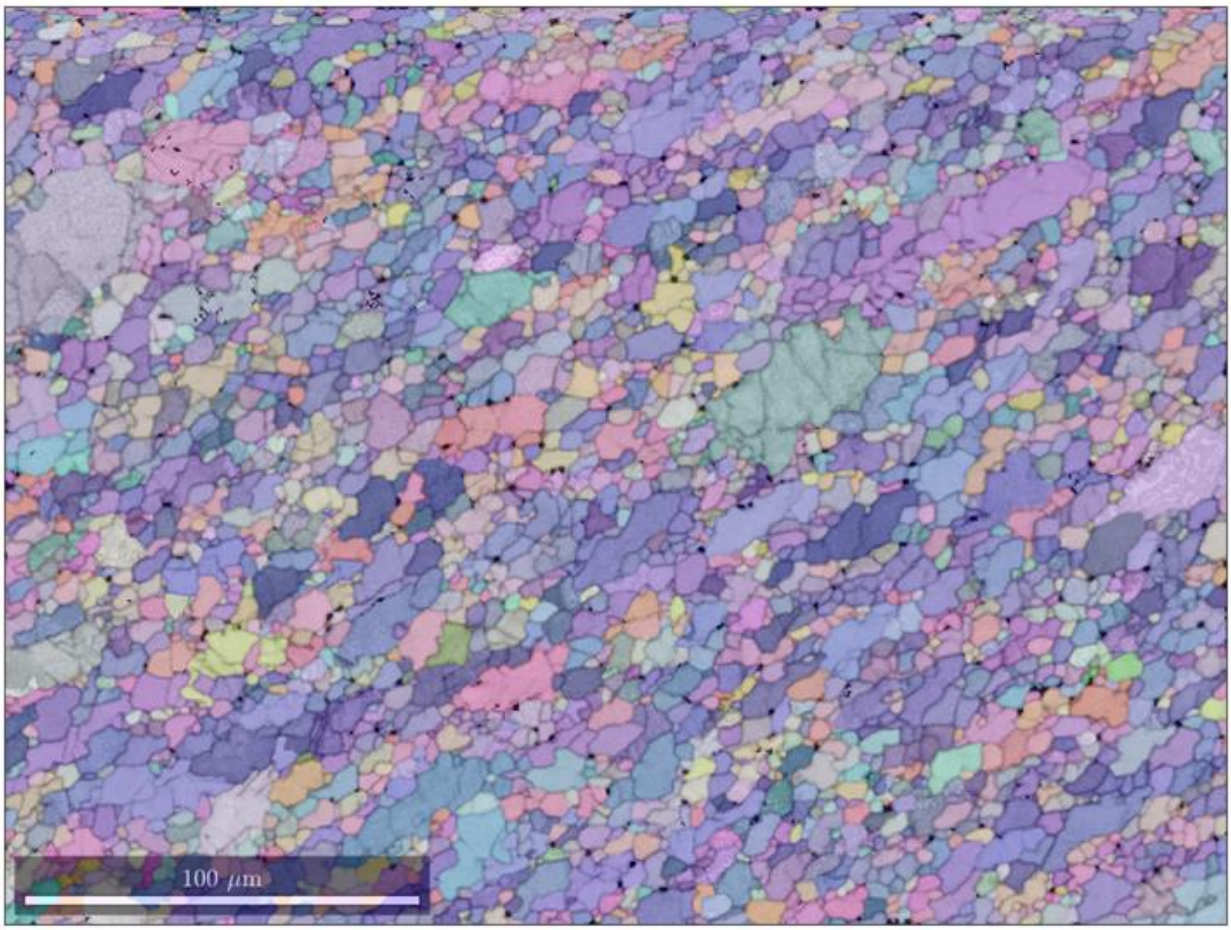

Figure 10: EBSD map of a tangential section of deformed sample, PT1226, represented with the band contrast overlain by semi-transparent inverse pole figure (IPF) coloring.

Figure 3-11: EBSD map of deformed sample, PT1292

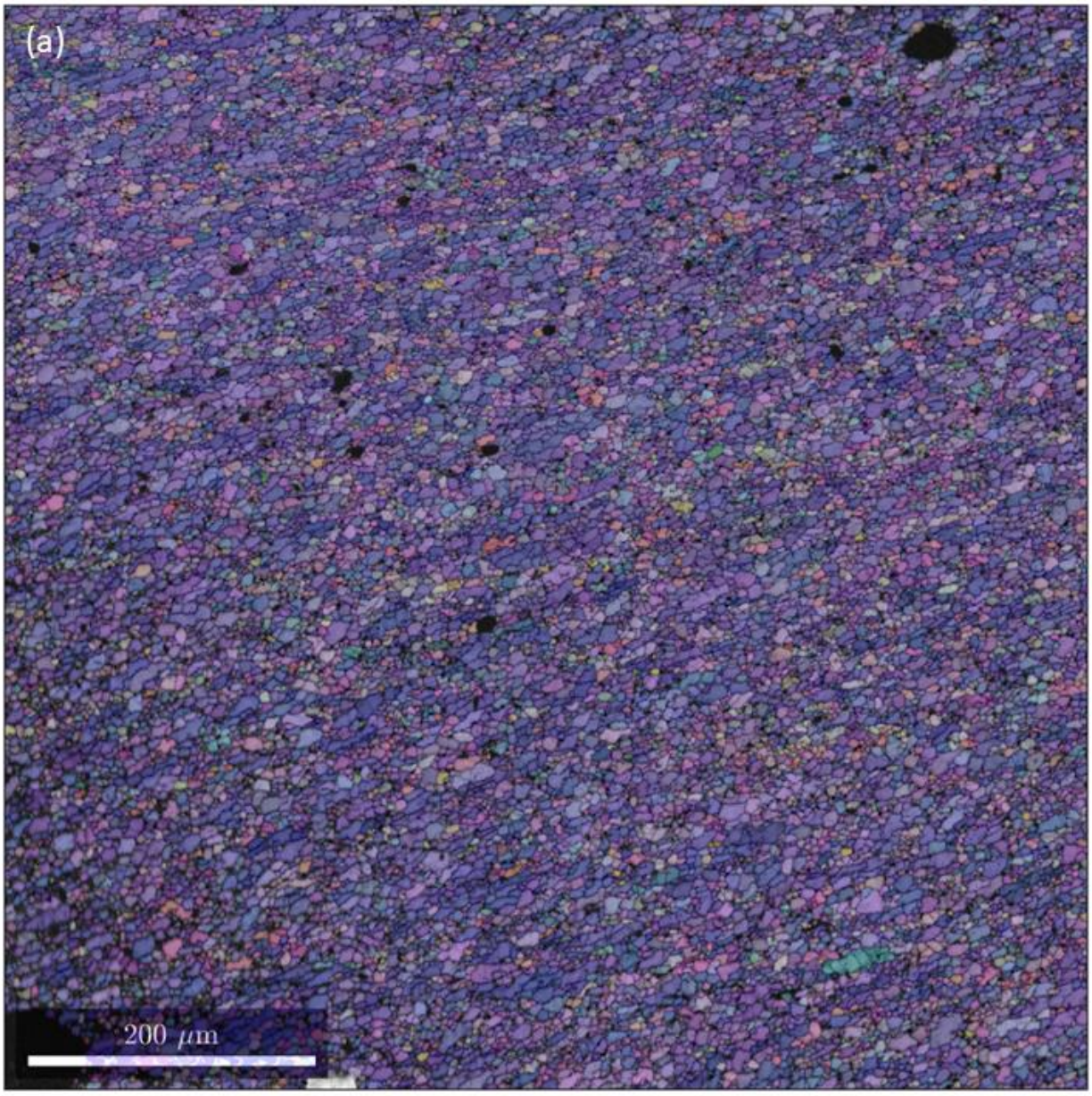

Figure 11a: EBSD map of a tangential section of deformed sample, PT1292, represented with the band contrast overlain by semi-transparent inverse pole figure (IPF) coloring.

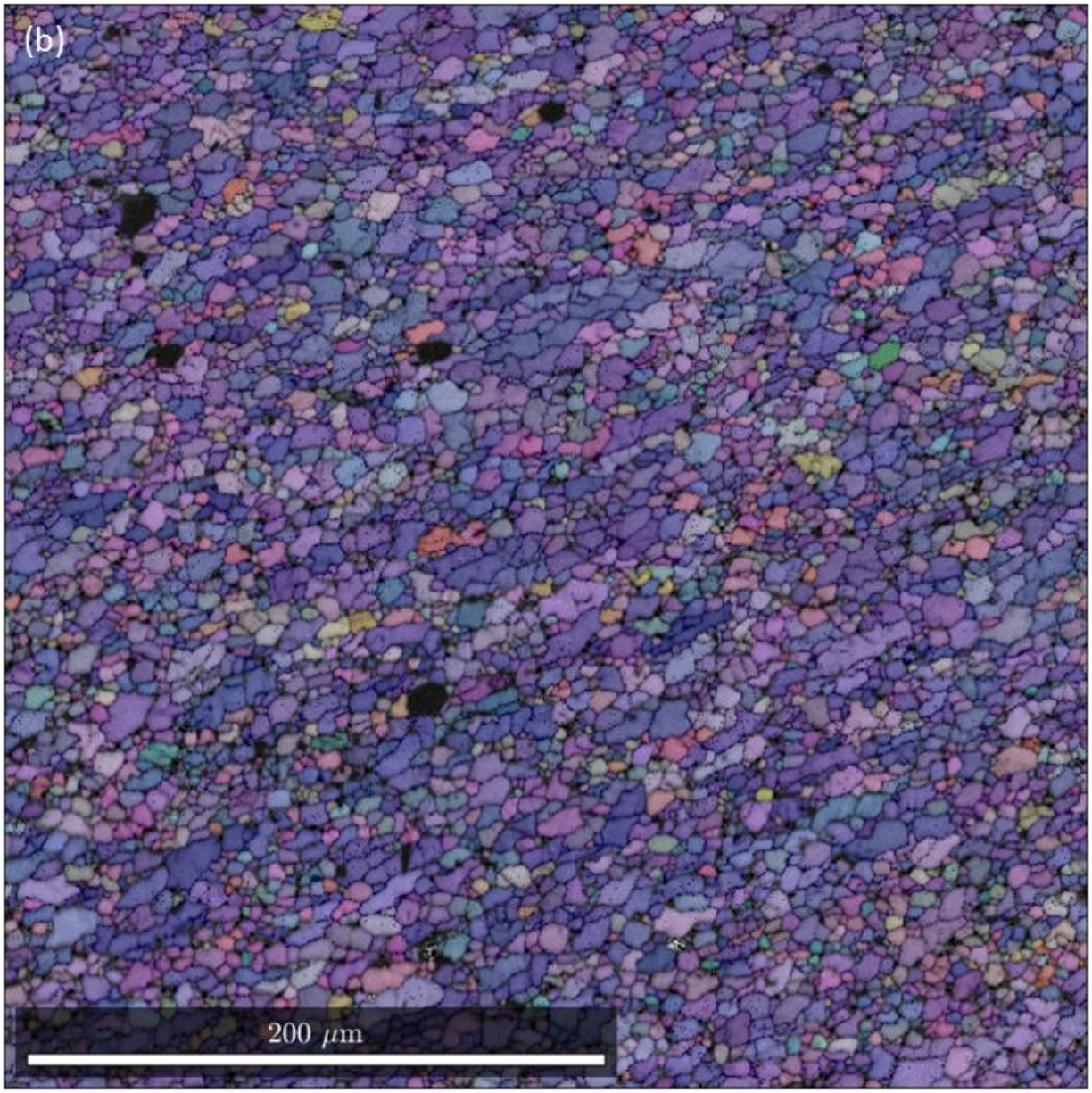

Figure 11b: Magnified inset of EBSD map of a tangential section of deformed sample, PT1292, represented with the band contrast overlain by semi-transparent inverse pole figure (IPF) coloring.

Figure 3-12: EBSD map of deformed sample, PT1296

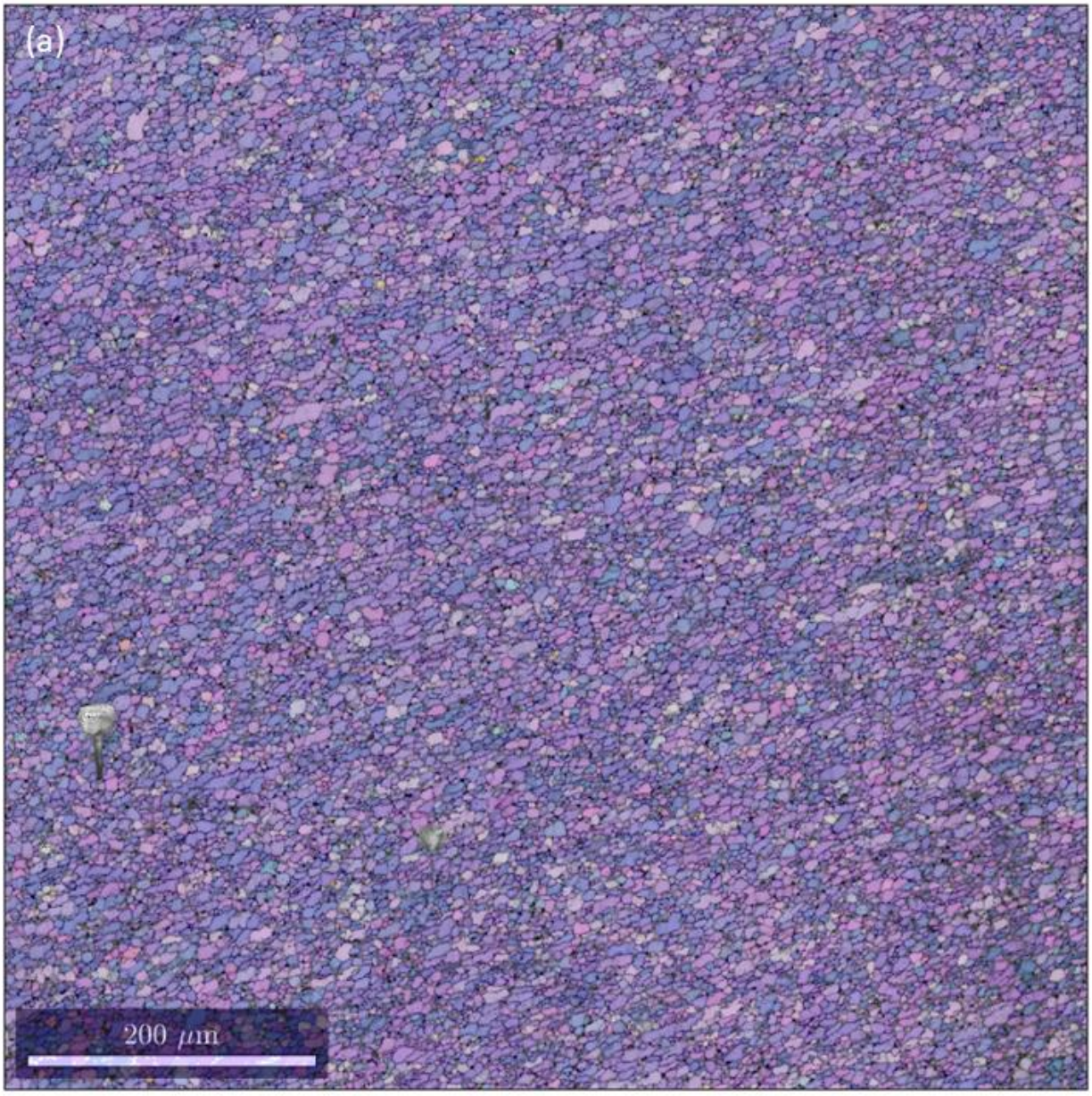

Figure 12a: EBSD map of a tangential section of deformed sample, PT1296, represented with the band contrast overlain by semi-transparent inverse pole figure (IPF) coloring.

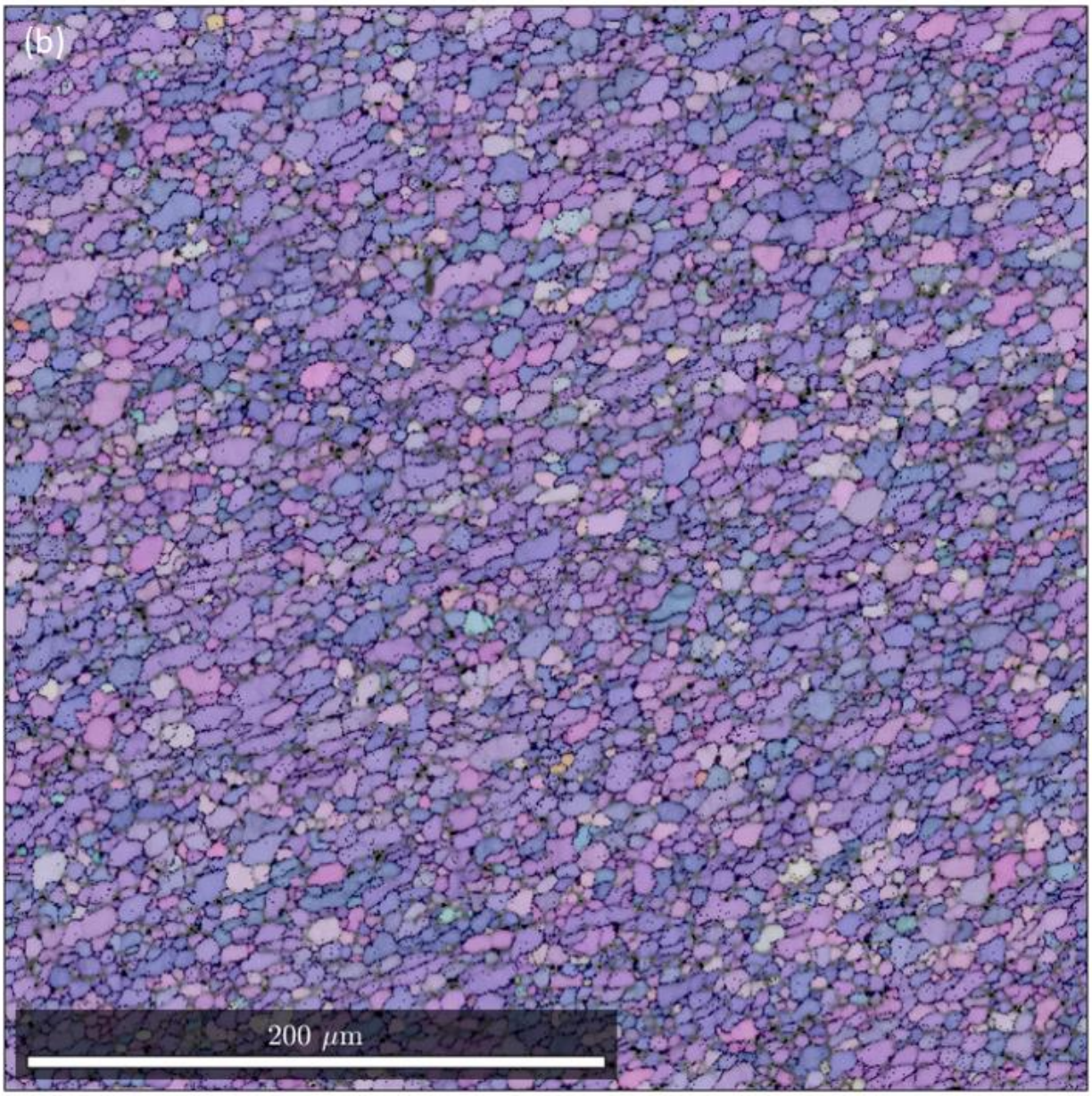

Figure 12b: Magnified inset of EBSD map of a tangential section of deformed sample, PT1296, represented with the band contrast overlain by semi-transparent inverse pole figure (IPF) coloring.

Figure 3-13: EBSD map of deformed sample, PT1297

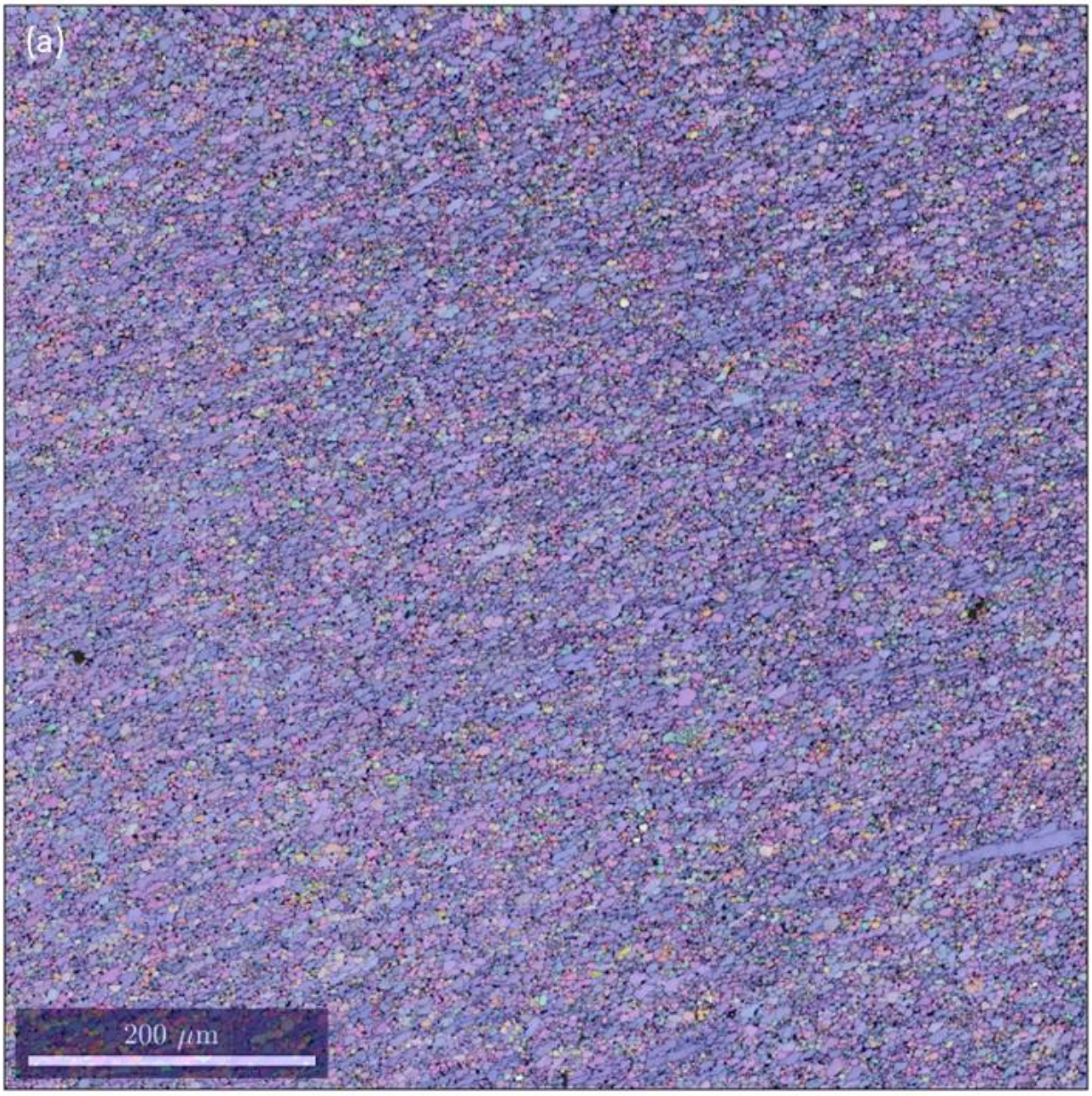

Figure 13a: EBSD map of a tangential section of deformed sample, PT1297, represented with the band contrast overlain by semi-transparent inverse pole figure (IPF) coloring.

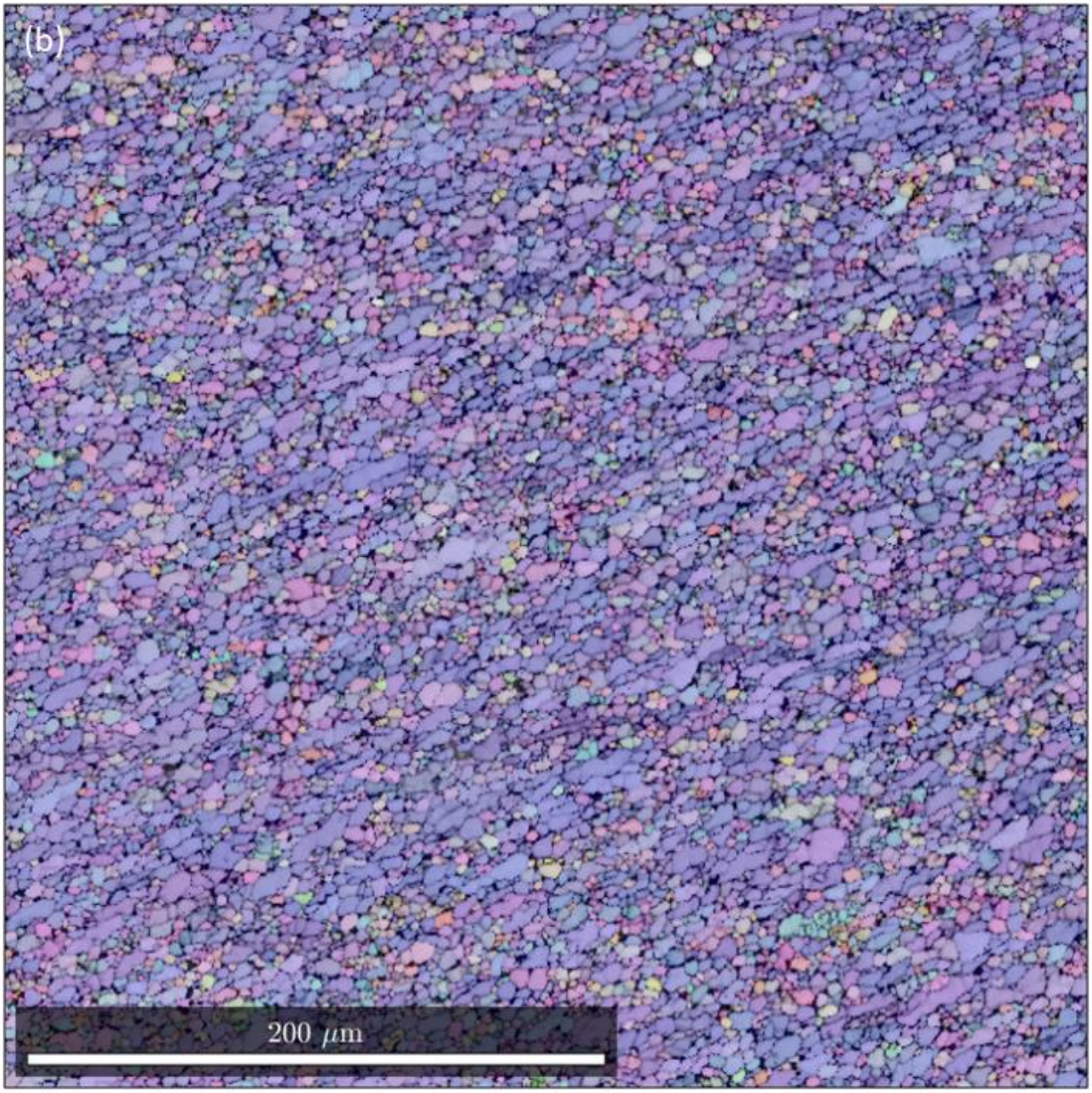

Figure 13b: Magnified inset of EBSD map of a tangential section of deformed sample, PT1297, represented with the band contrast overlain by semi-transparent inverse pole figure (IPF) coloring.

Figure 3-14: EBSD maps of radial sections of deformed samples, IPF coloring

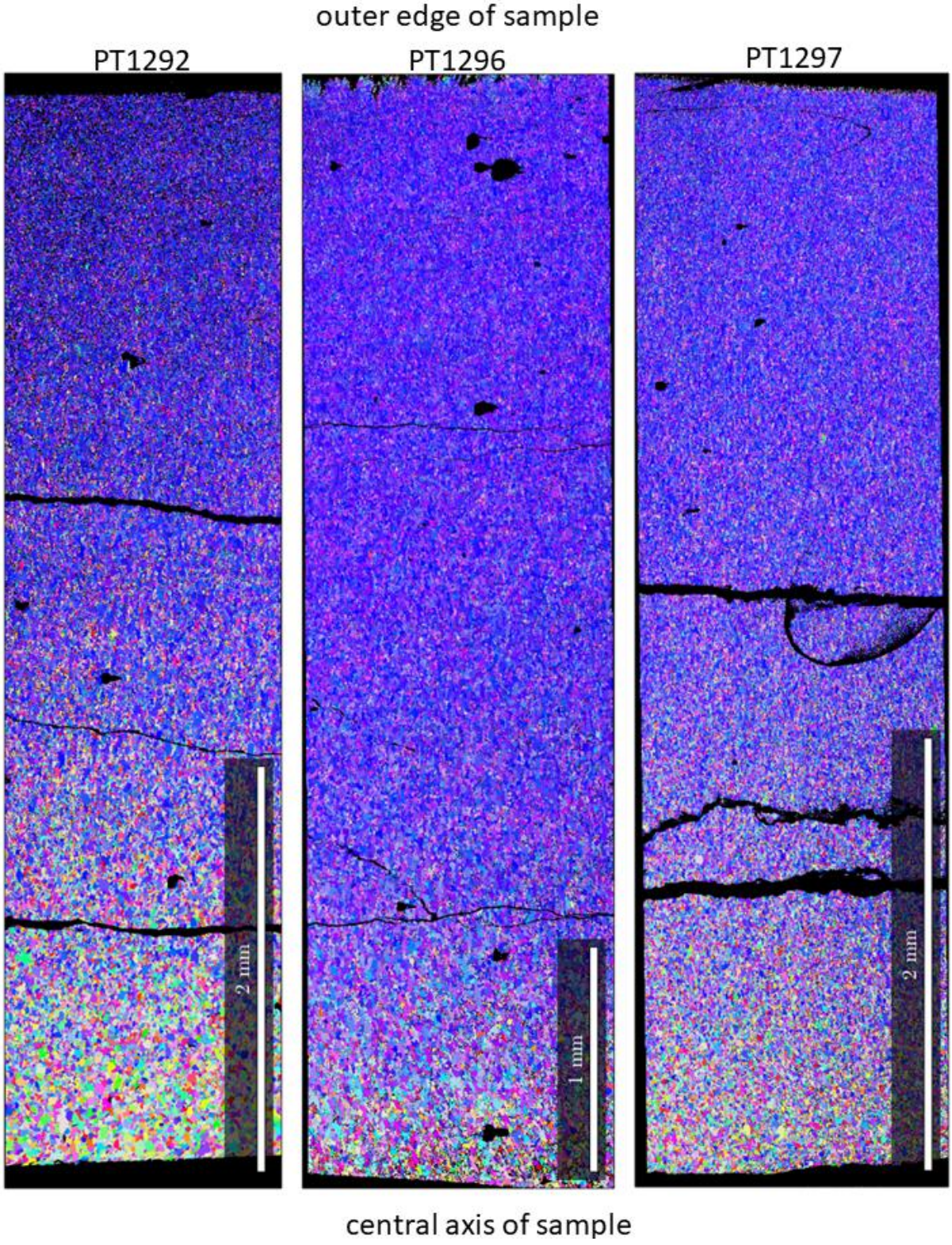

Figure 14: EBSD map of radial sections of deformed samples, PT1292, PT1296, and PT1297, represented by inverse pole figure (IPF) coloring. These figures demonstrate the strengthening of the CPO with increasing strain (i.e., toward the outer edge of the sample).

Figure 3-15: EBSD maps of radial sections of deformed samples, grain size coloring

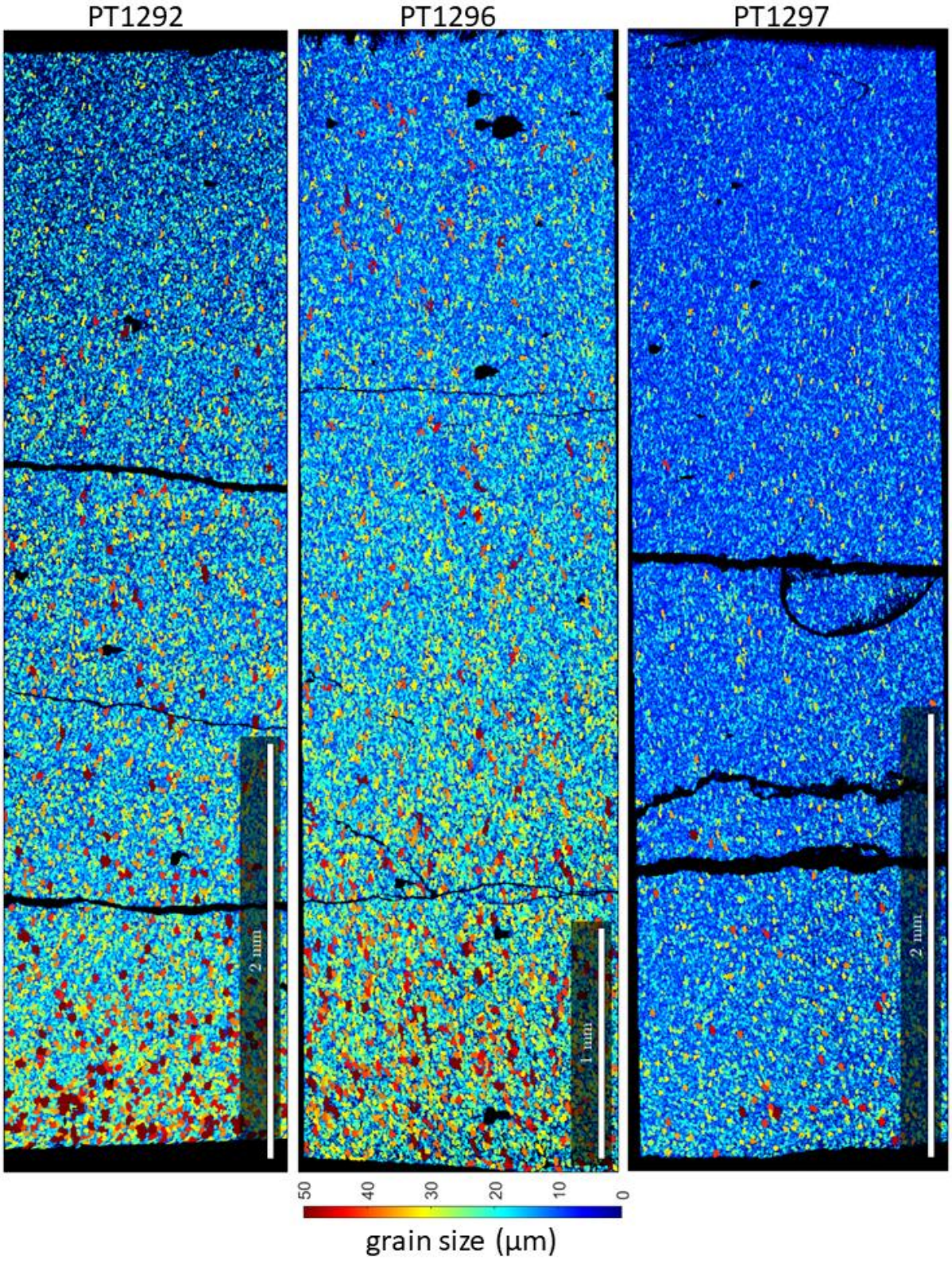

Figure 15: EBSD maps of radial sections of deformed samples, PT1292, PT1296, and PT1297, represented by grain-size coloring. These figures demonstrate the grain-size gradient in the sample with coarser grains near the central axis of the sample and finer grains near the outer edge.

Figure 3-16: Grain size distributions of tangential sections

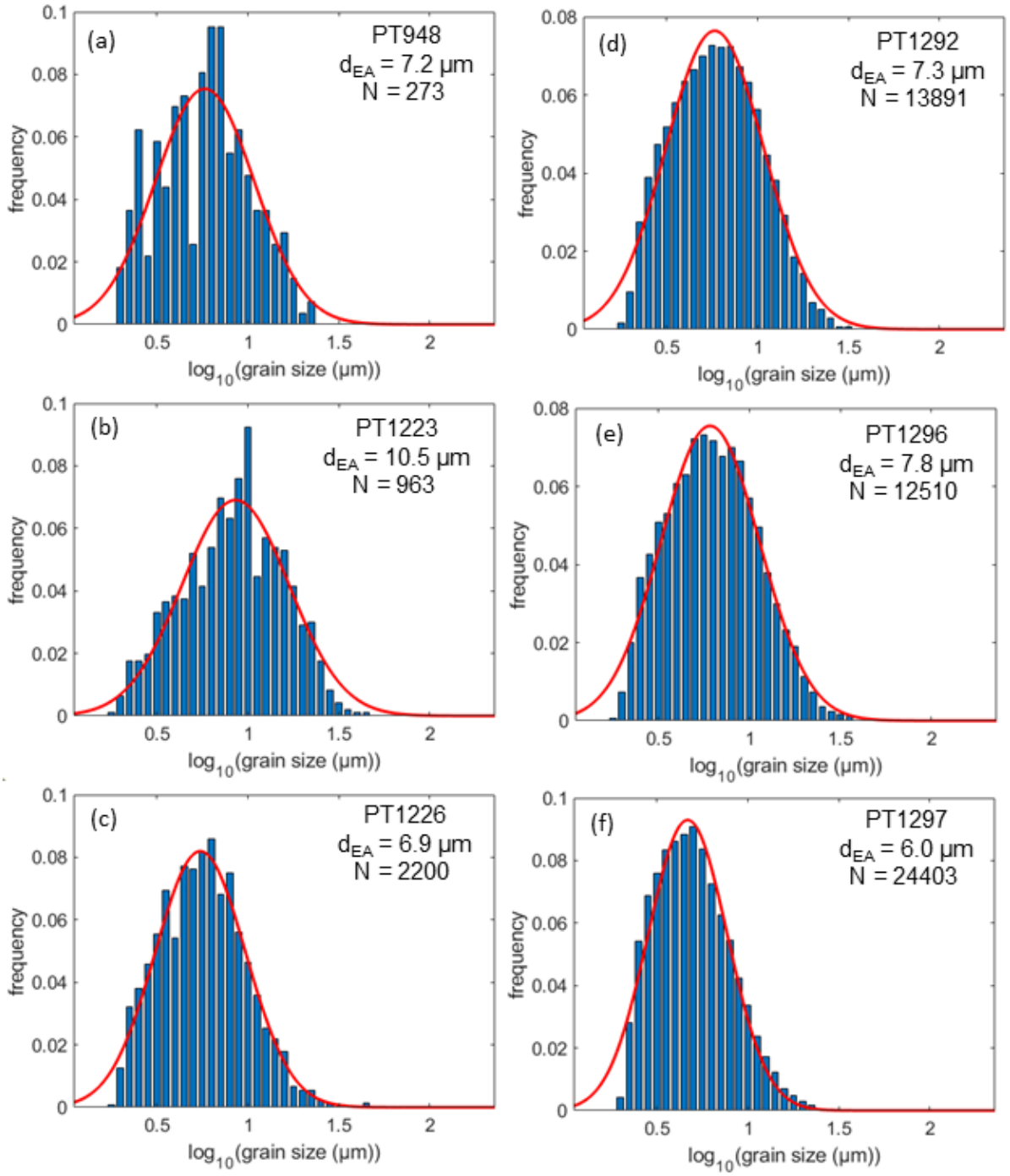

Figure 16: Grain size distributions generated from EBSD maps of tangential sections of deformed samples. The red curve is the fit of a log-normal distribution to the data. The maps used to generate figures (a-c) had substantially fewer grains than those used to generate figures (d-f). Using these large grain populations (N>10000) the distribution is smoother and fits more closely to a log-normal distribution, however, it appears that the actual distribution may be slightly skewed towards smaller grain sizes.

Figure 3-17: Grain size versus equivalent stress

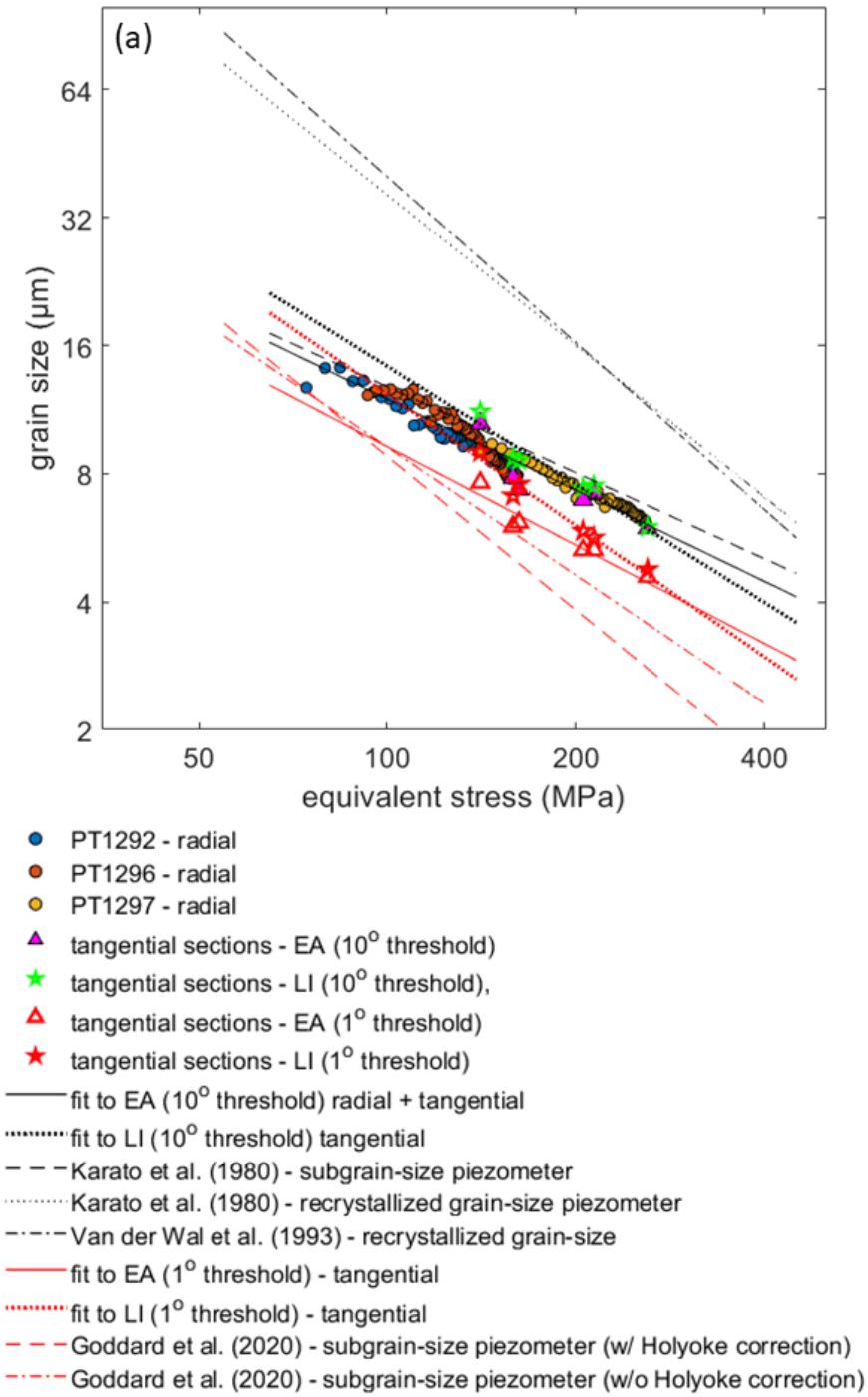

Figure 17a: Plot of grain size against the calculated equivalent stress including data from both tangential and radial sections of our deformed samples using both linear intercept (LI) and equivalent area (EA) measurements (radial sections are only characterized by EA). Published piezometers are also plotted for comparison, in addition to fits to the data. The results do not correspond well with published recrystallized grain-size piezometers. However, the grain-size measured in our samples correspond closely with subgrain-size piezometers.

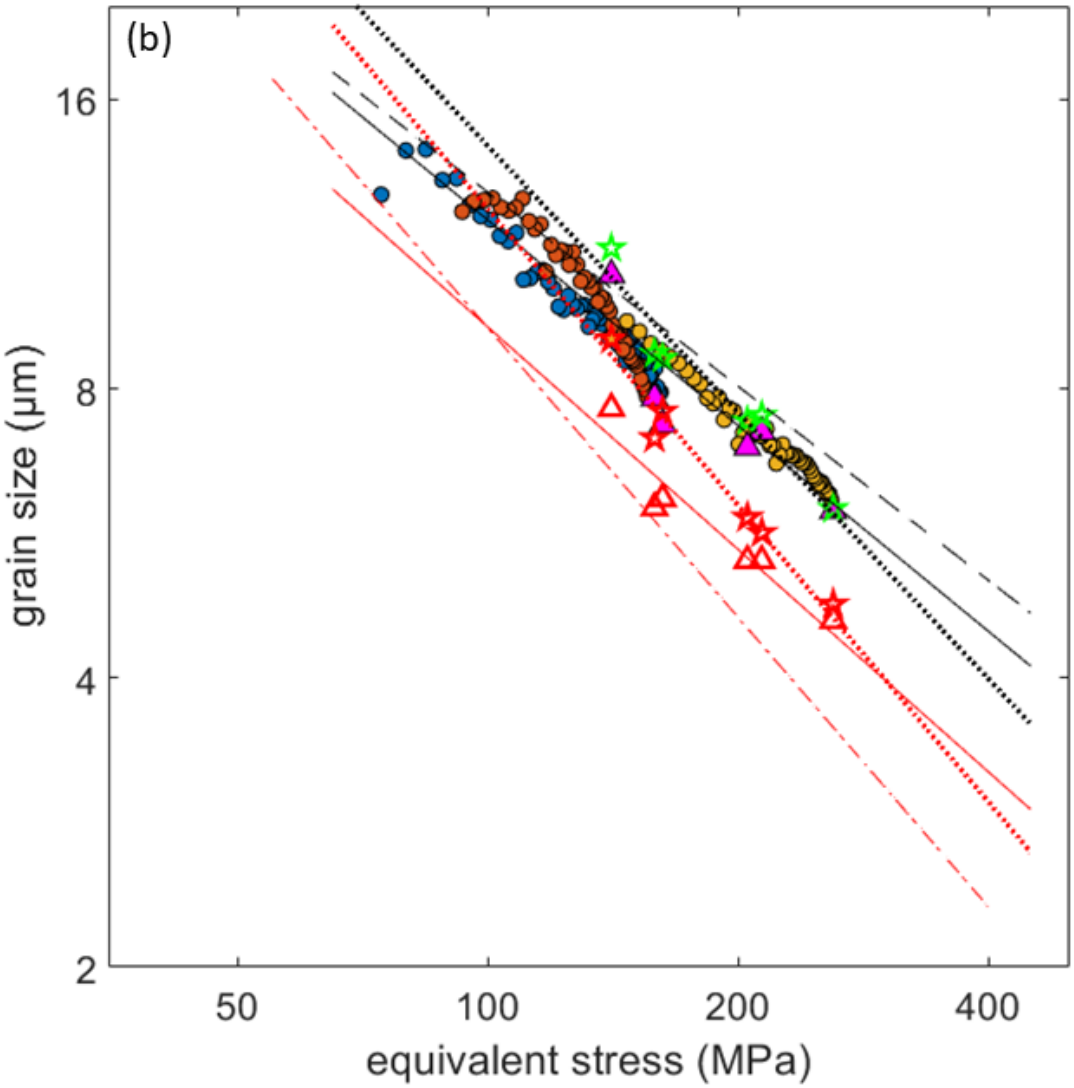

Figure 17b: Enlarged inset of previous figure for clarity.

Figure 3-18: Ratio of grain size and number using 1° and 10° threshold

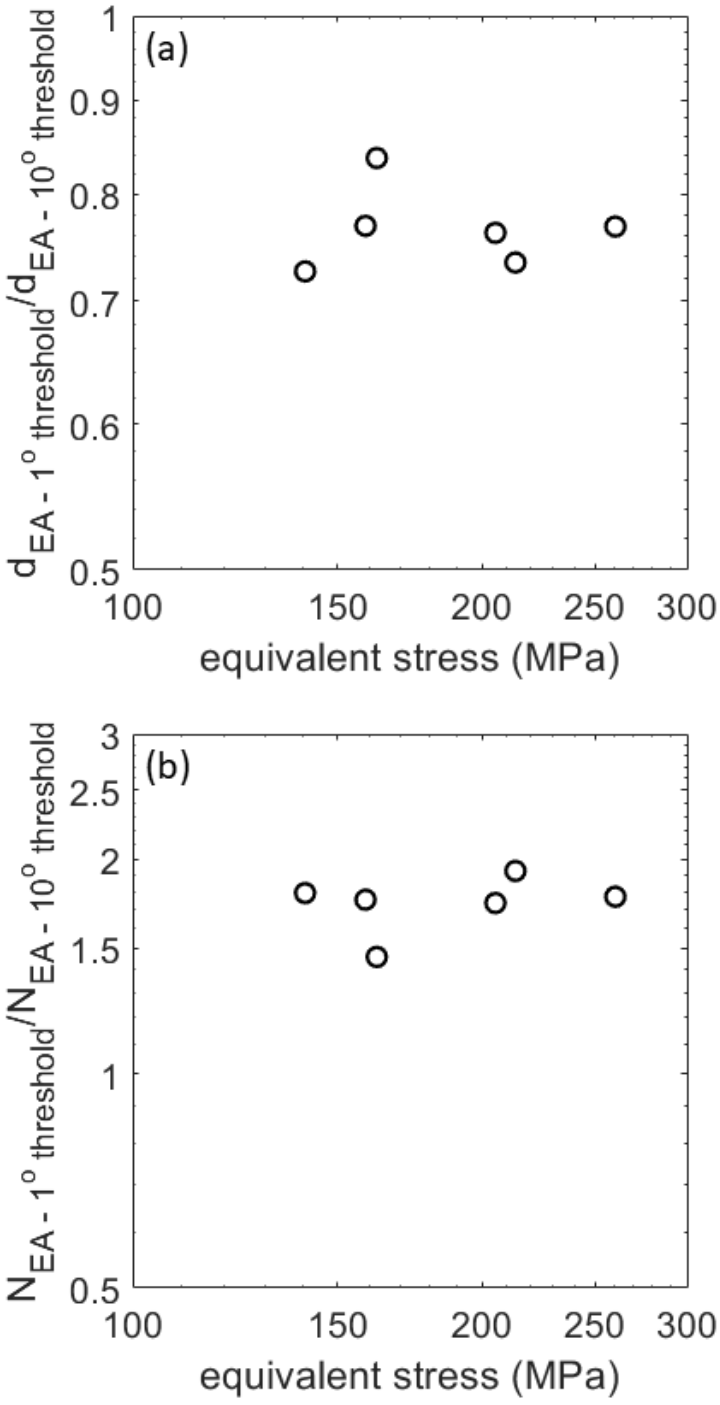

Figure 18: (a) Ratio of the grain size determined with a 1° threshold to that determined with a 10° threshold. (b) Ratio of the number of grains determined with a 1° threshold to that determined with a 10° threshold. These figures indicate that the subgrain size is similar to the grain size and that typically grains bounded by high angle boundaries only contain up to 1 subgrain boundary (with many grains containing no subgrain boundaries). Additionally, the number of subgrains per grain does not appear to be correlated with stress.

Figure 3-19: Grain boundary specimen angle distribution and synthetic mean grain shapes

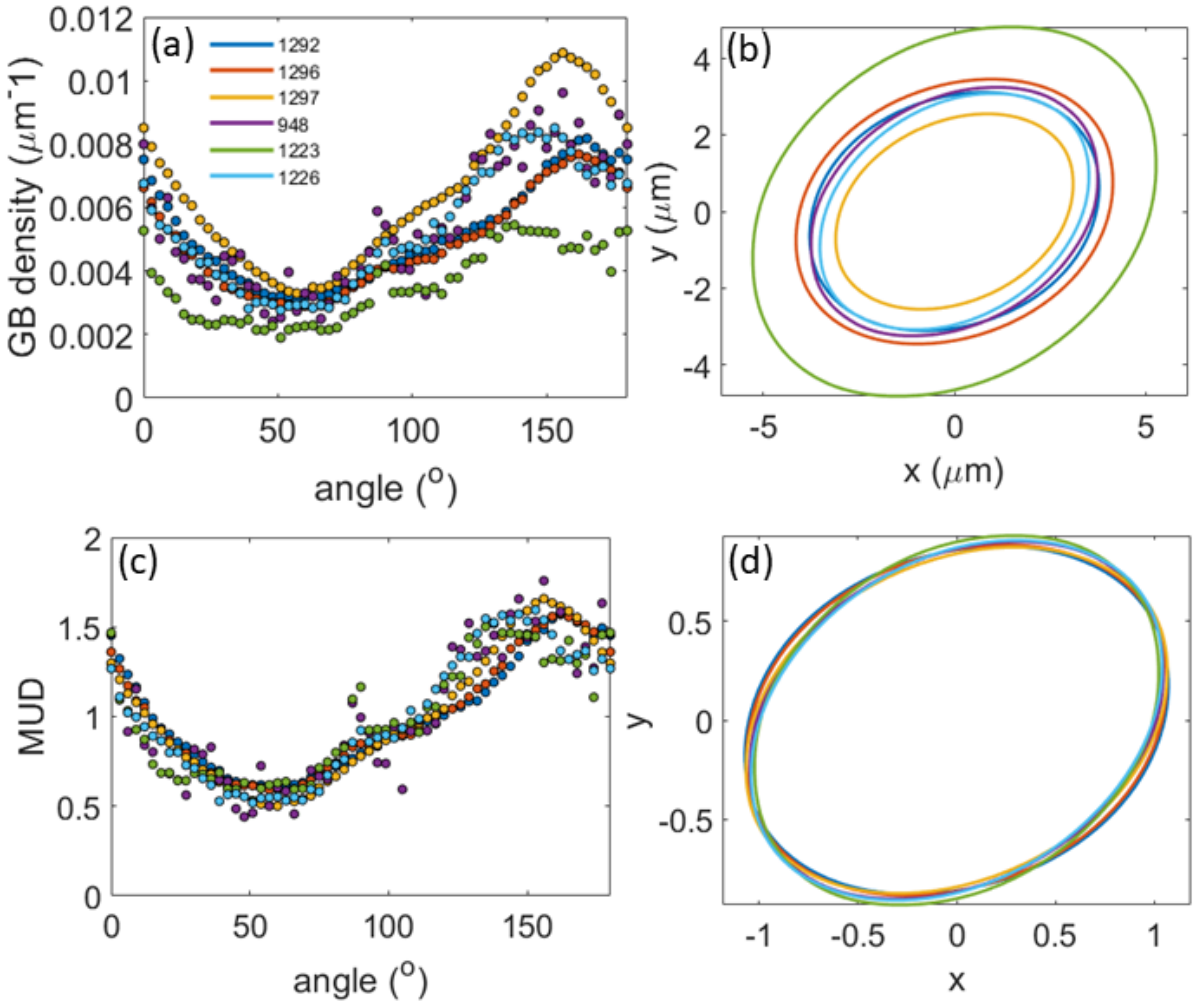

Figure 19: (a) Grain boundary specimen angle distribution, (b) synthetic mean grain shapes, (c) grain boundary specimen angle distribtuion normalized to the mean grain boundary density, and (d) synthetic mean grain shapes normalized to the mean radius.

Figure 3-20: Aspect ratio determined from synthetic mean grain shape versus stress

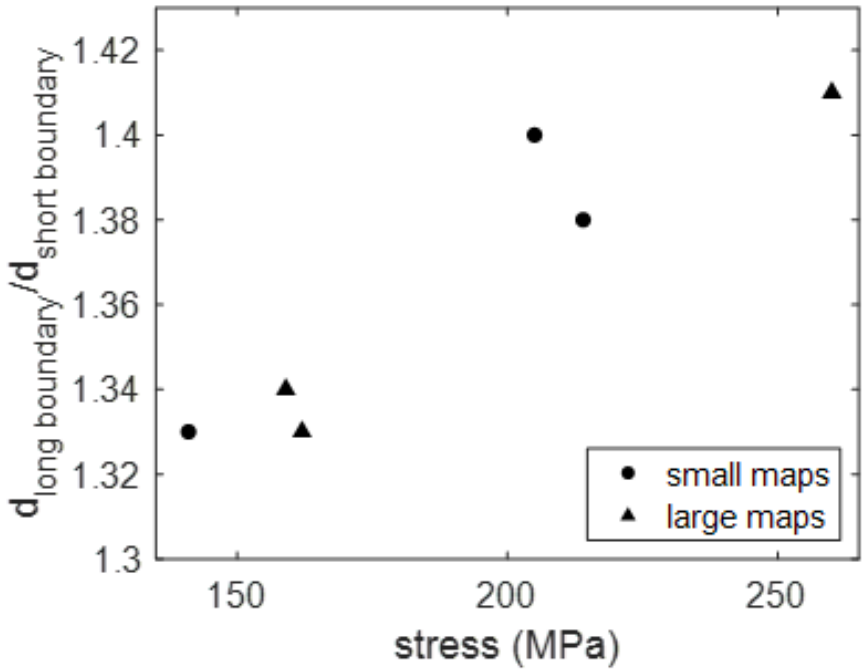

Figure 20: Strength of SPO, characterized by the aspect ratio of the synthetic mean grain shape calculated from the grain boundary angle distribution (plotted in Fig 19), plotted against stress. These data indicate that stress is correlated to the strength of the SPO. (small maps: N < 10000; large maps N > 10000).

Figure 3-21: Specimen angular distribution of mean linear intercept length

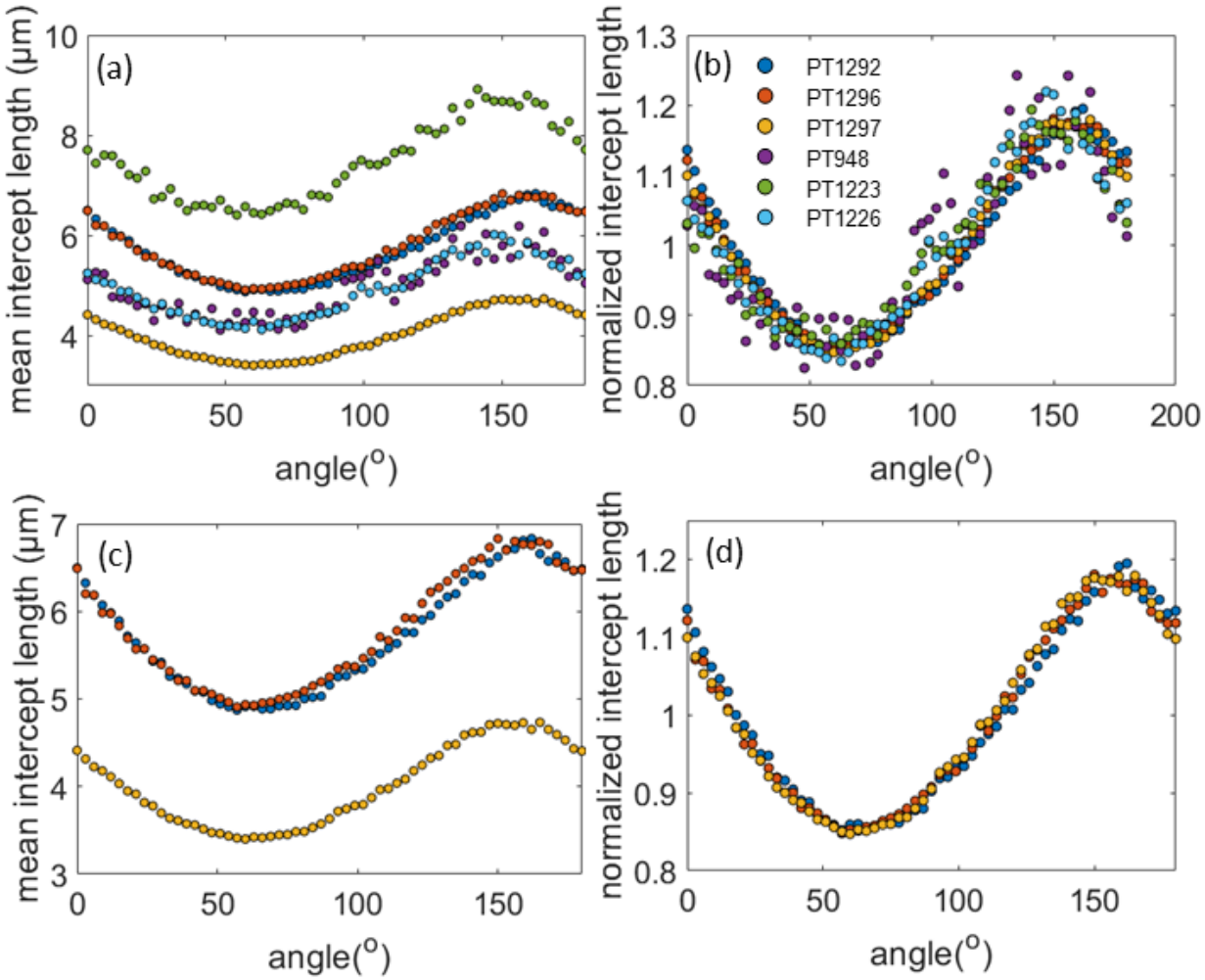

Figure 21: (a) Specimen angular distribution of mean linear intercept length for all samples, (b) normalized specimen angular distribution of mean linear intercept length for all samples, (c) Specimen angular distribution of mean linear intercept length for samples with N>10000, and (d) normalized specimen angular distribution of mean linear intercept length for samples with N>10000.

Figure 3-22: Pole figures of undeformed sample and tangential sections of deformed samples

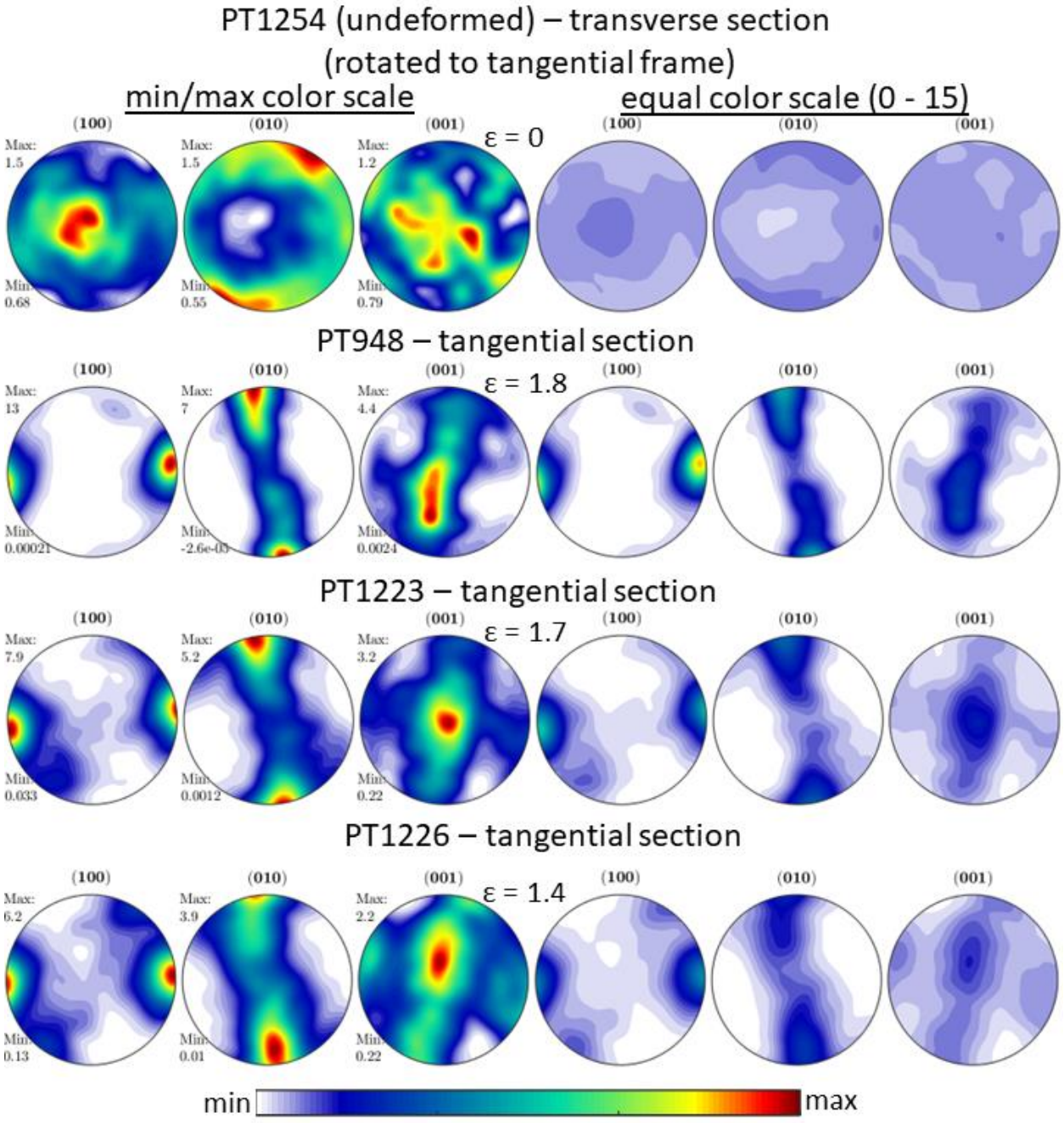

Figure 22: Pole figures of undeformed starting material (PT1254) and tangential sections of deformed samples (PT948, PT1223, and PT1226) that do not have corresponding analysis radial sections

Figure 3-23: Pole figures of sample PT1292 (radial and tangential sections)

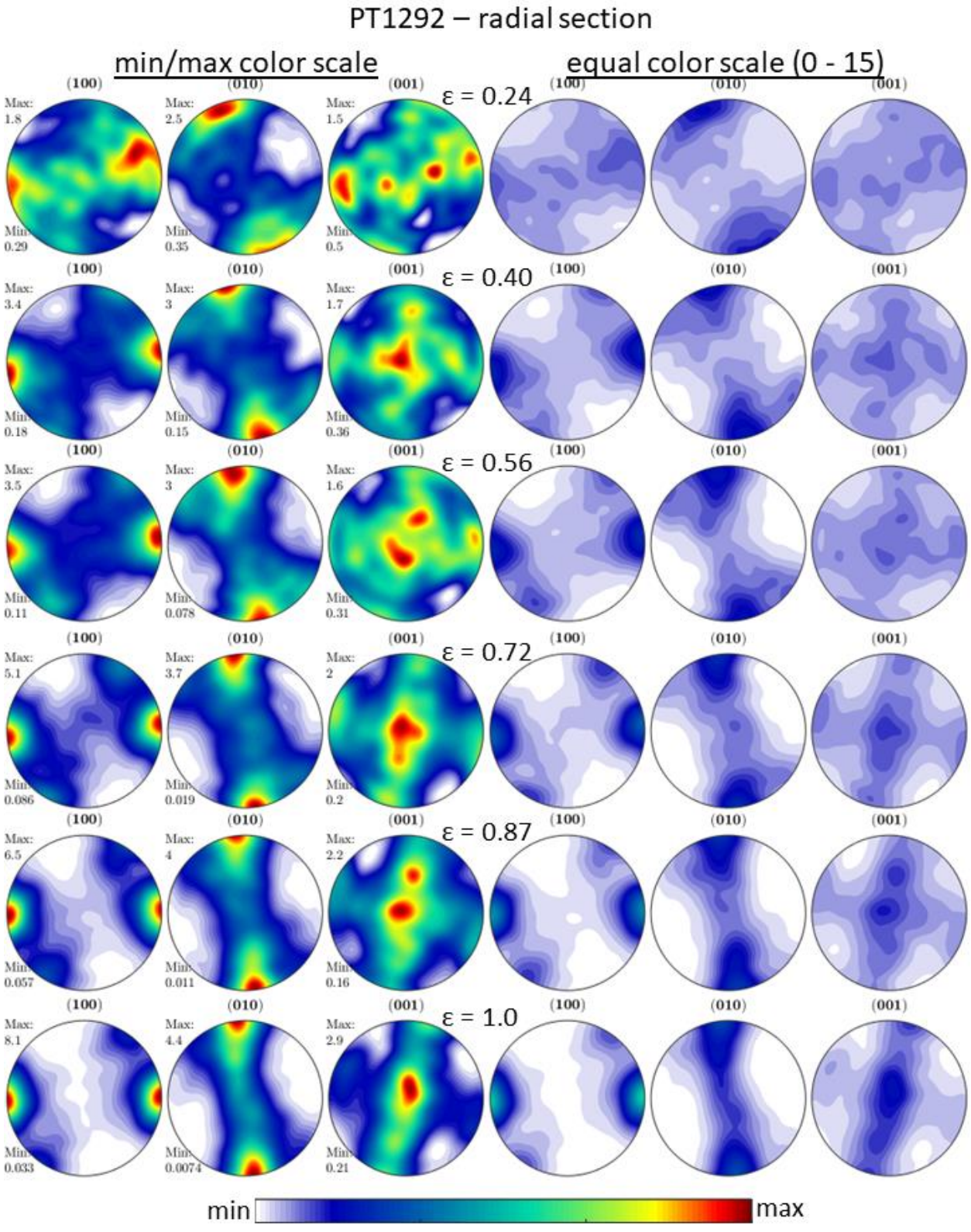

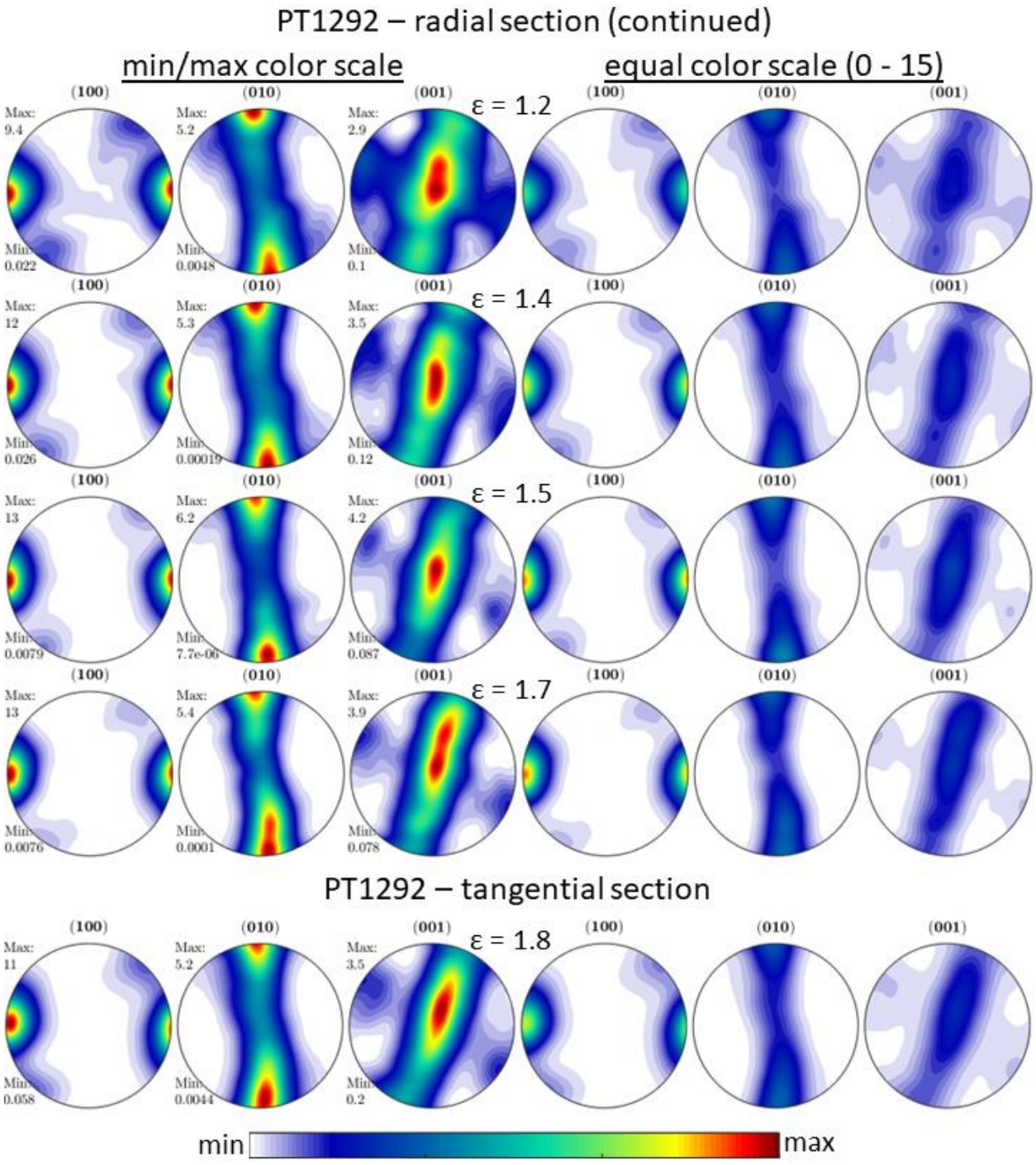

Figure 23: Pole figures of PT1292 taken from radially binned radial sections and a tangential section

Figure 3-24: Pole figures of sample PT1296 (radial and tangential sections)

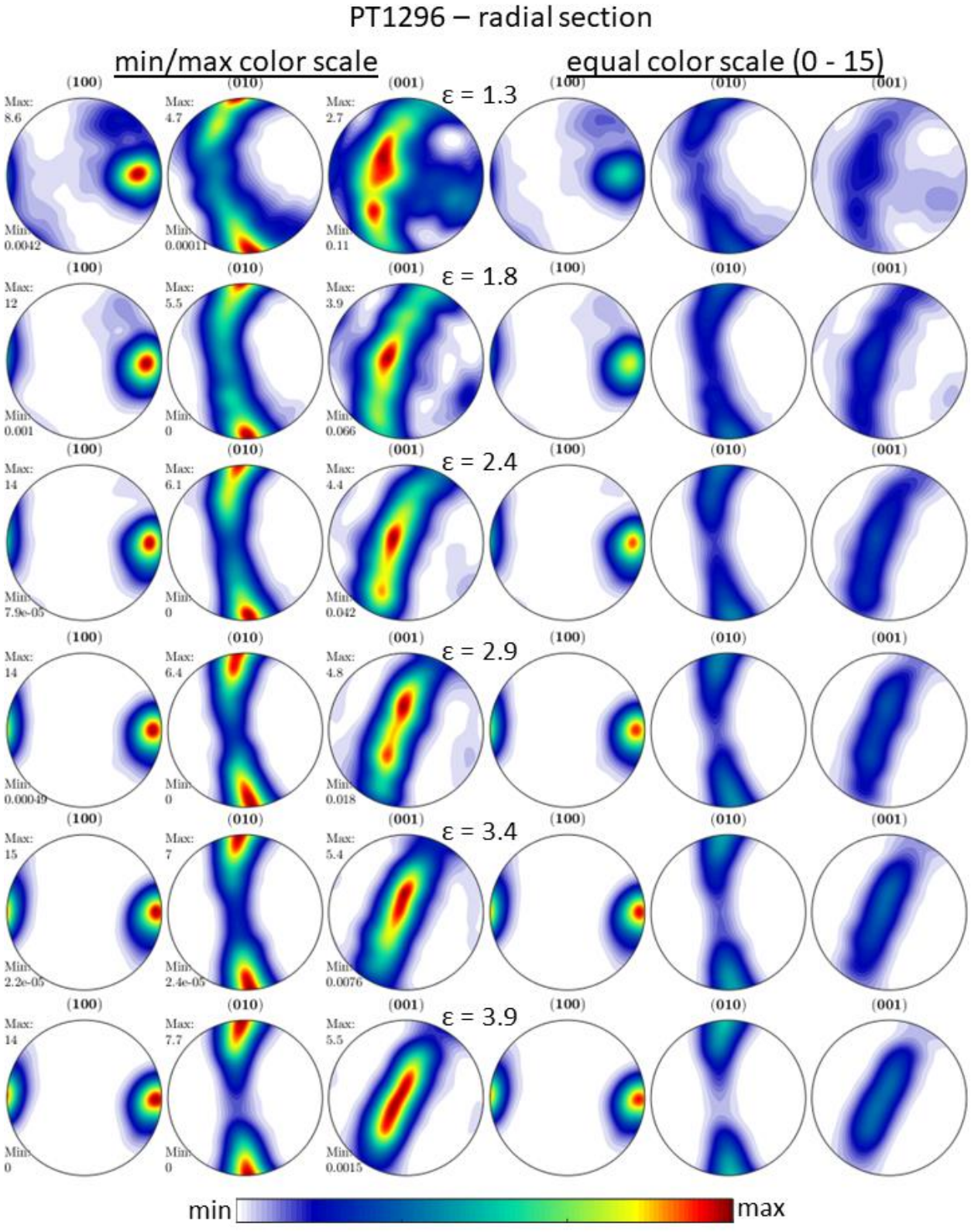

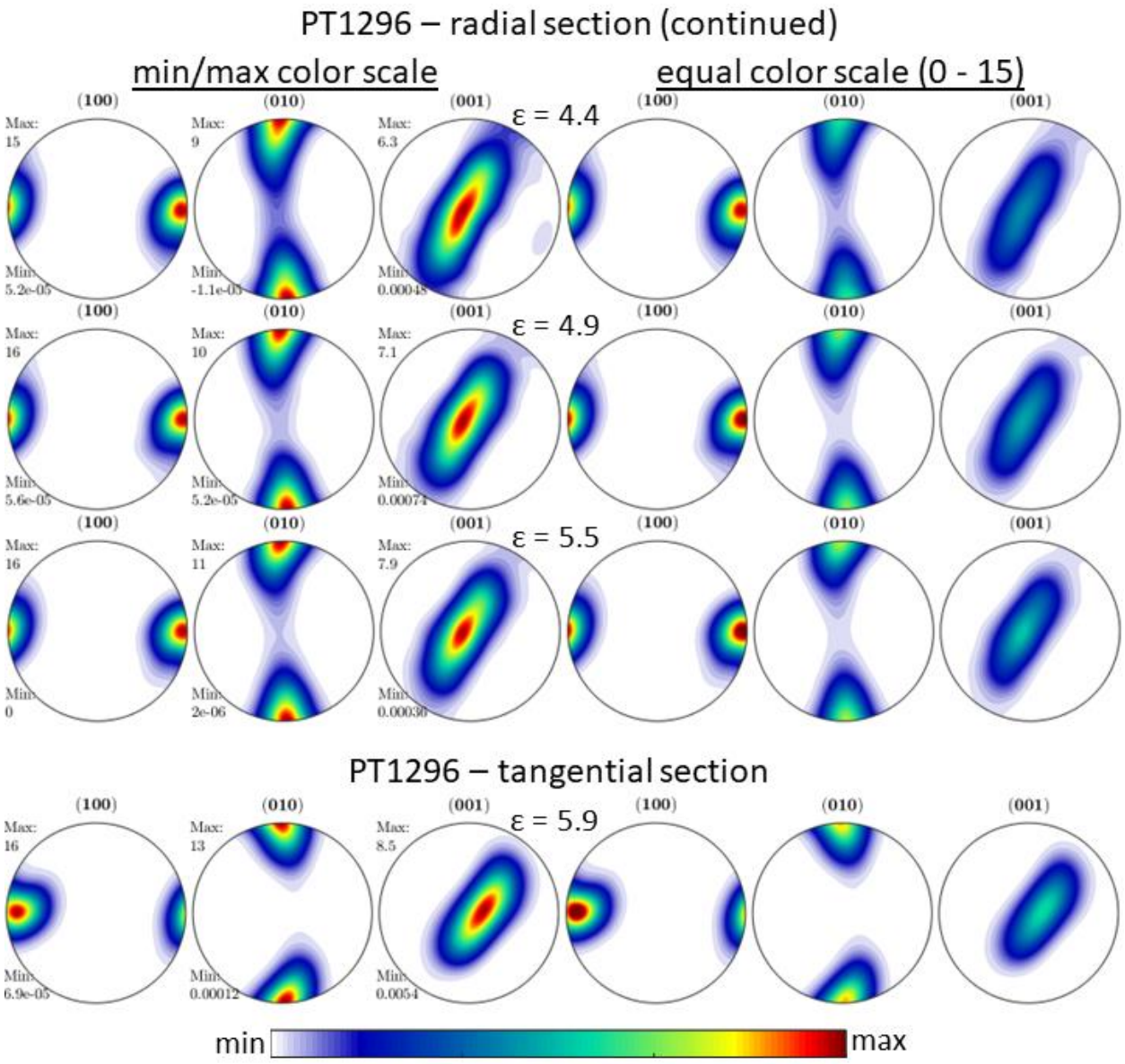

Figure 24: Pole figures of PT1296 taken from radially binned radial sections and a tangential section

Figure 3-25: Pole figures of sample PT1297 (radial and tangential sections)

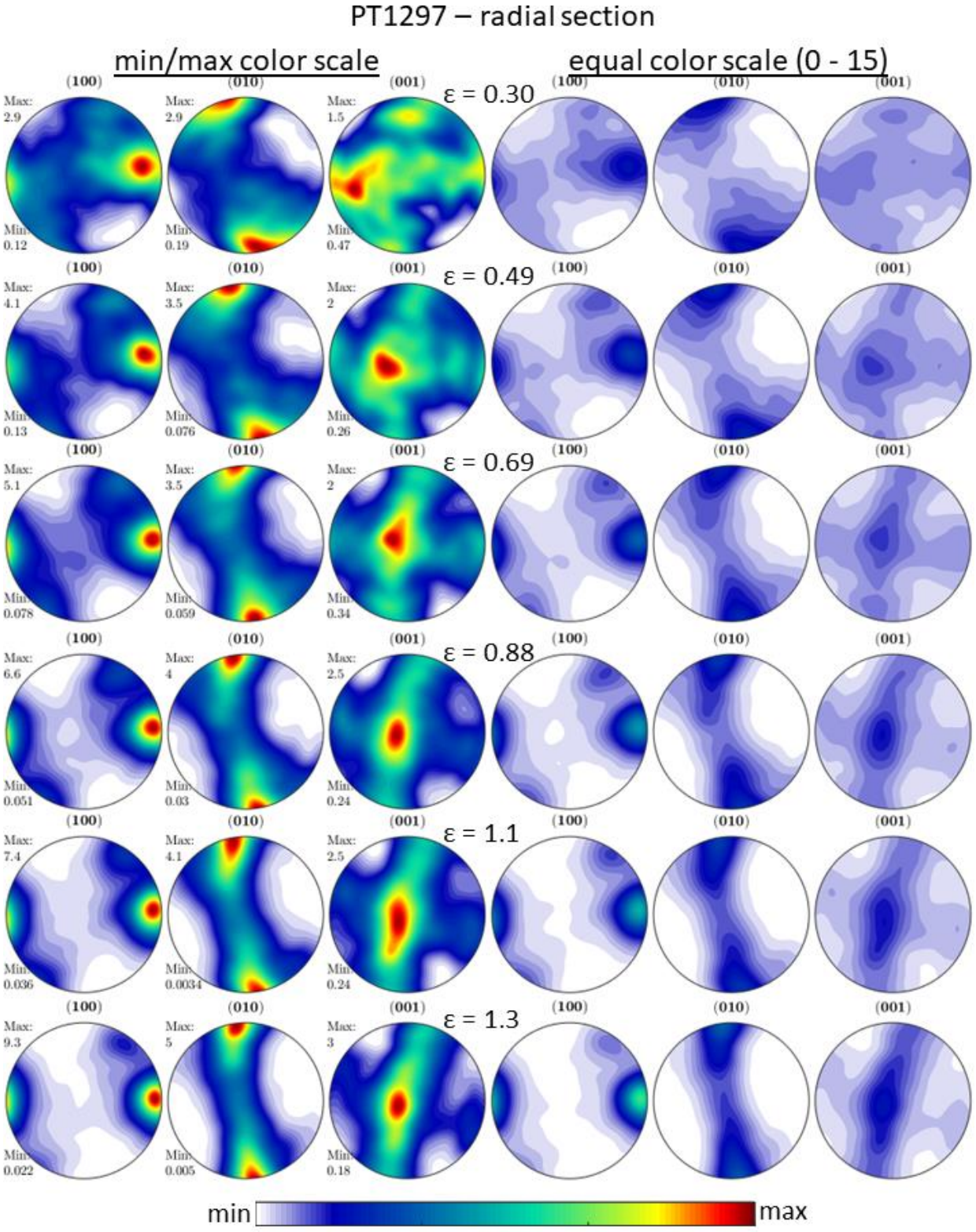

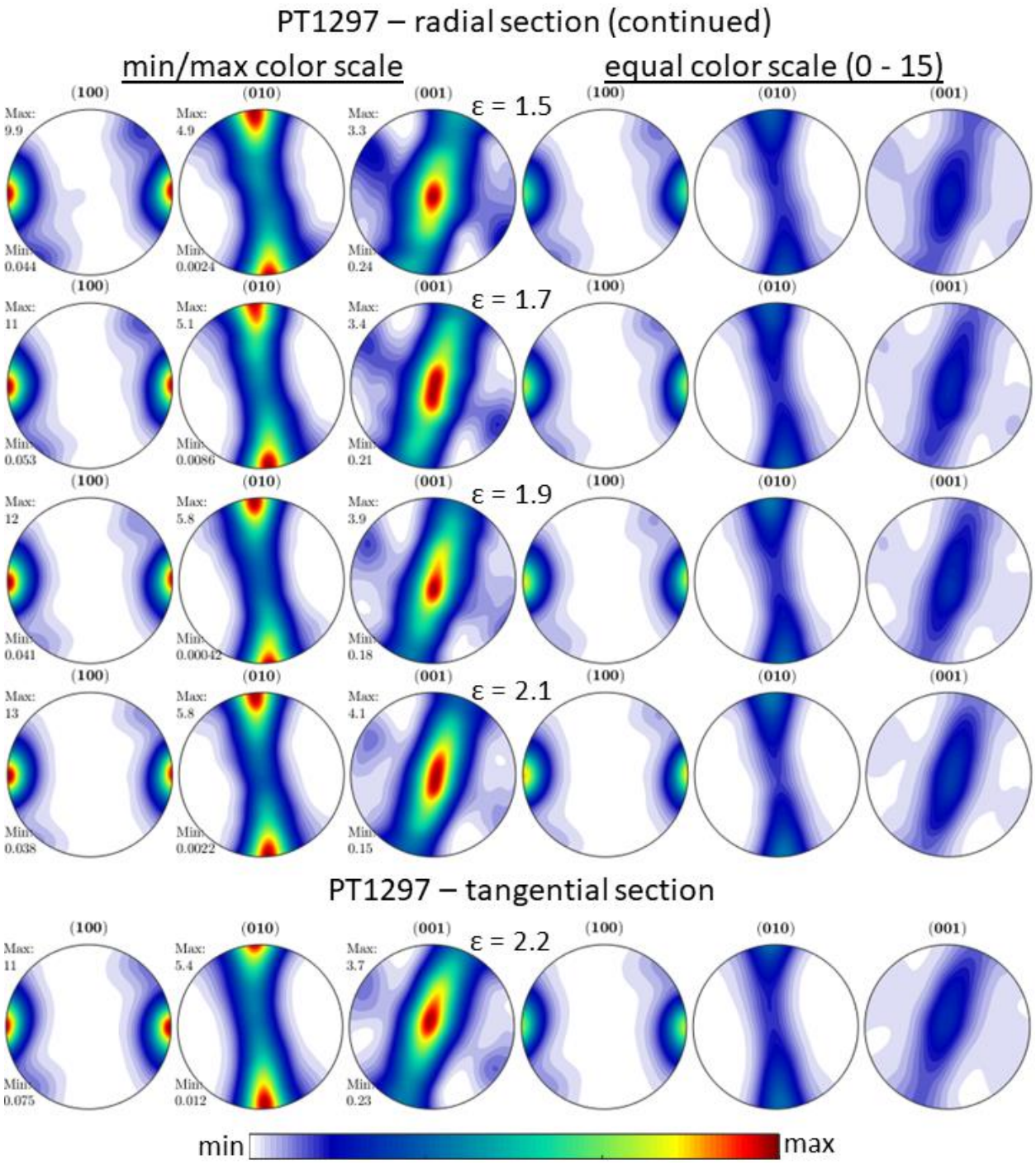

Figure 25: Pole figures of PT1297 taken from radially binned radial sections and a tangential section

Figure 3-26: Fabric strength analyses and angle of [100] direction to shear plane versus strain

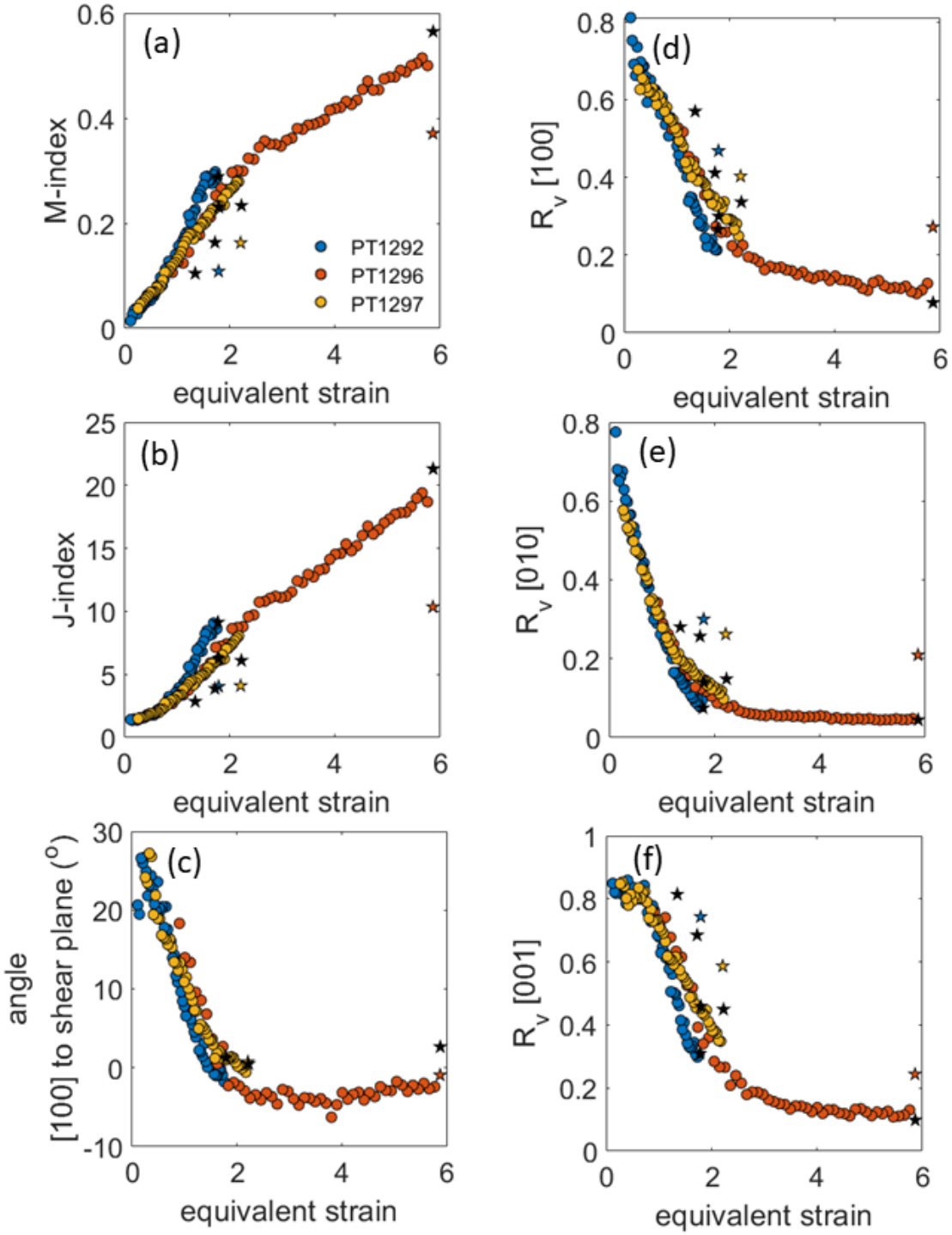

Figure 26: (a) M-index, (b) J-index, (c) angle of [001] direction, and (d-f) R-value for each principle direction plotted against equivalent strain for radial (colored data) and tangential (black stars) sections. The outermost radial bin for each sample is plotted as a colored star.

Figure 3-27: Eigenvalue analyses of pole figures from deformed samples (Woodcock)

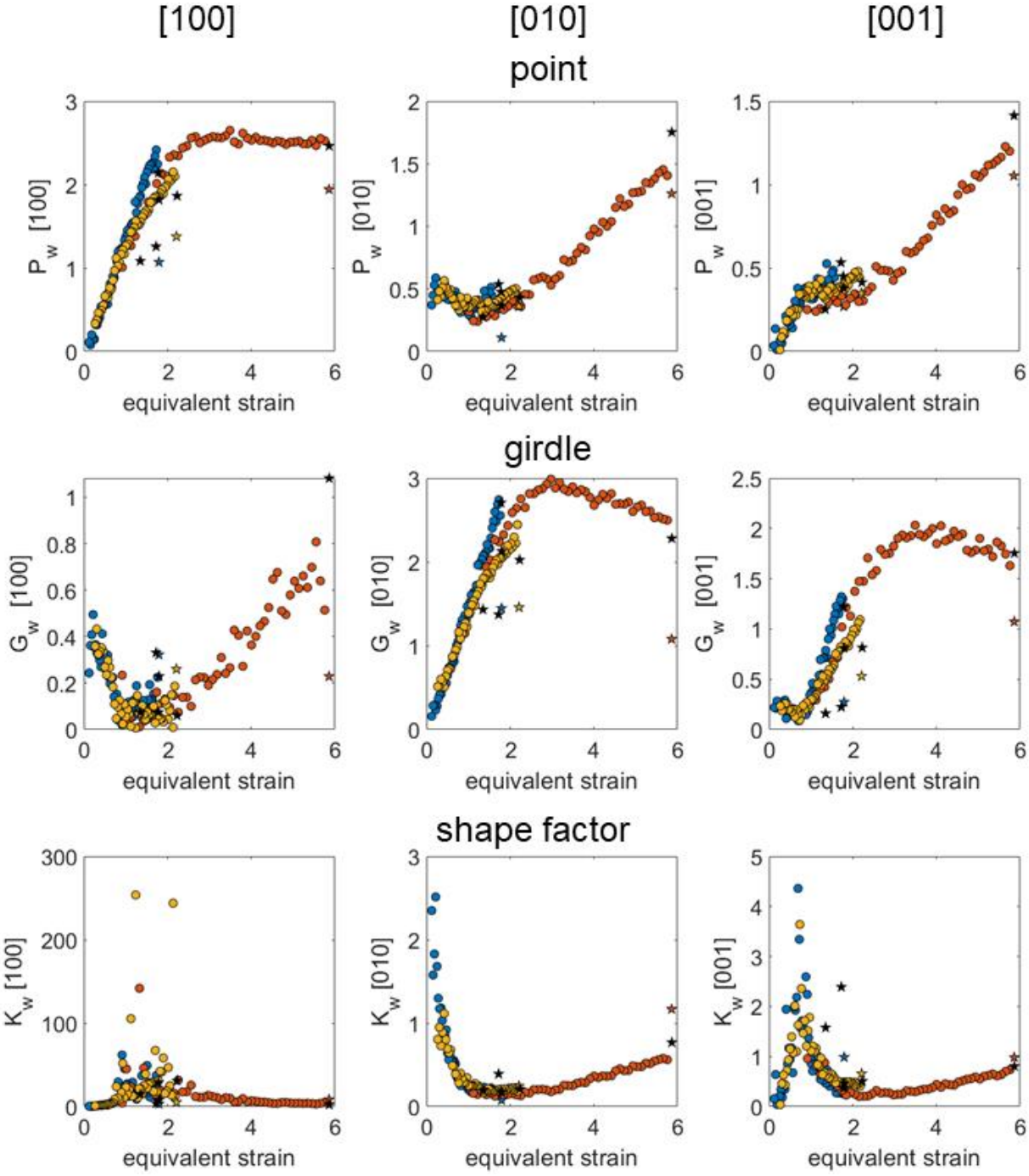

Figure 27: Eigenvalue analysis, using measures proposed by Woodcock (1977), plotted against equivalent strain for radial (colored data) and tangential (black stars) sections. The outermost radial bin for each sample is plotted as a colored star.

Figure 3-28: Eigenvalue analyses of pole figures from deformed samples (Vollmer)

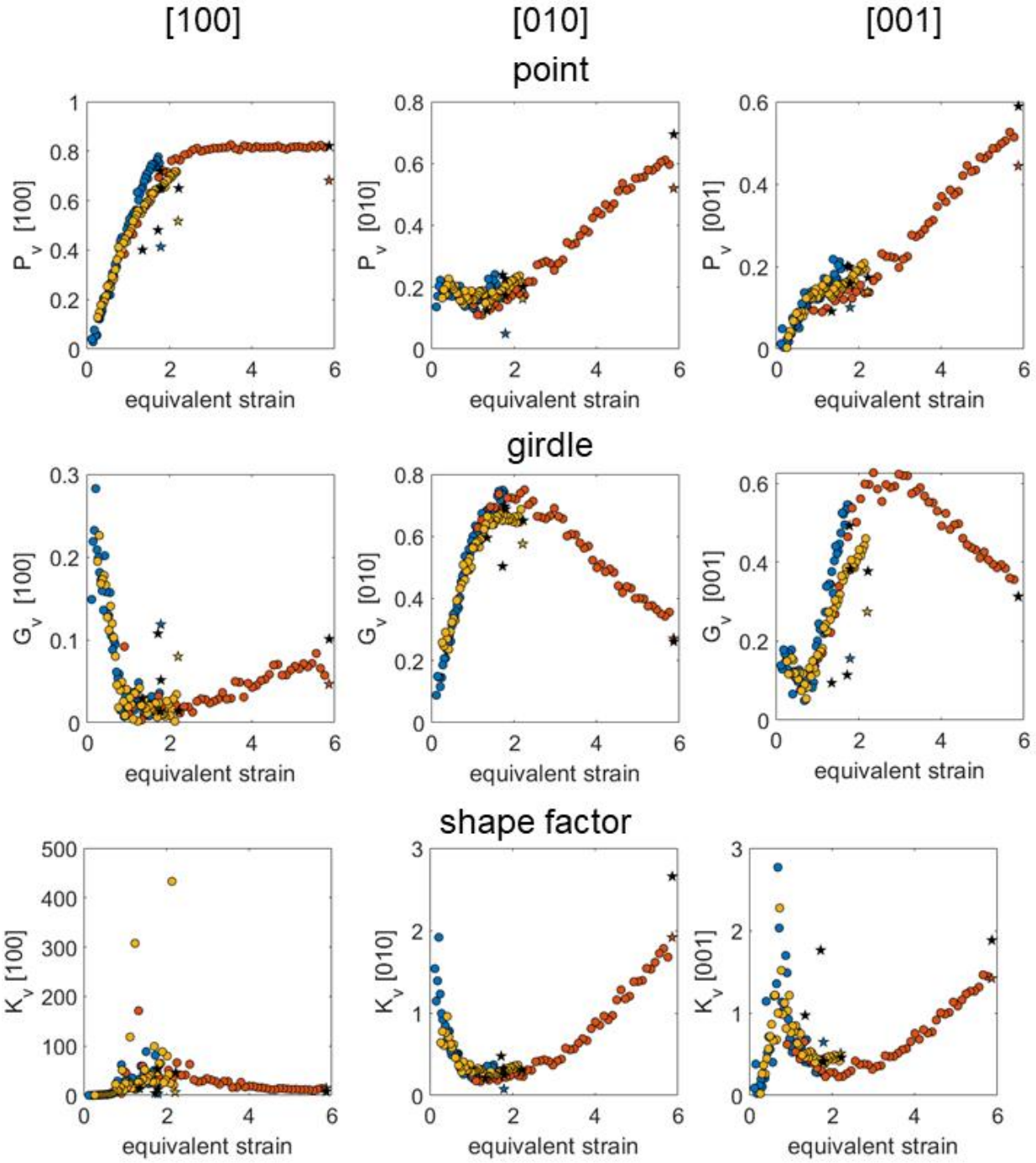

Figure 28: Eigenvalue analysis, using measures proposed by Vollmer (1990), plotted against equivalent strain for radial (colored data) and tangential (black stars) sections. The outermost radial bin for each sample is plotted as a colored star.

Figure 3-29: Ternary diagrams representing eigenvalue analysis of pole figures from deformed samples

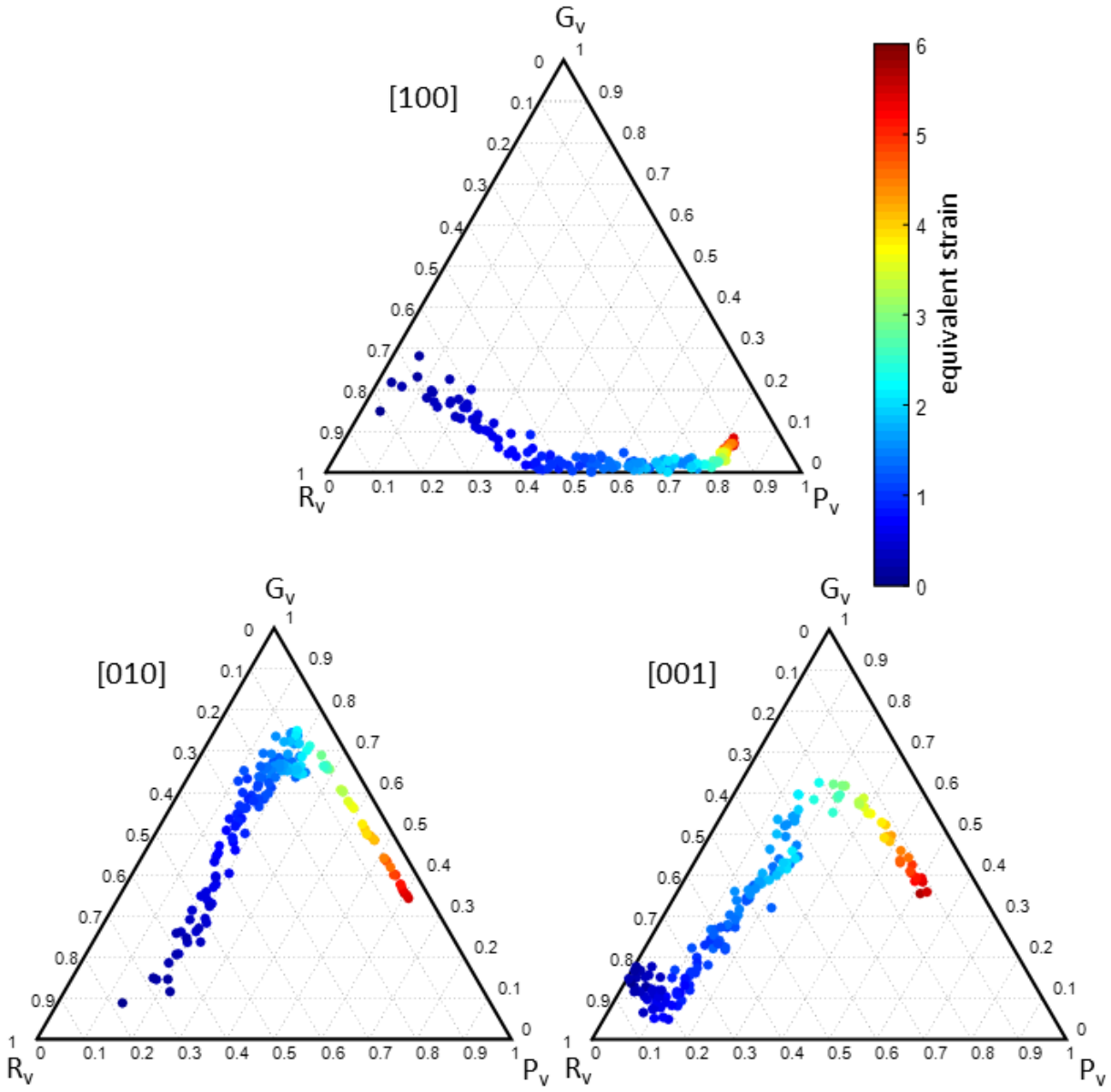

Figure 29: Ternary diagrams from eigenvalue analysis compiled across all radial sections for the primary crystallographic axes.

Figure 3-30: Cluster analysis of PT1292 grain orientations

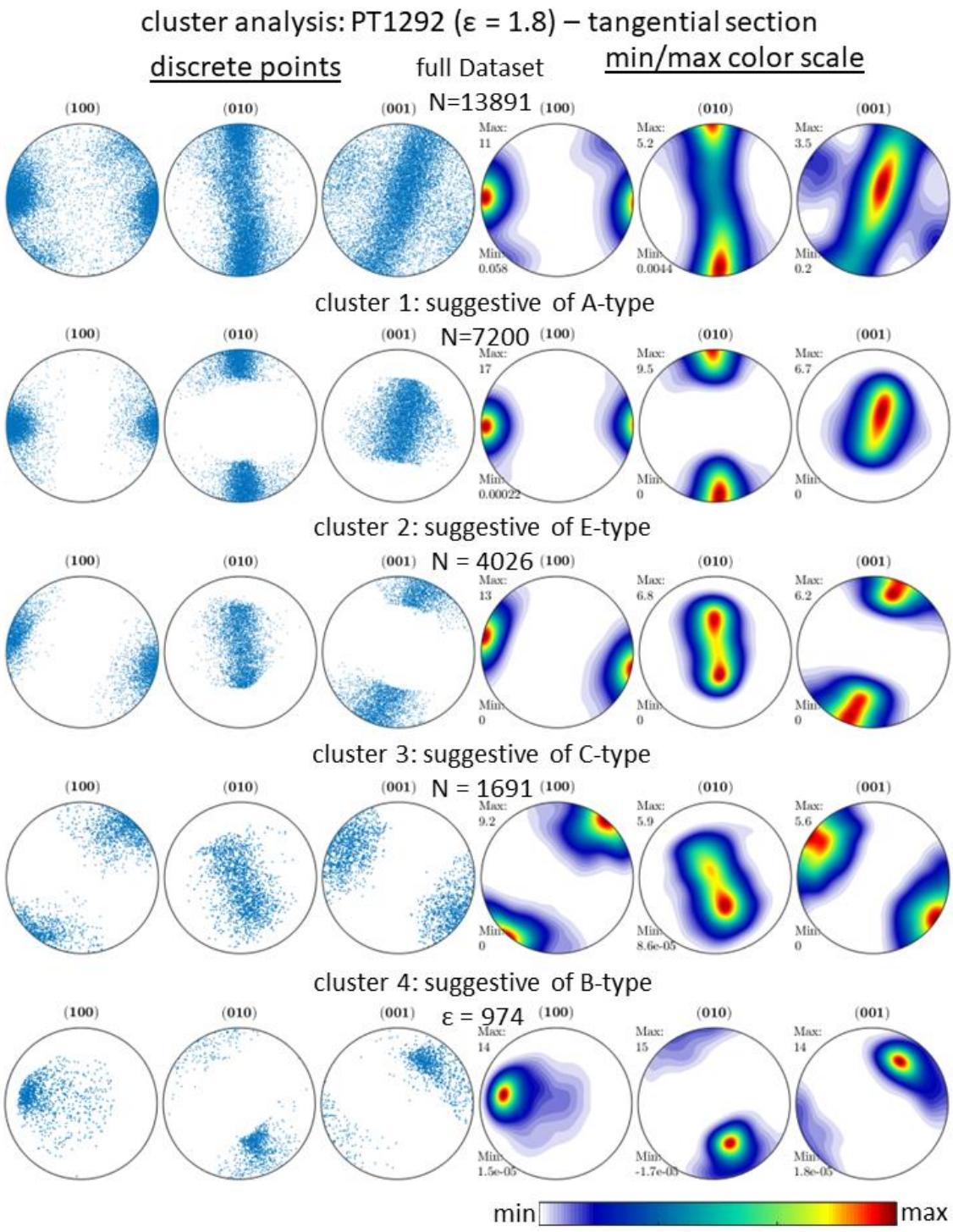

Figure 30: Pole figures resulting from orientation clustering analysis for sample PT1292 for which 4 clusters were generated.

Figure 3-31: Cluster analysis PT1296 grain orientations

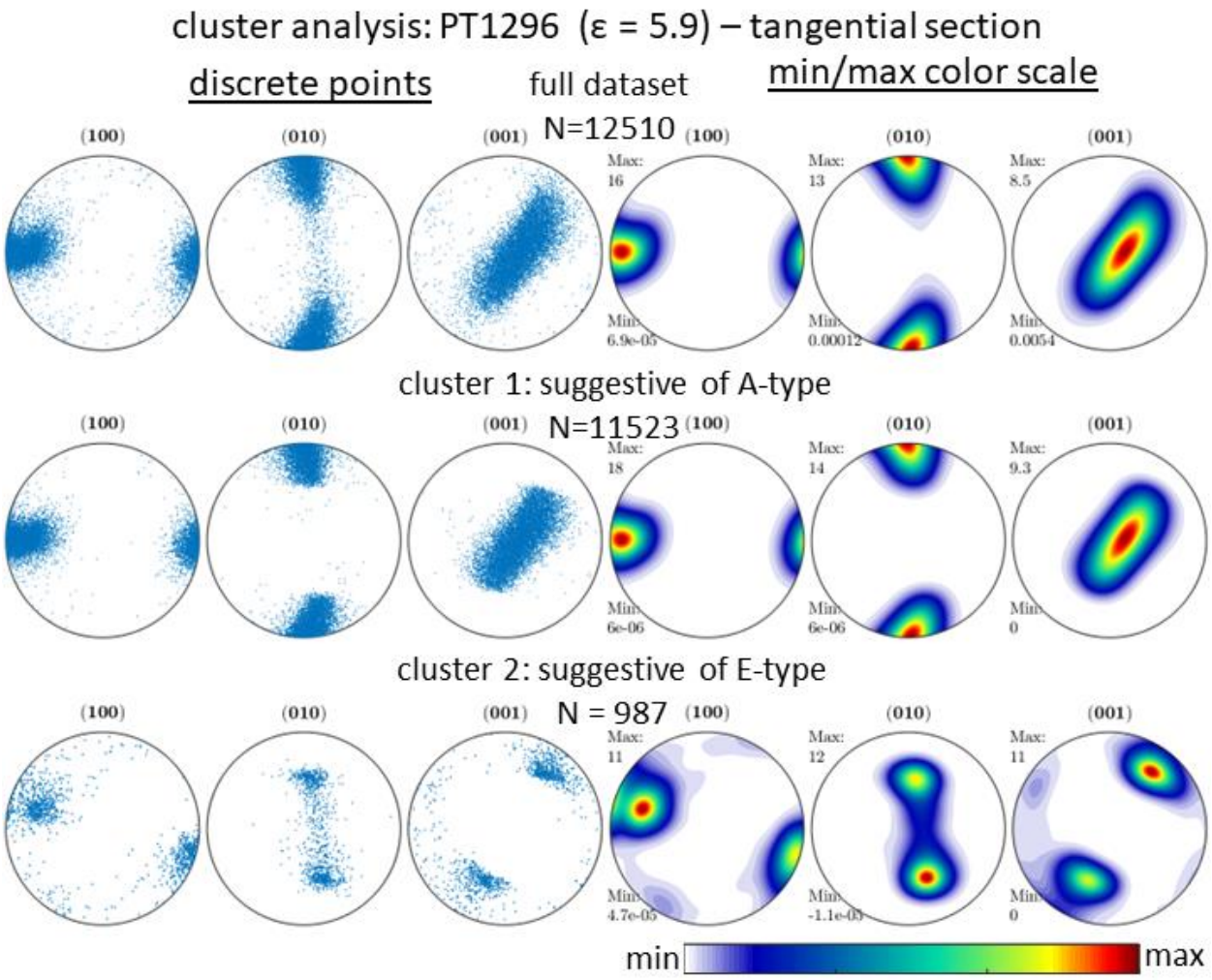

Figure 31: Pole figures resulting from orientation clustering analysis for sample PT1296 for which 2 clusters were generated. If 4 clusters were generated, the two minor clusters contained <2% of the data.

Figure 3-32: Cluster analysis of PT1297 grain orientations

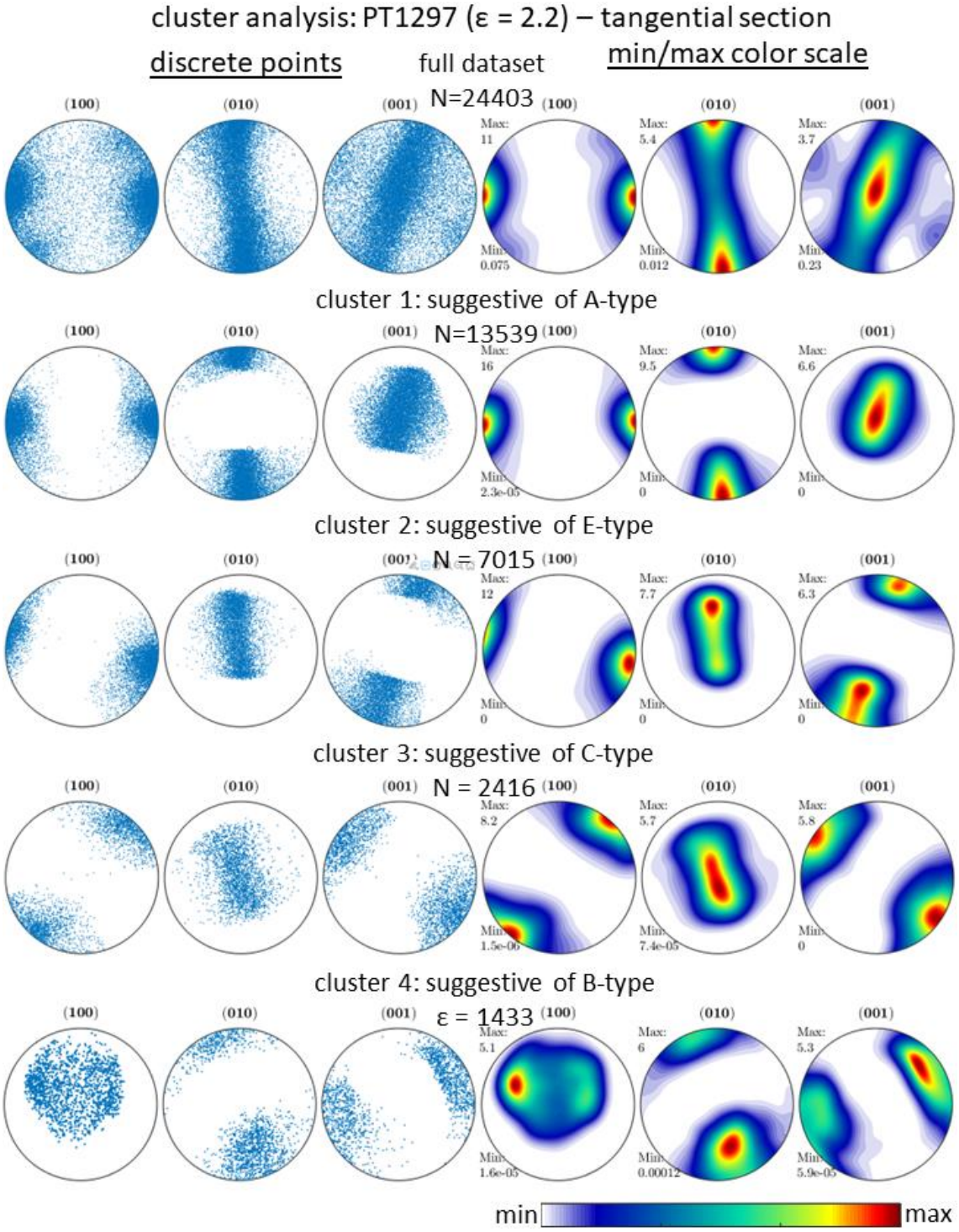

Figure 32: Pole figures resulting from orientation clustering analysis for sample PT1297 for which 4 clusters were generated.

Figure 3-33: Grain boundary specimen angle distribution of low-angle boundaries

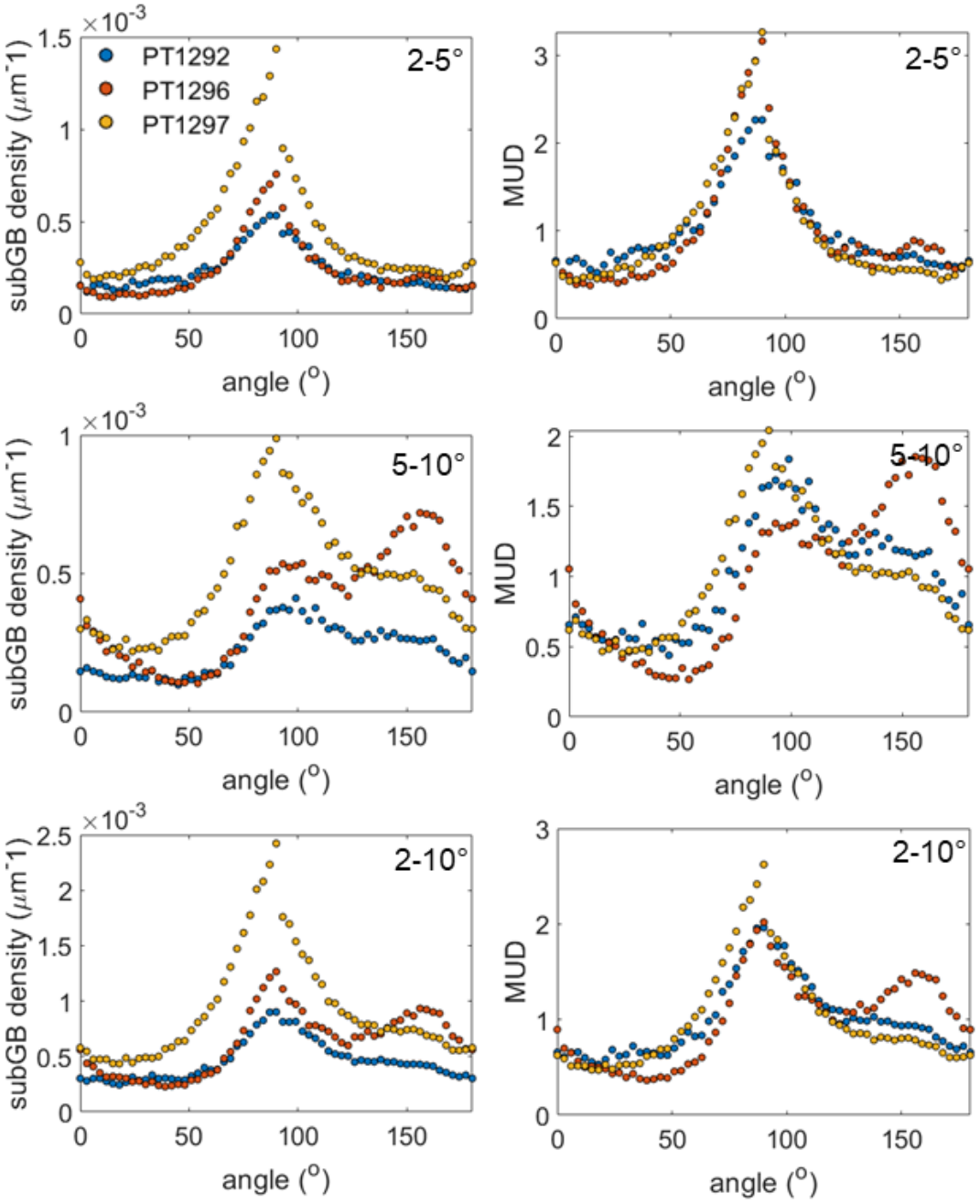

Figure 33: Subgrain boundary angle distribution in the specimen coordinates showing both absolute subgrain boundary densities (left) and normalized subgrain boundary densities right). If subgrain boundaries with angular misorientation >5° are included, the distribution appears overprinted by the sample scale SPO. However, boundaries with 2-5° angular misorientaton are generally oriented normal to the shear direction (termed, subgrain walls).

Figure 3-34: Subgrain boundary misorientation axes and boundary normal distributions

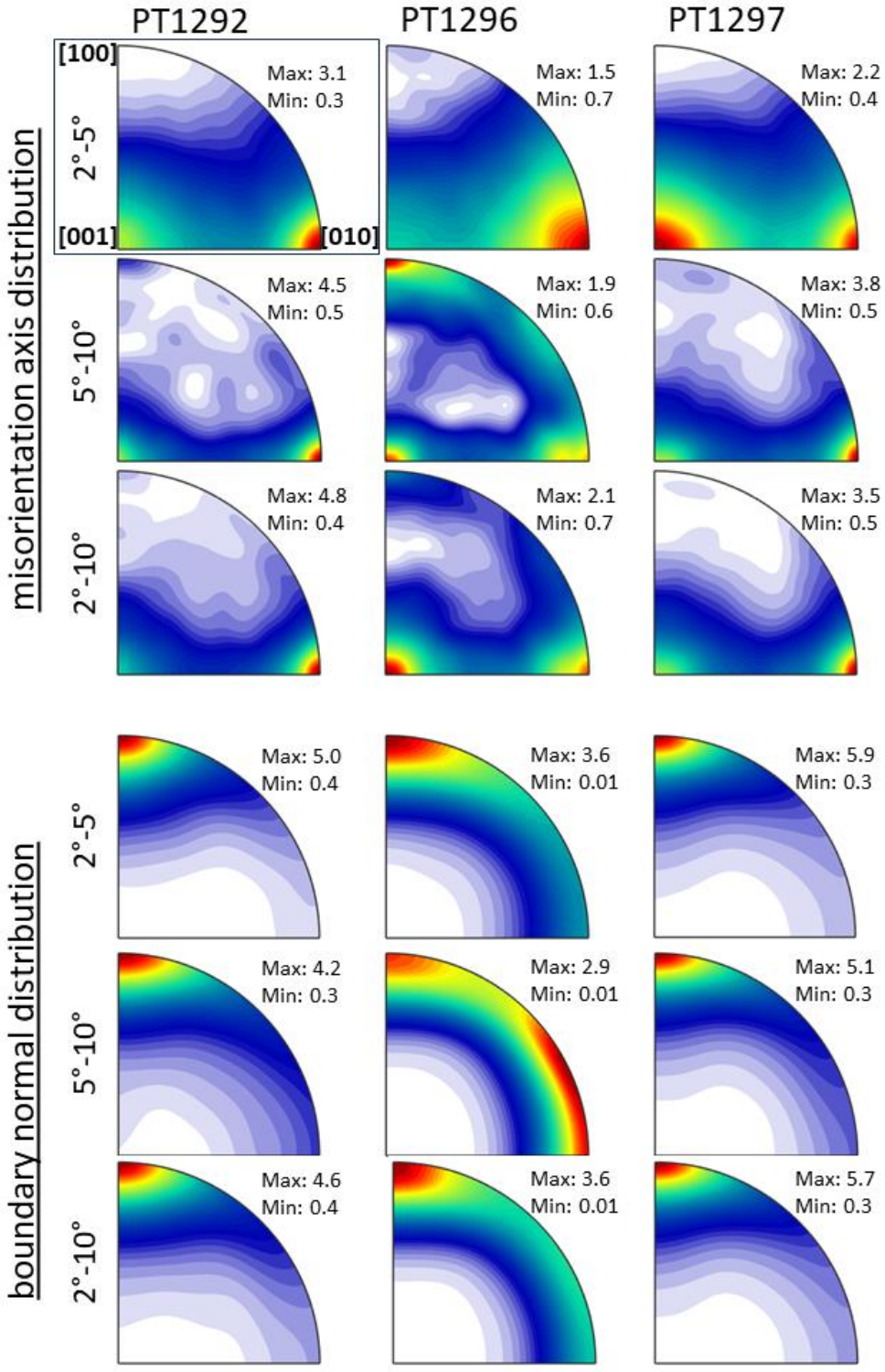

Figure 34: Subgrain boundary character analysis, wherein the crystallographic misorientation axes and boundary normal distributions are plotted on inverse pole figures for selections of low-angle boundaries.

Chapter 4 Diffusion Creep of San Carlos Olivine Aggregates Deformed at 1 atm

4.1 Abstract

Creep experiments in a controlled-atmosphere, dead-load apparatus were performed on fine-grained, evacuated hot-pressed San Carlos olivine aggregates at 1129° to 1229°C and pO_2 near the Ni/NiO buffer to investigate the high-temperature rheological behavior of olivine aggregates at relatively low-stress, low-strain rate conditions. This study includes data from three constant-temperature, load-stepping experiments and one constant-load, temperature-stepping experiment. We determined a stress exponent of $n \approx 1$ from load-stepping experiments, indicating deformation dominated by diffusion creep. We measured higher strengths than predicted by published flow laws for naturally derived olivine aggregates, especially at the lowest temperatures tested. Further, published flow laws for San Carlos olivine aggregates predict that deformation should have occurred by dislocation-accommodated, grain-boundary sliding (disGBS) with a stress exponent of $n = 2.9$ at our experimental conditions (Hansen et al., 2011). However, our data are broadly consistent with results from Ca- and Al-doped, vacuum-sintered, oxide-derived olivine aggregates deformed at 1 atm (Yabe et al., 2020), highlighted by a relatively high apparent activation energy across the range of experimental temperatures. An analysis of data from similar experimental studies, combined with the results from our study, yields modified flow law fits for olivine. We explore the implications of these fits using deformation mechanism maps. We conclude that disGBS was suppressed in our experiments due to the nucleation barrier for activating dislocation sources (Frank-Read sources) at relatively low stresses and fine grain-sizes.

4.2 Introduction

Flow laws based on rheological data from high-temperature deformation experiments on fine-grained olivine aggregates form much of the basis for modeling viscous flow in Earth's upper mantle (Schwenn and Goetze, 1977; Karato et al., 1986; Hirth and Kohlstedt, 1995a; Mei and Kohlstedt, 2000; Mei and Kohlstedt 2000a; Hirth and Kohlstedt, 2003; Faul and Jackson 2007; Faul et al., 2011; Hansen et al., 2011; Yabe et al., 2020). Experimentally verified flow

laws – constitutive equations describing the relationship of deformation conditions (such as stress, temperature, pressure, and chemical environment) and material characteristics (such as grain-size and chemical composition) to the resulting strain-rate – are needed to extrapolate data collected under laboratory conditions to the timescales and lengthscales of deformation in Earth's mantle. At high-temperature and relatively low-stress conditions, relevant to understanding convective flow in Earth's mantle, a handful of deformation mechanisms have been identified. Deformation mechanism maps, based on results from laboratory experiments, which typically include the diffusion creep, dislocation-accommodated grain-boundary sliding (disGBS), dislocation creep, and low-temperature plasticity regimes, are useful for predicting the dominant deformation mechanisms and the appropriate constitutive equation for modeling deformation in Earth's upper mantle (Karato and Wu, 1993; Hirth and Kohlstedt 2003; Hansen et al. 2011). While a variety of experimental studies have consistently identified the same deformation regimes, there are broad differences amongst flow-law parameters due to differences in selection of starting materials, sample synthesis approaches, experimental techniques, and/or analytical methods. When extrapolating to mantle conditions, these discrepancies lead to uncertainty in the appropriate flow law(s) to use for modeling mantle flow.

In this study, we performed deadweight creep experiments on evacuated hot-pressed aggregates of San Carlos olivine at 1 atm under controlled-pO_2 conditions at 1129° to 1229°C and compared our results to a selection of previously published flow laws and experimental data from the studies referenced above. In general, it is challenging to deform conventionally hot-pressed, naturally derived olivine aggregates at ambient pressure under high enough stresses to study steady-state creep due to the disaggregation that occurs without elevated confining pressure. Small, trapped, high-pressure pores in conventionally hot-pressed samples grow in the absence of high confining pressure and assist in disaggregation during creep. At stresses low enough to avoid disaggregation, the limitations of laboratory timescales make it difficult to reach steady-state deformation. However, synthesis of nearly pore-free San Carlos olivine aggregates, using the evacuated hot-pressing method, yielded samples with <0.1% porosity after quenching, as measured by SEM (see Ch. 2). We demonstrated that these samples could withstand stresses greater than 150 MPa without microfracturing and disaggregating at 1 atm pressure. Dead-weight creep experiments have the advantage of high stress resolution and ease of running experiments at longer timescales than typically achievable in a high-pressure, gas-medium apparatus. Our experiments add to the body of deformation data on olivine

aggregates and expand the range of deformation conditions explored by laboratory experiments. We compare our data and interpretations to those of similar published studies.

4.3 Background

4.3.1 High-Temperature Deformation Mechanisms and Flow Laws

Our understanding of the processes of mantle deformation relies heavily on extrapolation of laboratory-derived flow laws to natural conditions. Frequently, high-temperature creep mechanisms are described by a power-law flow law with the generalized form

$$\dot{\varepsilon} = A\sigma^{n} d^{-p} \, exp\left(-\frac{Q}{\mathrm{R}T}\right), \quad (1)$$

where $\dot{\varepsilon}$ is strain rate, A is a material-dependent parameter, σ is stress, n is the stress exponent, d is the grain size, p is the grain-size exponent, Q is the activation energy, R is the gas constant, and T is the temperature. The exponential temperature dependence is derived from statistical mechanics as a form that is common to thermally activated processes that depend on the frequency of atomic motion and the concentration of defects. The stress and grain-size exponents are characteristic of the micro-scale physics of the underlying deformation mechanism.

Previous experimental results have revealed that, at relatively small grain sizes and low stresses, diffusion creep is the dominant deformation mechanism. Diffusion creep occurs by the diffusion of ions through constituent grain volumes or boundaries in response to stress-induced gradients in chemical potential. The creep rate depends on the diffusion distance and stress gradient, which leads to an implicit dependence on the length-scale of grains and rate-limiting diffusional pathway (grain volumes or boundaries). Theory describing this process predicts linear stress dependence $n = 1$ and non-linear grain-size dependence with $p = 2$ for volume diffusion (Nabarro-Herring creep; Nabarro, 1948; Herring, 1950) and $p = 3$ for grain boundary diffusion (Coble creep: Coble, 1963).

At higher stresses and large grain sizes, dislocation creep is activated, which occurs by the motion of line defects (dislocations) in response to stress. This process is independent of grain size ($p = 0$) but depends non-linearly on stress ($n = 3$-5) (e.g., Weertman, 1970). High-temperature experiments on coarse-grained dunites and olivine single crystals have repeatedly

measured a stress exponent of $n \approx 3.5$ for samples deforming by dislocation creep (Bai and Kohlstedt, 1991; Hirth and Kohlstedt, 2003; Keefner et al., 2011). At fine grain sizes and relatively high stresses, deformation by disGBS occurs, involving the combination of dislocation motion and sliding at grain boundaries. This results in both a grain-size dependence (p = 2,1) and a stress dependence (n = 2,3) (Langdon, 2006; Hansen et al., 2011; Hansen et al., 2012). The specific values of the grain-size and stress exponents that are predicted from theory depend on the specifics of the micro-scale physics used to model this process. Hansen et al. (2011) measured $p \approx 1$ and $n \approx 3$ during high-temperature deformation of fine-grained olivine aggregates, supporting the inference that disGBS was the dominant deformation mechanism in their experiments.

Previous experimental results have led to the broad consensus that high-temperature deformation in Earth's mantle occurs dominantly by diffusion creep, disGBS, dislocation creep, or some combination of these mechanisms. However, additional mechanisms have been identified in the laboratory. At very fine grain sizes and low stresses, interface-controlled diffusion creep has been identified experimentally at conditions that are unlikely to be relevant to our experiments nor dominant in Earth's mantle (Yabe et al., 2020). This mechanism is unlikely to dominate in Earth's mantle because it requires extremely fine grain sizes that could not be maintained at high temperatures on geologic timescales. At very high stresses, power-law breakdown or low-temperature plasticity (characterized by increasingly non-linear deformation with increasing stress) occurs, wherein creep is controlled by dislocation glide. This process is also unlikely to be relevant to our experiments or dominant during high temperature deformation in the upper mantle due to the very high stresses necessary to activate this mechanism. However, this mechanism is likely important to deformation in the Earth's lithosphere where stresses are high and temperatures are relatively low (Hansen et al., 2019).

Considering these three mechanisms as independent processes has led to fitting experimental data with a combination of flow laws represented by

$$\dot{\varepsilon}_{total} = \dot{\varepsilon}_{diff} + \dot{\varepsilon}_{GBS} + \dot{\varepsilon}_{disl}, \quad (2)$$

where $\dot{\varepsilon}_{\mathrm{total}}$ is the total strain rate, $\dot{\varepsilon}_{\mathrm{diff}}$ is the strain-rate contribution from diffusion creep, $\dot{\varepsilon}_{\mathrm{GBS}}$ is the strain-rate contribution from disGBS, and $\dot{\varepsilon}_{\mathrm{disl}}$ is the strain-rate contribution from dislocation creep. Often only two mechanisms (two terms) are considered in Equation 2, when fitting experimental data (Hirth and Kohlstedt, 2003; Hansen et al., 2011). Because the range of stress, temperature, and grain size over which more than two mechanisms contribute

significantly to deformation is generally narrow. Results from published work (referenced above) lead to the expectation that deformation of our samples at the imposed experimental conditions will occur by a combination of diffusion creep and a secondary non-linear mechanism (disGBS or dislocation creep), with diffusion creep dominant under low applied stresses with an increasing contribution from non-linear, dislocation mechanisms at higher applied stresses. We, therefore, present our experimental results in the context of this well-established expectation.

4.4 Methods

4.4.1 Synthesis of Evacuated Hot-Pressed Starting Material

Fine-grained, nearly pore-free polycrystalline aggregates of San Carlos olivine were synthesized by evacuated hot-pressing. The methods for synthesis and properties of these aggregates are described in Chapter 2. In summary, the powder used to prepare samples for our experiments was obtained by pulverizing hand-picked San Carlos single crystals by fluid-energy milling. The volumetric mean powder size of this material was 6.2±2.6 μm, measured by laser diffraction. The powder was dried at 1 atm at ~1100°C for 10 h in a CO/CO_2 gas mixture that set the pO_2 near the Ni/NiO buffer. The dried powder was subsequently uniaxially cold-pressed into a Ni capsule, applying a uniaxial stress of roughly 100 MPa with a hydraulic press. The powder and the cold-pressed compact were stored in a vacuum oven at ~100°C between processing steps. Next, the cold-pressed cylinder was densified in a gas-medium apparatus (Paterson, 1990) at 1250°C and 300 MPa for roughly 3 h. During this hot-pressing step, the powder compact was actively vented through a porous alumina end cap that connected to a vacuum of <0.2 mbar through axial holes in the alumina pistons. Nickel oxide powder was added to the sealed end of the capsule to react with the Ni capsule and maintain pO_2 conditions within the stability field of San Carlos olivine.

After densification, the evacuated hot-pressed cylinder of San Carlos olivine was cut into rectangular pillars for deformation, as shown in Figure 1a. Due to the very low porosity of these aggregates, samples are transparent at the millimeter-thick scale, as demonstrated in Figure 1b. The densified aggregates formed a fine-grained ceramic with <0.1% porosity, as determined from backscattered scanning electron microscope (SEM) images of oxidation decorated specimens, such as the one presented in Figure 1c. In such images, samples have a roughly uniform, fine grain size with some heterogeneously distributed dislocation structures. The grain

size of the starting material was ~5 μm based on electron backscatter diffraction (EBSD) maps, such as the one presented in Figure 2.

4.4.2 Deformation Experiments

Axial-compression deformation experiments were performed at high temperature in a 1-atm, deadweight creep apparatus under controlled pO_2 conditions in a flowing CO/CO_2 gas mixture. Parallelepipeds with dimensions of approximately 5.7 × 2.3 × 2.5 mm, cut from evacuated hot-pressed aggregates, were deformed between alumina platens to <12% axial strain. A photograph of an undeformed sample is presented in Figure 1a. The deformation apparatus, described in detail by Mackwell et al. (1990), applied a load to the sample by weights hung from a cantilever connected to a SiC piston. The SiC piston led into a gas-sealed, high-temperature furnace tube. Sample deformation was monitored by an internal, direct-current linearly variable displacement transducer (DCDT) that measured the relative displacement between the top and bottom alumina platens, minimizing the influence of thermal expansion of apparatus components on measured displacement. A second, external DCDT monitored displacement of the SiC piston relative to the frame of the deformation rig to verify the displacement measured with the internal DCDT. Temperature was monitored with a thermocouple adjacent to the sample. Deformation experiments were carried out at constant temperature between 1129° and 1229°C under applied loads of 30 to 97 kg, resulting in differential stresses of 50 to 166 MPa. One experiment was conducted under constant load with stepped-temperature conditions, allowing for thermal stabilization at constant temperature between steps. The gas mixture for each experimental temperature was chosen to set the pO_2 near that imposed by a Ni/NiO solid-state buffer. When fitting flow laws to our data, we did not include parameters to account for changes in pO_2 associated with changes in temperature, however, other flow laws determined for polycrystalline San Carlos olivine were typically determined using a solid Ni/NiO buffer to set the pO_2, making our results directly comparable to these studies. After deformation, the dimensions of each sample were measured using a micrometer to confirm that total displacement measured by the internal DCDT accurately reflected deformation of the sample.

Stresses and strain rates were calculated from the forces resulting from the applied weight and DCDT displacement measurements, assuming constant-volume deformation. Strain rates were calculated from linear fits to segments of the displacement-time curves during which the creep rate had stabilized to a nearly constant value, as assessed by plotting strain-rate

against strain. As an example, a creep curve used to calculate the strain rate at each load step is shown in Figure 3. Applied stresses and resulting strain rates calculated from each creep experiment were used to fit the data to the flow law presented in Equation 1.

4.4.3 Microstructural Characterization

Microstructural properties, including mean grain size and porosity, were characterized for both the undeformed starting material and deformed samples using reflected-light optical microscopy, SEM imaging, and EBSD analyses. Each sample was cut in half parallel to the deformation axis and polished with diamond lapping film to a final grit of 0.5 μm followed by polishing with colloidal silica (Syton). Optical micrographs of polished surfaces were used to characterize the porosity of each deformed sample by generating a binary image segmented to isolate pores from grain surfaces. The polished section of each sample was also mapped by EBSD with a step-size of 0.1 or 0.2 μm. EBSD data were processed using iterative band contrast masking and nearest neighbor interpolation, such that grain boundary locations computed from indexed crystal orientation data matched closely to those indicated from band contrast maps (Prior et al., 2009). EBSD maps were used to characterize grain size, employing both the mean equivalent-area circular diameter and the linear-intercept methods. Equivalent-area circular diameter and mean linear intercepts were computed using the MATLAB based MTEX toolbox (Bachmann et al., 2010). A correction factor accounting for stereographic sectioning effects of $4/\pi$ and 1.5 for equivalent-area and linear-intercept methods, respectively, was applied as is common in interpretation of grain size from 2-D sections (Underwood, 1972; Hirth and Kohlstedt, 1995a; Hansen, 2011). For ease of comparison with other studies, we used the linear intercept value as the representative grain size when fitting mechanical results. The linear intercept method was used in each comparable study that we analyzed, except by Yabe et al. (2020); however they characterized the relationship between grain size measured by both methods, therefore, we consider that our measurements of grain size are larger by a factor of $4/\pi$ if using the equivalent-area circular diameter method or a factor of 1.5 if using the linear-intercept method than those of Yabe et al. (2020), when considering an identical microstructure.

Prior to deformation, the surfaces of each sample were polished, such that thermal grooving of the grain boundaries that occurs at high temperature could be observed by optical microscopy after quenching. This approach provides a secondary view of the fine-grained microstructure of our samples.

4.4.4 Data Analysis and Fitting of Flow Laws

Mechanical data and grain-size measurements were used to fit our results to Equations 1 and 2. Further, we included data from Karato et al. (1986), Hirth and Kohlstedt (1995a), Mei and Kohlstedt (2000), Faul and Jackson (2007), Hansen et al. (2011), Keefner et al. (2011), and Yabe et al. (2020) in a comparative analysis aimed at assessing flow-law fits across data sets. The generalized power law presented in Equation 1 has four fittable parameters (*A*, *n*, *p*, and *Q*). If three mechanisms are combined, Equation 2 has 11 fittable parameters (given that dislocation creep is considered to be strictly grain size independent). When fitting a combined flow law to a relatively limited data set, some simplifying assumptions are required. Thus, in general, we fixed the values of the grain size and stress exponents (*p* and *n*, respectively) based on published theoretical and experimental work. We used a combined grid-search and non-linear regression approach to fit flow laws to the data, in which a grid of *Q* values was defined, and corresponding *A* values were fit by regression given all possible combinations of *Q* values chosen from the predefined grid. This method is efficient because only a single parameter, the pre-exponential value (*A*), is fit by regression for each deformation mechanism, which is strongly covariant with the activation energy (*Q*) chosen for that mechanism. The best fit is taken as the grid point that minimizes the mean-squared error, with the error defined as

$$\chi = log(\dot{\varepsilon}_{measurment}) - log(\dot{\varepsilon}_{fit}). \quad (3)$$

The grid-search approach produces a result at each grid-point allowing easy comparison of fit quality given different combinations of parameters, highlighting the range of reasonable fits to the data; however, this approach is time consuming and can be limited by grid range and resolution. Thus, the grid range and resolution were expanded and refined until we obtained smooth variation in error between neighboring grid points and further grid expansion did not influence the results. More rigorous fitting methods, such as Markov chain Monte Carlo (Korenaga and Karato, 2008; Mullet et al., 2015; Jain et al., 2019) that deal with measurement uncertainty and parameter bias, are beyond the scope of our study, which is limited to the presentation of new experimental data and first-order comparison to similar datasets, in the context of published interpretations (flow laws). We, therefore, did not attempt to characterize the complex uncertainties of the fitted parameters. Instead, we use visual representation of the available data alongside a variety of fit results to demonstrate similarities and differences between experimental studies.

4.5 Results

4.5.1 Microstructural Characterization

Microstructural analyses demonstrated that deformed samples remained fine-grained despite hours to days at high-temperature conditions. EBSD maps of deformed samples revealed fine-grained microstructures with roughly log-normal grain-size distributions. EBSD maps and the corresponding grain-size distribution measured by equivalent circular area are presented in Figures 4 and 5. Differences in polishing quality between samples led to differing index rates; however, in all cases grain-size distributions were easily resolved. The grain sizes determined from mean equivalent-area circular diameter and mean linear-intercept methods are presented alongside mechanical data in Table 1. The relatively small variations in grain size among samples indicate grain growth was limited; however, grain size correlates with the maximum temperature of each constant-temperature, load-stepping deformation experiment. The grain size determined from the temperature-stepping experiment was slightly smaller than those of other deformed samples; however, this sample experienced a complicated temperature-time path that only included short duration deformation steps at the highest experimental temperatures. Grain sizes determined by the linear-intercept method were slightly larger than those determined by the mean equivalent-circular area method. The relationship between the two approaches is roughly consistent with the results of Yabe et al. (2020), which demonstrated that, if the stereographic sectioning correction factors are excluded, the two methods yield similar values. In the case of our analysis, we chose to apply the stereographic correction factors. For ease of comparison with other studies, we used linear-intercept values as the representative grain size when fitting mechanical data.

Subgrain boundaries, which were identified from EBSD maps, are highlighted in red in the examples presented in Figure 6. We defined the subgrain boundary threshold at 10° misorientation. While differences in indexing quality between EBSD maps made quantitative comparisons challenging, qualitatively subgrain boundaries were less common in the deformed samples than in the starting material. Subgrain boundaries in the starting material are likely inherited from powder pulverization or are formed from large contact stresses at the initial stages of powder compaction during hot-pressing. These subgrain boundaries appear to undergo recovery during the course of our high-temperature deformation experiments.

Images of thermally grooved sample surfaces likewise reveal the fine-grained microstructures of our samples. Reflected light micrographs of the thermally grooved sample

surfaces are presented in Figure 7. Analysis of thermal grooving at the sample surfaces yields a grain-size distribution that is comparable to that determined by EBSD mapping.

The porosity of the experimentally deformed samples was ~2-3% based on reflected light micrographs of polished sections. In the micrograph in Figure 8, pores appear as dark spots with the microscope focused on the plane of the sample surface and as bright reflections with the microscope focused below the surface. Bright reflections from below the sample surface confirm an increase in porosity during deformation at 1 atm, noting that surface features can be introduced during polishing. We, therefore, consider our reflected-light quantification of porosity to be an upper bound of total porosity. Thus, our determination of porosity reflects the sample properties and is not an artifact of surface preparation and imaging. Volume increases of <2% were measured with a micrometer; therefore, the magnitude of the porosity measured from optical micrographs is a robust measure of the total porosity of the deformed samples. Deformed samples were milky green and no longer transparent after the deformation experiment, which is characteristic of the pore growth described above (see Chapter 2).

4.5.2 Mechanical Data

The mechanical results for all experiments, which are reported in Table 1, were fit to the flow law presented in Equation 1 in several ways to understand the impact of different assumptions on our interpretation of the data. For example, in some cases we fixed some parameters or excluded data to see the impact on fits to the data. The resulting values for *A, n, p,* and *Q* are presented in Table 2.

The stress and strain rate recorded during load-stepping experiments are plotted in Figure 9a along with examples of flow laws obtained from by fitting the data to Equation 1. In Figure 9b, all of the mechanical results are presented in an Arrhenius plot, with values of strain rate normalized using the flow-law that was fit to the full dataset (with fixed *p*) and plot the corresponding flow law. This fit yields an activation energy of Q = 715 kJ/mol. The data correspond closely to a diffusion-creep flow law if n is fixed at 1; if the stress exponent is allowed to vary, n = 1.4. Since the data are slightly non-linear in stress (n = 1.4), it is likely that a secondary mechanism such as disGBS or dislocation creep contributes to deformation; however, our data do not span a large enough stress range to permit a strong constraint on the secondary mechanism. As a demonstration of this interpretation, the data were fit to a flow law with fixed diffusion creep + dislocation creep, which is plotted in Figure 9a. This approach is intended to illustrate that the experimental data can be interpreted as resulting from the

contribution of multiple deformation mechanisms. Furthermore, this result motivates combining our dataset with published data to explore similarities and differences with the goal of constraining a multi-mechanism flow law for olivine, such as presented in Equation 2.

4.6 Discussion

4.6.1 Background on Experimentally Determined Flow Laws for Olivine Aggregates

While previous experimental work has resulted in a consensus around the most important high-temperature deformation mechanisms, differences among experimental results have led to differing flow law parameters and conclusions about which mechanisms dominate in the Earth. We present a summary of flow laws resulting from similar experimental high-temperature deformation studies on dry olivine aggregates in Table 3, along with a brief description of the experimental designs. Where necessary, flow laws were modified to include stereographic correction of grain-size measurements, consistent with those applied in our analysis. For example, Yabe et al. (2020) did not apply a stereographic correction when fitting their flow law such that the flow law must be scaled to make direct comparisons with other studies. We compared our data to the flow laws presented by Karato et al. (1986), Hirth and Kohlstedt (2003), Faul and Jackson (2007) plus Faul et al. (2011), Hansen et al. (2011), and Yabe et al. (2020). Below we briefly describe the relevant details of these studies.

Karato et al. (1986) fit a high-temperature flow law to data from deformation experiments performed at constant displacement rate on hot-pressed San Carlos olivine aggregates of variable grain size at a confining pressure of 300 MPa and 1300°C in a gas-medium apparatus. Although their study included water-added, “wet” samples, aimed at understanding the role of water on viscosity, we only compared our data to results from experiments on nominally “dry” samples. The authors fit their data with the assumption that deformation resulted from a combination of diffusion creep and dislocation creep. Under dry conditions, they obtained a grain-size exponent of p = 2, indicating deformation rate-limited by volume diffusion. Because they carried out all of their experiments at the same temperature, the two activation energies were fixed in their flow-law fit. They chose an activation energy for dislocation creep of Q = 540 kJ/mol, a value equal to that determined from experiments on coarse-grained dunites and single crystals (Durham and Goetze,1977; Karato and Ogawa, 1982; Chopra and Paterson, 1981). They chose an activation energy for diffusion creep of Q = 290 kJ/mol, a value equal to the

activation energy for Mg-Fe lattice diffusion (Buening and Buseck, 1973). Finally, we also note that their experimental samples were jacketed in iron and were therefore at more reducing conditions than in our experiments and in other experiments that used nickel jackets. The Fe/FeO buffer is out of the stability field of San Carlos olivine, which contains a small amount of Ni and forms Fe/Ni-alloy "blebs" when annealed at pO_2 controlled by the Fe/FeO buffer (Boland and Duba, 1985; Karato et al., 1986)

Hirth and Kohlstedt (2003) based their flow laws on experimental data from a number of studies. They presented flow laws for wet and dry diffusion creep, wet and dry dislocation creep, and dry disGBS. Their analysis was largely focused on the results of experiments originally presented by Hirth and Kohlstedt (1995a) and (1995b) as well as Mei and Kohlstedt (2000a) and (2000b). These studies of high-temperature deformation of hot-pressed San Carlos olivine aggregates explored the role of added melt and water. In our analysis, we only included data from experiments on nominally melt-free, dry material. Evidence from the systematic variation of grain-size in fine-grained aggregates yielded a grain-size exponent of $p = 3$ in the diffusion-creep regime, indicating deformation rate-limited by grain-boundary diffusion. They analyzed the results of experiments performed across a broader range of conditions than considered by Karato et al. (1986) and, therefore, had better constraint on the grain-size dependence of diffusion creep. They attribute the grain-size exponent of $p = 2$ determined by Karato et al (1986) for diffusion creep to the influence of a component of dislocation creep. Following this result, we used $p = 3$ for diffusion creep in our analyses, consistent with the other studies described in this section. Further, Hirth and Kohlstedt (2003) obtained an activation energy for dry diffusion creep of $Q = 375$ kJ/mol. In their fit for activation energy, they include high-temperature data from experiments on San Carlos olivine aggregates (1200-1300°C) and somewhat lower temperature data from experiments on hot-pressed spinel lherzolite aggregates (1100-1150°C) from Kohlstedt and Zimmerman (1996). The data from deformation experiments on spinel lherzolite aggregates have a strong influence on the fitting results. We do not include them in our analyses because the solidus temperature is lower for these rocks than for San Carlos olivine aggregates, and the creep results are strongly influenced by melting above 1150°C. Additionally, Hirth and Kohlstedt (2003) fit data with a combined flow law including both diffusion and dislocation creep. They determined a stress exponent of dislocation creep of $n = 3.5$, identical to that determined from single crystal creep experiments (Durham and Goetze, 1977; Bai and Kohlstedt, 1991). We also used this value in our analyses. Hirth and Kohlstedt (2003) also discuss evidence for disGBS, presenting a flow law fit for dry disGBS based on the

experimental studies described above. They found strong evidence for a disGBS regime, but their flow laws predict that it is dominant only over a narrow range of conditions.

Hansen et al. (2011) followed with experiments on nominally dry, melt-free, hot-pressed San Carlos olivine aggregates, specifically designed to explore the role of grain size. Hansen et al. (2011) used EBSD data to determine grain size, rather than optical micrographs of etched sections employed in earlier studies. An analysis of a sample that was originally presented in Hirth and Kohlstedt (1995a) led to the assertion that the grain sizes from optical measurements should be reduced by a factor of 2 when compared to determinations from EBSD measurements. While this assertion is likely incorrect at large grain sizes, (above about 15 μm), we apply both the originally reported grain size and the factor of 2 modified grain size. when analyzing data from experimental studies in which the grain size was measured optically. Hansen et al. (2011) found strong evidence for deformation in the disGBS regime and fitted their data to a combined flow law that included diffusion creep and disGBS mechanisms. Because their experiments did not extend to low stress (<80 MPa), they included data modified from the those reported by Hirth and Kohlstedt (1995a) in their analysis to constrain the diffusion creep flow law. They adopted the activation energy for diffusion creep presented by Hirth and Kohlstedt (2003) instead of fitting for a new value. Their analysis greatly expanded the range of conditions for the disGBS field relative to that determined in the analysis of Hirth and Kohlstedt (2003).

Deformation of chemically controlled, synthetic olivine aggregates, prepared from sol-gel or oxide powders, have further contributed to our understanding of high-temperature deformation of olivine. Faul and Jackson (2007) and Faul et al. (2011) presented data from deformation experiments on high purity, iron-bearing olivine aggregates synthesized using the sol-gel method. Faul and Jackson (2007) determined that their samples deformed in the diffusion-creep regime are considerably stronger than San Carlos olivine aggregates. At higher stresses, creep experiments on sol-gel derived aggregates yielded a value of n = 7-8, which the authors attributed to power-law breakdown but described as dislocation creep (Faul et al., 2011).

The influence of chemical impurities on diffusion creep of olivine was investigated in an experimental study by Yabe et al. (2020), wherein undoped and chemically doped (with Ca and Al), iron-bearing olivine aggregates were deformed at relatively low stresses in a controlled-atmosphere, high-temperature apparatus at ambient pressure (1 atm). The experimental

conditions were similar to those in our experiments. The aggregates used in their study were prepared by vacuum-sintering nano-powders derived from high-purity oxides. The strengths of undoped samples were similar to those of sol-gel derived aggregates of Faul and Jackson (2007). However, aggregates doped with Ca and Al were weaker than undoped samples above 1150°C. Yabe et al. (2020) attributed this effect to a chemically induced change in grain boundary properties. The authors assert that chemical impurities led to “pre-melting” (disordering of grain boundaries) at high temperatures that can explain the discrepancies between experiments on San Carlos olivine aggregates and high-purity olivine aggregates. These authors fit their data using a flow law with a temperature-dependent activation energy to describe the pre-melting process based on the analysis of Yamauchi and Takei (2016). They parameterize the thermal activation of diffusion creep such that it scales with solidus temperature, allowing extrapolation of their results to olivine-rich rocks of different composition or water content (Yabe and Hiraga, 2020). Accounting for their temperature dependent parameterization of activation energy, at high temperatures their flow law predicts a high effective activation energy of $Q \approx 730$ kJ/mol.

4.6.2 Description of Flow Law from Yabe et al. (2020)

The flow law presented by Yabe et al. (2020) is distinctive in two ways. First, it is parameterized with a temperature-dependent activation energy that depends on the solidus temperature (T_s), aimed at describing a pre-melting (grain-boundary disordering) effect. Second, it includes two serial processes (deformation mechanisms), interface-controlled and diffusion-controlled creep. Diffusion creep models generally assume that grain boundaries are perfect sources and sinks for vacancies; however, diffusion creep can be limited by point defect reactions at grain boundaries. The authors identify a nonlinear ($n \approx 3$) deformation regime at their lowest stresses and finest grain sizes that they attribute to interface-controlled creep. Because diffusion creep and interface-controlled creep are serial processes the following form of the flow law is used:

$$\dot{\varepsilon}_{total} = (\dot{\varepsilon}_{diff}{}^{-1} + \dot{\varepsilon}_{int}{}^{-1})^{-1}. \quad (4)$$

Each deformation mechanism is described by a modified form of Equation 1 that includes an additional pre-melting term, such that

$$\dot{\varepsilon}_{diff} = A_{diff}\sigma^{1}d^{-3}\exp\left(-\frac{Q_{diff}}{\mathrm{RT}}\right); T < 0.92T_s \quad (5a)$$

$$\dot{\varepsilon}_{diff} = A_{diff}\sigma^{1}d^{-3}\exp\left(-\frac{Q_{diff}}{\mathrm{R}T}\right)\exp\left(-\frac{\Delta Q}{\mathrm{R}}\left(\frac{1}{T}-\frac{1}{0.92T_s}\right)\right);\ T \geq 0.92T_s \quad (5b)$$

and

$$\dot{\varepsilon}_{int} = A_{int}\sigma^{3}d^{-1}\exp\left(-\frac{Q_{int}}{\mathrm{R}T}\right);T < 0.84T_s \quad (6a)$$

$$\dot{\varepsilon}_{int} = A_{int}\sigma^{3}d^{-1}\exp\left(-\frac{Q_{int}}{\mathrm{R}T}\right)\exp\left(-\frac{\Delta Q}{\mathrm{R}}\left(\frac{1}{T}-\frac{1}{0.84T_s}\right)\right);\ T \geq 0.84T_s \quad (6b)$$

In the analyses that follow, we explore the implications of applying this flow law because it provides a good description of our dataset. We also draw comparisons to the other available datasets.

4.6.3 Comparison of Our Data to Published Flow Laws

In Figure 10, we compare our data from load-stepping experiments with the flow laws of Hirth and Kohlstedt (2003), Hansen et al. (2011), Faul and Jackson (2007) + Faul et al. (2011), and Yabe et al. (2020). Each flow law is plotted using the appropriate measure of grain size for comparison based on the methods used in the published study. All of the flow laws determined from deformation of San Carlos olivine aggregates under predict the strength observed in our experiments, especially at the lowest experimental temperatures. In contrast, our data correspond well with the flow law determined from high-purity sol-gel derived aggregates of Faul et al. (2007) at the lowest experimental temperature (1129°C); however, strength is over predicted at higher temperatures. Our data have the closest correspondence, across the full range of our experimental conditions, with the flow law of Yabe et al. (2020) determined from chemically doped, oxide-derived aggregates.

This agreement includes the relatively high activation energy determined from our data, which is comparable to that determined by Yabe et al. (2020). Their flow law incorporates a dependence on the solidus temperature of the sample material. The poorly constrained solidus temperature of hot-pressed San Carlos olivine likely depends on the quality and composition of hand-picked, inclusion-free single crystals as well as the impurities introduced during pulverization. In Figure 11, we applied a solidus temperature of 1225°C, a value equal to that for the samples with the highest dopant concentrations used by Yabe et al. (2020). Yabe and Hiraga (2020) assert that the solidus temperature of San Carlos olivine aggregates is equal to that for spinel lherzolite, parameterized by Hirschmann (2000), that is, 1121°C at 1 atm and 1160°C at a confining pressure of 300 MPa. However, this value was calculated for an average

peridotite composition, which is not a reasonable representation of our samples. The solidus temperature increases as the peridotite composition becomes increasingly depleted (Wasylenki et al., 2003). Further, based on SEM micrographs, we found no evidence of melt in our samples synthesized at 1250°C. Hirth and Kohlstedt (1995a) added minor, naturally sourced Bamble enstatite to their sample, which resulted in an aggregate with a significantly lower solidus temperature. SEM micrographs of our evacuated hot-pressed starting material do not resemble micrographs of nominally melt-free aggregates presented in their study (ref. Figure 9a in Hirth and Kohlstedt, 1995a), which have melt-filled triple junctions with a melt fraction of up to 1%. We therefore conclude that a solidus close to that of the most highly doped samples synthesized by Yabe et al. (2020) is appropriate for our sample material. Variation of solidus temperature, and its relationship to pre-melting, may explain some of the variation in mechanical properties between studies that use different preparation techniques for synthesizing samples.

4.6.4 Comparative Analyses of Available Experimental Data

We further present comparative analyses of high-temperature deformation data from experiments on nominally dry, melt-free, fine-grained olivine aggregates collected from a variety of studies. We calculated the error, χ, for both our data and the data collected from other studies relative to the flow laws discussed above. The results of this analysis are plotted in Figure 12 against the experimental strain rate. The symbols in each plot are colored by the grain size reported in the study from which they were taken. In this study, we used the grain size determined by the mean linear-intercept method because this method was employed by Hansen et al. (2011), a key comparison in our analysis. Additionally, in cases in which grain size was measured optically, a modified grain size is also included, following the assertion of Hansen et al. (2011) that grain size measured by EBSD is a factor of 2 smaller than that measured optically (we use open symbols to represent a modified grain size and closed symbols for the reported grain size). While this relationship may not hold at large grain sizes, it is useful for visualizing the effect of a factor of 2 error in grain size, which is likely the upper bound of the error associated with optical grain size measurements. The mean-squared error is minimized if data cluster along the dotted line ($\chi = 0$). We plotted the 10^{χ}, against strain rate, with 10^{χ} being the factor by which the experimental strain rate varies from that predicted by the flow used for each analysis. The grey band in each plot, which is centered about the mean error for each dataset, is the width of two standard deviations of the dataset, plotted to help guide the eye in

assessing how well the flow law fits the data. The red band is similarly plotted for calculations using a modified grain size.

In Figure 12a, the compiled data are plotted relative to the diffusion creep + disGBS flow law presented by Hansen et al. (2011). Our data plot below the dotted line, indicating that our samples are stronger than predicted by the Hansen et al. (2011) flow law especially at the lowest strain rates, that is, from experiments performed at the lowest temperatures. The flow law predicts strain rates up to one order of magnitude larger than those measured in our experiments. The data from Hansen et al. (2011) fit well to their flow law presented in the same study with a small range of scatter. Datasets from Hirth and Kohlstedt (1995a), Mei and Kohlstedt (2000a), and Karato et al. (1986), analyzed using the originally published grain-size determinations, are weaker than predicted by the flow law. However, decreasing the grain size by a factor of 2 brings the data into rough correspondence with the flow law of Hansen et al. (2011).

As illustrated in Figure 12b, the diffusion creep + dislocation creep flow law of Hirth and Kohlstedt (2003), which was determined from a combination of data from the studies by Hirth and Kohlstedt (1995a), Mei and Kohlstedt (2000a,b), and Karato et al. (1986), fits well to these datasets,. Scatter is large in the dataset presented by Karato et al. (1986), which we attribute to their use of constant strain-rate conditions, under which mechanical steady-state occurs over a larger strain interval than in constant-stress conditions due to feedbacks between the applied stress and the deformation-produced microstructure. The Hirth and Kohlstedt (2003) flow law fits the data from Hansen et al. (2011) only for samples with the largest grain sizes. For samples with the smallest grain sizes, the flow law under predicts the strain rate by over an order of magnitude. Hansen et al. (2011) concluded that this behavior reflected the discrepancy between optical and EBSD measurements of grain size. The Hirth and Kohlstedt (2003) flow law under predicts the strain rate measured in our experiments by up to two orders of magnitude, a difference that is unlikely to be associated with the method of grain size measurement. The systematic variation of our data relative to their flow law is mostly a reflection of the temperature dependence, as the activation energy used in the flow law is roughly a factor of two lower than the activation energy determined in our experiments.

As demonstrated in Figure 12c, the flow law produced by Karato et al. (1986) is a good fit to the data from the same study and is also a good fit to the data from Mei and Kohlstedt (2000a). However, data from Hirth and Kohlstedt (1995a) has a systematic variation in error

relative to strain rate, such that the data are not centered about the dotted line. Data from Hansen et al. (2011) plot fall below the dotted line and similarly show systematic variation in error in both strain rate and grain size. It bears repeating that Karato et al. (1986) did not experimentally vary temperature and thus fixed the activation energy by applying the assumptions described above. Systematic errors of other datasets relative to this flow law are likely attributable to these assumptions.

In Figure 12d, these datasets are plotted relative to the flow laws presented by Faul and Jackson (2007) + Faul et al. (2011), based on experimental deformation of high-purity sol-gel derived olivine aggregates. As mentioned previously, the diffusion creep component of this flow law is significantly stronger than that determined from the referenced studies on San Carlos olivine aggregates. In addition, at higher stresses deformation becomes highly non-linear with n = 7-8. This behavior is distinct from non-linear deformation reported for San Carlos olivine aggregates with $n \approx 3.5$. However, our dataset, which is nearly linear (confined to the diffusion creep regime), corresponds well to this flow law at the lowest strain rates (temperatures) tested, as discussed previously. At higher strain rates (temperatures), our data are about an order of magnitude weaker than predicted by the Faul and Jackson (2007) + Faul et al. (2011) flow law.

Finally, in Figures 12e-f, we compare the compiled data to the flow law of Yabe et al. (2020), which combines the serial diffusion and interface-controlled creep processes for Ca + Al doped synthetic samples. This flow law was determined on fine-grained samples at low stresses and does not contain a dislocation-mediated mechanism; therefore, it does not capture non-linear deformation that is typically observed at high stresses and coarse grain sizes. As presented in the previous section, this flow law fits our data well as indicated by the clustering of our data near the dotted line in the left panel of Figure 12e. However, this flow law does not fit any of the other datasets produced from experiments on San Carlos olivine aggregates. This result is attributed to significant contributions from non-linear dislocation-mediated mechanisms at higher stresses. Figure 12f demonstrates that it is possible to bring the flow law into agreement with the data from Hansen et al. (2011) by adding a disGBS component (using the activation energy, stress exponent and, grain size exponent for disGBS presented by Hansen et al., 2011). However, this combined flow law predicts slightly lower strengths than those measured in our experiments, perhaps indicating that disGBS is suppressed in our experiments relative to the experiments by Hansen et al. (2011). In the following section, we combine our experimental data with others and assess the fit of a multi-mechanism flow law aimed at

describing the data across large ranges of stress and grain size. Given the close correspondence of our data to the flow law produced by Yabe et al. (2020), we adopt their representation of the diffusion creep (+ interface-controlled creep) flow law, which we combine with disGBS and dislocation creep, as in Equation 2, to model data combined from this and other studies. We further explore the implications of this interpretation with deformation mechanism maps.

4.6.5 Multi-Mechanism Flow Law Fits to a Combined Dataset

Data compiled from our experiments as well as those from Hansen et al. (2011) and Keefner et al. (2011) were combined in an analysis aimed at fitting a multi-mechanism flow law to describe this data set across broad ranges of stress and grain size. The experiments from Keefner et al. (2011) were performed on a coarse grained dunite ($d \approx 900$ μm), which are expected to deform dominantly by dislocation creep with a negligible contribution from grain-size sensitive deformation mechanisms at the imposed experimental conditions. We used only data from experiments on samples jacketed in nickel, such that all of the data used in our analyses were obtained near the Ni/NiO oxygen fugacity buffer. The data from Hansen et al. (2011) were obtained from samples very similar to those used in the present study; however, their experiments were performed in a gas-medium apparatus at 300 MPa confining pressure, at higher average differential stresses, and over a wider range in grain size. These experiments are expected to be dominated by disGBS but may also have significant contributions from both diffusion and dislocation creep. Our data, collected exclusively from fine grained samples at relatively low differential stresses, yielded nearly linear stress versus strain rate results indicating that diffusion creep dominated. However, based on previous experimental work (Hansen et al., 2011), a significant contribution from disGBS may be expected. We excluded other experimental datasets on San Carlos olivine aggregates (for example, those included in Figure 12) because of potential inconsistencies between the fine grain sizes determined by optical measurements and those obtained from EBSD analyses. Below, we present the results of combining the constraints from these three datasets, which span a broad range of grain size and stress conditions, to fit a multi-mechanism flow law of the form expressed by Equation 2.

Given the large number of potentially fittable parameters and the relatively small number of data points (N = 184), we simplified the problem by fixing the stress exponents and grain size exponents of each mechanism a priori. We adopted the flow law of Yabe et al. (2020) to represent the diffusion creep component (Equations 4-6), including their values for the stress

and grain size exponents and the activation energy terms determined from their study. The close correspondence of our data to their flow law (Fig. 12e) justifies using it in this fitting analysis to explore the implications of interpreting data from naturally derived aggregates through the lens of the conclusions presented in their study. Because this flow law depends on the solidus temperature, which is not well constrained for our samples, we fit for this parameter assuming a consistent solidus temperature for all experiments. While conducting this analysis, we found that small changes in the solidus temperature used in the fitted flow law have little impact on the interpretation of the results of the overall analysis. The disGBS component is modeled using a fixed stress exponent of $n = 3$ and grain size exponent of $p = 1$, corresponding to the models described by Langdon (2006). These values are close to those determined by Hansen et al. (2011) of $n = 2.9$ and $p = 0.7$. Additionally, we fixed the stress exponent for dislocation creep to $n = 3.5$, following the conclusions of several studies (Durham and Goetze, 1977; Bai and Kohlstedt, 1991; Hirth and Kohlstedt, 2003; Keefner et al., 2011; Hirth and Kohlstedt, 2015). The pre-exponential terms (A_{gbs} and A_{dis}) were fit for disGBS and dislocation creep given a generously constrained grid of reasonable values for the activation energies (Q_{gbs} and Q_{dis}) and solidus temperatures (T_s). The combination of fit parameters that minimized the root mean square error (Equation 3) are presented in Table 4.

We repeated the analysis in several ways, excluding the data from individual studies and testing the impact of fixing either the solidus temperature (appearing in the diffusion creep flow law) or the activation energy for dislocation creep. For each case, we plotted the error for each data point versus strain rate (similar to the presentation of data in Figure 12). We also plotted the data normalized to a grain size of 5 μm at 1200°C on a stress – strain-rate plot and normalized to a stress of 100 MPa at 1200 °C on a grain-size – strain-rate plot. Ternary diagrams are presented showing the relative contribution of each term of the flow law to the total modeled strain rate for each of the compiled experimental data points. For each fit, a deformation mechanism map was constructed across the range of experimental temperatures. Experimental data collected at ±25°C from the temperature for which the map was calculated are plotted for comparison. This exercise is meant to illustrate the implications of different interpretations of the data using this fitting approach.

In Figure 13, we present the results of the fit that combines all three of the datasets (Row 1, Table 4). In this case, a multi-mechanism flow law results wherein the samples from the present study are expected to deform dominantly by diffusion creep and disGBS with both

mechanisms contributing significantly. Using this flow law, the data from Hansen et al. (2011) mostly fall in the disGBS or dislocation creep fields, depending on grain size, however, the flow law also indicates a significant contribution still resulting from diffusion creep. The data from Keefner et al. (2011) are dominated by dislocation creep with negligible contributions from grain-size sensitive mechanisms, as anticipated. Overall, this fit does a good job of describing the data with two notable exceptions. The strain rate data from the lowest temperature load-stepping experiment from our study (PT1285_2) are roughly a factor of 6 slower than the flow law predicts, and the data from each load-stepping experiment are predicted by the flow law to be more nonlinear in stress than measured. While the overall magnitude of strain rate agrees well with the flow law, this contradiction in apparent stress exponent between the fit and our data may be an indication that disGBS and/or dislocation creep is suppressed in our experiments. Deformation mechanism maps (DMMs) calculated across the range of experimental conditions are presented in Figure 14. These DMMs demonstrate that applying this multi-mechanism flow law predicts a disGBS field that is prominent at low temperatures and shrinks in favor of both diffusion and dislocation creep as temperature increases, due to the difference in activation energy of the different mechanisms. The data plotted on the mechanism map are consistent with the fields presented in the ternary diagram in Figure 13.

We repeated this analysis excluding the data from Keefner et al. (2011), which resulted in a fit that minimized error by not including a disGBS contribution (Row 2, Table 4). This result is unexpected since data from Hansen et al. (2011) are included in the fit, which, alone, are best described by a disGBS flow law. The fitting results and deformation mechanism maps are plotted in Figures 15 and 16. This fit under predicts the strain rate of the Keefner et al. (2011) data by up to a factor of 6. However, it does a reasonable job of fitting the Hansen et al. (2011) data. The discrepancy between the data from the present study and the flow law is the same as that noted for the first fitting case. The mechanism maps reflect the exclusion of the disGBS field that resulted from the fitting algorithm. Since the Keefner et al. (2011) data provide a strong constraint on the dislocation creep field, this interpretation of the data (wherein the disGBS field is excluded by the fit) is unfavorable.

Next, we repeated the analysis excluding the data from the present study (Row 3, Table 4) with the results presented in Figures 17 and 18. This procedure results in a fit with a lower solidus temperature; however, the basic features of the fit to the data are similar to those found in the first fitting case. The disGBS field is smaller in this case, because the lower solidus

temperature results in a larger contribution from diffusion creep. Even though we excluded our data altogether from the fit procedure, the resulting flow law is still in agreement with most of the data from our experiments, again with the exception of our data collected at the lowest experimental temperature. Despite excluding our data from the fitting procedure, the diffusion creep field, described by the flow law of Yabe et al. (2020), extends across the majority of the conditions tested in our experiments, as plotted in the deformation mechanism maps in Figure 18.

If we exclude the data from Hansen et al. (2011) from the analysis, predictably, the results yield a fit that minimizes error by eliminating the disGBS field. This result (Row 4, Table 4), which is plotted in Figures 19 and 20, is similar to the second fitting case in which the Keefner et al. (2011) data were excluded. In the present case, the dislocation creep flow law does a good job of fitting the Keefner et al. (2011) data from coarse-grained dunites; however, the Hansen et al. (2011) data are poorly fit with errors of up to about one order of magnitude at the finest grain sizes of their experiments. This result again leads to the conclusion that an interpretation that excludes the disGBS field is less favorable.

We also tested the effect of fixing the solidus temperature to 1225°C, the same temperature that was applied when assessing our data alone in previous sections (Row 5, Table 4). If all datasets are included in the fit, the multi-mechanism fit is very similar to that found in the third fitting case (Row 3, Table 4). The results are plotted in Figures 21 and 22, demonstrating a relatively narrow disGBS field.

Finally, we tested the effect of fitting the Hansen et al. (2011) data alone, fixing the activation energy of dislocation creep to that used in Hirth and Kohlstedt (2003) (Row 6, Table 4). This case resulted in an expanded disGBS field relative to the other fits presented above, as illustrated in Figures 23 and 24. This model over predicts the strain rates of our experiments and under predicts the strain rate of the Keefer et al. (2011) data. It also predicts a small but significant contribution (<5%) of disGBS to the deformation of coarse grained dunite in the Keefner et al. (2011) data, because it favors the disGBS field. The inconsistency of this fit with the two other datasets makes it a less favorable interpretation.

We presented the above analyses as a demonstration of possible interpretations of the data in an attempt to fit a flow law across a broad ranges of grain size and stress. Because of the consistency of our data with the flow law presented by Yabe et al. (2020), we chose to adopt this flow law in order to explore the implications for interpreting the data for naturally derived

olivine aggregates through the lens of the conclusions of Yabe et al. (2020). In contrast, in Figure 25 we present deformation mechanism maps at experimental temperatures using the flow laws originally presented in Hansen et al. (2011). These DMMs have a much more prominent disGBS field than results from the fits presented in this study.

We note that the fitting procedure does not address potential systematic errors or parameter biases. Further, we used fixed values for stress and grain size exponents to reduce the number of fittable parameters, which is helpful for fitting the relatively small dataset included in this study. Despite these drawbacks, the above analysis demonstrates that incorporating the flow law presented by Yabe et al. (2020) into a multi-mechanism flow law including disGBS and dislocation creep, produces a reasonable interpretation of the compiled data across a ranges of grain size and stress. However, looking in detail, it is clear that some of the data from the current study are in direct disagreement with a handful of data points from Hansen et al. (2011), which were collected at similar stress, grain size, and temperature conditions. This conclusion applies especially to the results from the lowest temperature experiments. The analysis above appears to suggest that the contradictions between the two datasets is due to a limited contribution of disGBS in our experiments relative to its role in those of Hansen et al. (2011). Our data include experiments at lower stress and temperature conditions than those performed in high-pressure experimental studies on hot-pressed San Carlos olivine aggregates, using an apparatus with superior resolution and the ability to conduct multi-day deformation experiments. More experiments at both high and low pressure are needed to resolve the contraction between datasets identified in this study. These experiments are challenging to perform due to the long times needed to make accurate strain rate measurements at relatively low stresses and temperatures.

4.6.6 Microstructural Differences Between this Study and Hansen et al. (2011)

Although the samples of Hansen et al. (2011) were also produced by a method of hot-pressing fine San Carlos olivine powders, significant differences exist in the microstructures of the samples used in their study relative to those synthesized for this study. First, we used an evacuated hot-pressing method with a 6 μm (volumetric mean) starting powder to synthesize our samples. This approach resulted in a sample with a ~5 μm grain size and <0.1% initial porosity. After high-temperature deformation experiments at 1-atm confining pressure, the final porosity was ~2% (Figure 8). Hansen et al. (2011) used a conventional hot-pressing method, starting with an olivine powder with a <3 μm grain size. This method of sample fabrication

resulted in an aggregate with ~1% porosity, which was maintained during deformation experiments at 300-MPa confining pressure. Hansen et al. (2011) used a series of annealing times to produce aggregates with different grain sizes. They identified structures associated with abnormal grain growth, especially in their finest grained samples. The grain boundaries of their deformed samples were serrated, and subgrain boundaries were prevalent. In their experiments, coarse grains, which presumably resulted from abnormal grain growth, also contain many subgrain boundaries (see Figure 2, Hansen et al., 2011). Both serrated grain boundaries and subgrain boundaries are microstructural features that are often attributed to dislocation activity during deformation. In contrast, the samples produced for our study have microstructures that are distinct in several ways. First, they have a narrower grain size distribution and are less affected by abnormal grain growth. Ter Heege et al. (2004) presented an analytical argument demonstrating that differences in grain size distribution can have a strong impact on the observed mechanical behavior of a sample, especially at conditions near the boundary between diffusion and dislocation-mediated creep. Additionally, in our samples, grain boundaries appear straight or slightly curved (not serrated). Further, the density of subgrain boundaries decreased, rather than increased, during deformation of our samples. In contrast with the samples from Hansen et al. (2011), the largest grains in the samples from our study tend to have straight boundaries that appear to be crystallographically controlled and do not have subgrain boundaries.

Differences in the microstructures between studies likely reflect differences both in the starting material and in the deformation conditions. While our experiments explored lower stresses (50-166 MPa, mean of 125 MPa), the experiments of Hansen et al. (2011) tended toward larger stresses (81-441 MPa, mean of 230 MPa). It is likely that differences in the microstructure are responsible for differences in the mechanical data. Specifically, we argue that dislocation formation was suppressed in our experiments relative to those of Hansen et al. (2011). It is possible that size effects associated with nucleating dislocations suppressed disGBS in our experiments (this point is discussed in detail in the Appendix). We do not have a precise interpretation of what led to the difference between these datasets, but we argue that it is related to complex feedbacks between the microstructure and deformation conditions, consistent with the obvious differences in microstructures between the two studies.

4.6.7 Extrapolation of a Multi-Mechanism Flow Law to Natural Conditions

To further explore the implications of our analysis, we calculated deformation mechanism maps extrapolated to geological conditions using a multi-mechanism flow law obtained by fitting data from this study, Hansen et al. (2011), and Keefner et al. (2011) (Row 1, Table 4) and compare those to maps produced using the flow laws presented by Hansen et al. (2011). These DMMs are extrapolated to the same conditions used in the deformation mechanism maps that are presented in their original paper (see Figure 8, Hansen et al., 2011) and are plotted in Figure 26. Different deformation mechanisms are expected to dominate at extrapolated natural conditions if the data are interpreted using the model presented in this study versus that given by Hansen et al. (2011). Based on our model, at low temperatures, disGBS is expected to dominate over diffusion creep over a broad range of conditions, while diffusion creep is expected to dominate over disGBS at very high temperatures, which is due to the high activation energy for diffusion creep relative to that for disGBS. In contrast, the maps produced by Hansen et al. (2011) indicate that both the diffusion creep and disGBS fields are prominent across the range of temperatures plotted.

While we argue that the multi-mechanism fits presented in this study do a better job of explaining the data across a range of stress and grain size conditions, we caution that other processes may play a critical role during deformation in the Earth's mantle. For instance, in Figure 26, data are extrapolated to 1400°C, which is likely above the solidus temperature. The samples analyzed in this study were nominally melt-free. If melting occurs, the role of melt in promoting, for example, "short-circuit" diffusion should be considered (Cooper and Kohlstedt, 1986; Takei and Holtzman, 2009). Melt is also likely to have a strong influence on the disGBS regime. Additionally, dunite was used as the starting material in all of these experiments, which is dominantly composed of olivine with a very small fraction of secondary phases. However, Earth's mantle has a peridotite composition that includes substantial fractions of pyroxene and clinopyroxene. Secondary phases may play a key role in pinning the grain size, resulting in enhanced grain size-sensitive creep mechanisms (Tasaka et al., 2020), allowing chemically coupled diffusion (Sundberg and Cooper, 2008) or activating a phase-boundary creep mechanism (Zhao et al., 2019). Likewise, the experiments of Yabe et al. (2020) indicate that differences in trace element composition also plays an important role in modifying deformation in Earth. Therefore, it is possible that deformation mechanism maps constructed from data

obtain from experiments on nominally melt-free dunites should be consider as a limiting case of the deformation mechanisms that are dominant in Earth's mantle.

4.6.8 Discussion of the Activation Energy Measured in this Study

While unresolved questions remain regarding the interpretation of our experimental results, our experiments provide strong constraints on diffusion creep of olivine. The consistency of our results with those of Yabe et al. (2020) lend support to the pre-melting hypothesis presented in their study. This point is specifically highlighted by the relatively high value of the effective activation energy that we determined. High activation energies for deformation in the diffusion creep regime have been measured in other olivine-rich rocks. Kohlstedt and Zimmerman (2004) present data demonstrating an increased temperature dependence for deformation of spinel lherzolite at temperatures above the solidus relative to deformation below the solidus, which they argue is due to an increasing melt fraction with temperature. Similarly, Bunton (2001) measured a high activation energy for olivine-rich aggregates prepared from pulverized Twin Sisters dunite deformed in the diffusion creep regime. In both cases, the samples were considerably weaker than predicted by our data obtained on aggregates of hand-picked San Carlos olivine. In these cases, it could be interpreted that the high measured activation energy resulted from the combination of both thermally activated diffusion along with a contribution from an increasing melt fraction with increasing at temperatures above the sample solidus. We did not observe melt in our samples using standard SEM imaging and therefore rule out this effect in our study, which would require significant melt fraction (Kohlstedt and Zimmerman, 2004). We propose that the high apparent activation energy that we measured is related to the same processes active in the experiments performed by Yabe et al. (2020), in which a high activation energy was measured during deformation at temperatures below the conventional solidus. It is possible that this behavior is related to a "pre-melting" process, wherein the structure of the grain boundaries changes near the solidus temperature. Because all our data were collected at temperatures near this transition, we observed a high effective activation energy, however, it is possible that at temperatures below those tested there is a transition to a lower effective activation energy, similar to the temperature dependence observed by Yabe et al. (2020).

4.7 Conclusions

We present new high-temperature deformation data on evacuated hot-pressed San Carlos olivine aggregates. Samples were deformed in a deadweight creep apparatus, which provides exceptional resolution in stress and strain rate. The results of our experiments demonstrated a nearly linear relationship between strain rate and stress, indicating deformation dominated by diffusion creep. These data were fit well using the functional forms usually applied to deformation data with little scatter. Additionally, our creep results were remarkably consistent with the results of Yabe et al. (2020). However, our data are inconsistent with previously published flow laws generated from other high-temperature deformation experiments on conventionally hot-pressed San Carlos olivine aggregates, which predicted non-linear deformation associated with disGBS (Hansen et al., 2011). We demonstrated the differences between the available experimental data and the interpretations of the original studies that present them (Figure 12). Finally, we examined fits of multi-mechanism flow laws to a dataset compiled from several studies, applying the flow law originally presented by Yabe et al. (2020). Despite refitting the data, unresolved inconsistencies remain between the data from this study and those produced by Hansen et al. (2011). We speculate that differences in the microstructure of the samples used in the different studies are responsible. The fine-grain size and relatively low stresses of our experiments may lead to limited disGBS due to the barrier of nucleating dislocation loops at small length scales (i.e., small grain sizes). This study expands the range of deformation conditions explored in experiments on olivine samples and produces new, strong constraints on the mechanics of diffusion creep. The consistency of our results to those of Yabe et al. (2020), based on deformation of Ca and Al doped, oxide-derived olivine aggregates, lends support to the pre-melting hypothesis presented in their study.

4.8 Appendix: Dislocation Length Scale Effects at Fine Grain Sizes

Dislocation mediated deformation mechanisms are likely impacted by size effects, if the grain size is similar to the length-scale of the long-range elastic stresses that arise from the presence of dislocations. Dislocations must be continuously nucleated and annihilated for these mechanisms to be active. A Frank-Read source is a classical model for dislocation nucleation wherein a dislocation segment, pinned between two points, becomes progressively bowed under an increasing applied stress until the bowing becomes so severe that the segment

nucleates as a loop. The critical shear stress (τ) necessary to nucleate a dislocation using this mechanism is

$$\tau = \frac{2Gb}{l}\ , \qquad \text{(A1)}$$

where *G* is the shear modulus, *b* is the length of the Burgers vector, and *l* is the length of the pinned segment (Frank and Read, 1950; Sundberg and Cooper, 2008). The maximum length of a pinned segment is set by the grain size. For olivine, this constraint is further impacted by the limited number of available dislocation slip systems. For this reason, it is necessary to consider the resolved shear stress resulting from the orientation of the dislocation slip systems relative to the applied shear stress, such that

$$\sigma = \frac{2Gb}{lS} \qquad \text{(A2)}$$

where σ is the applied differential stress and *S* is the Schmid factor. For an aggregate with a random distribution of grain orientations, we calculated the average number of slip systems with resolved shear stresses greater than the critical resolved shear stresses for ranges of grain size and applied stress, allowing four possible slip systems in olivine: (010)[100], (001)[100], (100)[001], and (010)[001]. The average number of critically stresses dislocation slip systems (AvSS) are plotted in Figure 27, including contours at AvSS = 0, 1, and 2. The experimental data from this study and Hansen et al. (2011) are plotted. The data from this study fall near the AvSS = 2 contour, while the data from Hansen et al. (2011) are generally at conditions where AvSS > 2. In this plot, we also include the subgrain-size piezometers of Goddard et al. (2020) and Karato et al. (1980), since subgrains require dislocations to form. It is interesting to note the correspondence of the subgrain-size piezometer of Goddard et al. (2020) to the AvSS = 2 contour, indicating that these same size effects may determine the length scales at which subgrains are stable.

The role of this size effect is further impacted by the fact that real samples have a range of grain sizes. We applied this same analysis using the EBSD map generated from our starting sample material. We plotted the number of critically stressed dislocation creep slip systems for each grain across a range of applied stresses. Maps representing this analysis are presented in Figure 28, demonstrating that larger grains are critically stressed at lower stresses than smaller grains. At stresses <200 MPa, many grains have one or fewer critically stressed dislocation slip systems, which is expected to impact dislocation mediated deformation processes. In Figure 29 (top row), the average number of critically stressed slip systems (by grain and by areal fraction)

are plotted against applied stress. In the middle and bottom rows of Figure A3, the fraction (by grain and area) with zero and one critically resolved slip systems are plotted against resolved stress. These plots demonstrate that length-scale effects related to dislocation nucleation in the stress range of our experiments should be expected. These plots further demonstrate that differences in grain size distribution may have important and unexpected implications for mechanical behavior.

To take this speculative discussion to completion, we plot deformation mechanism maps to explore the effect of limiting dislocation-mediated deformation processes (disGBS and dislocation creep) to stresses for which AvSS > 2. The results are plotted for both experimental and extrapolated conditions in Figure 30. In Figure 31, the data are plotted normalized using both with and without the size constraint described in this Section at a stress of 100 MPa. It should be noted that the sharp transitions illustrated in these figures would likely be blunted in reality due to grain size distribution effects and the large range of stresses over which available dislocation slip systems become critically stressed (the threshold for dislocation mediated mechanisms may not be at AvSS = 2, as speculated here). It is possible that these effects are important in explaining why disGBS appears to be suppressed in our experiments relative to those of Hansen et al. (2011), some of which were conducted on samples with a similar nominal grain sizes but significantly different microstructures.

4.9 References

Bachmann, F., Hielscher, R., & Schaeben, H. (2010). Texture Analysis with MTEX – Free and Open Source Software Toolbox. Solid State Phenomena, 160, 63–68.

Bai, Q., Mackwell, S. J., & Kohlstedt, D. L. (1991). High-temperature creep of olivine single crystals, 1, mechanical results for buffered samples: J Geophys Res V96, NB2, Feb 1991, P2441–2463. International Journal of Rock Mechanics and Mining Sciences and Geomechanics Abstracts, 28(6), A343–A343.

Boland, J. N., & Duba, A. (1985). Defect mechanisms for the solid state reduction of olivine. Point defects in minerals, 31, 211-225.

Buening, D. K., & Buseck, P. R. (1973). Fe-Mg lattice diffusion in olivine. Journal of Geophysical Research, 78(29), 6852-6862.

Bunton, J. H., (2001). The Impact of Grain Size on the Shear Creep and Attenuation Behavior of

Polycrystalline Olivine. M.S. Thesis, University of Wisconsin - Madison.

Chopra, P. N., & Paterson, A. M. (1981). The experimental deformation of dunite. Tectonophysics, 78(1-4), 453-473.

Cooper, R. F., & Kohlstedt, D. L. (1986). Rheology and structure of olivine-basalt partial melts. Journal of Geophysical Research: Solid Earth, 91(B9), 9315-9323.

Coble, R. L. (1963). A Model for Boundary Diffusion Controlled Creep in Polycrystalline Materials. Journal of Applied Physics, 34, 1679–1682.

Durham, W.B. & Goetze, C. (1977a)

Durham, W. B., Goetze, C., & Blake, B. (1977). Plastic flow of oriented single crystals of olivine: 2. Observations and interpretations of the dislocation structures. Journal of Geophysical Research, 82(36), 5755-5770.

Faul, U. H., Fitz Gerald, J. D., Farla, R. J. M., Ahlefeldt, R., & Jackson, I. (2011). Dislocation creep of fine-grained olivine. Journal of Geophysical Research: Solid Earth, 116(1), 1–12.

Faul, U. H., & Jackson, I. (2007). Diffusion creep of dry, melt-free olivine. Journal of Geophysical Research: Solid Earth, 112(4), 1–14.

Frank, F. C., & Read Jr, W. T. (1950). Multiplication processes for slow moving dislocations. Physical Review, 79(4), 722.

Goddard, R. M., Hansen, L. N., Wallis, D., Stipp, M., Holyoke III, C. W., Kumamoto, K. M., & Kohlstedt, D. L. (2020). A subgrain-size piezometer calibrated for EBSD. Geophysical Research Letters, 47(23), e2020GL090056.

Hansen, L. N., Zimmerman, M. E., & Kohlstedt, D. L. (2011). Grain boundary sliding in San Carlos olivine: Flow law parameters and crystallographic-preferred orientation. Journal of Geophysical Research: Solid Earth, 116(8), 1–16.

Hansen, L. N., Zimmerman, M. E., & Kohlstedt, D. L. (2012). The influence of microstructure on deformation of olivine in the grain-boundary sliding regime. Journal of Geophysical Research: Solid Earth, 117(9), 1–17.

Hansen, L. N., Kumamoto, K. M., Thom, C. A., Wallis, D., Durham, W. B., Goldsby, D. L., ... & Kohlstedt, D. L. (2019). Low‐temperature plasticity in olivine: Grain size, strain hardening, and the strength of the lithosphere. Journal of Geophysical Research: Solid Earth, 124(6), 5427-5449.

Herring, C. (1950). Diffusional Viscosity of a Polycrystalline Solid. Journal of Applied Physics,

21, 437–445.

Hirth, G., & Kohlstedt, D. L. (1995a). Experimental constraints on the dynamics of the partially molten upper mantle : Deformation in the diffusion creep regime. Geology, 100(B2), 1981–2001.

Hirth, G., & Kohlstedt, D. L. (1995b). Experimental constraints on the dynamics of the partially molten upper mantle: 2. Deformation in the dislocation creep regime. Journal of Geophysical Research: Solid Earth, 100(B8), 15441-15449.

Hirth, G., & Kohlstedt, D. L. (2003). Rheology of the Upper Mantle and Mantle Wedge: A View from the Experimentalists. Geophysical Monograph: Inside the Subduction Factory, 138, 83–105.

Hirth, G., & Kohlstedt, D. L. (2015). The stress dependence of olivine creep rate: Implications for extrapolation of lab data and interpretation of recrystallized grain size. Earth and Planetary Science Letters, 418, 20–26.

Hirschmann, M. M. (2000). Mantle solidus: Experimental constraints and the effects of peridotite composition. Geochemistry, Geophysics, Geosystems, 1(10).

Jain, C., Korenaga, J., & Karato, S. I. (2019). Global analysis of experimental data on the rheology of olivine aggregates. Journal of Geophysical Research: Solid Earth, 124(1), 310-334.

Karato, S. I., & Ogawa, M. (1982). High-pressure recovery of olivine: implications for creep mechanisms and creep activation volume. Physics of the Earth and Planetary Interiors, 28(2), 102-117.

Karato, S. I., Paterson, M. S., & FitzGerald, J. D. (1986). Rheology of synthetic olivine aggregates: Influence of grain size and water. Journal of Geophysical Research: Solid Earth, 91(B8), 8151-8176.

Karato, S. I., Toriumi, M., & Fujii, T. (1980). Dynamic recrystallization of olivine single crystals during high-temperature creep. Geophysical Research Letters, 7(9), 649-652.

Karato, S. I., & Wu, P. (1993). Rheology of the upper mantle: A synthesis. Science, 260(5109), 771-778.

Keefner, J. W., Mackwell, S. J., Kohlstedt, D. L., & Heidelbach, F. (2011). Dependence of dislocation creep of dunite on oxygen fugacity: Implications for viscosity variations in Earth's mantle. Journal of Geophysical Research: Solid Earth, 116(B5).

Kohlstedt, D. L., & Zimmerman, M. E. (1996). Rheology of partially molten mantle rocks. Annual

Review of Earth and Planetary Sciences, 24, 41-62.

Zimmerman, M. E., & Kohlstedt, D. L. (2004). Rheological properties of partially molten lherzolite. Journal of Petrology, 45(2), 275-298.

Korenaga, J., & Karato, S. I. (2008). A new analysis of experimental data on olivine rheology. Journal of Geophysical Research: Solid Earth, 113(B2).Langdon, T. G. (2006). Grain boundary sliding revisited : Developments in sliding over four decades. J. Mater. Sci., 41, 597–609.

Mackwell, S.J., Kohlstedt, D.L., Durham, W.B. (1990) High-resolution creep apparatus, in The Brittle-Ductile Transition in Rocks, The Heard Volume, eds. A.G. Duba, W.B. Durham, J.W. Handin, W.F. Wang, American Geophysical Union, Washington, 235-238,

Mei, S., & Kohlstedt, D. L. (2000a). Influence of water on plastic deformation of olivine aggregates: 1. Diffusion creep regime. Journal of Geophysical Research: Solid Earth, 105(B9), 21457-21469.

Mei, S., & Kohlstedt, D. L. (2000b). Influence of water on plastic deformation of olivine aggregates: 2. Dislocation creep regime. Journal of Geophysical Research: Solid Earth, 105(B9), 21471-21481.

Mullet, B. G., Korenaga, J., & Karato, S. I. (2015). Markov chain Monte Carlo inversion for the rheology of olivine single crystals. Journal of Geophysical Research: Solid Earth, 120(5), 3142-3172.

Prior, D. J., Mariani, E., & Wheeler, J. (2009). EBSD in the earth sciences: applications, common practice, and challenges. In Electron backscatter diffraction in materials science (pp. 345-360). Springer, Boston, MA.

Schwenn, M. B., & Goetze, C. (1978). Creep of olivine during hot-pressing. Tectonophysics, 48(1-2), 41-60.

Sundberg, M., & Cooper, R. F. (2008). Crystallographic preferred orientation produced by diffusional creep of harzburgite: Effects of chemical interactions among phases during plastic flow. Journal of Geophysical Research: Solid Earth, 113(B12).

Tasaka, M., Zimmerman, M. E., & Kohlstedt, D. L. (2020). Rheological weakening of olivine+ orthopyroxene aggregates due to phase mixing: Effects of orthopyroxene volume fraction. Journal of Geophysical Research: Solid Earth, 125(9), e2020JB019888.

Ter Heege, J. H., De Bresser, J. H. P., & Spiers, C. J. (2004). Composite flow laws for crystalline materials with log-normally distributed grain size: theory and application to olivine. Journal of Structural Geology, 26(9), 1693-1705.

Underwood, E. E. (1972). The Mathematical Foundations of Quantitative Stereology. In Stereology and Quantitative Metallography (pp. 3–38).

Yabe, K., Sueyoshi, K., & Hiraga, T. (2020). Grain-boundary diffusion creep of olivine: 1. Experiments at 1 atm. Journal of Geophysical Research: Solid Earth, 125(8), e2020JB019415.

Yabe, K. and Hiraga, T. (2020). Grain-Boundary Diffusion Creep of Olivine: 2. Solidus Effects and Consequences for the Viscosity of the Oceanic Upper Mantle. Journal of Geophysical Research: Solid Earth, 125(8), e2020JB019416

Yamauchi, H., & Takei, Y. (2016). Polycrystal anelasticity at near-solidus temperatures. Journal of Geophysical Research: Solid Earth, 121(11), 7790-7820.

Wasylenki, L. E., Baker, M. B., Kent, A. J., & Stolper, E. M. (2003). Near-solidus melting of the shallow upper mantle: partial melting experiments on depleted peridotite. Journal of Petrology, 44(7), 1163-1191.

Weertman, J. (1970). The Creep Strength of the Earth ' s Mantle. Reviews of Geophysics and Space Physics, 8(1), 145–168.

Zhao, N., Hirth, G., Cooper, R. F., Kruckenberg, S. C., & Cukjati, J. (2019). Low viscosity of mantle rocks linked to phase boundary sliding. Earth and Planetary Science Letters, 517, 83-94.

4.10 Tables

Table 4-1: Experimental data

Table 1: Experimental data

$\boldsymbol{Experiment\ \#}$	$\boldsymbol{T}$ $(°\boldsymbol{C})$	$\boldsymbol{\sigma}$ $(\boldsymbol{MPa})$	$\boldsymbol{\dot{\varepsilon}}$ $(\boldsymbol{10^{-6}s^{-1}})$	$\boldsymbol{\varepsilon}$ (%)	$\boldsymbol{d}$ (EA) $(\boldsymbol{\mu m})$	$\boldsymbol{d}$ (LI) $(\boldsymbol{\mu m})$	$\boldsymbol{n}$	**M-index**
PT1285	-	-	-	-	3.9	4.4	-	0.021
PT1285_1	1179	100	1.06	0.68	4.2	5.3	1.0	0.005
		119	1.13	0.86				
		139	1.38	0.71				
		158	1.58	0.76				
		98	0.91	0.08				
PT1285_2	1131	117	0.133	1	4.1	5.1	1.6	0.014
		135	0.174	0.92				
		154	0.209	1.15				
		95	0.0972	0.61				
		113	0.119	0.8				
PT1285_3	1229	126	5.15	0.83	4.6	6.1	1.4	0.019
		147	6.61	1.02				
		166	8.52	1.09				
		102	4.13	0.98				
		50	1.7	1.01				
		80	2.93	1.04				
		99	3.88	1.17				
		118	5.21	0.73				
		137	6.91	0.66				
		156	9.34	0.65				
PT1285_4	1229	140	9.35	1.36	4.0	4.7	-	0.013

1204	138	5.16	1.64
1181	136	2.18	1.41
1157	134	0.994	1.43
1133	133	0.363	1.7
1156	131	1.15	0.87
1181	130	2.32	1.03
1204	128	6.25	1.35

Table 4-2: Power law fits to experimental data

Table 2: Power law fits to experimental data

Fit Description	$log_{10}(\boldsymbol{A})$ $log_{10}(\mathrm{MPa}^{-\boldsymbol{n}}\mu\mathrm{m}^{m})$	$\boldsymbol{n}$	$\boldsymbol{p}$	$\boldsymbol{Q}$
(1) Full data set Nothing fixed	19.80	1.4	3.4	728
(2) Full data set, *p* fixed	19.04	1.4	3	715
(3) Full data set, *n* and *p* fixed	19.66	1	3	709
(4) Full data set grain size adjusted to 5 µm, *p* fixed	19.45	1.7	3	623
(5) All load stepping experiments *p* fixed	20.13	1.4	3	746
(6) All load stepping experiments *n* and *p* fixed	20.74	1	3	740
(7) Temperature stepping experiment *n* and *p* fixed	14.67	1.4	3	592
(8) Full data set, diffusion+dislocation creep flow law *n* and *p* fixed,	19.97	1	3	719
Q for dislocation creep fixed (HK2003)	4.87	3.5	0	530

Table 4-3: Published flow laws

Table 3: Published flow laws

Flow Law Description	Experimental Basis	$log_{10}(A)$ $log_{10}(\mathrm{MPa}^{-n}\mu\mathrm{m}^{m})$	n	p	Q (kJ/mol)
Hirth and Kohlstedt (2003)	Compilation of various studies, largely hot-pressed San Carlos and natural dunites	9.18	1	3	375
parralel diffusion + dislocation creep		5.04	3.5	0	530
Hansen et al., (2011)	Hot-pressed San Carlos, gas apparatus, 300 MPa P_c, constant stress	7.6	1	3	375
parallel diffusion creep + disGBS		4.8	2.9	0.7	445
Faul and Jackson (2007) and Faul et al (2011)	Sol-gel derived olivine, gas apparatus 300 MPa P_c, constant stress	10.3	1.37	3	484
parallel diffusion creep + nonlinear creep		-0.52	8.2	0	682
Karato et al. (1986)	Hot-pressed San Carlos, gas apparatus 300 MPa P_c, constant strain rate	-1.11	1	2	290
parallel diffusion + dislocation creep		5.38	3.5	0	540
Yabe et al. (2020)	Oxide derived olivine ±Ca and Al dopants, 1 atm P_c, constant stress	10.58(LI)			470
		10.36(EA)			ΔQ=470
serial diffusion + interface creep		12.15(LI)	1	3	610
with premelting term		12.30(EA)	3	1	ΔQ=230

Table 4-4: Multi-mechanism fits to data

Table 4: Multi-mechanism fits to data

Datasets Used in Fit	**deformation mechanism**	$log_{10}(\boldsymbol{A})$ $log_{10}(\mathrm{MPa}^{-\boldsymbol{n}}\mu\mathrm{m}^{m})$	$\boldsymbol{n}$	$\boldsymbol{p}$	$\boldsymbol{Q}$	$\boldsymbol{T_s}$ (℃)
(1) This study, Hansen et al. (2011), Keefner et al. (2011)	diffusion creep	10.58	1	3	470; ΔQ=230	
	disGBS	2.79	3	1	400	
	dislocation creep	2.45	3.5	0	450	1265
(2) This study, Hansen et al. (2011)	diffusion creep	10.58	1	3	470; ΔQ=230	
	disGBS	-	-	-	-	
	dislocation creep	0.63	3.5	0	390	1250
(3) Hansen et al. (2011), Keefner et al. (2011	diffusion creep	10.58	1	3	470; ΔQ=230	
	disGBS	1.09	3	1	350	
	dislocation creep	2.44	3.5	0	450	1210
(4) This study Keefner et al. (2011	diffusion creep	10.58	1	3	470; ΔQ=230	
	disGBS	-	-	-	-	
	dislocation creep	2.79	3.5	0	460	1240
(5) This study, Hansen et al. (2011), Keefner et al. (2011) Ts=1225^{o}C (fixed)	diffusion creep	10.58	1	3	470; ΔQ=230	
	disGBS	1.60	3	1	370	
	dislocation creep	2.11	3.5	0	440	1225
(6) Hansen et al. (2011) Qdis = 530 (fixed)	diffusion creep	10.58	1	3	470; ΔQ=230	
	disGBS	2.31	3	1	380	
	dislocation creep	5.09	3.5	0	530	1240

4.11 Figures

Figure 4-1: Images of starting material

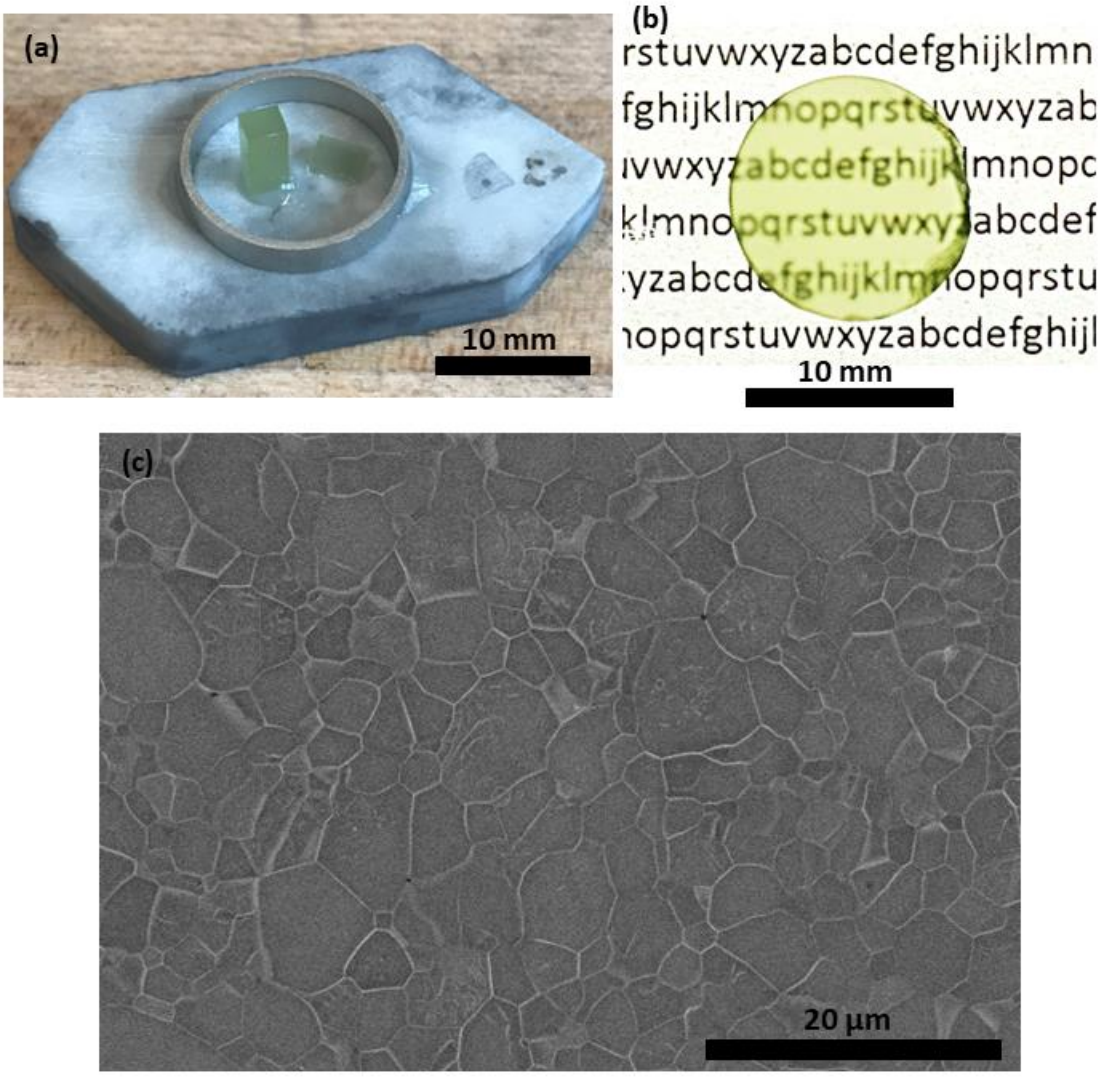

Figure 1: (a) Photograph of a rectangular parallelepiped sample prepared for deformation next to a chip of sample material, sitting on an alumina platen. A Ni ring surrounds the sample to help buffer the pO_2. (b) Photograph of a 1 mm thick slice of evacuated hot-pressed starting material on text, illuminated by transmitted light. (c) Backscattered SEM image of an oxidation decorated portion of evacuated hot-pressed starting material.

Figure 4-2: EBSD map of starting material

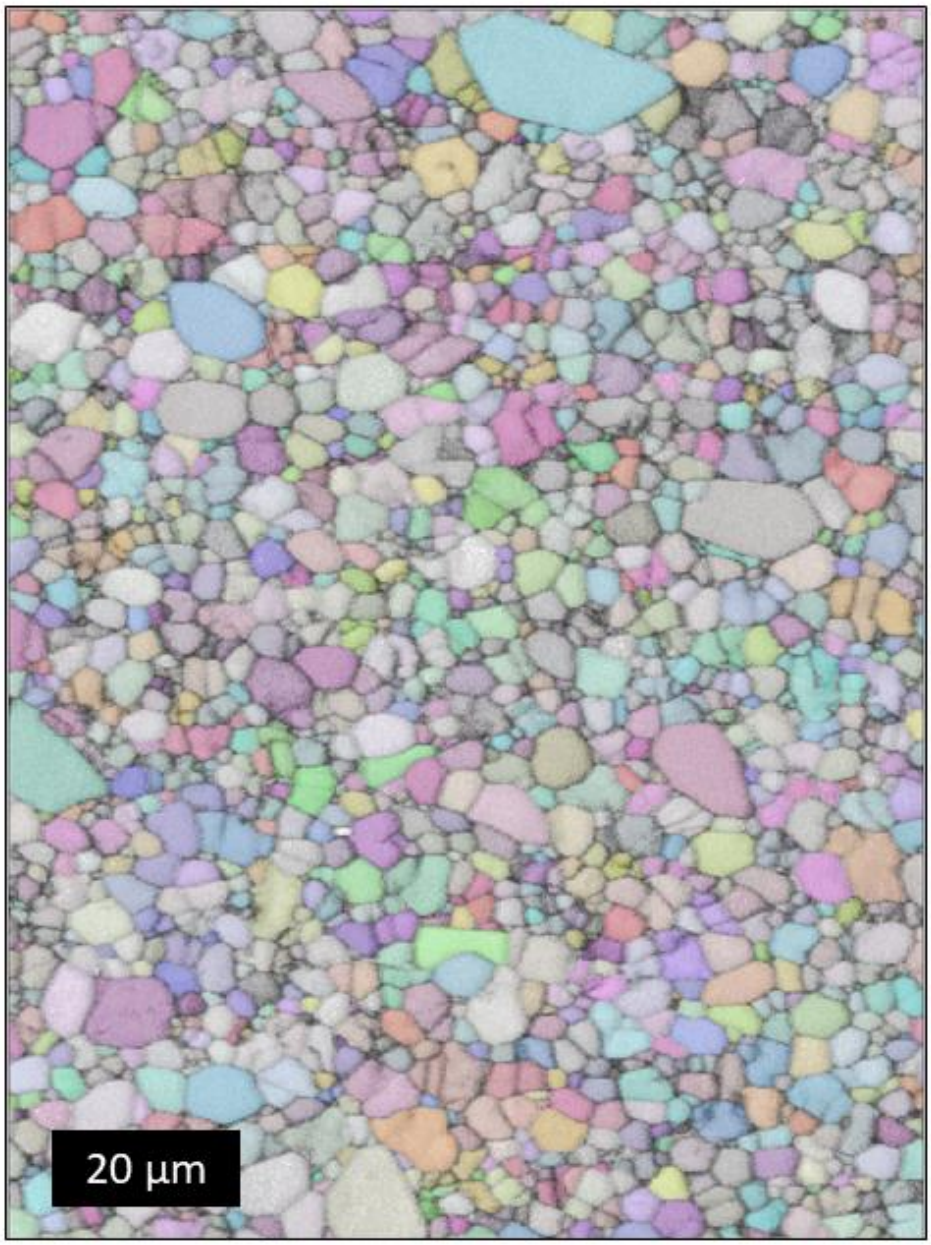

Figure 2: EBSD map of evacuated hot-pressed San Carlos olivine starting material.

Figure 4-3: Example creep curve

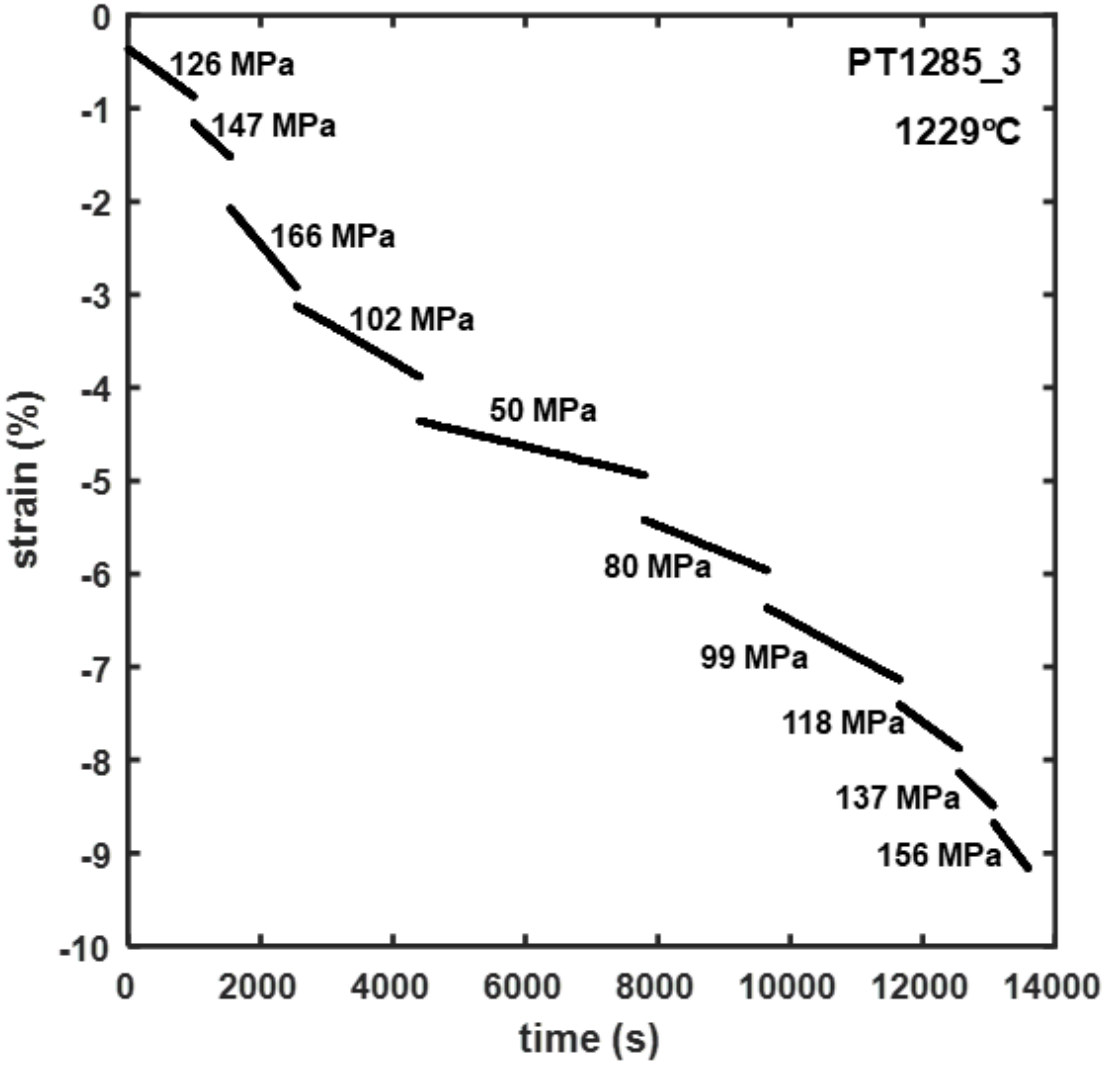

Figure 3: Example creep curve from experiment PT1285_3, used to generate estimates of strain rate. Transients between load steps have been removed for clarity.

Figure 4-4: EBSD maps of deformed specemens

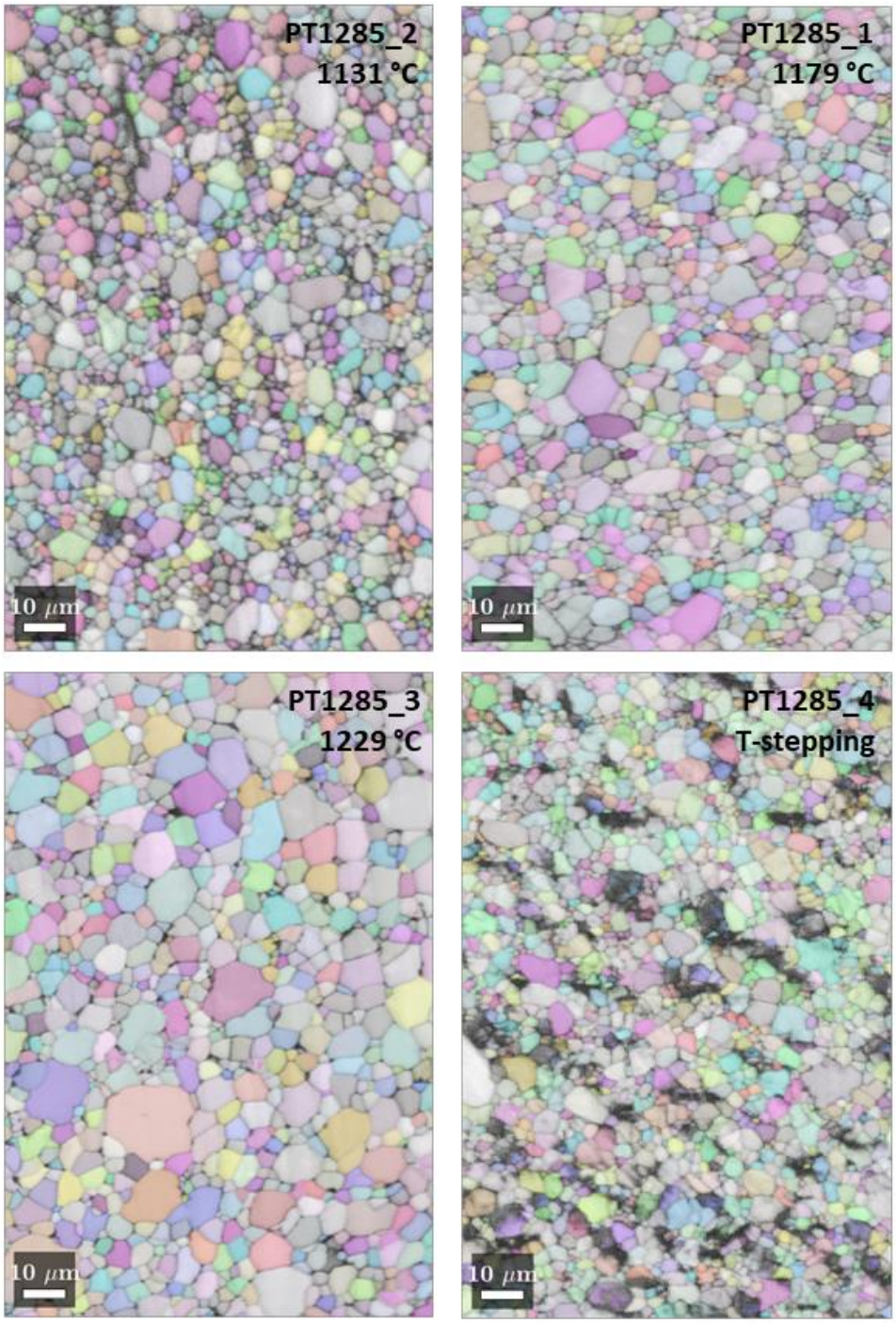

Figure 4: EBSD maps of deformed specimens

Figure 4-5: Histograms of grain-size distribution

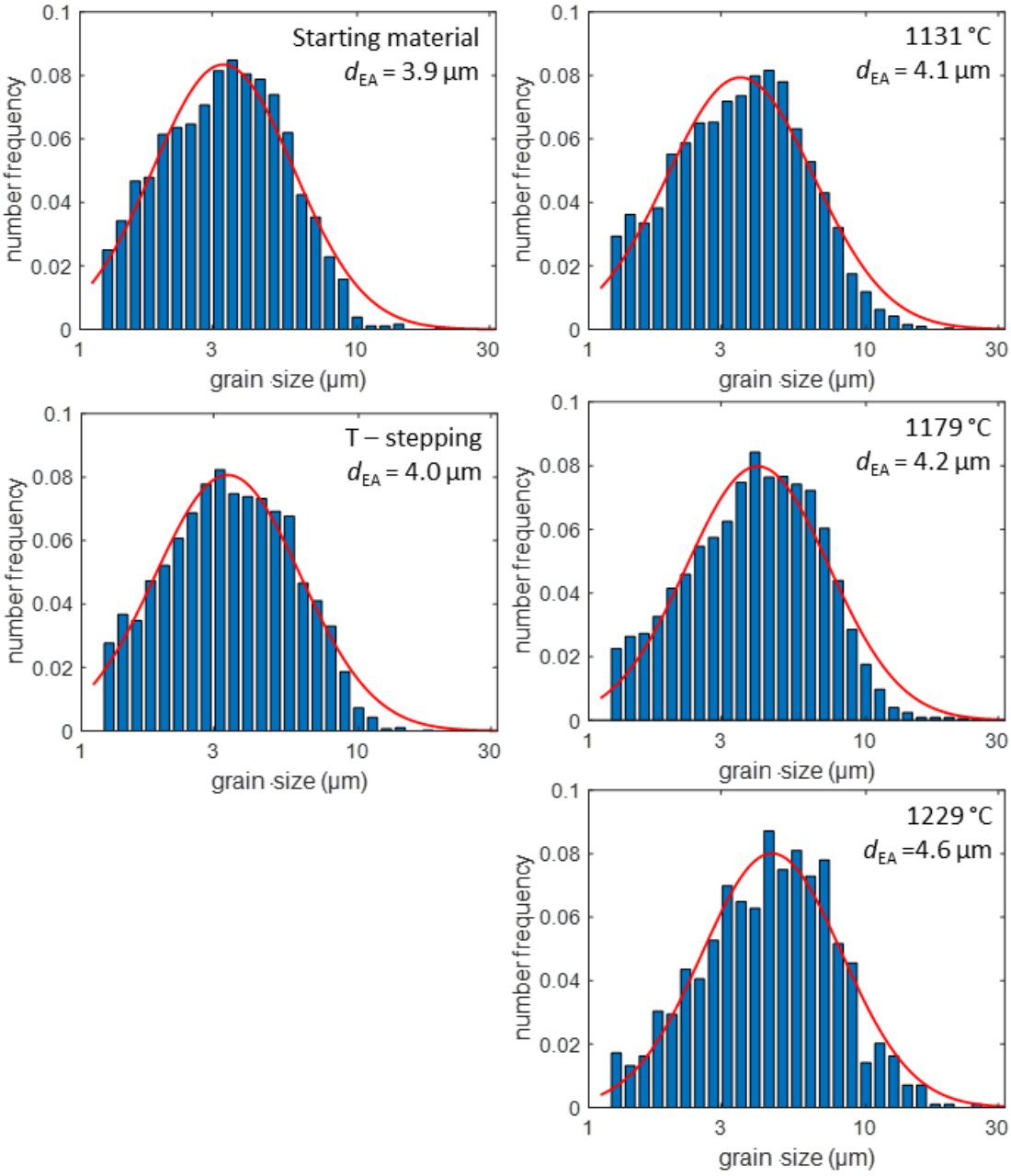

Figure 5: Histograms of the equivalent area (EA) grain-size distribution determined from EBSD maps. Red curve is a log-normal distribution fit to the data.

Figure 4-6: Example EBSD maps

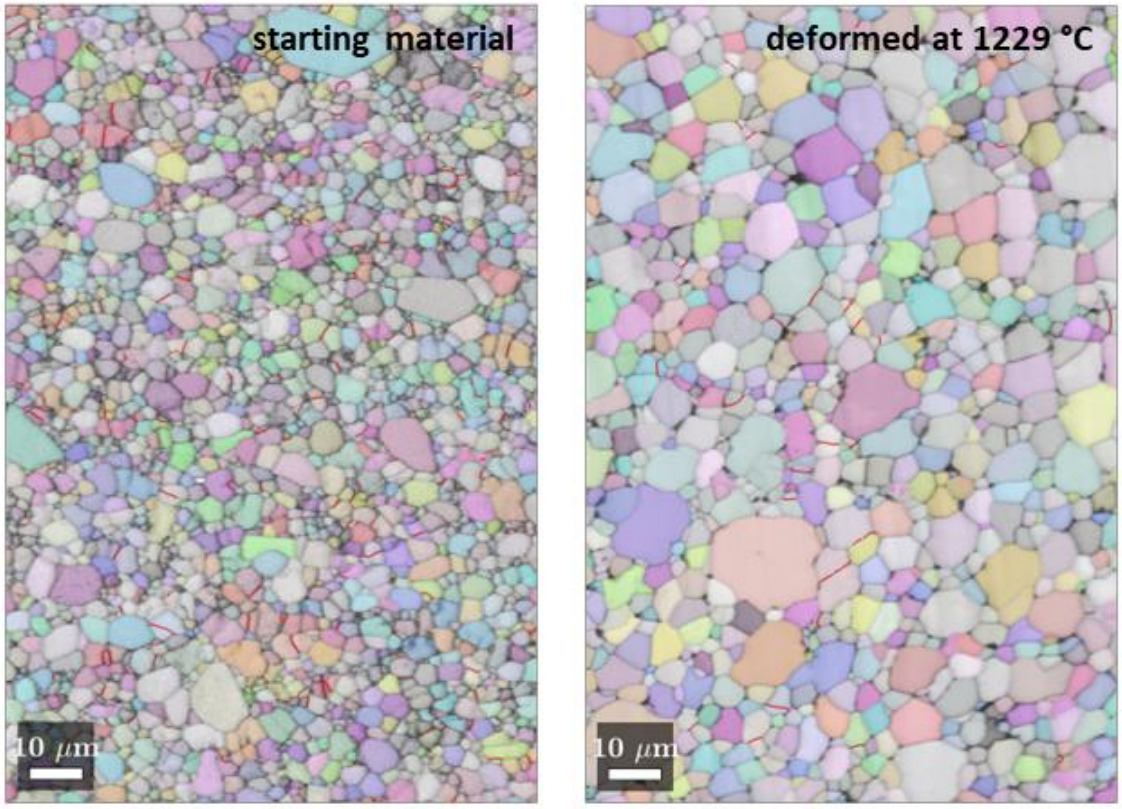

Figure 6: EBSD maps of deformed specimens with subgrain boundaries (misorientation <10°) highlighted in red.

Figure 4-7: Reflected light micrographs of thermally etched specimens

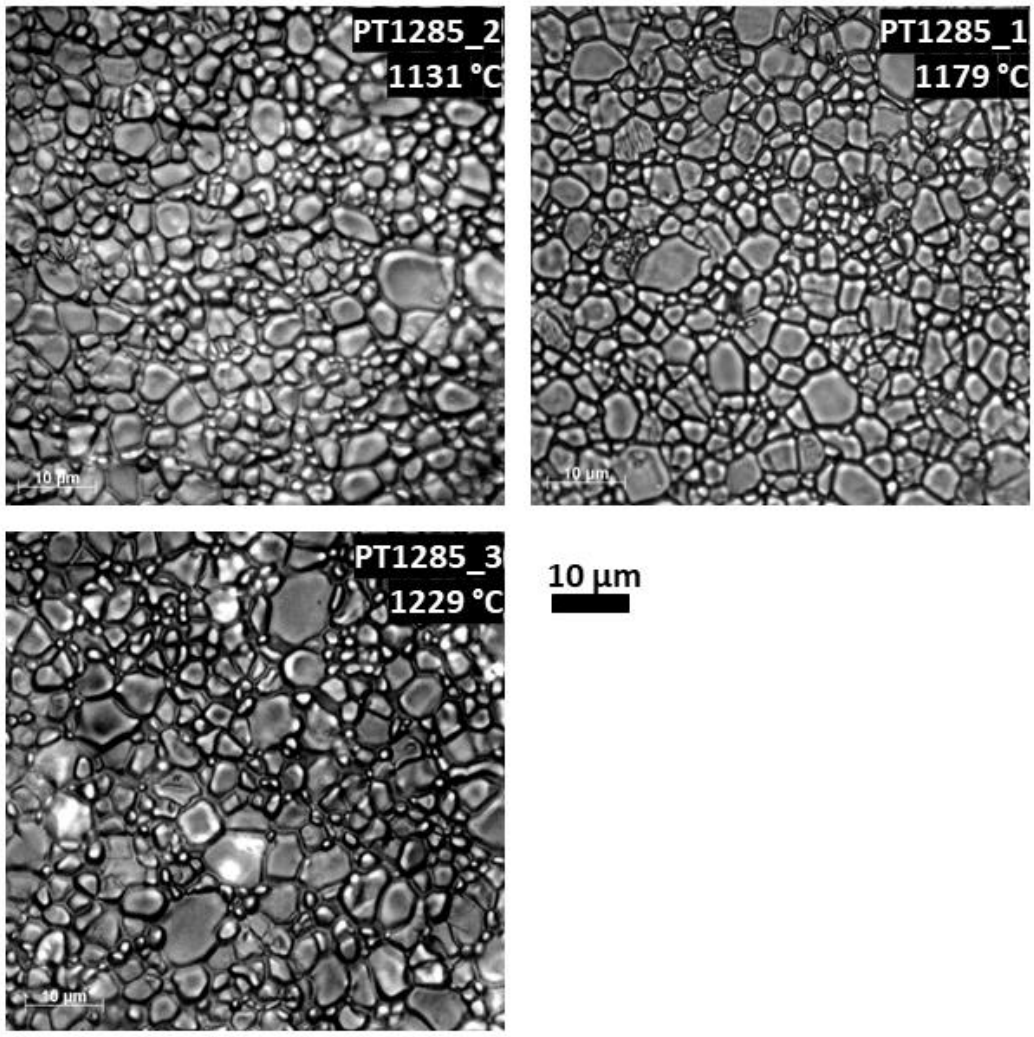

Figure 7: Reflected light micrographs of the surfaces of samples that were deformed at high temperature. Topography is formed from thermal grooving of grain boundaries, which occurred during the deformation experiments at high temperatures.

Figure 4-8: Porosity estimation from reflected light micrographs of polished sections

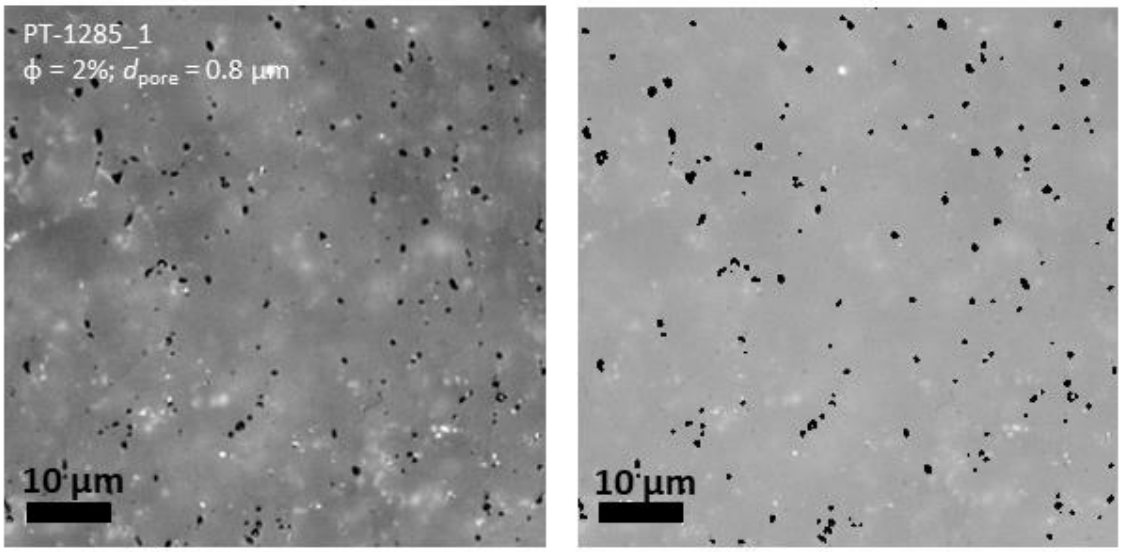

Figure 8: Reflected light micrographs of flat-polished halved deformation samples, used to generate binary images for estimating porosity.

Figure 4-9: Mechanical data

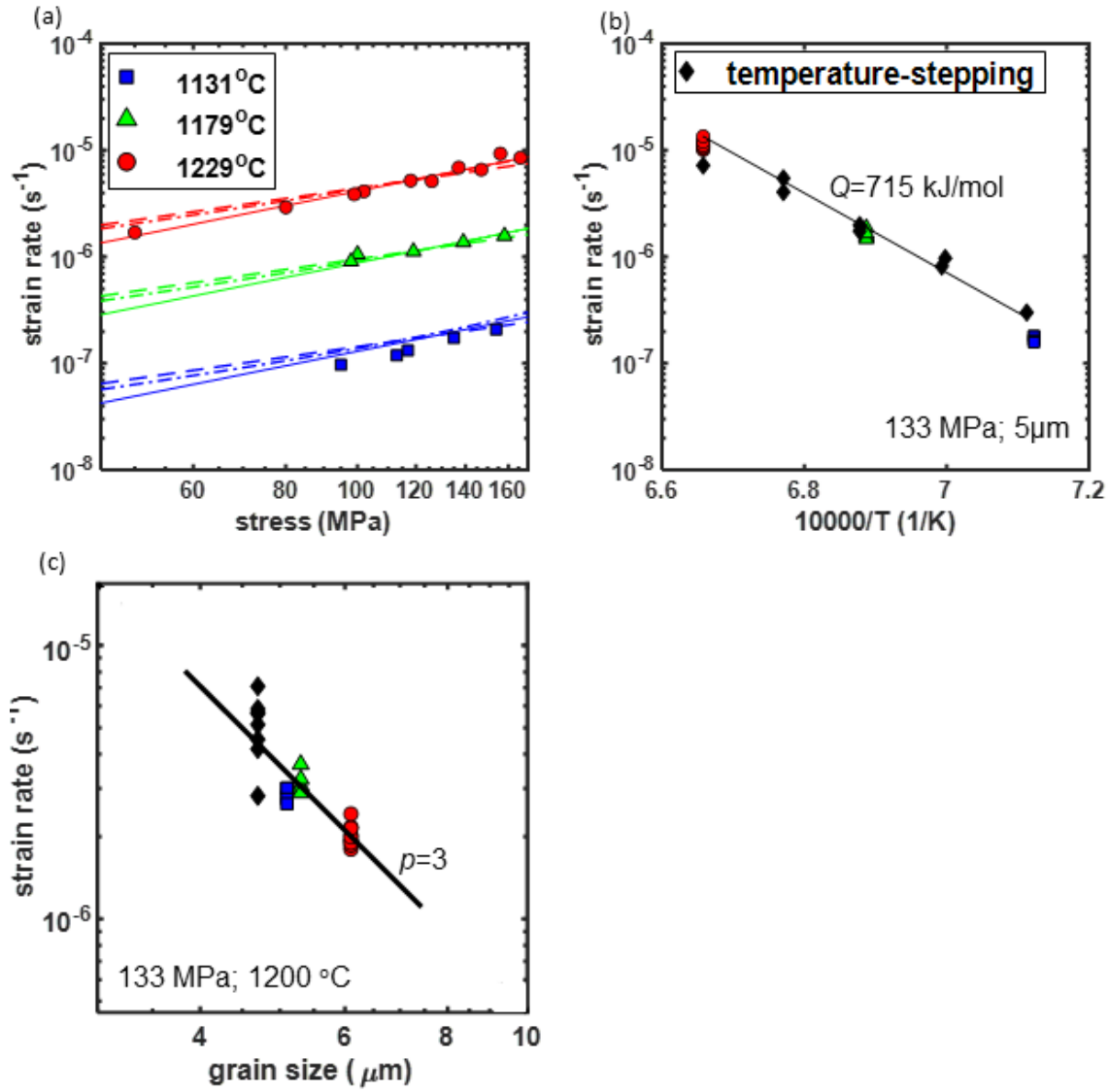

Figure 9: Mechanical data from deformation experiments. (a) stress – strain-rate results from load-stepping experiments with fits to the data (n=1.4, Row 2 Table 2 – solid line; n=1, Row 3 Table 2 – dashed line; dif+dis creep, Row 8 Table 2 – dashed-dotted line). (b) Arrhenius plot of experimental data normalized using a flow law with n=1.4. (c) grain-size – strain-rate plot of experimental data normalized using a flow law with n=1.4, slope of line represents the theoretical value of p=3.

Figure 4-10: Comparison of mechanical data to published flow laws

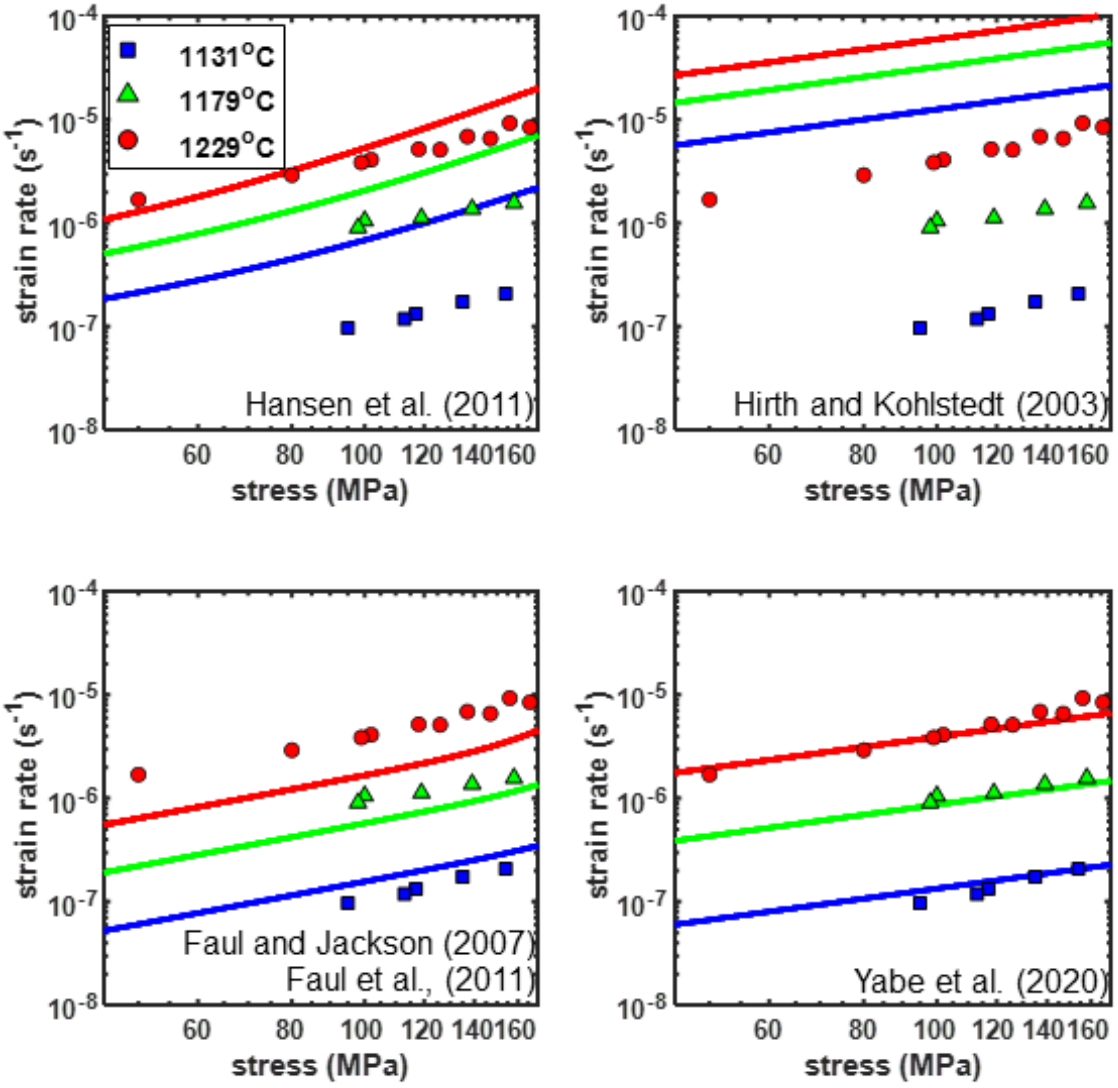

Figure 10: Experimental data from load stepping experiments plotted along with published flow laws calculated for the same conditions using the appropriate grain size measurement (EA vs. LI) for comparison to the published study.

Figure 4-11: Comparison of mechanical data to flow law of Yabe et al. (2020)

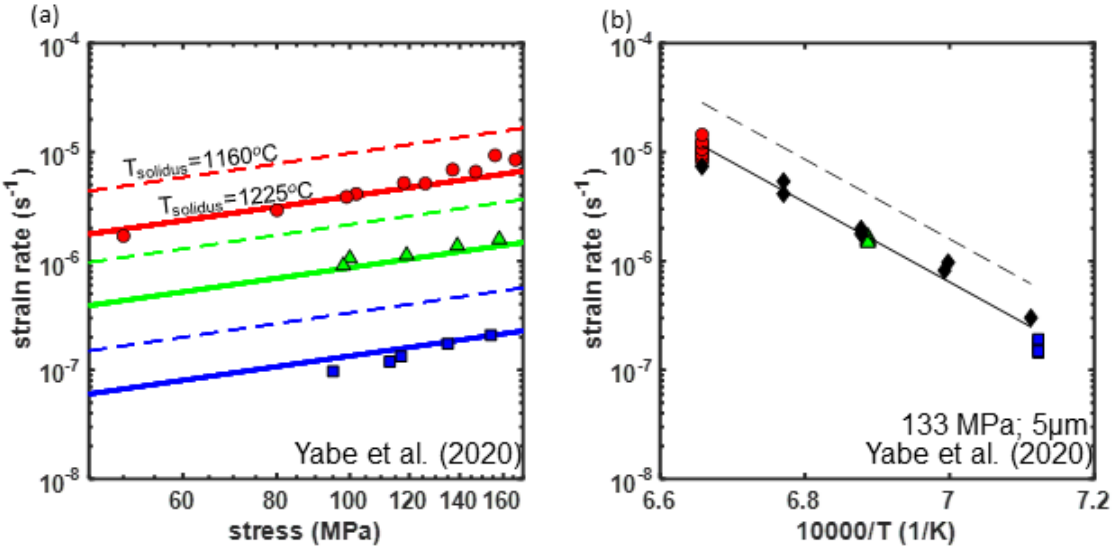

Figure 11: (a) Experimental data from load stepping experiments plotted with the flow law from Yabe et al. (2020) calculated with solidus temperatures of 1160°C (dotted line) and 1225°C (solid line). (b) Arrhenius plot of all experimental data normalized by the flow law of Yabe et al. (2020); again dotted and solid lines indicate the solidus temperature used in the flow law.

Figure 4-12: Error of compiled experimental data relative to selected published flow laws

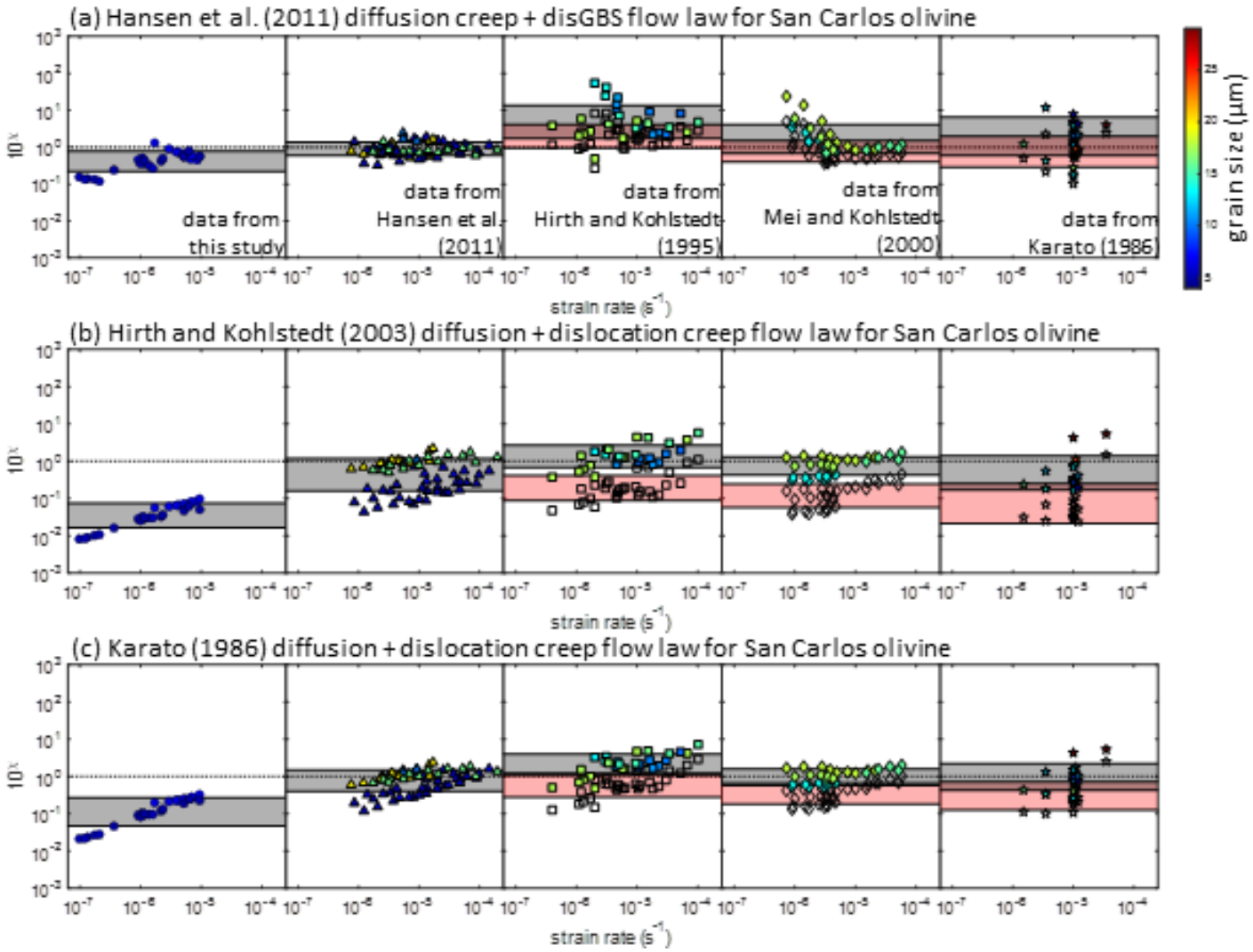

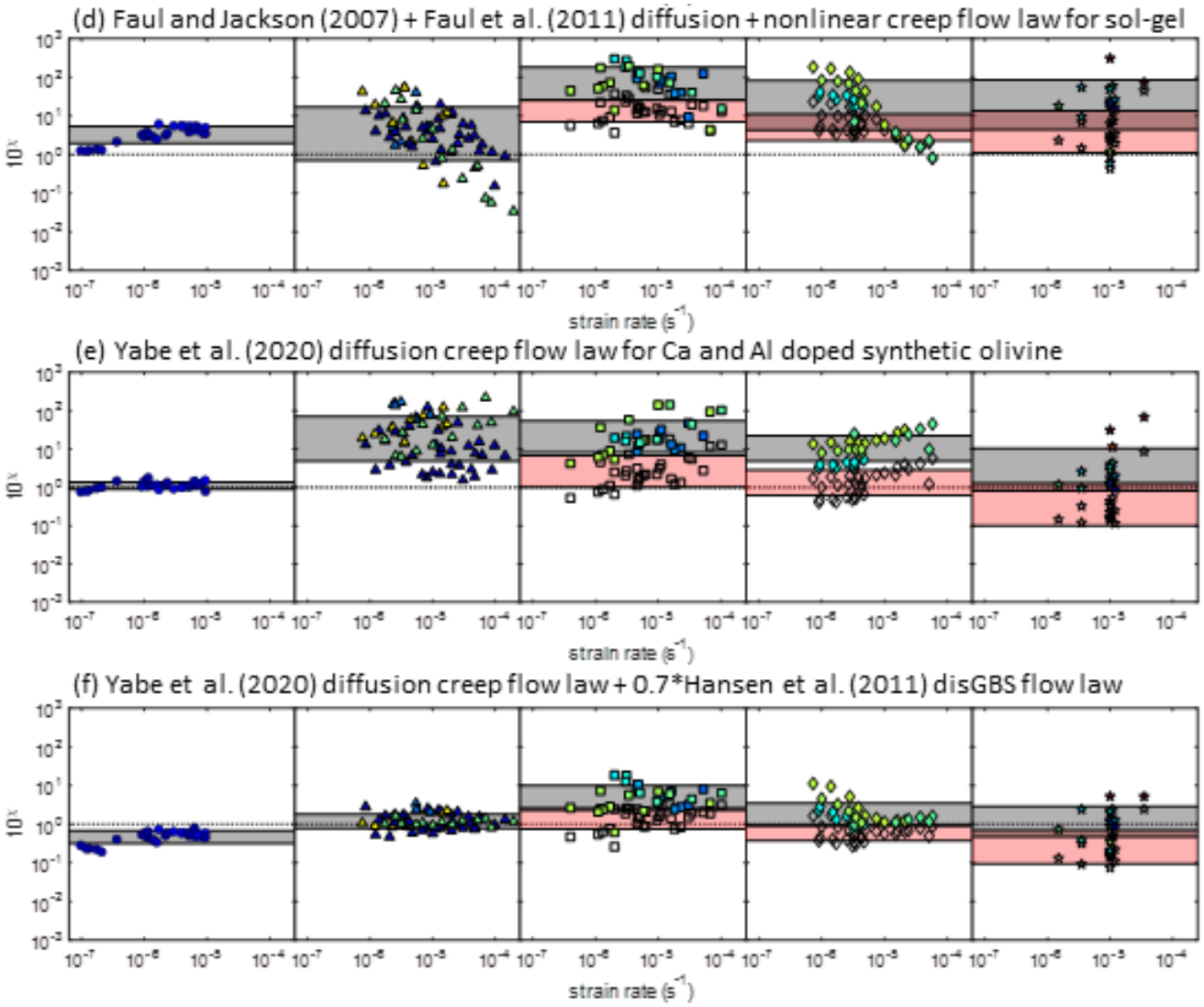
(d) Faul and Jackson (2007) + Faul et al. (2011) diffusion + nonlinear creep flow law for sol-gel
strain rate (s^{-1})
(e) Yabe et al. (2020) diffusion creep flow law for Ca and Al doped synthetic olivine
strain rate (s^{-1})
(f) Yabe et al. (2020) diffusion creep flow law + 0.7*Hansen et al. (2011) disGBS flow law
strain rate (s^{-1})

Figure 12: Plot of the error of compiled experimental data relative to a selection of published flow laws. Each row is calculated for a given flow law and the data are compiled from the studies listed in each panel of (a). In each case data are colored by the grain size. In cases where grain size was measured optically, the analysis was additionally recalculated with a modified grain size (corrected by a factor of 0.5), following the analysis of Hansen et al. (2011), which is represented by open symbols. The dotted line corresponds to no error from the flow law. The grey band represents ± one standard deviation of the error for each dataset to help guide the eye in assessing the quality of each flow law to individual datasets. The red band is the corresponding indicator for the grain size modified data.

Figure 4-13: Multi-mechanism fit (Row 1, Table 4)

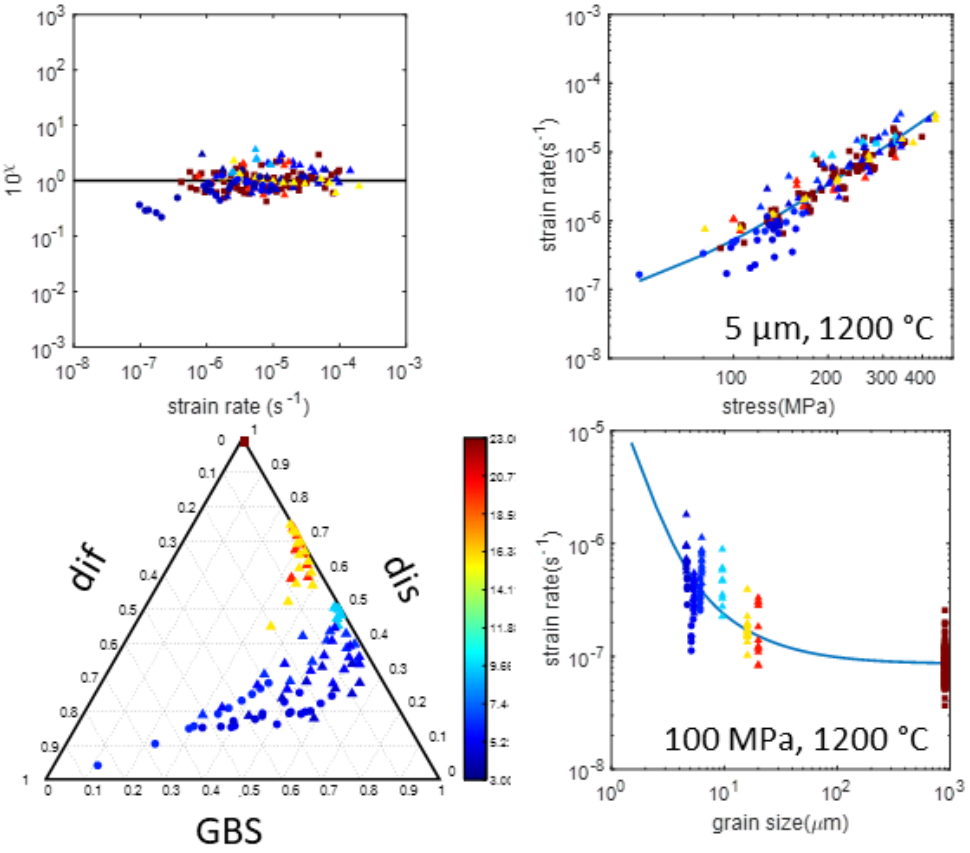

Figure 13: Analysis of multi-mechanism fit to data using data from this study, Hansen et al. (2011) and Keefner et al. (2011) in the fit (Row 1, Table 4). [this study – circles; Hansen et al., 2011 – triangles, Keefner et al., 2011 – squares; symbols are colored by grain size].

Figure 4-14: Deformation mechanism maps (Row 1, Table 4)

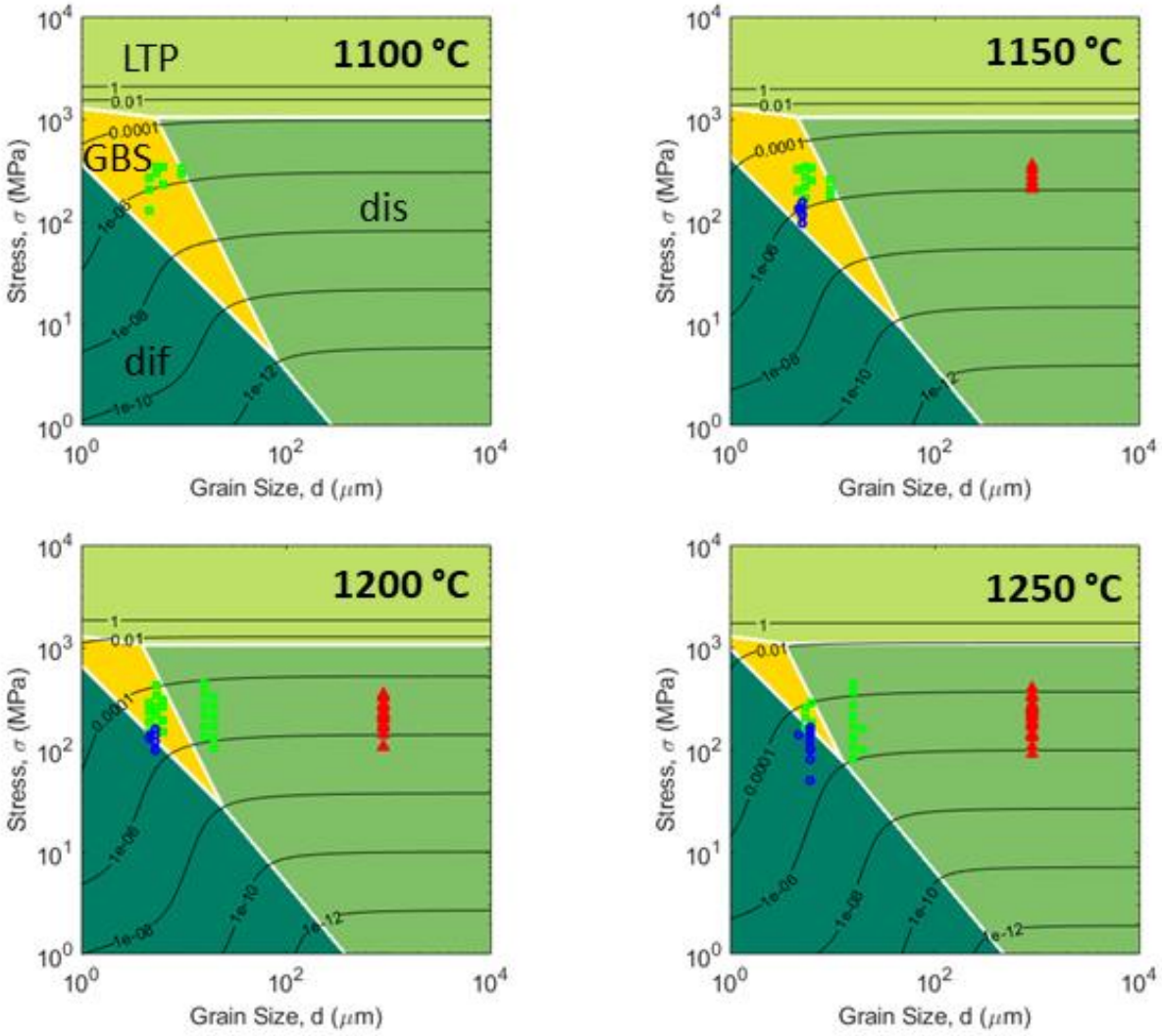

Figure 14: Deformation mechanism map of fit to data using data from this study, Hansen et al. (2011) and Keefner et al. (2011) in the fit (Row 1, Table 4). [this study – blue circles; Hansen et al., 2011 – green squares, Keefner et al., 2011 – red triangles]

Figure 4-15: Multi-mechanism fit (Row 2, Table 4)

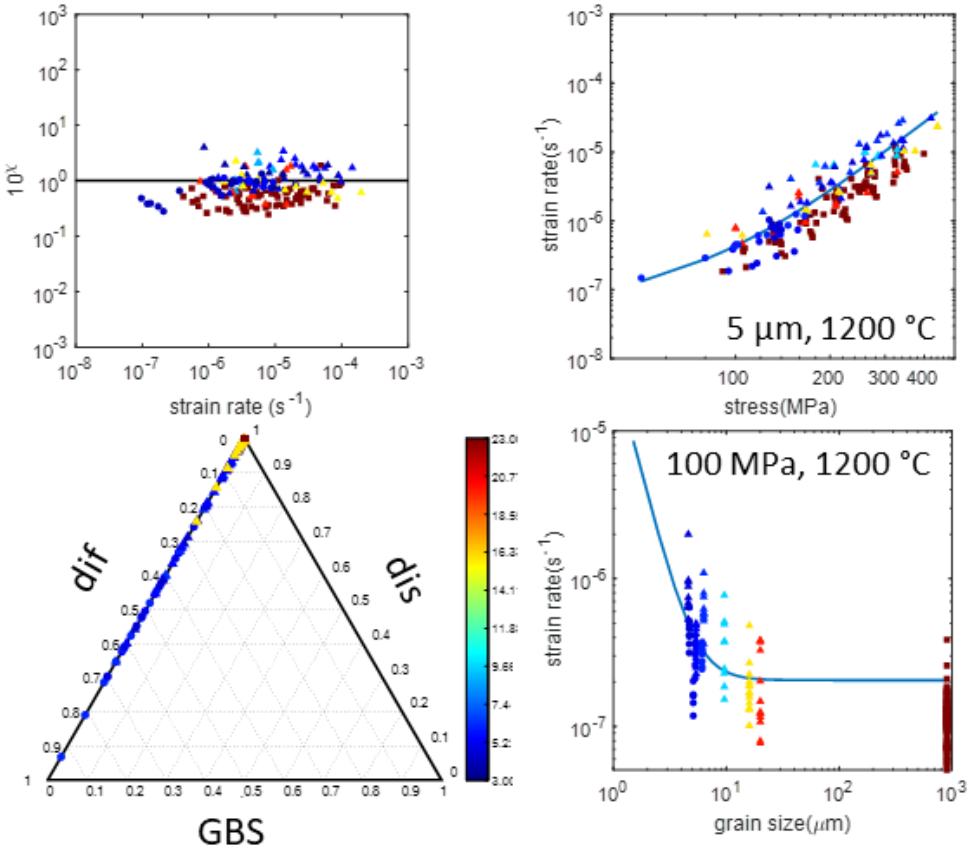

Analysis of multi-mechanism fit to data using data from this study and Hansen et al. (2011) in the fit (Row 2, Table 4). [this study – circles; Hansen et al., 2011 – triangles, Keefner et al., 2011 – squares; symbols are colored by grain size]

Figure 4-16: Deformation mechanism maps (Row 2, Table 4)

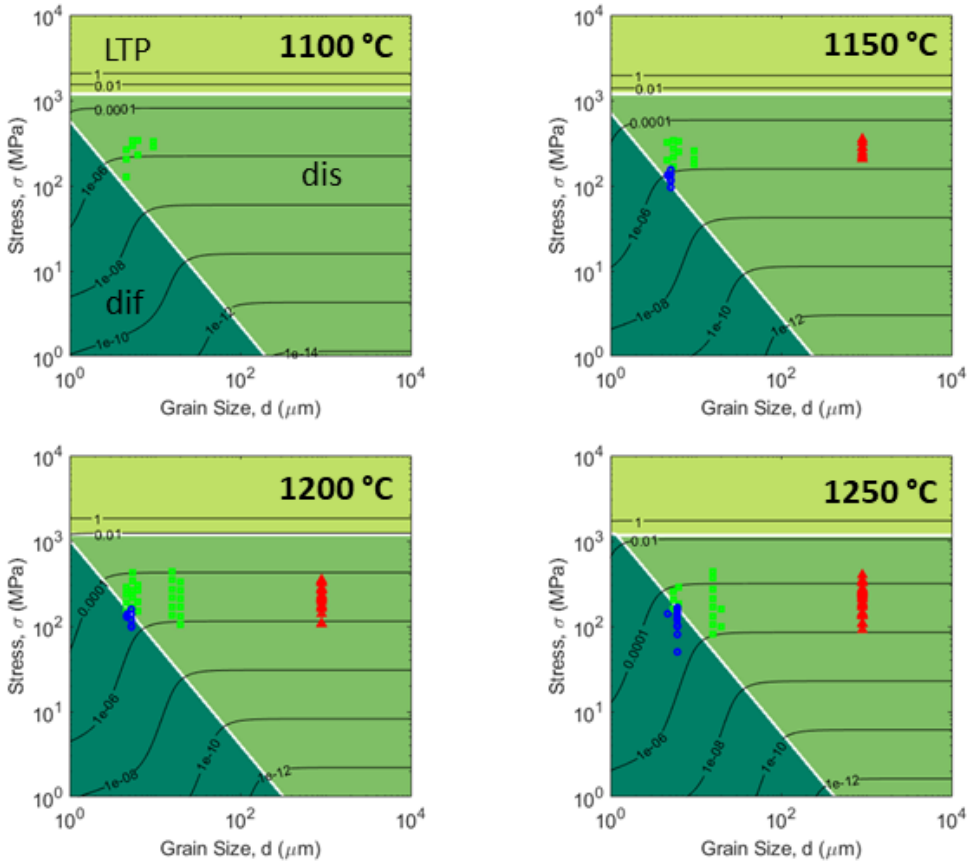

Figure 16: Deformation mechanism map of fit to data using data from this study and Hansen et al. (2011) in the fit (Row 2, Table 4). [this study – blue circles; Hansen et al., 2011 – green squares, Keefner et al., 2011 – red triangles]

Figure 4-17: Multi-mechanism fit (Row 3, Table 4)

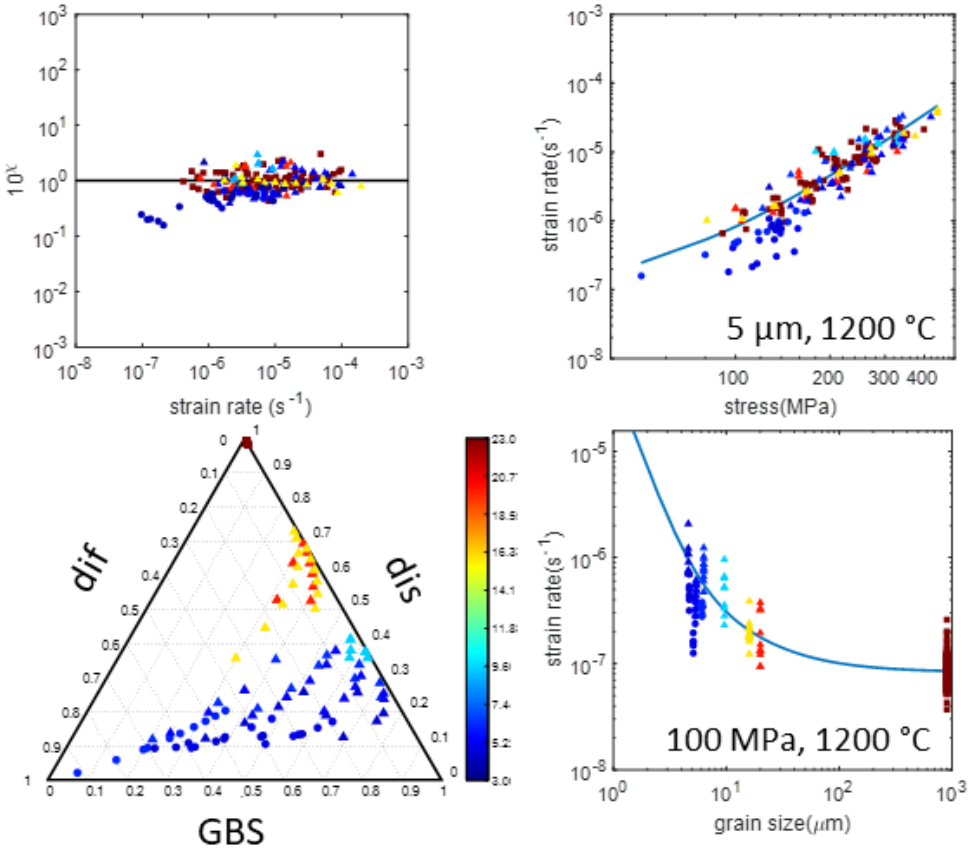

Figure 17: Analysis of multi-mechanism fit to data using data from Hansen et al. (2011) and Keefner et al. (2011) in the fit (Row 3, Table 4). [this study – circles; Hansen et al., 2011 – triangles, Keefner et al., 2011 – squares; symbols are colored by grain size]

Figure 4-18: Deformation mechanism maps (Row 3, Table 4)

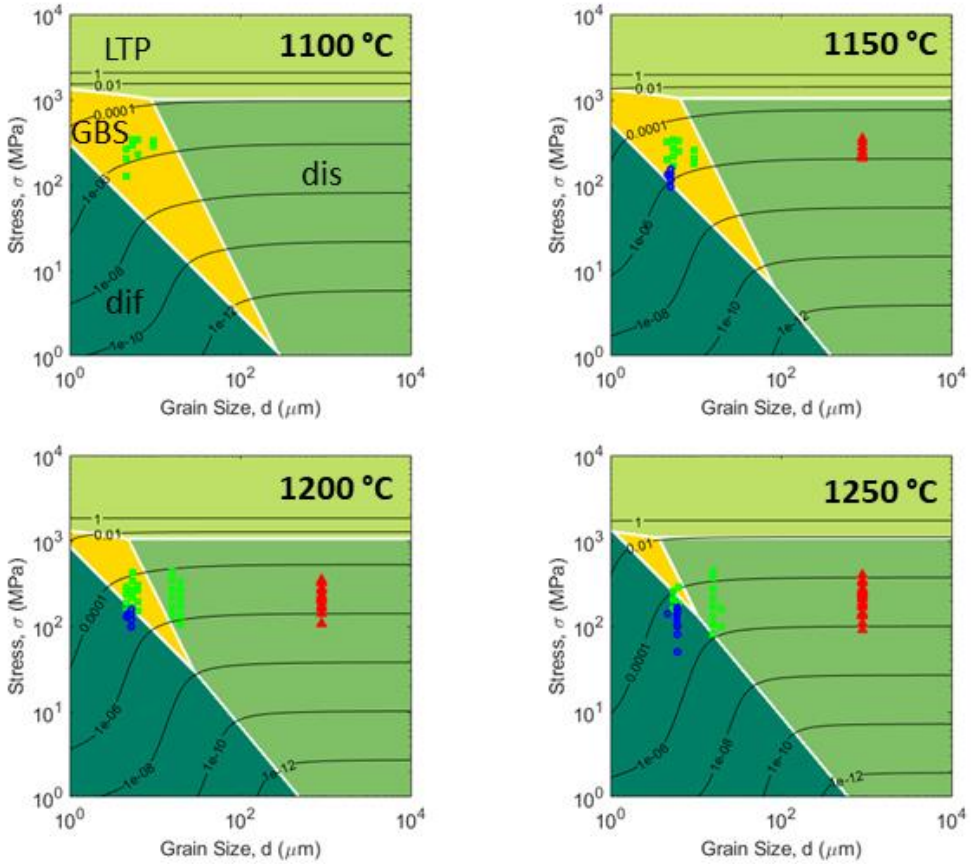

Figure 18: Deformation mechanism map of fit to data using data from Hansen et al. (2011) and Keefner et al. (2011) in the fit (Row 3, Table 4). [this study – blue circles; Hansen et al., 2011 – green squares, Keefner et al., 2011 – red triangles]

Figure 4-19: Multi-mechanism fit (Row 4, Table 4)

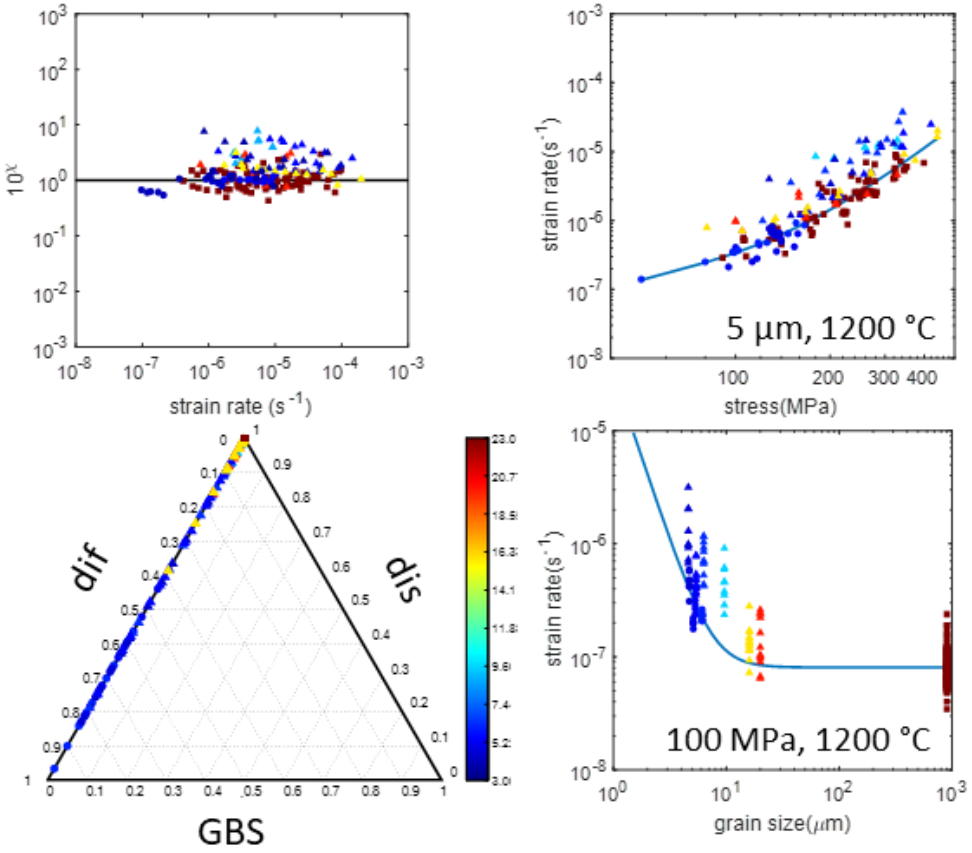

Figure 19: Analysis of multi-mechanism fit to data using data from this study and Keefner et al. (2011) in the fit (Row 4, Table 4). [this study – circles; Hansen et al., 2011 – triangles, Keefner et al., 2011 – squares; symbols are colored by grain size]

Figure 4-20: Deformation mechanism maps (Row 4, Table 4)

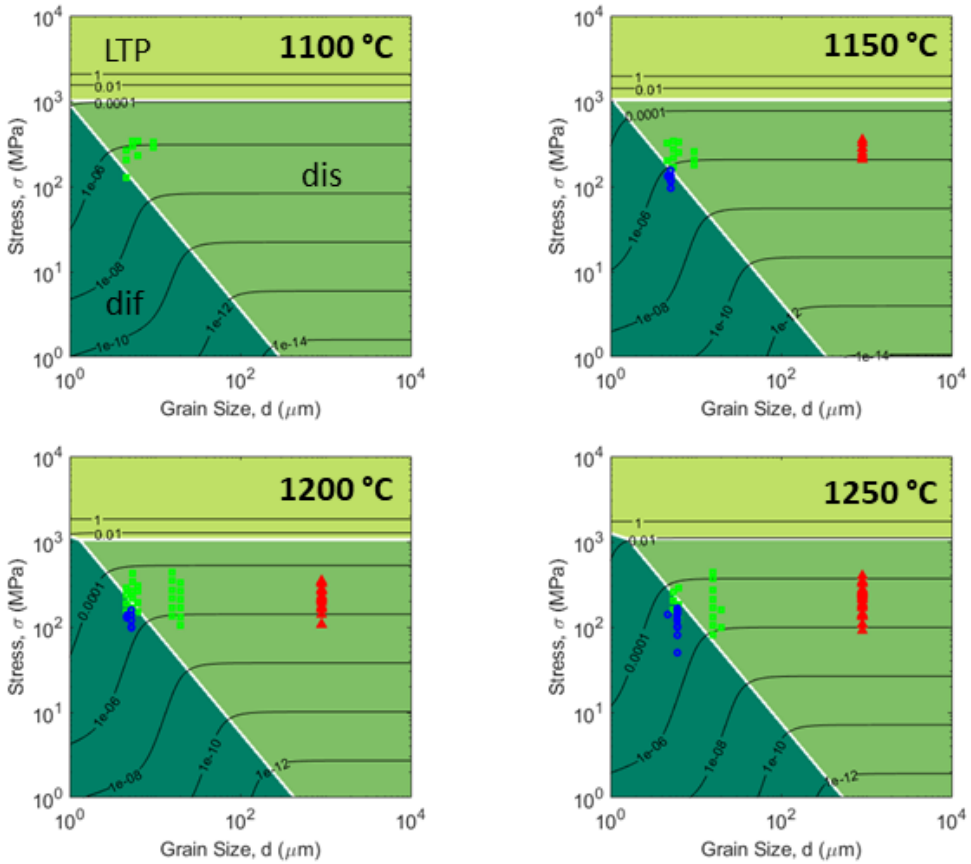

Figure 20: Deformation mechanism map of fit to data using data from this study and Keefner et al. (2011) in the fit (Row 4, Table 4). [this study – blue circles; Hansen et al., 2011 – green squares, Keefner et al., 2011 – red triangles]

Figure 4-21: Multi-mechanism fit (Row 5, Table 4)

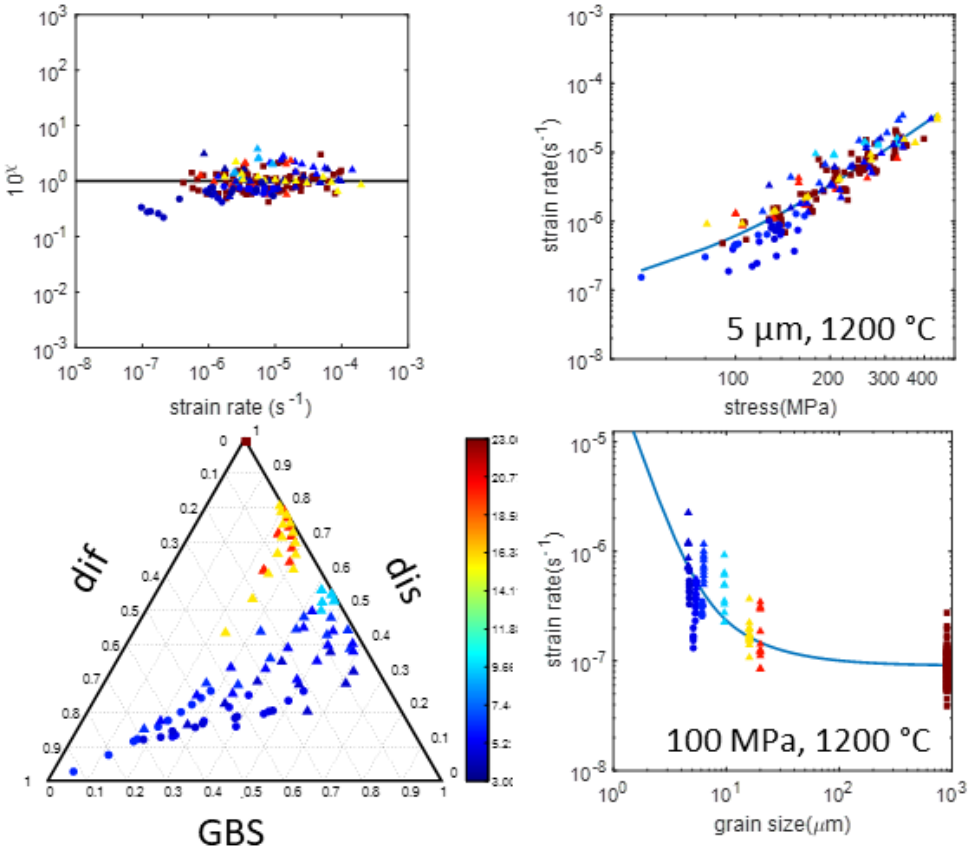

Figure 21: Analysis of multi-mechanism fit to data using data from this study, Hansen et al. (2011) and Keefner et al. (2011) in the fit, with Ts=1225 °C fixed (Row 5, Table 4). [this study – circles; Hansen et al., 2011 – triangles, Keefner et al., 2011 – squares; symbols are colored by grain size]

Figure 4-22: Deformation mechanism maps (Row 5, Table 4)

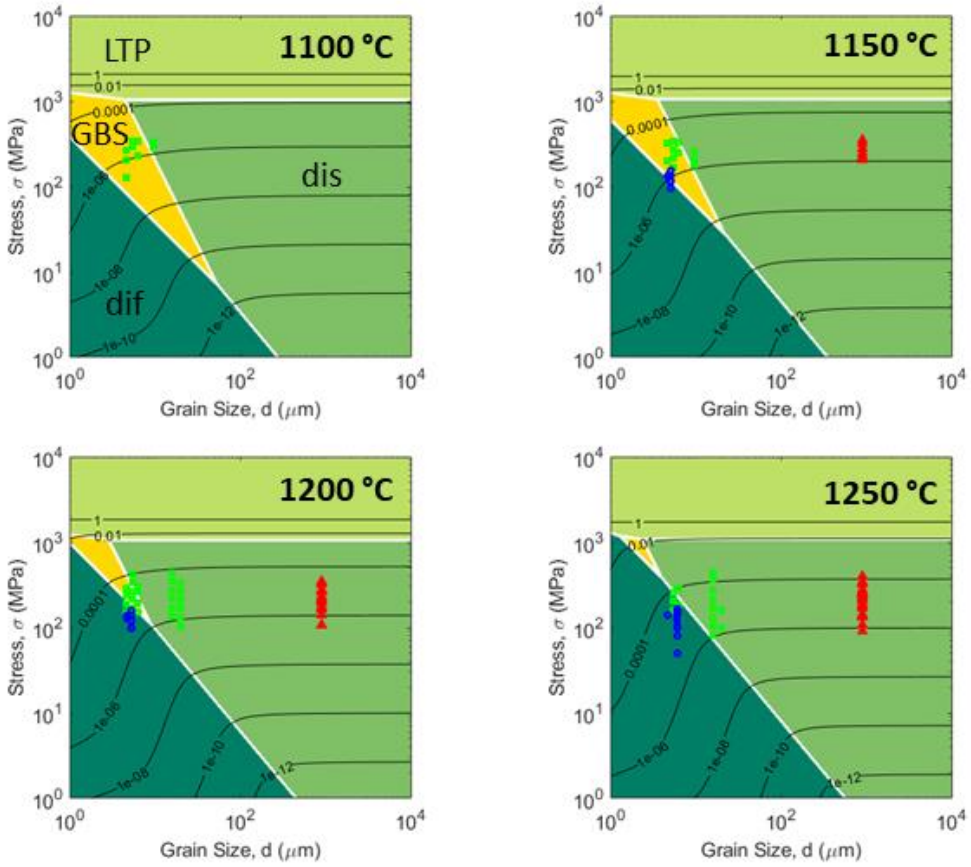

Figure 22: Deformation mechanism map of fit to data using data from this study, Hansen et al. (2011) and Keefner et al. (2011) in the fit, with Ts=1225 °C fixed (Row 5, Table 4). [this study – blue circles; Hansen et al., 2011 – green squares, Keefner et al., 2011 – red triangles]

Figure 4-23: Multi-mechanism fit (Row 6, Table 4)

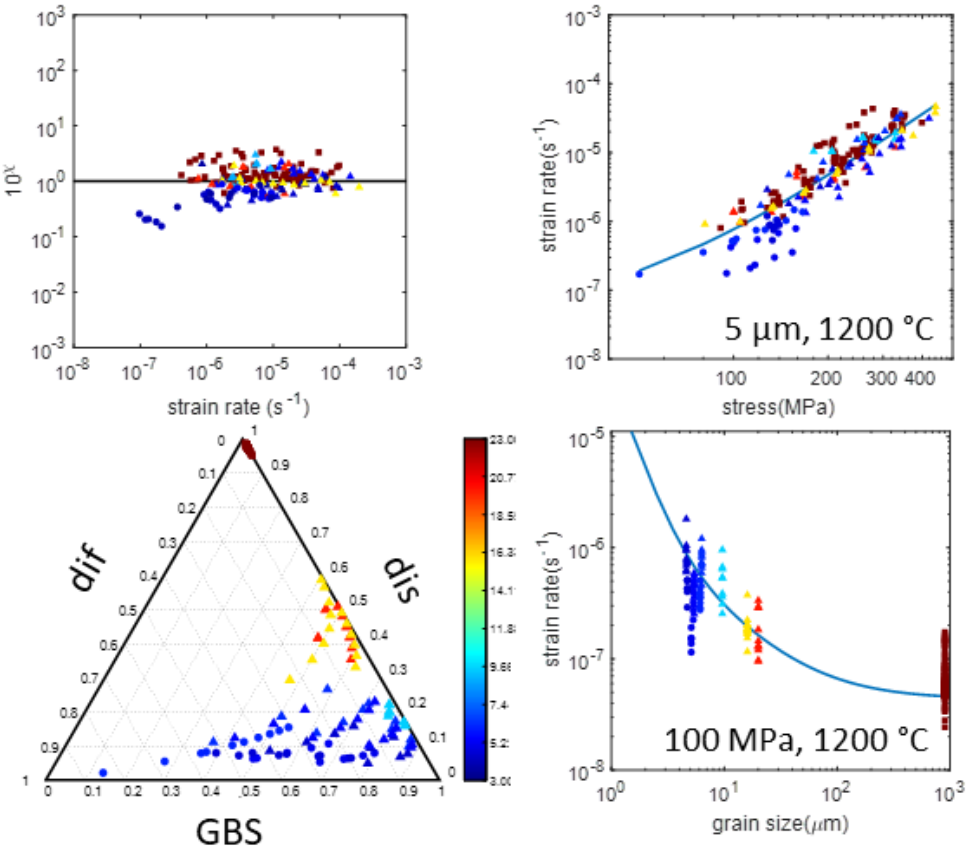

Figure 23: Analysis of multi-mechanism fit to data using data from Hansen et al. (2011) only, with Qdis = 530 kJ/mol (as in Hirth and Kohstedt, 2003) fixed (Row 6, Table 4). [this study – circles; Hansen et al., 2011 – triangles, Keefner et al., 2011 – squares; symbols are colored by grain size]

Figure 4-24: Deformation mechanism maps (Row 6, Table 4)

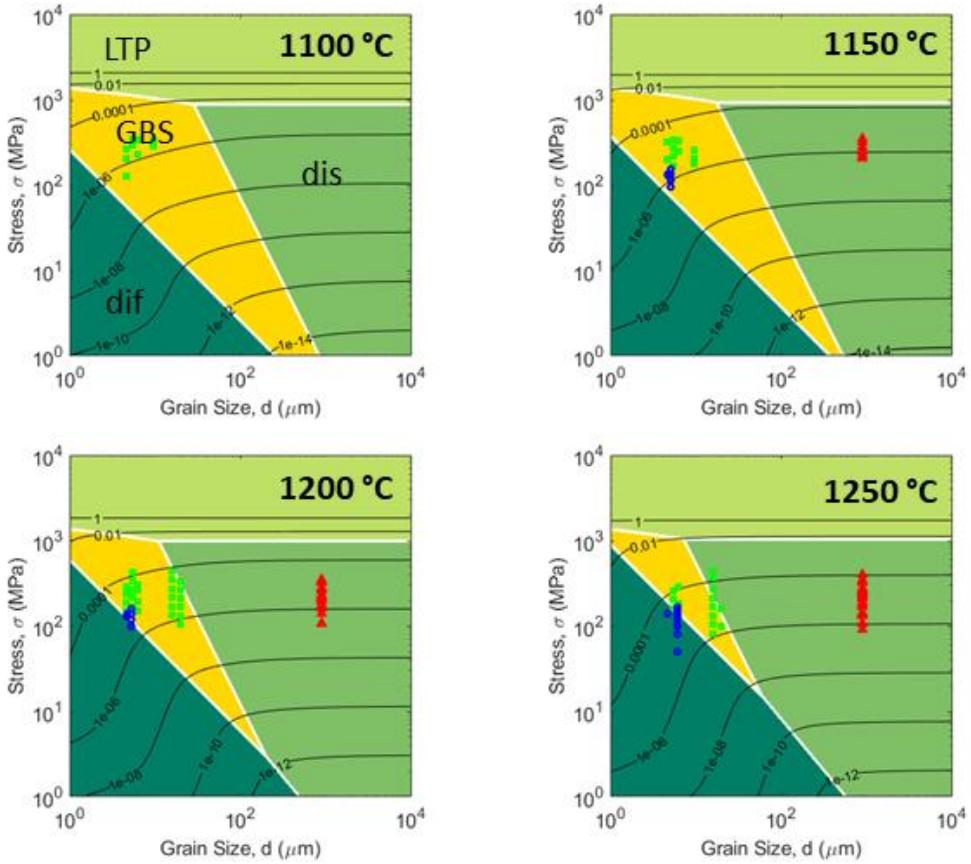

Figure 24: Deformation mechanism map of fit to data using data from Hansen et al. (2011) only, with Qdis = 530 kJ/mol (as in Hirth and Kohstedt, 2003) fixed (Row 6, Table 4). [this study – blue circles; Hansen et al., 2011 – green squares, Keefner et al., 2011 – red triangles]

Figure 4-25: Deformation mechanism maps using flow laws from Hansen et al. (2011)

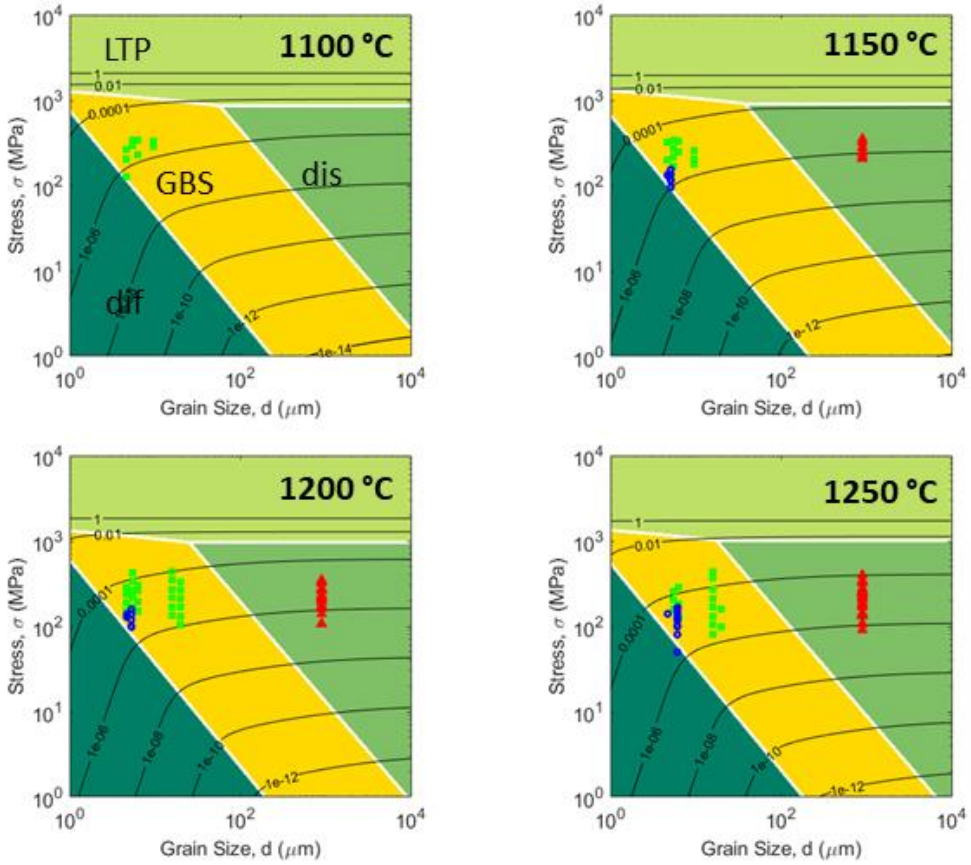

Figure 25: Deformation mechanism map plotted for experimental conditions using the flow laws originally presented in Hansen et al. (2011). [this study – blue circles; Hansen et al., 2011 – green squares, Keefner et al., 2011 – red triangles]

Figure 4-26: Deformation mechanism maps for extraplated conditions

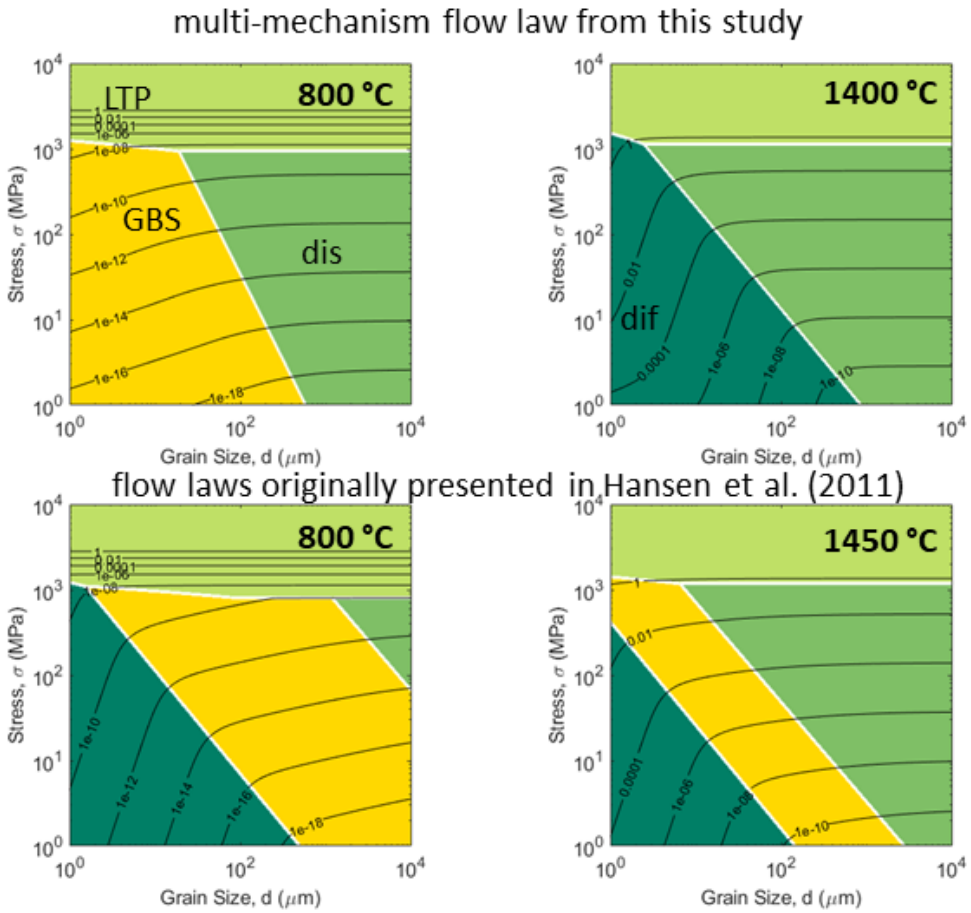

Figure 26: Deformation mechanism map plotted for extrapolated conditions for a multi-mechanism fit to the data (Row 1, Table 4 – top plots) and using the flow laws originally presented in Hansen et al. (2011) (bottom plots). [this study – blue circles; Hansen et al., 2011 – green squares, Keefner et al., 2011 – red triangles]

Figure 4-27: Average number of critically stressed dislocation slip systems

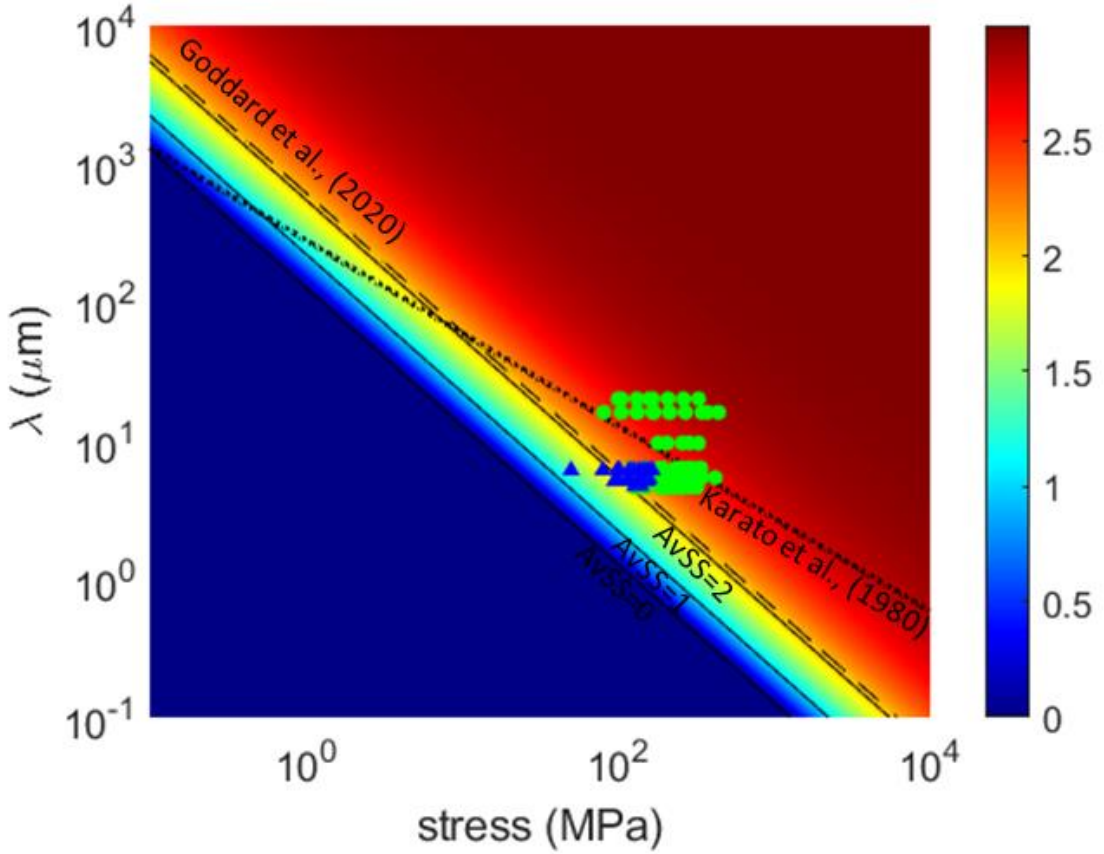

Figure 27: Plot of the average number of critically stresses dislocation slip systems for a random distribution of olivine orientations and a pinning length scale of λ. Contours of AvSS = 0,1, and 2 are labeled along with the subgrain piezometers of Goddard et al. (2020) and Karato et al. (1980). [this study – blue triangles; Hansen et al., 2011 – green circles]

Figure 4-28: Maps of critically stressed dislocation slip systems

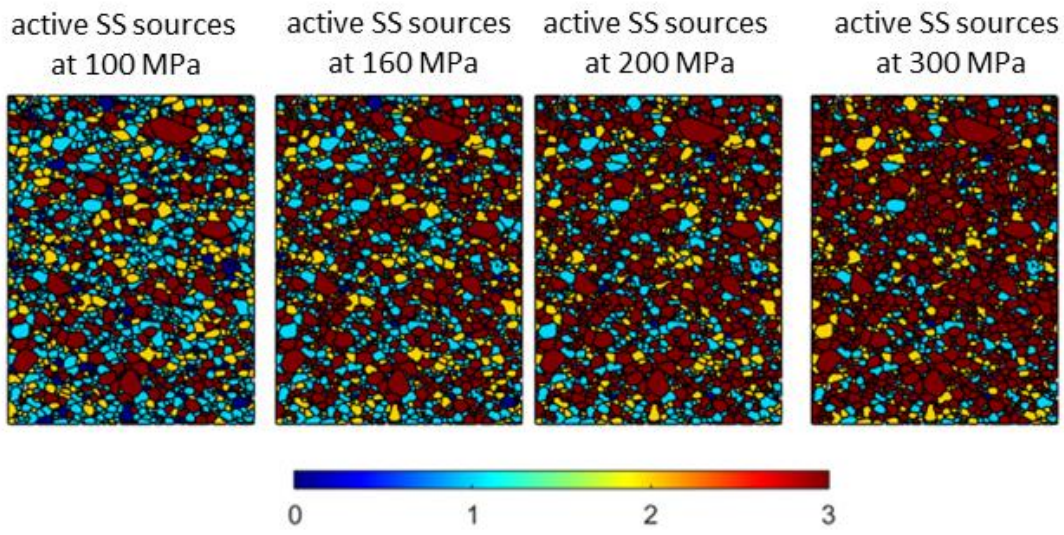

Figure 28: Maps of the number of critically stresses dislocation slip systems calculated from an EBSD map of the hot-pressed starting material. Maps are plotted at stresses of 100, 160 (the maximum stress of our experiments), 200, and 300 MPa.

Figure 4-29: Average number of critically stressed dislocaton slip systems versus stress

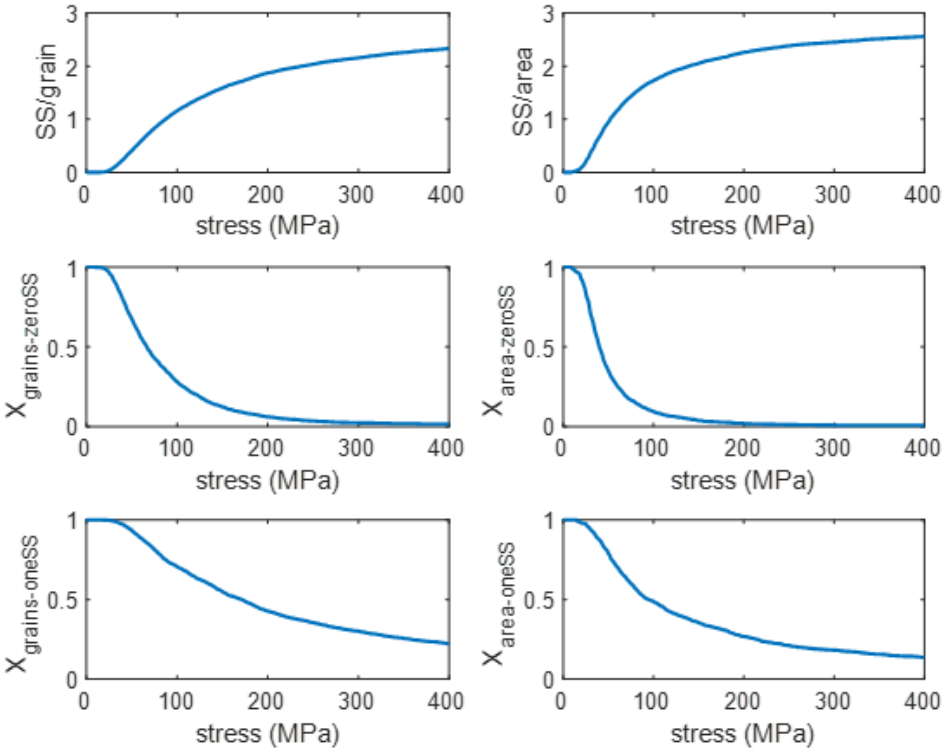

Figure 29: Plots of the number of average critically stresses dislocation slip systems calculated from an EBSD map of the hot-pressed starting material for a given applied stress, calculated for grain and area fraction (top row); plots of the fraction of grains or area with zero critically stressed dislocation slip systems (middle row); and plots of the fraction of grains or area with one critically stressed dislocation slip system (bottom row).

Figure 4-30: Deformation mechanism maps considering length-scale effects

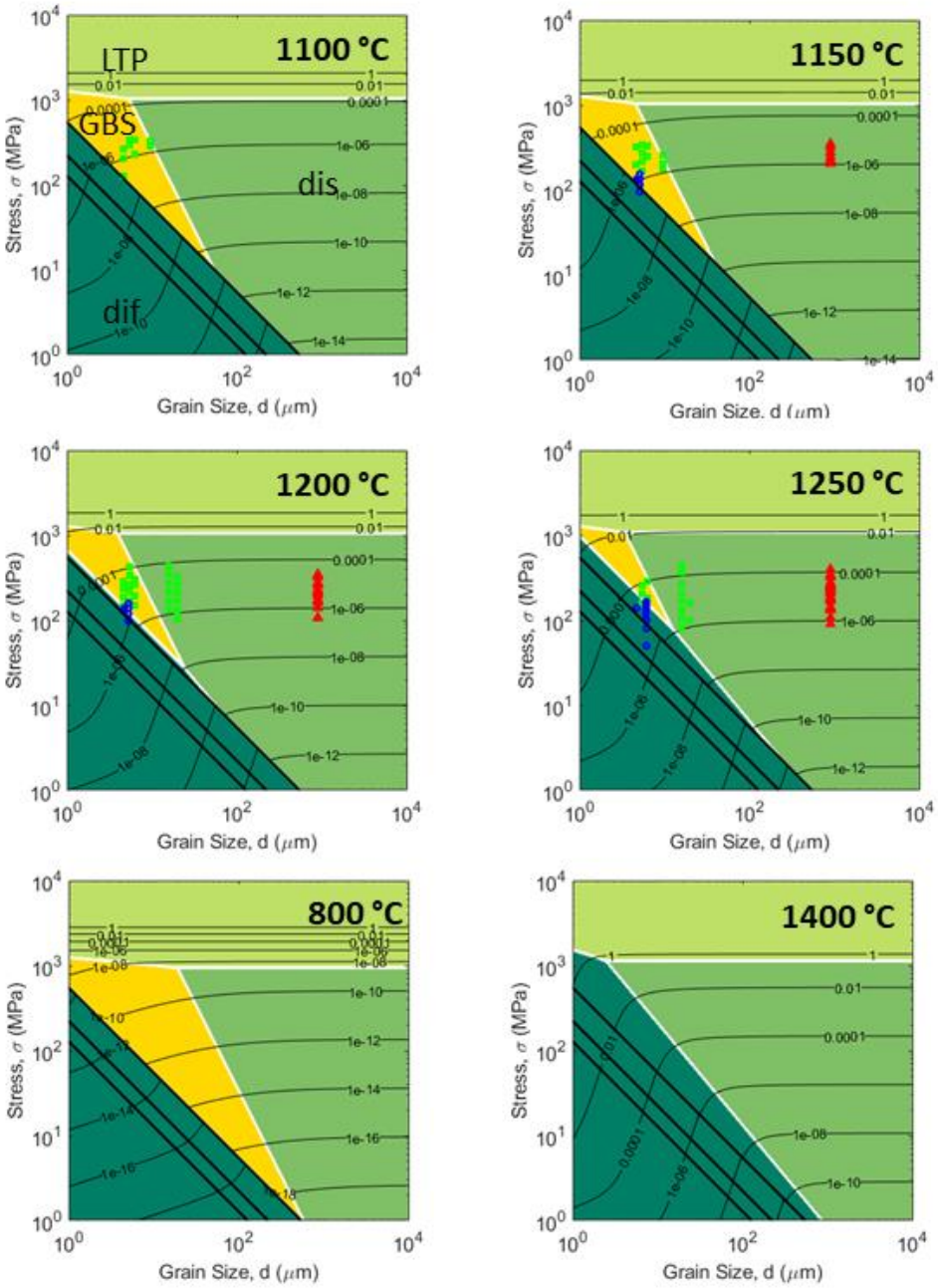

Figure 30: Deformation mechanism maps for a multi-mechanism flow law fit in this study (Row 1, Table 4), wherein disGBS and dislocation creep are limited to stresses where AvSS > 2 plotted for experimental and extrapolated conditions.

Figure 4-31: Normalized experimental data compared to flow law (considering length-scale effects)

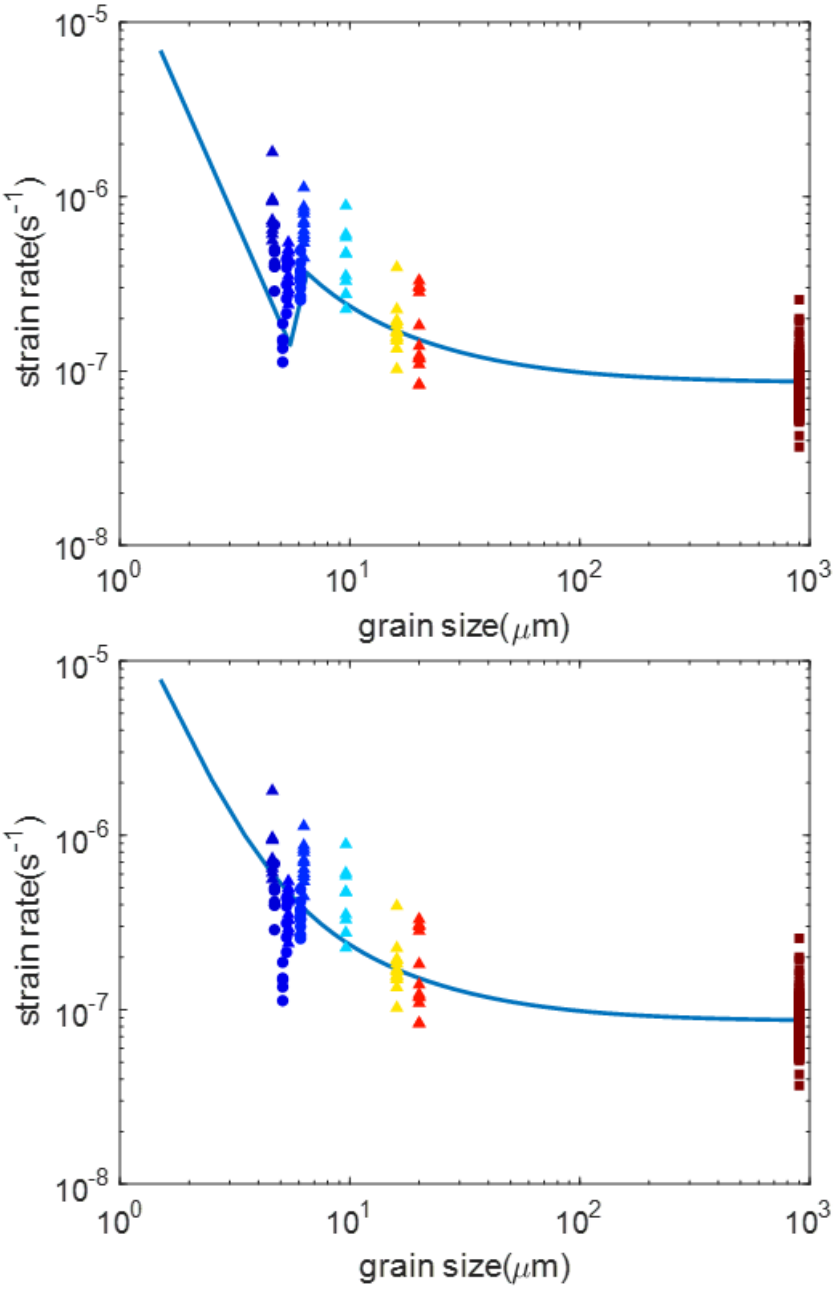

Figure 31: Plots of experimental data from this study (circles), Hansen et al. (2011 - triangles), and Keefner et al. (2011 – squares) normalized using the flow law presented in the mechanism maps in Figure A4 (top row) and the same flow law without length-scale effects (bottom row). Data are colored by grain-size as in previous figures.

Chapter 5 Experimental Measurements of Anisotropic Viscosity in Naturally Sourced Dunite with a Pre-Existing CPO

5.1 Abstract

Naturally deformed dunite cores with a preexisting crystallographic preferred orientation (CPO), collected from a shear zone in the Josephine peridotite (southwest Oregon, USA), were deformed experimentally in triaxial compression. The compression axis was varied relative to the CPO geometry to measure the anisotropy in viscosity of these rocks. Deformation experiments were performed in a gas-medium apparatus at three constant displacement-rate steps, at a temperature of 1250°C and a confining pressure of 300 MPa. Cores were dehydrated at 1200°C in a controlled CO/CO_2 atmosphere prior to deformation to achieve nominally dry conditions. Data from individual experiments were fit by a power-law, yielding a stress exponent of $n \approx 3.6$, indicative of deformation by dislocation creep. The maximum difference in viscosity was a factor of 2.6 at constant stress. The CPO of the olivine grains was measured after deformation by electron backscatter diffraction (EBSD). The flow stress correlated with the mean Schmid factor (or resolved shear stress) on the easiest dislocation slip systems, calculated from grain orientations determined from EBSD analyses. Analysis of our data with a simplified effective-medium model, which incorporated constraints from published single-crystal flow laws, demonstrated the link between CPO and anisotropy in viscosity. Predictions from viscoplastic self-consistent (VPSC) models support our simplified analysis of the measured anisotropy.

5.2 Introduction

Grain-scale deformation in Earth's upper mantle allows convective flow that leads to plate-scale crystallographic alignment of olivine and other minerals, reflecting deformation kinematics. This crystallographic preferred orientation (CPO) imparts anisotropic physical properties to the upper mantle due to the anisotropic, orthorhombic crystal structure of the primary mineral, olivine. Distinct olivine CPOs are often observed in naturally deformed olivine-rich mantle rocks collected at Earth's surface from localities such as tectonically exhumed

ophiolites and mantle xenoliths ejected by volcanism (Ismail and Mainprice, 1998; Mehl et al., 2003; Warren et al., 2008; Skemer et al., 2013; Chatzaras et al., 2016). Seismic detection of elastic anisotropy provides strong evidence that olivine CPOs are pervasive throughout Earth's upper mantle (Long and Silver, 2009; Long and Becker, 2010). Magnetotelluric data similarly show plate-scale anisotropic electrical conductivity in the upper mantle (Gatzemeier and Moorkamp, 2005; Gatzemeier and Tommasi, 2006). Calculated seismic anisotropy from numerical models that combine grain-scale CPO formation and finite strain estimated from plate motions correlate well with measured seismic anisotropy, reinforcing the inference that the CPO of olivine is the underlying cause of upper mantle anisotropy (Tommasi et al., 1998; Becker et al., 2003; Becker et al., 2006).

High-temperature deformation experiments on olivine-rich rocks have reproduced olivine CPO formation in the laboratory by imposing high strains in torsion or in general (approximately simple) shear between angled pistons (Jung and Karato 2001; Bystricky et al., 2000; Katayama et al., 2004; Hansen et al., 2012a; Hansen et al., 2012b; Hansen et al., 2014; Tasaka et al., 2015; Tielke et al., 2016a). Typically, alignment of the easiest (weakest) dislocation slip system is thought to control CPO geometry. This conclusion is supported by experiments on olivine single crystals that quantify the relative strengths of the slip systems in olivine (Durham and Goetze, 1977; Ricoult and Kohlstedt, 1985; Bai et al., 1991; Bai and Kohlstedt, 1992; Tielke et al., 2016b). Four dominant slip systems have been identified: (010)[100], the paired (001)[100] and (100)[001], and (010)[001], listed in order of their relative weakness under dry upper mantle conditions. At these conditions, at a given stress, the strain rate differs by more than two orders of magnitude between the weakest and strongest slip systems. Such significant mechanical anisotropy leads to the prediction that an olivine-rich rock with a pronounced CPO should have strongly anisotropic viscosity as well.

Most geodynamic models of upper mantle flow do not account for anisotropic viscosity. However, depending on its magnitude, ignoring anisotropy may result in large errors when modeling dynamic processes (Pouilloux et al., 2007). Numerical simulations demonstrate that viscous anisotropy influences the spacing and timing of Rayleigh-Taylor instabilities, the thermal structure of the mantle wedge in subduction zones, the rate and geometry of post-glacial rebound, the shape and flow distribution of convection cells, and the geometry of lithospheric shear zones (Christensen, 1987; Han and Wahr, 1997; Lev and Hager, 2008; Tommasi et al., 2009; Lev and Hager, 2011). Multiscale models, incorporating experimentally determined

strengths for different slip systems, indicate a viscosity ratio of 1.5-3 between the strongest and weakest orientations of polycrystalline olivine with a CPO resulting from simulated high-strain deformation (Knoll et al., 2009; Tommasi et al, 2009).

Direct experimental measurements of the anisotropy of viscosity in textured olivine aggregates are limited. Wendt et al. (1998) performed axial compression experiments on naturally textured peridotites, deformed in different orientations relative to their preexisting foliation. These experiments were conducted on natural specimens collected from several locations and were experimentally deformed in a semi-brittle regime where high stress exponents (n = 5-25) were measured, such that viscous anisotropy was not easily quantified. In another set of studies, hot-pressed, iron-rich olivine aggregates were deformed in either torsion or axial extension, followed by deformation in the alternate geometry (Hansen et al. 2012b; Hansen et al., 2016a; Hansen et al., 2016b). These experiments yielded a maximum viscosity ratio of 14 at constant stress.

In the present study, samples prepared from a hand sample of naturally deformed dunite collected from a shear zone in the Josephine peridotite were experimentally deformed at high temperature in several different orientations relative to its preexisting CPO. Strain-rate stepping experiments were used to measure the strength of the rock in different orientations and thus quantify the anisotropy in viscosity. A simple mechanical model, incorporating weighted Schmid factors (resolved shear stress) for each of the dominant slip systems, was compared to the data to extend the results to broader application. While experimental deformation of naturally exhumed rocks brings about technical challenges that are avoided when using synthetic rocks, these experiments provide a framework for quantifying anisotropic viscosity in Earth's upper mantle and for verifying that CPO imparts anisotropic viscosity to naturally deformed dunites. Further, due to the coarse grain size and high experimental temperatures, these samples are expected to deform by dislocation creep, while previous experiments on hot-pressed olivine aggregates were deformed in the dislocation-accommodated grain boundary sliding (disGBS) regime.

5.3 Methods

Samples of a dunite with a preexisting CPO were cored in different orientations, dehydrated at 1 atm, and deformed in a gas-medium apparatus (Paterson, 1990) to measure its

viscous anisotropy. A dunite rock collected from a shear zone in the Josephine peridotite was selected as starting material. This rock was previously studied in detail by Warren et al. (2008), labeled as sample 3924J03b in their study. Based on structural field relationships, these researchers deduced that the dunite rock had undergone a shear strain of ~3.4. The chosen hand sample had an intermediate intensity A/D-type CPO, typical of deformation under dry conditions, with the [100] direction dominantly aligned with the shear direction and the [010] direction dominantly normal to the shear plane but somewhat girdled normal to the shear direction. The mean grain size of the chosen dunite rock is ~500 μm; however, the grain size is heterogeneous, with some grains several millimeters in dimension. This coarse-grained, heterogeneous microstructure is clear from the optical micrographs of thin sections shown in Figure 1. The dunite rock was oriented for deformation by measuring the mean orientation of the CPO from a large low-resolution (50 μm step size) EBSD map of a portion of it. Cores were then obtained along axes close to the [100], [010], [001], $[110]_c$, and $[101]_c$ directions of the mean orientation (where the c-subscript indicates use of a cubic crystallographic coordinates, as typical of experiments on olivine single crystals – see Durham and Goetze, 1977). The orientations of the axis of the cores relative to the mean orientation of the CPO are subsequently referred to as the nominal orientation of the core. These labels are useful for identifying core orientations relative to the CPO, but it is important to note that a broad range of crystallographic orientations exists in each sample. Cores with a diameter of 10 mm and a length of 12-21 mm were squared at the ends, placed in a Ni sleeve, and dehydrated for 12 h at 1200°C in a controlled-atmosphere furnace under mixed CO/CO_2, with a ratio such that the oxygen partial pressure, pO_2, was near the Ni/NiO buffer. Samples were hydrostatically annealed for an additional 3 h at 1250°C and 300 MPa in the deformation apparatus, prior to deformation.

Axial compression experiments were performed at 1250°C and 300 MPa in a gas-medium apparatus (Paterson, 1990) under constant displacement-rate conditions at three rates. Nominal strain-rates of 2×10^{-5}, 1×10^{-5}, and 5×10^{-6} s^{-1} were applied, allowing the stress to stabilize to a nearly steady-state value at each step. Each sample was deformed to a total strain of less than 12% with calculated stresses between 110 and 202 MPa. This approach for quantifying the mechanical properties of natural dunites is very similar to that taken by Chopra and Paterson (1984).

After deformation, samples were cut parallel to the compression axis in preparation for EBSD analyses. Sections were polished progressively on diamond lapping film to a final grit size of 0.5 µm, followed by polishing with colloidal silica (Syton). EBSD data were collected using a JEOL 6500 field emission SEM using Oxford Aztek software, which was then processed with the MTEX toolbox (Bachmann et al., 2010). EBSD maps were collected of an entire section (cut along the deformation axis) of each sample at a 10 µm step size. Non-indexed points with five or more neighboring points belonging to a single grain were interpolated. Schmid factors were calculated for the (010)[100], (010)[001], (001)[100], and (100)[001] slip systems from these maps, which were used in fitting a mechanical model designed to describe the viscous anisotropy of these samples.

5.4 Results

Anisotropic strength was measured during high-temperature deformation of cores of natural dunites with preexisting CPOs. The stress measured at the same nominal strain rate varied among samples. Stress-strain curves from each experiment are presented in Figure 2a. In each case, samples yielded at relatively low strain, then harden to a nearly steady-state stress at ~7% strain at the fastest applied strain rate. Upon stepped reduction of strain rate, samples relaxed to a new, nearly steady-state value over roughly 2.5% strain for each step. The final stress from each rate step was used to fit each experiment to a power law of the form

$$\dot{\varepsilon} = A\sigma^n \quad (1)$$

to the results from each experiment, where $\dot{\varepsilon}$ is the strain-rate, A is a material-dependent pre-factor, σ is the differential stress, and n is the stress exponent. As summarized in Figures 2b and 2c, a stress exponent of n = 3.2 to 3.9 was determined across all experiments, with a mean of n = 3.6. This value is broadly consistent with models of deformation by dislocation creep and those reported in other studies of experimental deformation of naturally sourced coarse-grained dunites (Chopra and Paterson, 1984; Keefner, 2011). This value for the stress exponent is also similar to those measured from deformation of olivine single crystals and synthetic, reconstituted dunites where deformation was attributed to dislocation creep (Durham and Goetze, 1977; Bai and Kohlstedt, 1991; Hirth and Kohlstedt, 2003; Hirth and Kohlstedt, 2015; Mullet et al., 2015). If n is fixed at 3.6 so that power-law relationships for all of the samples could be directly compared, the values of the pre-factor range from $A = 1.1\times10^{-13}$ $MPa^{-3.6}s^{-1}$ to $A = 2.9\times10^{-13}$ MPa^{-}

$^{3.6}s^{-1}$, a factor of 2.6 difference in viscosity at the same stress between the strongest and weakest orientations tested. The data are bounded by the strengths of single crystals oriented for slip on each of the dominant slip systems and fall near the strength of single crystals in the $[101]_c$ orientation (Bai et al., 1991), Figure 2b.

The samples have significant CPOs revealed by EBSD measurements, as summarized with the pole figures in Figure 3. The M-index, quantifying fabric strength (Skemer et al., 2005), measured from each deformed sample ranges from M = 0.11 to 0.17 (J-index = 2.5–2.9), slightly less than the M-index measured from the starting material of M = 0.20 (J-index = 3.4). These CPO strengths are consistent with those measured previously from nearby rocks collected from the same outcrop (Warren et al., 2008). A maximum of only 12% strain was imposed during our deformation experiments, such that the measured fabric is approximately representative of the preexisting CPO of each sample with only slight modification by the experimentally imposed deformation. EBSD maps of both the dehydrated starting material and the deformed samples, reveal a microstructure containing lobate grains and a broad grain-size distribution, as demonstrated in Figure 4. Grains are cut by pervasive relict fractures. Fracture surfaces appear to be open in the dehydrated starting material but closed after samples are heated and deformed under confining pressure. The closure of relict fractures is also apparent in the optical micrographs presented in Figure 1.

Maps of Schmid factor (relative resolved shear stress) for each of the primary dislocation slip systems demonstrate that samples in different orientations have broadly varying populations of grains well-oriented for slip (Fig. 5). Samples with the nominal orientations $[110]_c$ and $[101]_c$ contain many grains oriented with high resolved shear stress on the easiest slip systems, (010)[100] and the paired (001)[100] and (100)[001] (which always have the same resolved shear stress). Samples with the nominal orientations [001] and [010], however, have very few grains oriented with high resolved shear stress on these slip systems, but they do contain a significant number of grains oriented well for slip on the hard (010)[001] slip system. The sample with the nominal [100] orientation is intermediate, with some grains oriented reasonably well for slip on the two easiest slip systems and few well-oriented for slip on the hardest slip system. We emphasize that the notation of nominal orientation is useful for orienting the hand sample relative to the CPO but that each core contains a broad population of grain orientations. Given the large grain size of these samples, some sample-to-sample heterogeneity is expected, such

that large-scale EBSD maps of each sample are necessary to quantify the microstructure and relate that microstructure to measured mechanical properties.

Overall, the mean values of the Schmid factor measured for each sample on the easiest slip systems, (010)[100] and the (100)[001] and [100](001) pair, correlate with the measured relative strength. We applied a modified power-law equation with the form, $\dot{\varepsilon} = \mathrm{F}A_0\sigma^n$ to analyze the relative strengths measured in our experiments, where A_0 is a reference pre-factor and F is the strain-rate enhancement factor. The value of A_0 was taken as the pre-factor calculated from the power-law fit with the stress exponent fixed to n = 3.6 to the strongest orientation, where the [010] direction is dominantly aligned with the axis of the sample. The strain-rate enhancement, F, is plotted in Figure 6a against the mean value of the Schmid factor to evaluate the influence of CPO on anisotropic viscosity. A similar approach of comparing mean Schmid factor to strain-rate enhancement was used successfully by Azuma (1995) to interpret the mechanical behavior of ice with a preexisting CPO. A correlation between strain-rate enhancement and mean Schmid factors is clearly apparent in Figure 6a. In Figure 6b, the single-crystal flow laws from Bai et al., (1991) are added to highlight the relative strength of each of the slip systems, verifying that the trends in the data from this study are consistent with the relative strengths of the slip systems determined from single crystal deformation experiments. A simple mechanical model that incorporates single-crystal flow laws and measured values of Schmid factors is developed in the following section.

5.5 Discussion

Viscous anisotropy, with a maximum relative strength contrast of 2.6, was measured experimentally on a series of cores taken from a hand sample with an A/D-type CPO of intermediate fabric intensity. Broadly, the magnitude of the measured strengths of these samples were consistent with the results of similar experiments on nickel-jacketed samples by Keefner et al. (2011), intermediate relative to that measured from experiments on oriented single crystals and falling close to single crystals deformed in the $[101]_c$ orientation. Their study, however, did not specifically address anisotropy due to preexisting CPOs. The magnitude of anisotropy that we measured experimentally is broadly consistent with multiscale numerical models that simulated deformation of dunites with fabrics of similar intensity and geometry, yielding calculated strength contrasts ranging from 1.5 to 3 (Knoll et al. 2009). Results from

torsion experiments on samples of hot-pressed iron-rich olivine by Hansen et al. (2012b) predict a maximum strength contrast of roughly 5 for a similar fabric intensity. However, their experiments were performed in the dislocation-accommodated grain boundary sliding (disGBS) regime, and their samples also have strong grain shape preferred orientations (SPOs). Strong SPOs may lead to enhanced anisotropy in viscosity in the disGBS regime because alignment of grain boundaries may allow for enhanced sliding in the direction of the long axes of grains. Therefore, one might expect some disagreement between our results and theirs.

Calibration of multiscale models, incorporating grain-scale to continuum-scale deformation, with experiments on dunites with a preexisting CPO is a promising future path for a detailed understanding of anisotropic viscosity. Hansen et al. (2016b), who applied this type of approach, found generally good agreement between experiment and grain-scale models. Comparisons of experimental data on hot-pressed iron-rich olivine to grain scale modeling was further explored Mameri et al. (2019), using VPSC simulations. VPSC simulations have been broadly applied to model the CPO evolution during deformation of olivine aggregates (Tommasi et al., 2000; Boneh et al., 2015). VPSC models use a simplified approach to account for strain compatibility and grain neighbor interactions. However, the limited data currently available that address this problem, combined with the complexity of multiscale modeling, motivates the use of a simpler framework for assessing the anisotropic viscosity of deformed dunites. Below we apply a simple mechanical model to evaluate viscous anisotropy in our experiments.

5.5.1 Effective Medium Theory for Describing Anisotropic Viscosity

Stress – strain rate data from high-temperature deformation experiments on polycrystalline materials are often fit to a power-law relationship of the form

$$\dot{\varepsilon} = A'\sigma^n \, exp\left(-\frac{Q}{RT}\right). \quad (2)$$

where Q is the activation energy, T is the temperature, and R is the gas constant. This constitutive equation assumes that deformation occurs by a single, thermally activated mechanism and that the material is isotropic – simplifying the strain rate and stress tensors to single-valued scalars in the principal reference frame of deformation. Since our experiments were all conducted at the same temperature, we use the further simplified expression given in equation (1). However, non-linear, power-law behavior can be generalized for isotropic materials to an arbitrary spatial reference frame using the relation

$$\dot{\varepsilon}_{ij} = 3^{-(n+1)/2}\Phi\sigma_e^{n-1}\sigma_{ij}, \quad (3)$$

where σ_e is the equivalent (von Mises) stress, which is proportional to the second invariant of the deviatoric stress tensor, σ_{ij} and $\dot{\varepsilon}_{ij}$ are the components of the deviatoric stress tensor and strain-rate tensors, respectively, and Φ is a material dependent pre-factor equal to the fluidity (the inverse of viscosity) when *n* = 1 (Karato, 2008, p. 37).

For linear creep mechanisms (*n* = 1), such as diffusion creep, this formalism can be simply extended to anisotropic materials, such that

$$\dot{\varepsilon}_{ij} = \Phi_{ijkl}\sigma_{kl}, \quad (4)$$

where Φ_{ijkl} is the fourth-rank fluidity tensor (Kohlstedt and Hansen, 2015). The components of the fluidity tensor are further restricted by material symmetry and volume conservation, such that for orthorhombic olivine, only six components are independent (Hansen et al., 2012b). However, extension to non-linear deformation is less straightforward. Kohlstedt and Hansen (2015) proposed the use of the constitutive equation

$$\dot{\varepsilon}_i = 3^{-(n+1)/2}\Phi_{ij}\sigma_e^{n-1}\sigma_j, \quad (5)$$

converting to Voigt notation, where stress and strain rate are represented as six-component vectors and the fluidity tensor is represented as a six-by-six second-rank tensor. This approach was applied by Király et al. (2020) to model the role of viscous anisotropy on deformation in Earth's mantle. This constitutive equation incorporates anisotropy into non-linear deformation but restricts the stress exponent to a single isotropic value. However, it is possible to imagine unrealistic outcomes using this functional form. For example, for a crystal with a single slip system, the above flow law implies that the strain rate resulting from dislocation motion on the single slip system will be influenced by shear stresses on orthogonal planes. Such complications highlight the difficulty of fully representing anisotropic non-linear deformation.

Regardless, for general scenarios, the fluidity tensor may be convenient because it can be reasonably implemented in large-scale geodynamic models (Mameri et al., 2021). The bulk fluidity tensor can be estimated using grain scale models, such as the VPSC method, or, simply constrained by commonly employed effective-medium theories (Mainprice and Humbert, 1994). In the bound of uniform stress (Sachs, 1928), the bulk fluidity tensor can be calculated from individual grain fluidity tensors by averaging over them, such that

$$\Phi_{ij} = \frac{1}{N}\sum_g \Phi_{ij}^g \,, \tag{6}$$

where *g* is the grain index and *N* is the number of grains considered. Alternatively, in the bound of uniform strain rate (Taylor, 1938), the bulk fluidity tensor is calculated by averaging the inverse of the fluidity tensor of each grain, such that

$$\Phi_{ij} = \left(\frac{1}{N}\sum_g (\Phi_{ij}^g)^{-1}\right)^{-1}. \tag{7}$$

Empirical determination of the grain scale fluidity tensor from experimental data is a promising direction forward for analyzing anisotropic viscosity and assessing grain scale models, however, this analytical framework is considered still more complex than necessary for the analysis of our relatively simple set of experiments.

5.5.2 Simplified Schmid Factor (Resolved Shear Stress) Model for Describing Anisotropic Viscosity

We have applied a further simplified model to our experimental data, following the concepts of effective medium theory, described above, but limiting our analysis to the principal reference frame of deformation. We use Schmid's law to incorporate individual grain orientations and account for anisotropy. This model again reduces stress and strain rate to single-valued scalars and ignores cross terms that result from generalized anisotropy, wherein normal stresses can lead to shear strains. The analysis begins with the well-known Schmid's law, which states

$$\tau_r = S\sigma, \tag{8}$$

with

$$S = \cos(\varphi)\cos(\lambda), \tag{9}$$

where τ_r is the resolved shear stress on the dislocation slip system being considered; *S* is the Schmid factor, which relates the orientation of the slip system to the orientation of the applied stress; and $\varphi$and λ are the angles between the applied normal stress and the glide plane and the glide direction, respectively. The single-crystal flow laws from Bai et al. (1991), used in our analysis, were generated by axial compression experiments with known slip systems oriented for maximum resolved shear stress, such that *S* = 0.5. These flow laws generally take the form of equation (2). For an arbitrary compression orientation, considering only the contribution to axial shortening due to activity of the slip system isolated in the original compression

experiments, the following modification to the flow law must be made:

$$\dot{\varepsilon}_{ss} = \sqrt{2}\cos(\lambda)\, A'(2S\sigma)^n \exp\left(-\frac{Q}{\mathrm{R}T}\right). \quad (10)$$

To further simplify our model such that strain rates are a simple function of Schmid factor, applied stress, and temperature, we make the approximation that the geometric term, $\sqrt{2}\cos(\lambda)$, is equal to 1. This substitution implies that slip is evenly partitioned between shortening and lateral offset, which is only always true for the case of S = 0.5. However, for a given Schmid factor, the even partitioning of strain between shortening and lateral offset is the average of possible outcomes and is, therefore, a reasonable approximation. This analysis also assumes that strains are small and that lattice rotation is unimportant. An equivalent substitution was used in the analysis of Raterron et al. (2011).

With this substitution, single-crystal flow laws developed from the results of axial compression experiments can be used to generate an approximate axial compression flow law for an arbitrary orientation. For the dominant slip systems in olivine, flow laws for the orientations $[110]_c$, $[101]_c$, and $[011]_c$ become functions of the appropriate Schmid factors and are summed to generate a flow law for a grain in an arbitrary orientation as follows:

$$\dot{\varepsilon}_1 = \dot{\varepsilon}_{[110]c}\left(S_{(010)[100]}, \sigma_{\mathrm{applied}}, T, p\mathrm{O}_2\right),$$

$$\dot{\varepsilon}_2 = \dot{\varepsilon}_{[101]c}\left(S_{(010)[100]}, \sigma_{\mathrm{applied}}, T, p\mathrm{O}_2\right),$$

$$\dot{\varepsilon}_3 = \dot{\varepsilon}_{[011]c}\left(S_{(010)[100]}, \sigma_{\mathrm{applied}}, T, p\mathrm{O}_2\right),$$

and

$$\dot{\varepsilon}_{grain} = \dot{\varepsilon}_1 + \dot{\varepsilon}_2 + \dot{\varepsilon}_3. \quad (11)$$

We note that the paired (001)[100] and (100)[001] slip systems have the same Schmid factor and are both activated during $[101]_c$ compression, such that they cannot be accounted for separately. For a uniform grain size in the uniform-stress bound, the predicted aggregate strain rate is estimated as

$$\dot{\varepsilon}_{predicted} = \frac{1}{N}\sum \dot{\varepsilon}_{grain}. \quad (12)$$

In our analysis, we weight the contribution of each grain by its area in EBSD maps, thus approximating its fractional contribution to strain. This simple model ignores the necessity of strain compatibility and the role of neighbor-grain interactions.

When applied to our data, predicted strain rates from the model correlate well with the strain rates normalized to a constant stress, using power-law fits to the mechanical data. The correlation of the model to the relative strengths of differently oriented cores highlights the assertion that these experiments successfully measured viscous anisotropy in dunite with a preexisting CPO. However, at the stresses measured during our experiments, this analysis yields predicted strain rates that are consistently lower than those imposed in our experiments. This point is illustrated in Fig. 7a, where the correspondence between the data and the predictions from the model are plotted at the measured stress of each rate step (unnormalized). When normalized to a single stress (fixing the stress exponent to n = 3.6), the measured anisotropy is clear, and similar in magnitude to that predicted by the model, as demonstrated in Fig. 7b. Comparisons of the model predictions to the experimental data, normalized to 100, 150, and 200 MPa, using the experimentally determined stress exponent for each experiment (n) are also presented in Figure 7c, further illustrating the correlation between the predicted and measured anisotropy. This result is further explored with VPSC calculations in the Appendix.

The observation that experimental strain rates are faster than predicted by the model, suggests that other mechanisms besides dislocation creep, accommodated by intragranular slip, are important to deformation. The simple model used in our analysis predicts an upper bound on deformation attributable to intracrystalline deformation; therefore, other deformation mechanisms, such as diffusion creep and disGBS, must be active to account for the observed deformation. A similar analysis of high-pressure deformation experiments on olivine aggregates presented by Raterron et al., 2019 made the same inference. It is likely that grain boundary sliding of finer grained material along relict fracture surfaces contributes to deformation, which may relax neighbor-grain restrictions. Also, samples may contain a small amount of melt, which would also reduce the viscosity.

5.5.3 Experimental Limitations

The experimental results presented in this study demonstrate that the viscosity of dunites with a preexisting CPO is anisotropic; however, we note that the large grain size and complex microstructure of the starting material introduces some experimental limitations. After dehydration of alteration phases, a heavily fractured microstructure is left behind (Figs. 1a and 4). During hydrostatic annealing and deformation at 300 MPa confining pressure, these fractures close; however, fine-grained material is present along relict fracture interfaces. These fine-grained features are highlighted by the EBSD map presented in Figure 8, made with a step

size of 0.5 μm. While indexing of phases is poor in the fine-grained regions, band contrast maps reveal the grain-scale microstructure. Most of these grains are less than 5 μm and many were indexed as olivine. At the conditions of our experiments, diffusion creep and disGBS is likely active in these fine-grained regions. Some of the observed deformation is almost certainly accommodated by shear of fine-grained material along these relict fractures. However, bulk plastic flow was observed, and offsets along relict fractures at the edges of the sample were not observed after deformation, indicating that shear along relict fracture surfaces was limited. Further, the coincidence of relative strength and resolved shear stress on the dominant slip systems indicates that measured anisotropy was due to orientation of the preexisting CPO rather than secondary features. The large grain size of the dunite used in these experiments also makes sample-to-sample heterogeneity likely. Extension of this work might be best undertaken by identifying a finer grained dunite with minimal alteration and fractures.

5.6 Conclusions

We performed high-temperature deformation experiments on naturally sourced dunite with a preexisting CPO in order to investigate anisotropic viscosity. We measured a maximum effective viscosity contrast of 2.6 between the orientations tested when compared at constant stress. The dunite used in this study had an intermediate fabric intensity and, therefore, is likely to represent an intermediate viscous anisotropy. Further, the initial microstructure was heavily fractured, with fine-grained material along relict fracture interfaces, and may also contain a small amount of melt, both of which likely contribute to deformation and reduce the measured anisotropy. Therefore, our measurements likely represent a lower bound of the viscous anisotropy in Earth's mantle. A simplified effective-medium model fit the data reasonably well and demonstrated that viscous anisotropy was clearly measured in our experiments. This type of analysis may be a useful, simple formulation for analyzing anisotropic viscosity in future experimental studies. VPSC calculations, incorporating EBSD measurements made on our samples, also correlate well with our data, and support the interpretations drawn from our relatively simple analysis.

5.7 Appendix: VPSC Calculations

A set of VPSC calculations were performed to further support the analysis of our experimental results. The tangent VPSC model is described by Lebensohn and Tomé, (1993) and was applied to olivine by Tommasi et al. (2000), to predict CPO evolution in olivine aggregates. Later, the second order VPSC formulation was introduced (Ponte Castañeda, 2002), which was applied by Mameri et al. (2016) to model anisotropy in viscosity of experimentally deformed synthetic olivine aggregates. We modeled our experiments using the second order VPSC method such that a direct comparison can be made to this earlier study. The grain orientations measured from EBSD maps of the experimentally deformed samples were used as the initial texture of the modeled aggregates. In the calculations, an axial compression stress boundary condition was imposed (consistent with experimental conditions), and the modeled aggregate was deformed to 1% equivalent strain at a set rate. The nondimensional critical resolved shear stresses (CRSSs) used in our calculations are shown in Table 2 and are the same as used by Mameri et al. (2016). A stress exponent of n=3 was used for all slip systems in the calculation. Pyramidal slip systems with a slip plane of {111} are included as "dummy" slip systems to close the yield surface and mimic additional isotropic strain accommodation mechanisms. Variation of the CRSS of these systems (β) changes the relative contribution of secondary isotropic mechanisms. We ran calculations using β=50 and β=5, along with a lower-bound uniform stress model (Sachs, 1928) with the same CRSS values and boundary conditions as used for the VPSC models, to evaluate the role of secondary mechanisms in modeling our experimental results. Using the stresses predicted by our models we calculated the F value for each model run, using a stress exponent for the aggregate of n = 3.5 and normalizing by the strength of the strongest sample. The results of these calculations are presented in Figure 9.

Broadly, the results of these additional calculations correlate well with our experimental data and support the inference that strength variations that we measured experimentally are related anisotropy that results from the pre-existing CPO. When isotropic mechanisms are limited (β=50), the overall predicted magnitude of anisotropy is larger than measured experimentally. When secondary mechanisms are included (β=5 and lower-bound models) the overall magnitude of anisotropy is better predicted for most sample orientations, however the sample oriented down the [101]c direction is predicted to be relatively strong, in contrast to our experimental results. These results indicate that secondary mechanisms likely contribute to

deformation in our experiments, relaxing neighbor-grain restrictions, which supports the applicability of the simplified Schmid factor model used to analyze our experimental results.

5.8 Acknowledgements

This work is supported in part by the Department of Energy National Nuclear Security Administration Stewardship Science Graduate Fellowship (to C.D.M) and the National Science Foundation [grant number EAR-1755805] (to D.L.K.). Parts of this work were carried out in the Characterization Facility, University of Minnesota, which receives partial support from NSF through the MRSEC program. We would like to thank Lars Hansen and Jessica Warren for supplying the hand sample used for deformation experiments. We would also like to thank Zachary Michels for his help with EBSD measurements and Lucan Mameri for his assistance with VPSC calculations. In addition, we would like to thank Andréa Tommasi and an anonymous reviewer for their helpful comments.

5.9 References

Azuma, N. (1995). A flow law for anisotropic polycrystalline ice under uniaxial compressive deformation. Cold Regions Science and Technology, 23(2), 137–147.

Bachmann, F., Hielscher, R., & Schaeben, H. (2010). Texture Analysis with MTEX – Free and Open Source Software Toolbox. Solid State Phenomena, 160, 63–68.

Bai, Q., Mackwell, S. J., & Kohlstedt, D. L. (1991). High-temperature creep of olivine single crystals 1. mechanical results for buffered samples. Journal of Geophysical Research, 96(B2), 2441–2463.

Bai, Q., & Kohlstedt, D. L. (1992). High-temperature creep of olivine single crystals, 2. dislocation structures. Tectonophysics, 206(1–2), 1–29.

Becker, T. W., Chevrot, S., Schulte-Pelkum, V., & Blackman, D. K. (2006). Statistical properties of seismic anisotropy predicted by upper mantle geodynamic models. Journal of Geophysical Research: Solid Earth, 111(8), 1–16.

Becker, T. W., Kellogg, J. B., Ekström, G., & O'Connell, R. J. (2003). Comparison of azimuthal seismic anisotrophy from surface waves and finite strain from global mantle-circulation models. Geophysical Journal International, 155(2), 696–714.

Boneh, Y., Morales, L. F., Kaminski, E., & Skemer, P. (2015). Modeling olivine CPO evolution

with complex deformation histories: Implications for the interpretation of seismic anisotropy in the mantle. Geochemistry, Geophysics, Geosystems, 16(10), 3436-3455.

Bystricky, M., Kunze, K., Burlini, L., & Burg, J.-P. (2000). High shear strain of olivine aggregates: Rheological and seismic consequences. Science, 290(5496), 1564–1567.

Chatzaras, V., Kruckenberg, S. C., Cohen, S. M., Medaris, L. G., Withers, A. C., & Bagley, B. (2016). Axial-type olivine crystallographic preferred orientations: The effect of strain geometry on mantle texture. Journal of Geophysical Research: Solid Earth, 121(7), 4895–4922.

Christensen, U. R. (1987). Some geodynamical effects of anisotropic viscosity. Geophysical Journal of the Royal Astronomical Society, 91(3), 711–736.

Durham, W.B., & Goetze C. (1977). Plastic flow of oriented single crystals of olivine: 1. Mechanical data. Journal of Geophysical Research 82(36), 5737-5753.

Gatzemeier, A., & Moorkamp, M. (2005). 3D modelling of electrical anisotropy from electromagnetic array data: Hypothesis testing for different upper mantle conduction mechanisms. Physics of the Earth and Planetary Interiors, 149(3–4), 225–242.

Gatzemeier, A., & Tommasi, A. (2006). Flow and electrical anisotropy in the upper mantle: Finite-element models constraints on the effects of olivine crystal preferred orientation and microstructure. Physics of the Earth and Planetary Interiors, 158(2–4), 92–106.

Han, D., & Wahr, J. (1997). An analysis of anisotropic mantle viscosity, and its possible effects on post-glacial rebound. Physics of the Earth and Planetary Interiors, 102(1–2), 33–50.

Hansen, L. N., Zimmerman, M. E., & Kohlstedt, D. L. (2012). The influence of microstructure on deformation of olivine in the grain-boundary sliding regime. Journal of Geophysical Research: Solid Earth, 117(9), 1–17.

Hansen, L. N., Zimmerman, M. E., & Kohlstedt, D. L. (2012). Laboratory measurements of the viscous anisotropy of olivine aggregates. Nature, 492(7429), 415–418.

Hansen, L. N., Conrad, C. P., Boneh, Y., Skemer, P., Warren, J. M., & Kohlstedt, D. L. (2016). Viscous anisotropy of textured olivine aggregates: 2. Micromechanical model. Journal of Geophysical Research: Solid Earth, 121(10), 7137–7160.

Hansen, L. N., Warren, J. M., Zimmerman, M. E., & Kohlstedt, D. L. (2016). Viscous anisotropy of textured olivine aggregates, Part 1: Measurement of the magnitude and evolution of anisotropy. Earth and Planetary Science Letters, 445, 92–103.

Hansen, L. N., Zhao, Y. H., Zimmerman, M. E., & Kohlstedt, D. L. (2014). Protracted fabric

evolution in olivine: Implications for the relationship among strain, crystallographic fabric, and seismic anisotropy. Earth and Planetary Science Letters, 387, 157–168.

Hirth, G., & Kohlstedt, D. L. (2015). The stress dependence of olivine creep rate: Implications for extrapolation of lab data and interpretation of recrystallized grain size. Earth and Planetary Science Letters, 418, 20–26.

Hirth, G., & Kohlstedt, D. L. (2003). Rheology of the Upper Mantle and Mantle Wedge: A View from the Experimentalists. Geophysical Monograph: Inside the Subduction Factory, 138, 83–105.

Ismaïl, W. Ben, & Mainprice, D. (1998). An olivine fabric database: An overview of upper mantle fabrics and seismic anisotropy. Tectonophysics, 296(1–2), 145–157.

Jung, H., & Karato, S. (2001). Water-Induced Fabric Transitions in Olivine. Science, 293(5534), 1460–1463.

Karato, S. (2008). Deformation of Earth Materials: An Introduction to the Rheology of Solid Earth. 35-37

Katayama, I., Jung, H., & Karato, S. I. (2004). New type of olivine fabric from deformation experiments at modest water content and low stress. Geology, 32(12), 1045–1048.

Keefner, J. W., Mackwell, S. J., Kohlstedt, D. L., & Heidelbach, F. (2011). Dependence of dislocation creep of dunite on oxygen fugacity: Implications for viscosity variations in Earth's mantle. Journal of Geophysical Research, 116.

Király, Á., Conrad, C. P., & Hansen, L. N. (2020). Evolving viscous anisotropy in the upper mantle and its geodynamic implications. Geochemistry, Geophysics, Geosystems, 21(10), e2020GC009159.

Knoll, M., Tommasi, A., Logé, R. E., & Signorelli, J. W. (2009). A multiscale approach to model the anisotropic deformation of lithospheric plates. Geochemistry, Geophysics, Geosystems, 10(8), 1–18.

Kohlstedt, D. L., & Hansen, L. N. (2015). Constitutive Equations, Rheological Behavior, and Viscosity of Rocks. Treatise on Geophysics: Second Edition (Vol. 2). Elsevier B.V.

Lebensohn, R. A., & Tomé, C. N. (1993). A self-consistent anisotropic approach for the simulation of plastic deformation and texture development of polycrystals: application to zirconium alloys. Acta metallurgica et materialia, 41(9), 2611-2624.

Lev, E., & Hager, B. H. (2008). Rayleigh-Taylor instabilities with anisotropic lithospheric viscosity. Geophysical Journal International, 173(3), 806–814.

Lev, E., & Hager, B. H. (2011). Anisotropic viscosity changes subduction zone thermal structure. Geochemistry, Geophysics, Geosystems, 12(4), 1–9.

Long, M. D., & Becker, T. W. (2010). Mantle dynamics and seismic anisotropy. Earth and Planetary Science Letters, 297(3–4), 341–354.

Long, M. D., & Silver, P. G. (2009). Shear wave splitting and mantle anisotropy: Measurements, interpretations, and new directions. Surveys in Geophysics, 30(4–5), 407–461.

Mainprice, D., & Humbert, M. (1994). Methods of calculating petrophysical properties. Surveys in Geophysics, 15, 575–592.

Mameri, L., Tommasi, A., Signorelli, J., & Hansen, L. N. (2019). Predicting viscoplastic anisotropy in the upper mantle: a comparison between experiments and polycrystal plasticity models. Physics of the Earth and Planetary Interiors, 286, 69-80.

Mameri, L., Tommasi, A., Signorelli, J., & Hassani, R. (2021). Olivine-induced viscous anisotropy in fossil strike-slip mantle shear zones and associated strain localization in the crust. Geophysical Journal International, 224(1), 608-625.

Mehl, L., Hacker, B. R., Hirth, G., & Kelemen, P. B. (2003). Arc-parallel flow within the mantle wedge: Evidence from the accreted Talkeetna arc, south central Alaska. Journal of Geophysical Research, 108(B8).

Mullet, B. G., Korenaga, J., & Karato, S. (2015). Journal of Geophysical Research: Solid Earth Markov chain Monte Carlo inversion for the rheology of olivine single crystals. J. Geophys. Res., 120, 3142–3172.

Paterson, M. S. (1990). “Rock deformation experimentation.” The Brittle-Ductile Transition in Rocks, Geophys. Monogr. Ser 56 (pp. 187–194).

Ponte Castañeda, P. (2002). Second-order homogenization estimates for nonlinear composites incorporating field fluctuations: I—theory. Journal of the Mechanics and Physics of Solids, 50(4), 737-757.

Pouilloux, L., Kaminski, E., & Labrosse, S. (2007). Anisotropic rheology of a cubic medium and implications for geological materials. Geophysical Journal International, 170(2), 876–885.

Raterron, P., Chen, J., Geenen, T., & Girard, J. (2011). Pressure effect on forsterite dislocation slip systems: Implications for upper-mantle LPO and low viscosity zone. Physics of the Earth and Planetary Interiors, 188(1–2), 26–36.

Raterron, P., Bollinger, C., & Merkel, S. (2019). Olivine intergranular plasticity at mantle pressures and temperatures. Comptes Rendus Geoscience, 351(2-3), 80-85.

Ricoult, D. L., & Kohlstedt, D. L. (1985). Experimental evidence for the effect of chemical environment upon the creep rate of olivine. In Point Defects in Minerals, Geophys. Monogr. Ser 31 (pp. 171–184).

Sachs, G. (1928). The plastic deformation mode of polycrystals. Z. Ver. Dtsch. Ing., 72, 734.

Skemer, P., Katayama, I., Jiang, Z., & Karato, S.-I. (2005). The misorientation index: Development of a new method for calculating the strength of lattice-preferred orientation. Tectonophysics, 411(1–4), 157–167.

Skemer, P., Warren, J. M., Hansen, L. N., Hirth, G., & Kelemen, P. B. (2013). The influence of water and LPO on the initiation and evolution of mantle shear zones. Earth and Planetary Science Letters, 375, 222–233.

Tasaka, M., Zimmerman, M. E., & Kohlstedt, D. L. (2015). Creep behavior of Fe-bearing olivine under hydrous conditions. Journal of Geophysical Research : Solid Earth, 120, 6039–6057.

Taylor, G. (1938). Plastic deformation of metals. 1, J. Inst. Met., 62, 307.

Tielke, J. A., Hansen, L. N., Tasaka, M., Meyers, C., Zimmerman, M. E., & Kohlstedt, D. L. (2016). Observations of grain size sensitive power law creep of olivine aggregates over a large range of lattice-preferred orientation strength. Journal of Geophysical Research: Solid Earth, 121(2), 506–516.

Tielke, J. A., Zimmerman, M. E., & Kohlstedt, D. L. (2016). Direct shear of olivine single crystals. Earth and Planetary Science Letters, 455, 140–148.

Tommasi, A. (1998). Forward modeling of the development of seismic anisotropy in the upper mantle. Earth and Planetary Science Letters, 160(1–2), 1–13.

Tommasi, A., Mainprice, D., Canova, G., & Chastel, Y. (2000). Viscoplastic self‐consistent and equilibrium‐based modeling of olivine lattice preferred orientations: Implications for the upper mantle seismic anisotropy. Journal of Geophysical Research: Solid Earth, 105(B4), 7893-7908.

Tommasi, A., Knoll, M., Vauchez, A., Signorelli, J. W., Thoraval, C., & Logé, R. (2009). Structural reactivation in plate tectonics controlled by olivine crystal anisotropy. Nature Geoscience, 2(6), 423–427.

Warren, J. M., Hirth, G., & Kelemen, P. B. (2008). Evolution of olivine lattice preferred orientation during simple shear in the mantle. Earth and Planetary Science Letters, 272(3–4), 501–512.

Wendt, A.S., Mainprice, D., Rutter, E., Wirth, R. (1998). A joint study of experimental

deformation and experimentally induced microstructures of pretextured peridotites. Journal of Geophysical Research. 103: 18205-18221.

5.10 Tables

Table 5-1: Summary of experimental results

Nominal Orientation	**Strain Rate** (10^{-5} s^{-1})	**Stress** (MPa)	***n***	***A*** (MPa$^{-3.6}$ s^{-1}) (*n*=3.6)	***F*** (A_o=1.1e-13)	$S_{(010)[100]}$	$S_{(001)[100]/(100)[001]}$	$S_{(010)[001]}$
[100]	2.2	175	3.4	1.9e-13	1.7	0.21	0.20	0.09
	1.1	144						
	0.53	115						
[010]	2.2	202	3.2	1.1e-13	1.0	0.15	0.14	0.25
	1.2	166						
	0.59	134						
[001]	2.1	197	3.6	1.2e-13	1.1	0.14	0.18	0.31
	1.1	166						
	0.53	134						
$[110]_c$	2.0	150	3.9	2.9e-13	2.6	0.27	0.22	0.21
	1.1	128						
	0.60	110						
$[101]_c$	2.1	164	3.9	2.2e-13	2.0	0.19	0.18	0.22
	1.1	140						
	0.56	116						
		Mean:	3.6					

Table 5-2: Cricital resolved shear stresses for each slip system included in VPSC models.

Slip System	Critical Resolved Shear Stress
(010)[100]	1
(001)[100]	1.5
(010)[001]	2
(100)[001]	3
(011)[100]	4
(110)[001]	6
{111}<110>	β
{111}<011>	β
{111}<101>	β

5.11 Figures

Figure 5-1: Micrographs of starting material and deformed specimen

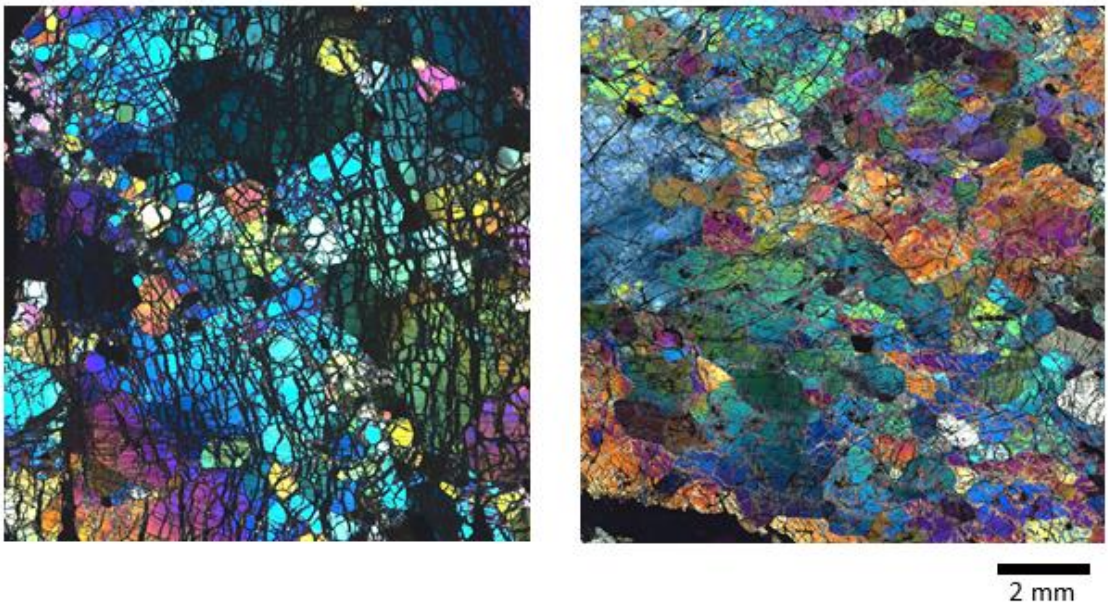

Figure 1: Cross-polarized optical micrographs of thin-sections prepared from dehydrated, undeformed material (left) and statically annealed, deformed material (right).

Figure 5-2: Mechanical data

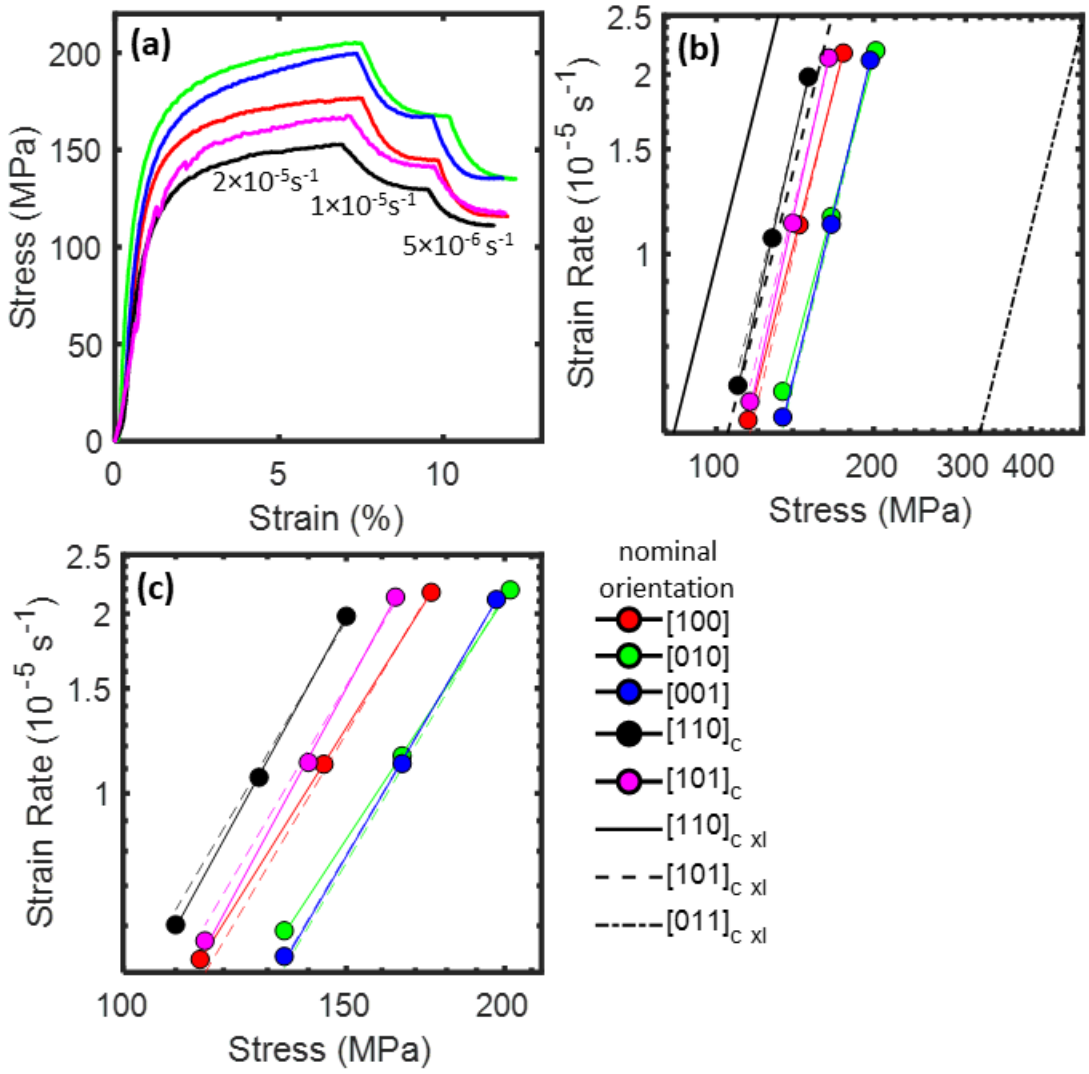

Figure 2: Mechanical data measured from deformation experiments. (a) Stress-strain records labeled with nominal strain rates. (b) Stress versus strain rate measured for dunite samples compared to single-crystal flow laws. Solid colored lines are fits of the data to a power-law equation, and dotted colored lines are fits of the data a power law with the stress exponent fixed at n = 3.6. (c) Stress versus strain rate measured from experiments, highlighting differences in strength between experiments on differently orientated cores.

Figure 5-3: Pole figures

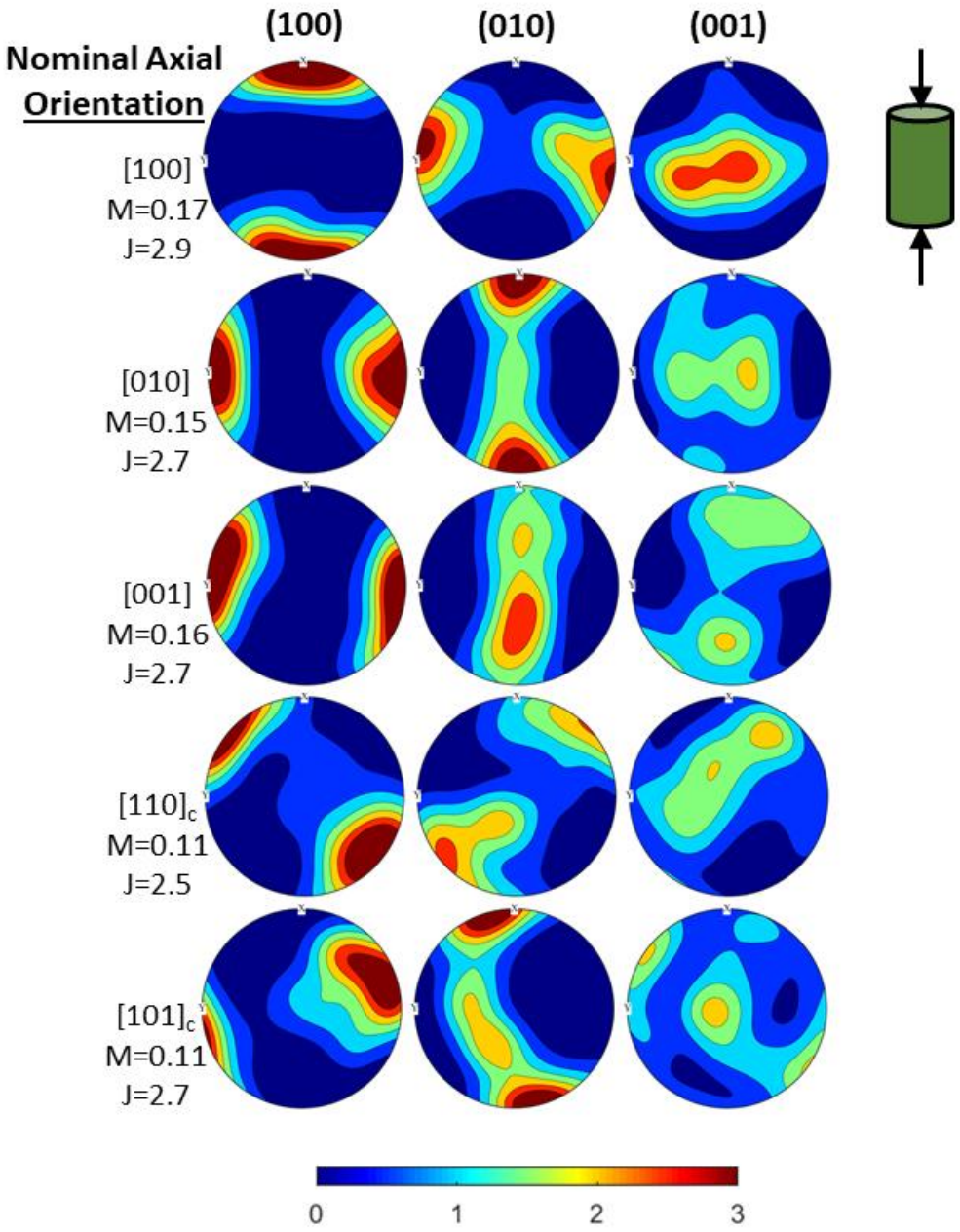

Figure 3: Pole figures calculated from EBSD maps of deformed samples in the specimen reference frame.

Figure 5-4: EBSD maps

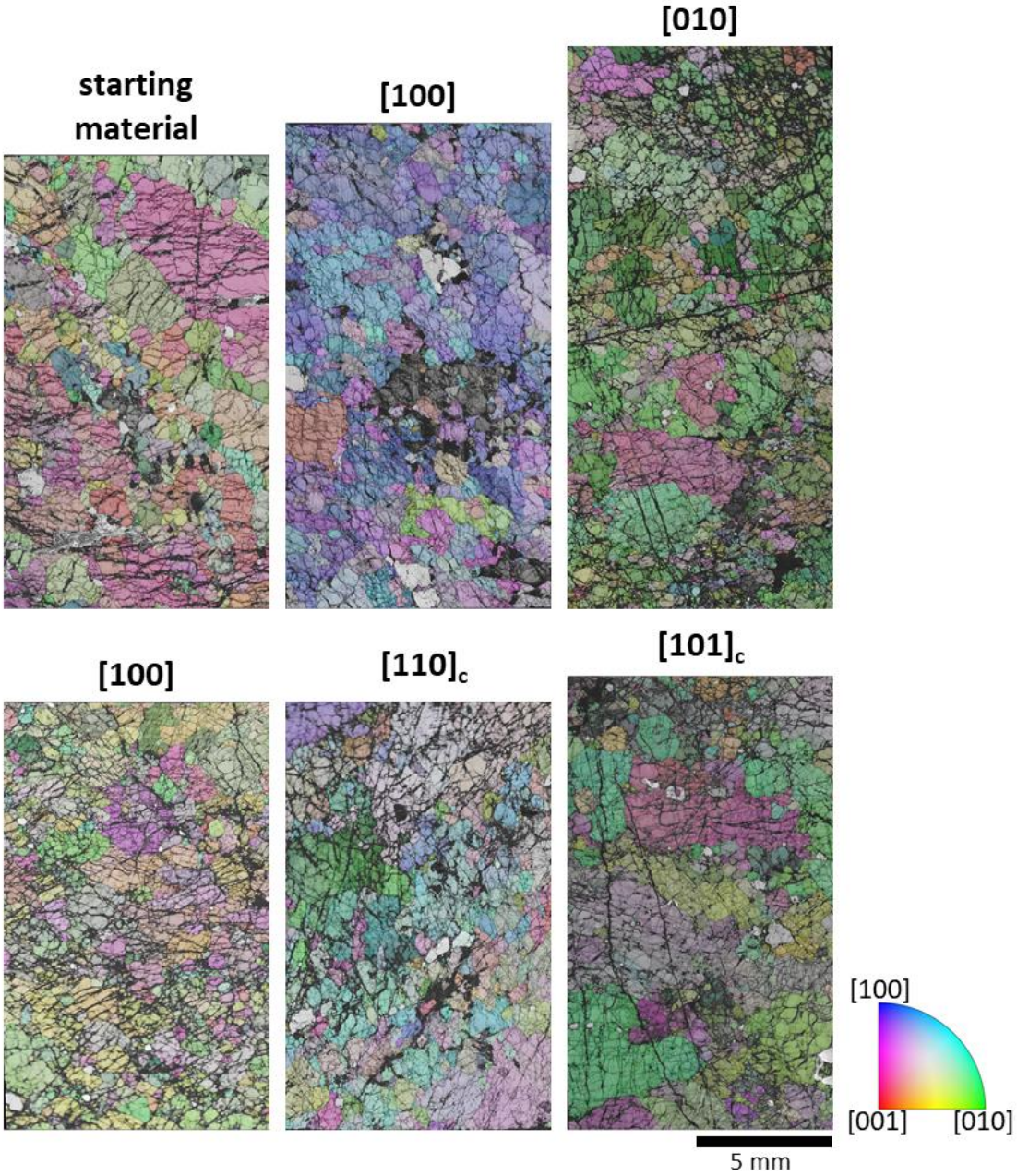

Figure 4: EBSD maps shaded by band contrast and with superimposed inverse pole figure (IPF) coloring (referenced to the compression direction) of indexed olivine grains from dehydrated starting material and deformed samples.

Figure 5-5: Schmid factor maps

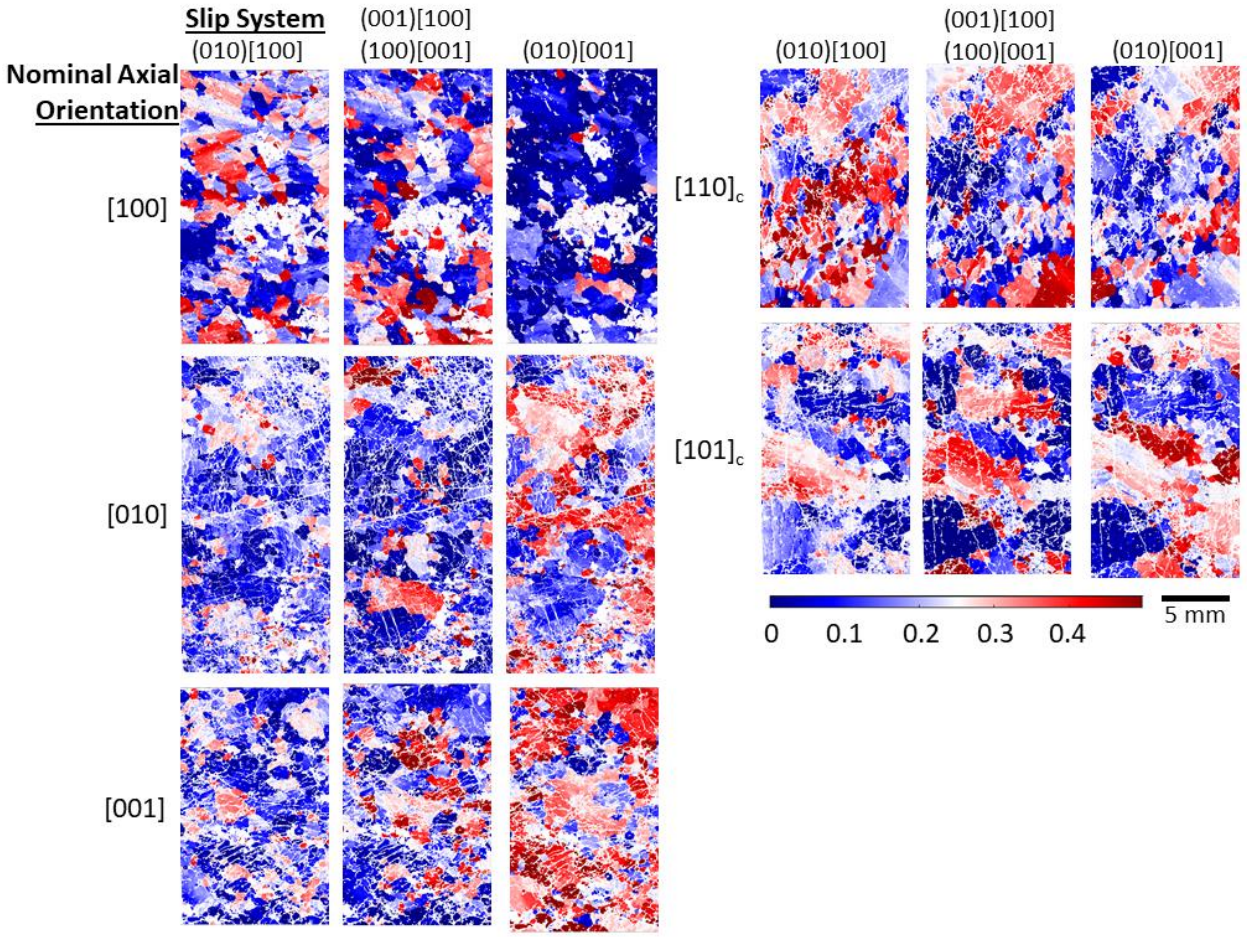

Schmid factor maps for the dominant olivine slip systems, calculated from EBSD maps of deformed samples.

Figure 5-6: Strain rate enhancement factor, F, versus mean Schmid factor

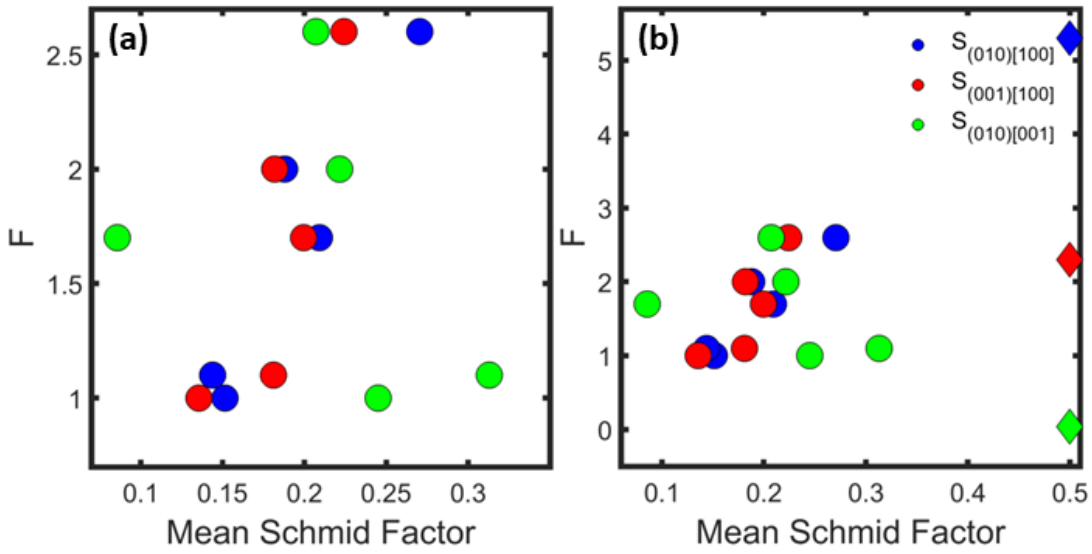

Figure 6: Strain rate enhancement factor, F, versus the mean Schmid factor for (a) the deformed samples and (b) both the deformed samples (circles) and single crystals (diamonds – calculated from single-crystal flow laws of Bai et al. (1991)).

Figure 5-7: Comparison of effective medium model to experimental data

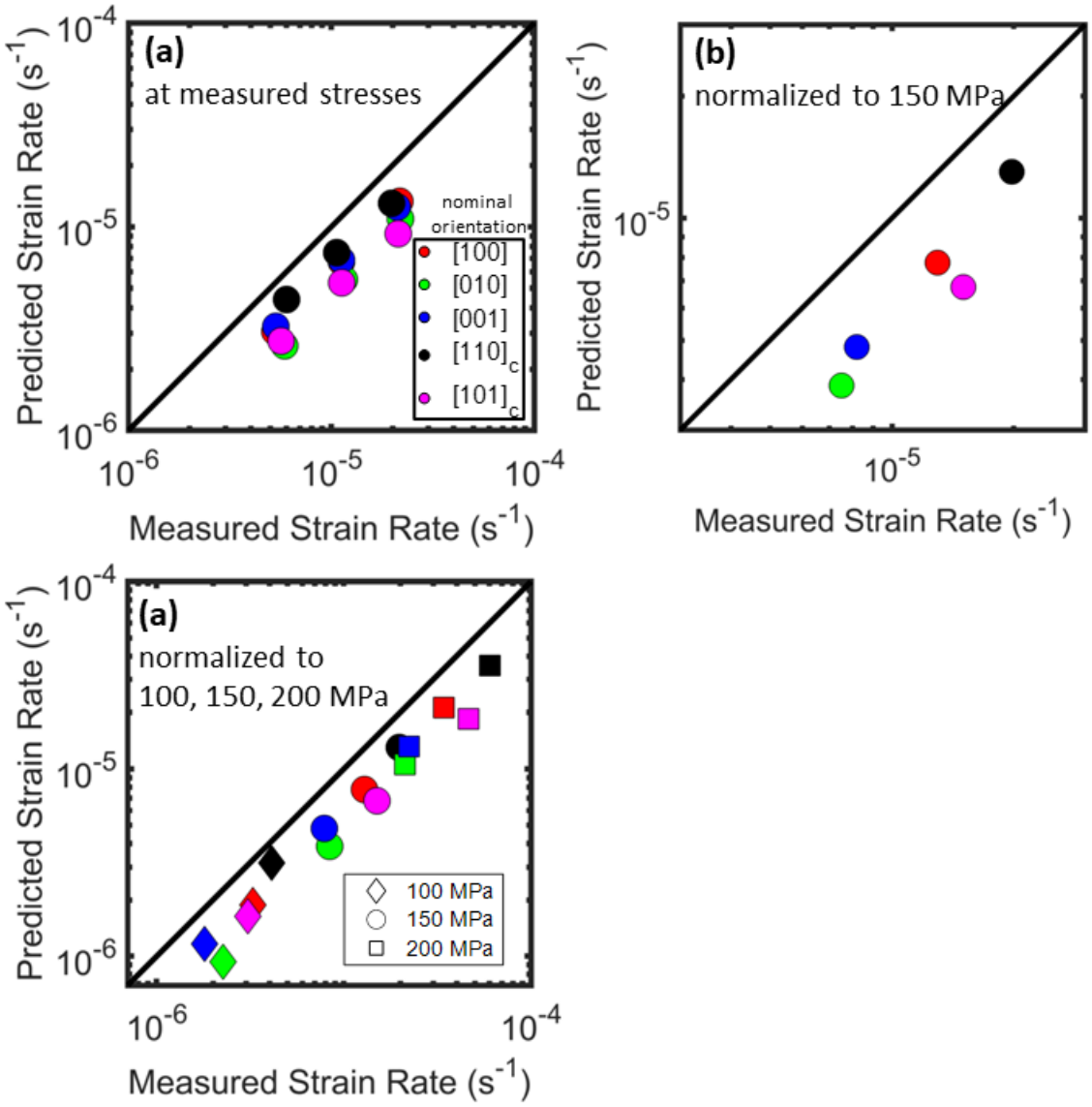

Figure 7: Comparison of measured strain rate to predicted strain rate from a simplified effective-medium model incorporating the single-crystal flow laws of Bai et al. (1991), (a) calculated using the final stress of each strain rate step, (b) calculated normalizing data to 150 MPa using power-law fits to the data with n fixed at 3.6, and (c) calculated normalizing data to 100, 150, and 200 MPa using the experimentally measured stress exponent, n. The solid lines indicate exact correlation between the model and the data.

Figure 5-8: High resolution EBSD map

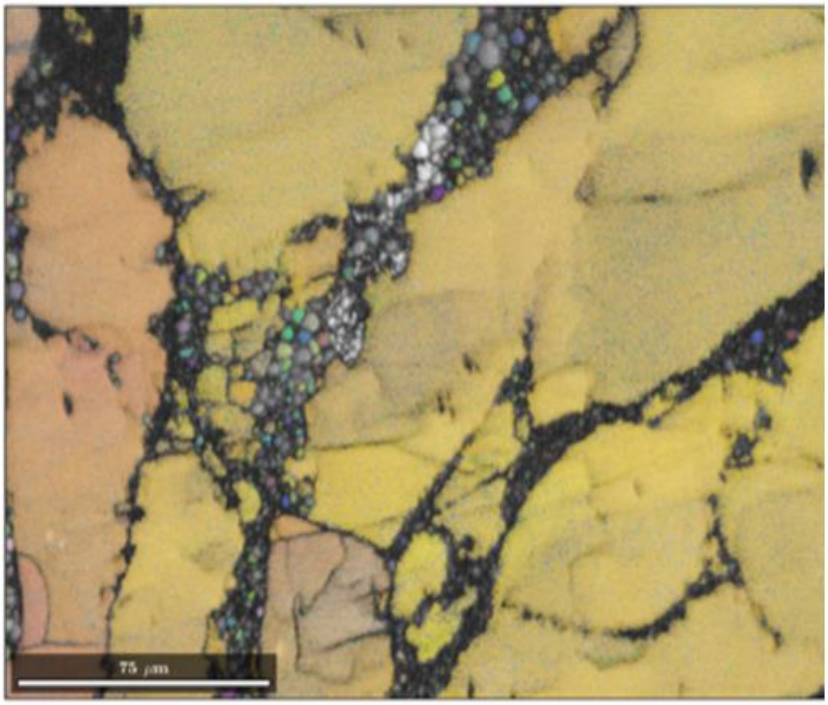

Figure 8: High resolution EBSD map (0.5 μm step size) of a portion of deformed sample material, shaded by band contrast and colored with IPF coloring of indexed olivine grains, demonstrating the presence of fine-grained material that fills relict fracture surfaces.

Figure 5-9: Comparison of VPSC model results to experimental data

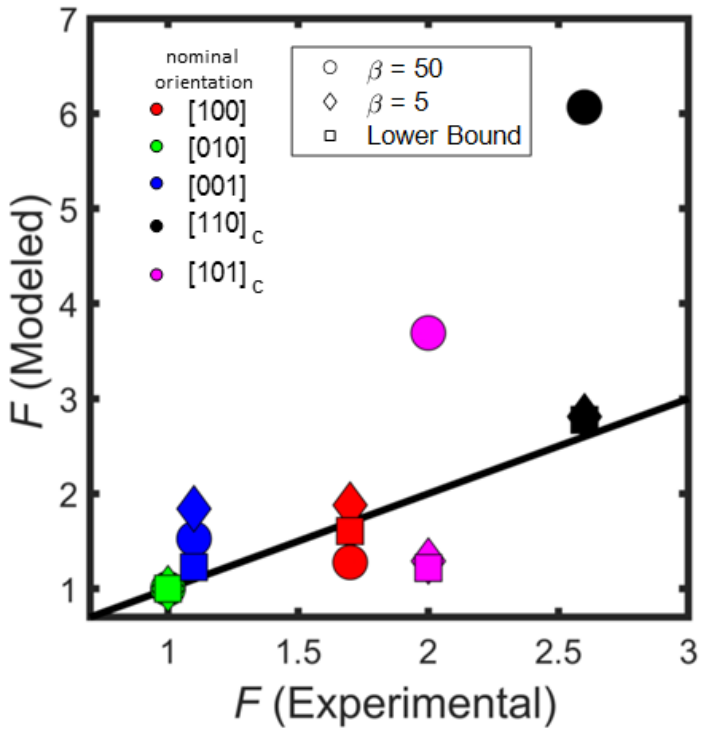

Figure 9: Comparison of modeled and experimentally measured F for β=50, β=5, and lower-bound models.